

DEPARTAMENTO DE ASTROFÍSICA

Universidad de La Laguna

**LOCAL HELIOSEISMOLOGY IN THE TACHOCLINE AND  
THE DEEP PART OF THE CONVECTION ZONE**

---

**HELIOSISMOLOGÍA LOCAL EN LA TACOCLINA Y LA  
PARTE PROFUNDA DE LA ZONA DE CONVECCIÓN**

Memoria que presenta don Manuel Díaz Alfaro  
para optar al grado de  
Doctor por la Universidad de La Laguna.

DIRECTORES DE TESIS:

Dr. D. Fernando J. Pérez Hernández

Dra. D.<sup>a</sup> Irene E. González Hernández



INSTITUTO DE ASTROFÍSICA DE CANARIAS

Junio de 2017

Este documento incorpora firma electrónica, y es copia auténtica de un documento electrónico archivado por la ULL según la Ley 39/2015.  
Su autenticidad puede ser contrastada en la siguiente dirección <https://sede.ull.es/validacion/>

Identificador del documento: 963882

Código de verificación: QDmfX6JG

Firmado por: MANUEL DIAZ ALFARO  
UNIVERSIDAD DE LA LAGUNA

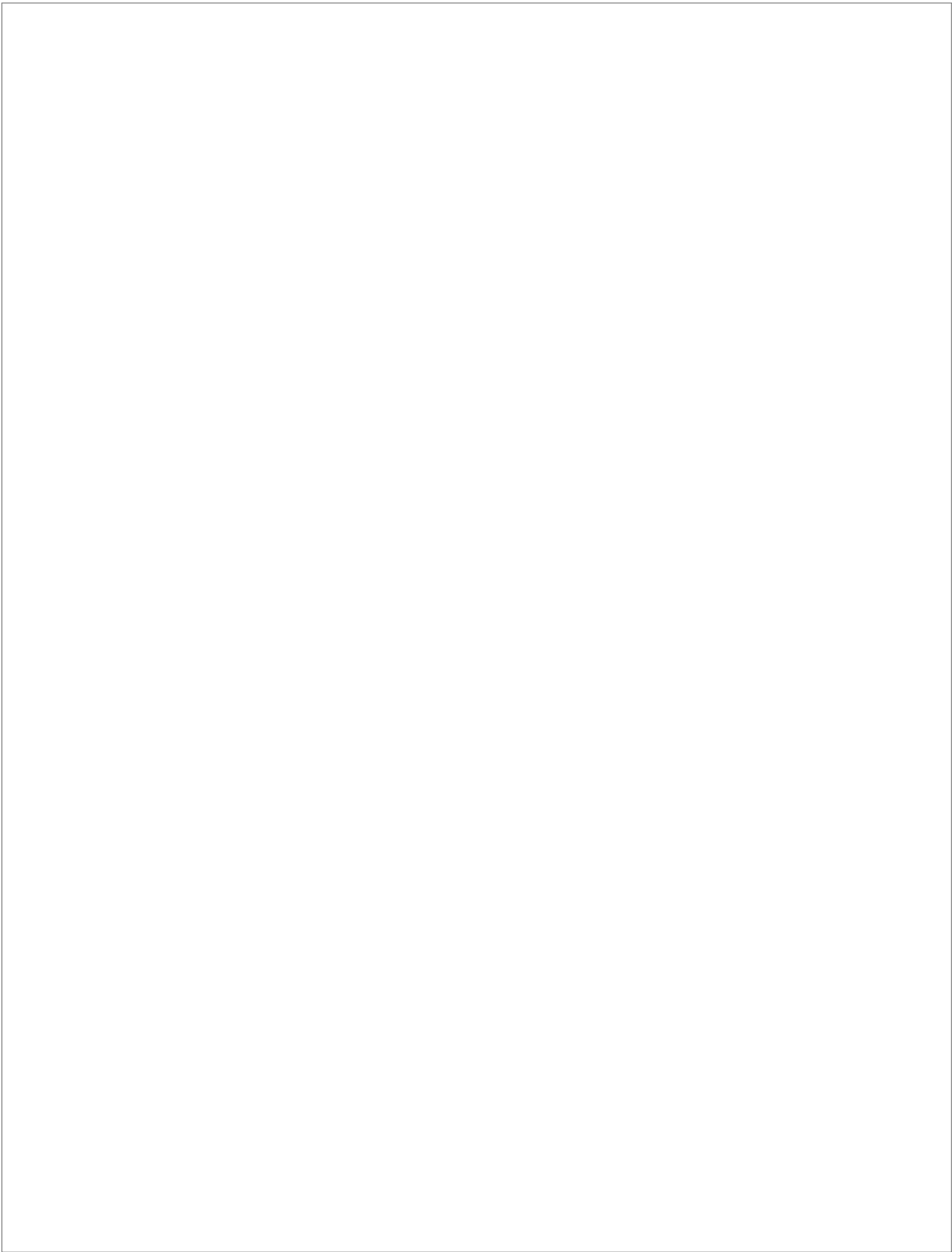
Fecha: 26/06/2017 15:24:15

FERNANDO JAVIER PEREZ HERNANDEZ  
UNIVERSIDAD DE LA LAGUNA

26/06/2017 15:25:57

ERNESTO PEREDA DE PABLO  
UNIVERSIDAD DE LA LAGUNA

28/06/2017 13:21:41



Este documento incorpora firma electrónica, y es copia auténtica de un documento electrónico archivado por la ULL según la Ley 39/2015.  
Su autenticidad puede ser contrastada en la siguiente dirección <https://sede.ull.es/validacion/>

Identificador del documento: 963882

Código de verificación: QDmfX6JG

Firmado por: MANUEL DIAZ ALFARO  
UNIVERSIDAD DE LA LAGUNA

Fecha: 26/06/2017 15:24:15

FERNANDO JAVIER PEREZ HERNANDEZ  
UNIVERSIDAD DE LA LAGUNA

26/06/2017 15:25:57

ERNESTO PEREDA DE PABLO  
UNIVERSIDAD DE LA LAGUNA

28/06/2017 13:21:41

## *Agradecimientos      Acknowledgements*

*El trabajo realizado cuyo fruto final se manifiesta en esta tesis doctoral no habría sido posible sin el concurso, la colaboración y el apoyo de un número importante de personas. En primer lugar me gustaría agradecer y reconocer la labor de mis directores de tesis Fernando e Irene en la supervisión de esta tesis doctoral. Su ánimo, interés, así como sus variadas sugerencias, a lo largo del desarrollo de esta tesis han constituido una contribución importante para haberla podido llevar a buen término. Me gustaría tener un recuerdo especial para Irene, que me acogió y ayudó de manera desinteresada durante el año que estuve viviendo en Tucson y colaborando con ella en el National Solar Observatory. Lamentablemente, la enfermedad ha impedido que pueda haber visto concluido el fruto de este trabajo.*

*Ich möchte auch eine besondere Anerkennung an Herrn Prof. Franx Kneer aussprechen, der mich während 2007-2008 in der Welt der astrophysikalischen Forschung im Bereich der Sonnenphysik eingeführt hat.*

*I would like to acknowledge Dr. Andrew P. Marble and Dr. Anna L. H. Hughes and all the other people from the Solar Interior Group of the NSO Integrated Synoptic Program who contributed to the GCNG ClassicMerge project. Andy and Anna always answered promptly and kindly to my questions about the progress of the merging process and the quality of the resulting merged data.*

*De igual modo, me gustaría agradecer también los comentarios y sugerencias de los revisores de esta tesis. Creo que sus sugerencias han contribuido a clarificar algunos de los argumentos expuestos y, en definitiva, a mejorar la calidad de la tesis.*

*No puedo dejar de mencionar a mi familia, cuyo apoyo continuo y desinteresado me ha ayudado a perseverar en el trabajo realizado en esta tesis. Nada de esto habría sido posible sin la educación y el apoyo de mis padres en todo momento, que siempre me han mostrado su apoyo, tanto cuando decidí empezar mis estudios de física y astrofísica como cuando decidí iniciar el arduo camino de realizar una tesis doctoral en física solar. Mi hermano y mi cuñada, con sus preguntas curiosas sobre las más variadas partes de mi trabajo también han formado un estímulo importante. También quiero hacer patente mi agradecimiento a mi abuela, q. e. p. d., por su continuo interés por saber donde estaba y principalmente por cuándo iba a volver a casa, lo que ha sido también un estímulo importante para continuar.*

*De igual manera, ha habido innumerables personas que me han apoyado y animado a continuar a lo largo de estos años de trabajo doctoral. De Tenerife quería agradecer a mis compañeras de despacho, Esther y Emma, por sus ánimos, consejos y momentos de necesaria desconexión, así como por los English lunches. A Tío Simón y Sobrina Laura por su interés y preguntas frecuentes. Igualmente a M.P.P.I por interesarse y recientemente por haber compartido todo tipo de valiosas informaciones y preocupaciones sobre el proceso de depósito. A los dineros por los numerosos momentos de evasión al solcito o en el interior. También a Lord*

Este documento incorpora firma electrónica, y es copia auténtica de un documento electrónico archivado por la ULL según la Ley 39/2015.  
Su autenticidad puede ser contrastada en la siguiente dirección <https://sede.ull.es/validacion/>

Identificador del documento: 963882

Código de verificación: QDmfX6JG

Firmado por: MANUEL DIAZ ALFARO  
UNIVERSIDAD DE LA LAGUNA

Fecha: 26/06/2017 15:24:15

FERNANDO JAVIER PEREZ HERNANDEZ  
UNIVERSIDAD DE LA LAGUNA

26/06/2017 15:25:57

ERNESTO PEREDA DE PABLO  
UNIVERSIDAD DE LA LAGUNA

28/06/2017 13:21:41

*Cacique y a Gonzalo por las múltiples discusiones científicas mantenidas a lo largo de los años. Igualmente quiero agradecer a Apucmo, Fátima y Lucía por su apoyo y sugerencias tanto durante mi estancia en la isla bonita como con posterioridad, especialmente las revisiones lingüísticas de Apucmo y las instrucciones pormenorizadas paso a paso para el depósito digital por parte de Lucía. También a todas las personas que, como Manuel, Rosa Irene, Sergio, Aitor y Kevin, me han apoyado y mostrado su interés y curiosidad en mi trabajo de investigación a lo largo de estos años. Me gustaría extender una muestra diferenciada de agradecimiento a mi buen amigo Sebastián que, siempre que encontraba dificultades y problemas, me infundía ánimos y me apremiaba a perseverar.*

*Por último, pero no por ello menos importante, me gustaría agradecer a Alejandro la revisión del léxico, de la ortografía y la gramática inglesa de esta tesis doctoral, así como su interés por mi trabajo de investigación en estos últimos meses de revisión final.*

ΟΥ ΓΑΡ ΕΣΤΙ ΤΙ ΚΡΥΠΤΟΝ Ο ΕΑΝ ΜΗ  
ΦΑΝΕΡΩΘΗ ΟΥΔΕ ΕΓΕΝΕΤΟ ΑΠΟΚΡΥΦΟΝ  
ΑΛΛ ΙΝΑ ΕΙΣ ΦΑΝΕΡΟΝ ΕΛΘΗ

*For there is nothing hidden except to be made visible;  
nothing is secret except to come to light. (Mt 4:22)*

*Porque no hay nada oculto que no deba ser revelado  
y nada secreto que no deba manifestarse. (Mc 4:22)*

Este documento incorpora firma electrónica, y es copia auténtica de un documento electrónico archivado por la ULL según la Ley 39/2015.  
Su autenticidad puede ser contrastada en la siguiente dirección <https://sede.ull.es/validacion/>

Identificador del documento: 963882

Código de verificación: QDmfX6JG

Firmado por: MANUEL DIAZ ALFARO  
UNIVERSIDAD DE LA LAGUNA

Fecha: 26/06/2017 15:24:15

FERNANDO JAVIER PEREZ HERNANDEZ  
UNIVERSIDAD DE LA LAGUNA

26/06/2017 15:25:57

ERNESTO PEREDA DE PABLO  
UNIVERSIDAD DE LA LAGUNA

28/06/2017 13:21:41

## Resumen

La tacoclina solar situada en la base de la zona de convección es la capa de cizalladura que conecta la rotación diferencial en la envoltura convectiva y la rotación rígida en el interior radiativo. Generalmente se cree que alberga la localización de la dinamo solar y desempeña un importante papel en la generación y almacenamiento de los campos magnéticos que originan el ciclo solar de actividad magnética. Con la ayuda de técnicas de modelado y de heliosismología global y local numerosos estudios han intentado mejorar nuestro conocimiento sobre el papel desempeñado por la base de la zona de convección y la tacoclina en los modelos de la dinamo solar.

La heliosismología constituye una técnica ideal con la que inferir propiedades de áreas del Sol no accesibles a la observación directa. Como tal, la holografía heliosísmica sensible a la fase ha demostrado ser una técnica satisfactoria para producir mapas de actividad magnética en el hemisferio no visible o lado lejano del Sol. En esta tesis, adaptamos ese método para detectar cambios en la velocidad del sonido en la vecindad de la tacoclina y la base de la zona de convección a lo largo del ciclo solar.

La validación de técnicas heliosísmicas para su uso en el interior solar no es trivial. Las simulaciones numéricas pueden ser de ayuda en esta tarea. Usamos una serie de simulaciones numéricas con perturbaciones en la velocidad del sonido a  $0.70 R_{\odot}$  para medir la respuesta de la técnica a variaciones en la velocidad del sonido, lo que se usa para establecer una relación de calibración entre cantidades sísmicas, es decir desfase, y variaciones en la velocidad del sonido. Evaluamos los posibles efectos colaterales en las profundidades de interés causados por perturbaciones menos profundas con la ayuda de otra serie de simulaciones numéricas con perturbaciones en la velocidad del sonido en la fotosfera y en la zona poco profunda de la subfotosfera.

La técnica finalmente se aplica a observaciones solares reales obtenidas por GONG con el fin de demostrar la factibilidad del método para detectar variaciones en la velocidad del sonido en el Sol real. Recuperamos un perfil de la velocidad del sonido en las capas profundas de la tacoclina y la base de la zona de convección, generalmente consistente con trabajos previos. También recuperamos variaciones en la velocidad del sonido entre periodos del ciclo solar con alta y baja actividad. Presentamos las limitaciones de la técnica actual y sugerimos algunos experimentos para mejorar su calibración.

CÓDIGOS UNESCO: 2106.02, 2106.04

Este documento incorpora firma electrónica, y es copia auténtica de un documento electrónico archivado por la ULL según la Ley 39/2015.  
Su autenticidad puede ser contrastada en la siguiente dirección <https://sede.ull.es/validacion/>

Identificador del documento: 963882

Código de verificación: QDmfX6JG

Firmado por: MANUEL DIAZ ALFARO  
UNIVERSIDAD DE LA LAGUNA

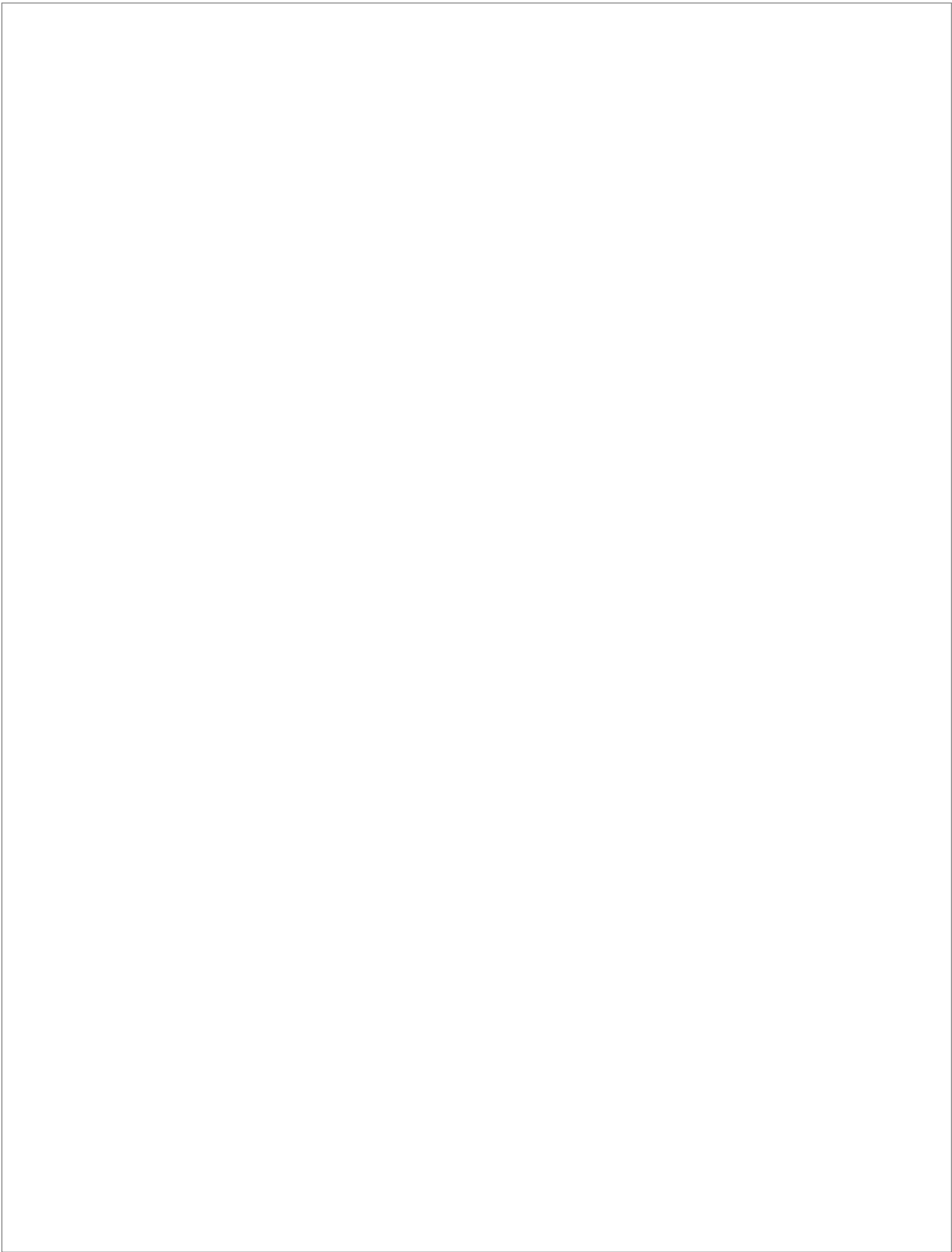
Fecha: 26/06/2017 15:24:15

FERNANDO JAVIER PEREZ HERNANDEZ  
UNIVERSIDAD DE LA LAGUNA

26/06/2017 15:25:57

ERNESTO PEREDA DE PABLO  
UNIVERSIDAD DE LA LAGUNA

28/06/2017 13:21:41



Este documento incorpora firma electrónica, y es copia auténtica de un documento electrónico archivado por la ULL según la Ley 39/2015.  
Su autenticidad puede ser contrastada en la siguiente dirección <https://sede.ull.es/validacion/>

Identificador del documento: 963882

Código de verificación: QDmfX6JG

Firmado por: MANUEL DIAZ ALFARO  
UNIVERSIDAD DE LA LAGUNA

Fecha: 26/06/2017 15:24:15

FERNANDO JAVIER PEREZ HERNANDEZ  
UNIVERSIDAD DE LA LAGUNA

26/06/2017 15:25:57

ERNESTO PEREDA DE PABLO  
UNIVERSIDAD DE LA LAGUNA

28/06/2017 13:21:41

## Abstract

The solar tachocline at the base of the convection zone is the shear layer that connects differential rotation in the convective envelope and rigid rotation in the radiative interior. It is generally believed to be the seat of the solar dynamo and plays important roles in the generation and storage of the magnetic fields that give rise to the solar cycle of magnetic activity. With the aid of modelling and global and local helioseismology techniques numerous studies have tried to improve our knowledge of the role played by the base of the convection zone and the tachocline in solar-dynamo models.

Helioseismology constitutes an ideal technique with which to infer properties of areas of the Sun that are not accessible to direct observation. As such, phase-sensitive helioseismic holography has proved a successful technique for mapping magnetic activity in the far-side non-visible hemisphere of the Sun. In this thesis, we adapt that method to detect changes in the sound speed in the vicinity of the tachocline and the base of the convection zone through the solar cycle.

The validation of helioseismic techniques for use in the solar interior is not straightforward. Numerical simulations can prove useful in this task. We use a series of numerical simulations with sound-speed perturbations at  $0.70 R_{\odot}$  to measure the response of the technique to sound-speed variations, which is used to establish a calibration ratio between seismic quantities, *i.e.* phase shift, and variations in the sound speed. We assess the possible side effects on the depths of interest caused by shallower perturbations with the aid of another series of numerical simulations with sound-speed perturbations in the photosphere and in the shallow subphotosphere.

The technique is finally applied to actual solar observations taken by GONG in order to demonstrate the feasibility of the method to detect sound-speed variations in the real Sun. We recover the sound-speed profile at the deep layers of the tachocline and the base of the convection zone, generally consistent with previous work. We also recover variations in the sound speed between periods of high and low activity of the solar cycle. We present the limitations of the current technique and suggest some experiments to improve the calibration thereof.

UNESCO CODES: 2106.02, 2106.04

Este documento incorpora firma electrónica, y es copia auténtica de un documento electrónico archivado por la ULL según la Ley 39/2015.  
Su autenticidad puede ser contrastada en la siguiente dirección <https://sede.ull.es/validacion/>

Identificador del documento: 963882

Código de verificación: QDmfX6JG

Firmado por: MANUEL DIAZ ALFARO  
UNIVERSIDAD DE LA LAGUNA

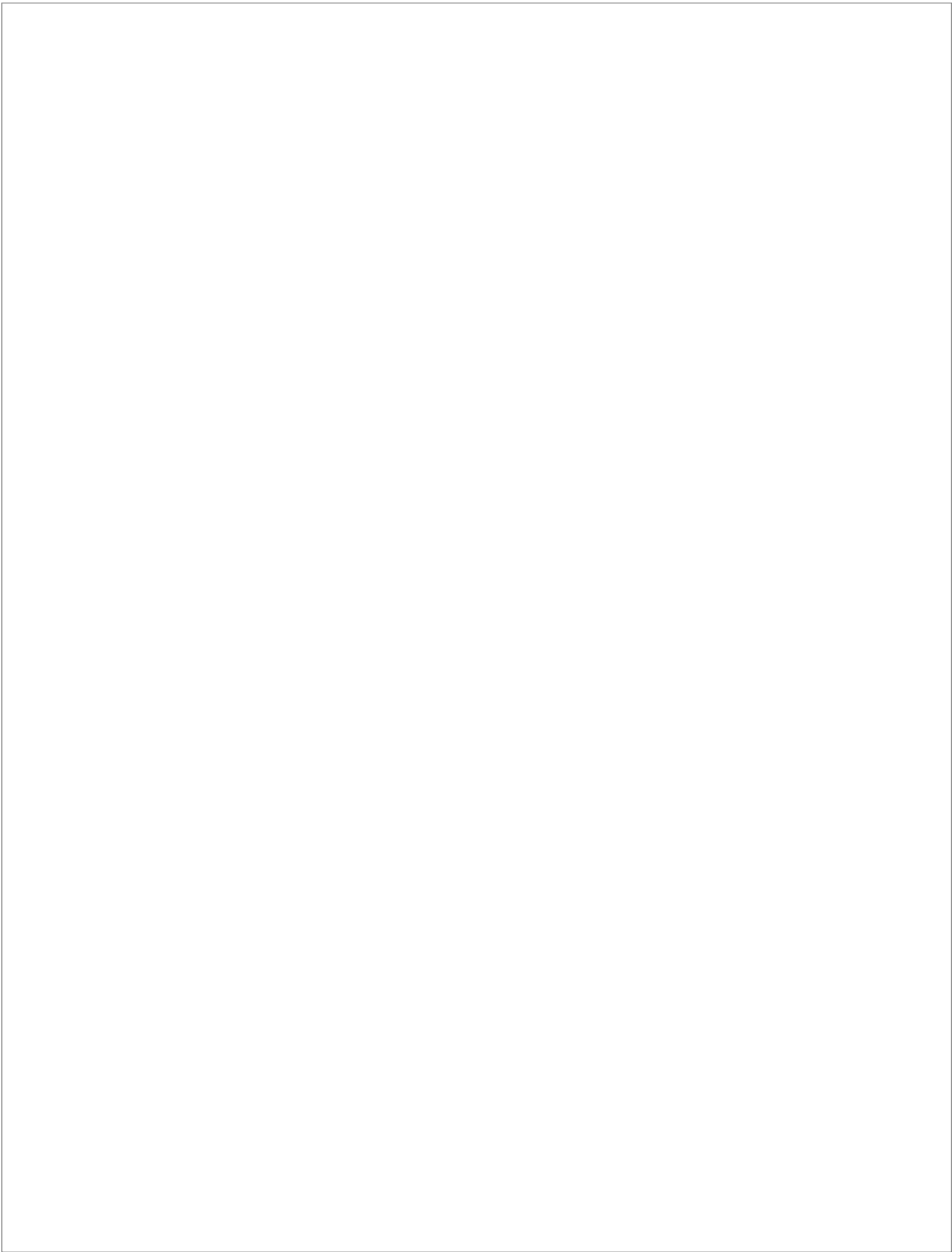
Fecha: 26/06/2017 15:24:15

FERNANDO JAVIER PEREZ HERNANDEZ  
UNIVERSIDAD DE LA LAGUNA

26/06/2017 15:25:57

ERNESTO PEREDA DE PABLO  
UNIVERSIDAD DE LA LAGUNA

28/06/2017 13:21:41



Este documento incorpora firma electrónica, y es copia auténtica de un documento electrónico archivado por la ULL según la Ley 39/2015.  
Su autenticidad puede ser contrastada en la siguiente dirección <https://sede.ull.es/validacion/>

Identificador del documento: 963882

Código de verificación: QDmfX6JG

Firmado por: MANUEL DIAZ ALFARO  
UNIVERSIDAD DE LA LAGUNA

Fecha: 26/06/2017 15:24:15

FERNANDO JAVIER PEREZ HERNANDEZ  
UNIVERSIDAD DE LA LAGUNA

26/06/2017 15:25:57

ERNESTO PEREDA DE PABLO  
UNIVERSIDAD DE LA LAGUNA

28/06/2017 13:21:41

# Contents

<b>Resumen</b>	<b>v</b>
<b>Abstract</b>	<b>vii</b>
<b>Contents</b>	<b>ix</b>
<b>1 Introduction</b>	<b>1</b>
1.1 The Solar Structure . . . . .	2
1.2 The Solar Cycle . . . . .	6
1.3 Helioseismology . . . . .	13
1.3.1 Acoustic modes . . . . .	13
1.3.2 Local helioseismology . . . . .	14
1.3.3 Helioseismic inferences about the base of the convection zone and tachocline . . . . .	16
1.4 Numerical simulations of the Sun . . . . .	17
1.5 Objectives . . . . .	18
<b>2 Methodology</b>	<b>19</b>
2.1 Acoustic egression and ingression . . . . .	19
2.2 Phase-sensitive seismic holography . . . . .	21
2.3 Green's functions . . . . .	22
2.3.1 Phase-shift correction . . . . .	24
2.4 Pupils . . . . .	25
2.5 Procedure . . . . .	28
<b>3 Numerical simulations with sound-speed perturbations</b>	<b>33</b>
3.1 Numerical simulations . . . . .	34
3.1.1 Sound-speed perturbations at $0.7 R_{\odot}$ . . . . .	35
3.1.2 Localized sound-speed perturbations in the photosphere . . . . .	36
3.1.3 Localized sound-speed perturbations in the shallow subphoto- sphere . . . . .	38
3.2 Technique . . . . .	39

Este documento incorpora firma electrónica, y es copia auténtica de un documento electrónico archivado por la ULL según la Ley 39/2015.  
 Su autenticidad puede ser contrastada en la siguiente dirección <https://sede.ull.es/validacion/>

Identificador del documento: 963882 Código de verificación: QDmfX6JG

Firmado por: MANUEL DIAZ ALFARO UNIVERSIDAD DE LA LAGUNA	Fecha: 26/06/2017 15:24:15
FERNANDO JAVIER PEREZ HERNANDEZ UNIVERSIDAD DE LA LAGUNA	26/06/2017 15:25:57
ERNESTO PEREDA DE PABLO UNIVERSIDAD DE LA LAGUNA	28/06/2017 13:21:41

3.3	Results . . . . .	41
3.3.1	Sound-speed perturbations at $0.7 R_{\odot}$ . . . . .	41
3.3.2	Localized sound-speed perturbations in the photosphere . . . . .	51
3.3.3	Localized sound-speed perturbations in the shallow subphoto- sphere . . . . .	56
3.4	Discussion . . . . .	59
<b>4</b>	<b>The Solar Interior through the solar cycle</b>	<b>61</b>
4.1	Observational Data . . . . .	61
4.2	Technique . . . . .	66
4.3	Results . . . . .	67
4.3.1	Inferred sound-speed at the base of the convection zone at solar minima . . . . .	67
4.3.2	Variations of the inferred sound speed along the solar cycle . . . . .	72
4.4	Discussion . . . . .	81
<b>5</b>	<b>Conclusions</b>	<b>85</b>
<b>A</b>	<b>Appendix: Green's functions</b>	<b>87</b>
A.1	Angular part . . . . .	89
A.2	Radial part . . . . .	90
A.3	Full expression . . . . .	91
	<b>References</b>	<b>93</b>

Este documento incorpora firma electrónica, y es copia auténtica de un documento electrónico archivado por la ULL según la Ley 39/2015.  
Su autenticidad puede ser contrastada en la siguiente dirección <https://sede.ull.es/validacion/>

Identificador del documento: 963882

Código de verificación: QDmfX6JG

Firmado por: MANUEL DIAZ ALFARO  
UNIVERSIDAD DE LA LAGUNA

Fecha: 26/06/2017 15:24:15

FERNANDO JAVIER PEREZ HERNANDEZ  
UNIVERSIDAD DE LA LAGUNA

26/06/2017 15:25:57

ERNESTO PEREDA DE PABLO  
UNIVERSIDAD DE LA LAGUNA

28/06/2017 13:21:41

# 1

## Introduction

Through history the Sun has played an important role in different human societies. Solar-related deities have held important positions in a number of cultures throughout Earth, such as Shamash in Mesopotamia, Ra in ancient Egypt, Helios in the Græco-Roman world, Inti in the pre-Columbian Inca empire, and Magec and Abora in the indigenous culture of the Canary Islands prior to the Castilian conquest.

Although we find scattered references to sunspots in Chinese and Korean astronomical records as early as 800 BC, we must wait until 1128 for the first drawing of a sunspot appearing in the *Chronicon ex chronicis* attributed to the English monk John of Worcester. And it was not until the beginning of the seventeenth century with the advent of the telescope that systematic observations and recordings of solar structural features began thanks to the contributions and observations of Thomas Harriot, Galileo Galilei, David and Johannes Fabricius, and Christoph Scheiner. However, their true nature as magnetic phenomena would remain unknown until the early twentieth century.

Another major step forward in the knowledge of the Sun came with the discovery of Fraunhofer lines and the invention of spectroscopic techniques in the second half of the nineteenth century. Most recently, in the last fifty years, a remarkable advance has been achieved in solar physics thanks to the contribution of helioseismology.

Besides a deeper and better understanding of stellar physics in general, the improvement of our knowledge of the Sun can still have an important practical impact on society nowadays. With an increasing dependence on technology, the disruptions of long-distance electrical grids or the failure of communication satellites due to geomagnetic storms originating in the Sun may have catastrophic consequences and cause major economic losses (Pulkkinen, 2007). Helioseismology has started to prove a reliable tool in space-weather forecasting (González Hernández, 2013) thanks to the detection of active regions in the far-side non-visible hemisphere of the Sun (Fontenla *et al.*, 2009; González Hernández *et al.*, 2014) or prior to their emergence at the photosphere (Zharkov and Thompson, 2008; Ilonidis, Zhao, and Kosovichev, 2011; Kholikov, 2013; Leka *et al.*, 2013; Birch *et al.*, 2013; Barnes *et al.*, 2014).

Este documento incorpora firma electrónica, y es copia auténtica de un documento electrónico archivado por la ULL según la Ley 39/2015.  
Su autenticidad puede ser contrastada en la siguiente dirección <https://sede.ull.es/validacion/>

Identificador del documento: 963882

Código de verificación: QDmfX6JG

Firmado por: MANUEL DIAZ ALFARO  
UNIVERSIDAD DE LA LAGUNA

Fecha: 26/06/2017 15:24:15

FERNANDO JAVIER PEREZ HERNANDEZ  
UNIVERSIDAD DE LA LAGUNA

26/06/2017 15:25:57

ERNESTO PEREDA DE PABLO  
UNIVERSIDAD DE LA LAGUNA

28/06/2017 13:21:41

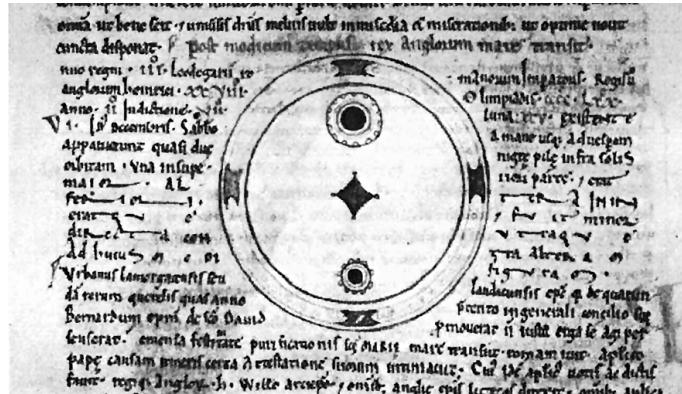


Figure 1.1: Earliest known record of the depiction of a sunspot dated in 1128, taken from the *Chronicon ex chronicis*, a history of the world up to 1140 produced in the Priory of Worcester and attributed to John of Worcester as its principal author and compiler. The picture appears on page 380 of the manuscript MS 157 of the chronicle, kept in the Corpus Christi College in Oxford.

Another topic of public interest today is climate change. Although the current overall rise in temperatures seems to be mainly of anthropogenic origin (*e.g.* Cook *et al.* (2013, 2016)), there has been in the past other climatic variations that could have been influenced, to some extent, by variations in solar activity (Haigh, 2007). A temporal coincidence is found between the Little Ice Age, a colder period in the seventeenth century, with the Maunder minimum, which left the Sun practically without sunspots at the surface for about half a century (Ribes and Nesme-Ribes, 1993). Similar temporal correlations are found between the Dalton minimum and another period with lower-than-average temperatures at the beginning of the nineteenth century. Although causality is not completely established and the corresponding physical mechanisms are not fully understood, the contribution of helioseismology to the description of the mechanisms that drive the solar dynamo could still improve our knowledge on the effects of the Sun on Earth's climate.

## 1.1 The Solar Structure

The Sun is a G-type main-sequence star, located at the centre of the Solar System and formed  $4.6 \cdot 10^9$  years ago, being approximately half-way through its life on the main sequence. It is in a state of thermal and hydrostatic balance in which energy produced in the core is transported up to the photosphere where it is released into space.

Solar observations at different wavelengths allow the study of different layers in the solar atmosphere, according to the height at which specific spectral lines are formed. However, the lack of possible direct observations of the solar interior, except for the neutrinos escaping it, requires the use of indirect techniques to study it. The

Este documento incorpora firma electrónica, y es copia auténtica de un documento electrónico archivado por la ULL según la Ley 39/2015.  
Su autenticidad puede ser contrastada en la siguiente dirección <https://sede.ull.es/validacion/>

Identificador del documento: 963882

Código de verificación: QDmfX6JG

Firmado por: MANUEL DIAZ ALFARO  
UNIVERSIDAD DE LA LAGUNA

Fecha: 26/06/2017 15:24:15

FERNANDO JAVIER PEREZ HERNANDEZ  
UNIVERSIDAD DE LA LAGUNA

26/06/2017 15:25:57

ERNESTO PEREDA DE PABLO  
UNIVERSIDAD DE LA LAGUNA

28/06/2017 13:21:41

construction of *ad hoc* models of the solar interior and the comparison of their upper layers with solar observations, together with inferences of solar structure made by helioseismic techniques, have contributed to a comprehensive consistent view of the structure of the solar interior, formed by a set of spherical shells, according to the classical theory of stellar structure.

The inner part of the Sun is occupied by the core, up to a radius of  $0.2 R_{\odot}$ , where the thermonuclear fusion of hydrogen into helium takes place, releasing energy and producing also an outflow of neutrinos. Above the core, we find the radiation zone, a quiescent region which extends up to a radius of  $0.71 R_{\odot}$ , through which the energy flux is radiatively transported from the core outwards. The high density of this zone makes photons travelling through this region experience a succession of scattering processes, that increases considerably the travel time of photons through this layer, estimated around a few tens or hundreds of thousands of years. On the contrary, the neutrinos formed in the core by the fusion of hydrogen hardly interact with the matter of the solar interior and leave the Sun quickly and practically unperturbed. Above the radiation zone lies the convection zone, a shell where high values of opacity do not allow the transmission of electromagnetic radiation. Therefore, the temperature gradient between the lower and upper boundaries favours the formation of convective cells with different sizes, which transport the energy flux toward the photosphere. Convection manifests externally as the typical pattern of granulation and supergranulation observed at the photosphere.

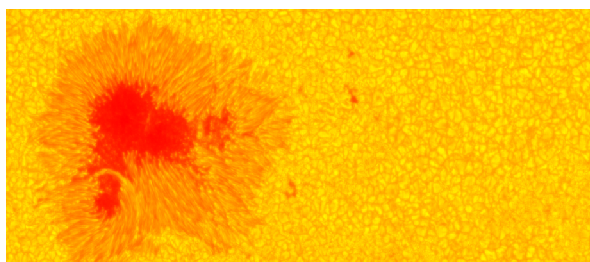


Figure 1.2: Image of active region AR 10953 and neighbouring quiet Sun illustrating the granulation taken on 1 May 2007 with the *Solar Optical Telescope* (SOT) onboard the Hinode spacecraft. Hinode is a Japanese mission developed and launched by ISAS/JAXA, with NAOJ as domestic partner and NASA and STFC (UK) as international partners. It is operated by these agencies in co-operation with ESA and NSC (Norway).

Whereas in terrestrial planets the location of the lower limit of the atmosphere is rather obvious, in stars we must resort to a more complex definition. Particularly, we define the atmosphere of the Sun as the region from which photons can escape freely into space, which for the Sun is immediately located on top of the convection zone. It comprises the photosphere, the chromosphere, and the corona. The photosphere is the layer from which the majority of the solar radiation is emitted into space and has a thickness of a few hundred kilometres. It produces a spectrum dominated by absorption lines. The overlying chromosphere has a thickness of about 10 Mm and its weaker spectrum is dominated by emission lines, being one of the

Este documento incorpora firma electrónica, y es copia auténtica de un documento electrónico archivado por la ULL según la Ley 39/2015.  
Su autenticidad puede ser contrastada en la siguiente dirección <https://sede.ull.es/validacion/>

Identificador del documento: 963882

Código de verificación: QDmfX6JG

Firmado por: MANUEL DIAZ ALFARO  
UNIVERSIDAD DE LA LAGUNA

Fecha: 26/06/2017 15:24:15

FERNANDO JAVIER PEREZ HERNANDEZ  
UNIVERSIDAD DE LA LAGUNA

26/06/2017 15:25:57

ERNESTO PEREDA DE PABLO  
UNIVERSIDAD DE LA LAGUNA

28/06/2017 13:21:41

strongest the  $H\alpha$  line of the Balmer series. A solar transition region couples the chromosphere and the corona above. The corona has variable shape and extension, extending millions of kilometres, and merging with the interplanetary medium of the heliosphere. Figure 1.3 illustrates the structure of the solar interior and atmosphere.

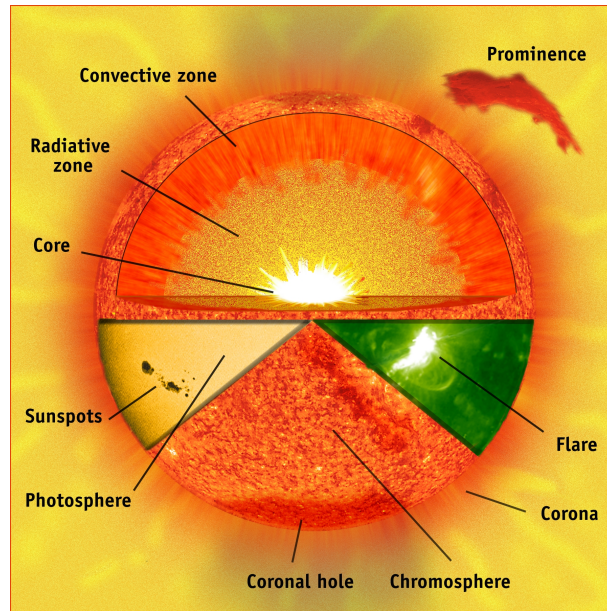


Figure 1.3: Composite image of the Sun with a cutaway of its basic internal structure in the upper half, comprising the core, the radiative zone, and the convection zone. The rest of the image of the Sun together with two overimposed sections are made of actual SOHO observations at different wavelengths and illustrate the components of the solar atmosphere: the photosphere, the chromosphere, and the corona. Some of the structural features that appear at these layers are also shown. Image by Steele Hill (NASA), courtesy of SOHO<sup>1</sup>.

As expected from a stratification governed by gravity, density and pressure reduce as we move away from the solar centre, both in the solar interior and in the atmosphere. The behaviour of temperature is similar in the solar interior and photosphere, with a decrease up to a value of approximately 6000 K in the photosphere. The chromosphere sees a further decrease in temperature in its lower layers, up to a minimum of about 3800 K, and beyond that point temperature increases again and reaches values as high as a few million kelvin in the corona. Although the origin of this phenomenon is not completely settled yet, two main theories have been proposed to explain the increase in temperature in the chromosphere and in the corona. The release of the energy contained in waves that dissipate in the area can explain the heating in the chromosphere (Biermann, 1946; Cuntz, Ulmschneider, and Musielak, 1998). However, when the waves eventually

<sup>1</sup><http://sohowww.nascom.nasa.gov/gallery/images/sunparts.html>

Este documento incorpora firma electrónica, y es copia auténtica de un documento electrónico archivado por la ULL según la Ley 39/2015.  
Su autenticidad puede ser contrastada en la siguiente dirección <https://sede.ull.es/validacion/>

Identificador del documento: 963882

Código de verificación: QDmfX6JG

Firmado por: MANUEL DIAZ ALFARO  
UNIVERSIDAD DE LA LAGUNA

Fecha: 26/06/2017 15:24:15

FERNANDO JAVIER PEREZ HERNANDEZ  
UNIVERSIDAD DE LA LAGUNA

26/06/2017 15:25:57

ERNESTO PEREDA DE PABLO  
UNIVERSIDAD DE LA LAGUNA

28/06/2017 13:21:41

reach the corona, their energy is practically exhausted. The other model is based on the release of magnetic energy through processes of magnetic reconnection, which can explain the coronal heating and could also contribute to the increase of temperature in the chromosphere (Narain and Ulmschneider, 1990, 1996).

By tracking sunspots, Richard Carrington discovered that solar rotation at the photosphere was not homogeneous but it varied with latitude (Carrington, 1858, 1859). The observation of sunspots and other structural features at the photosphere at different latitudinal locations shows that the rotation rate decreases as the latitude increases. Thus, while the rotation period at the equator is approximately 25 days, it is about 36 days at the poles. Helioseismic studies in the last decades have allowed the study of the rotation rate in the solar interior, too (Brown *et al.*, 1989; Schou and Bogart, 1998; Howe *et al.*, 2000, 2005). The radiative interior of the Sun—comprising the core and the radiative zone—seems to rotate approximately as a solid body with a period of about 27 days. The convection zone rotates differentially transitioning to the rigid-body rotation of the radiative interior in the tachocline, a thin shear layer located around the base of the convection zone which couples both rotation regimes. Another shear layer is observed in the shallow subphotosphere between the subsurface fastest-rotating layer at  $\approx 0.95 R_{\odot}$  and the slower overlying surface. Figure 1.4 illustrates the rotation rates throughout the convection zone and the upper layers of the radiative interior from helioseismic inferences. Howe (2009) presents a complete review about the rotation of the solar interior and its observed variations.

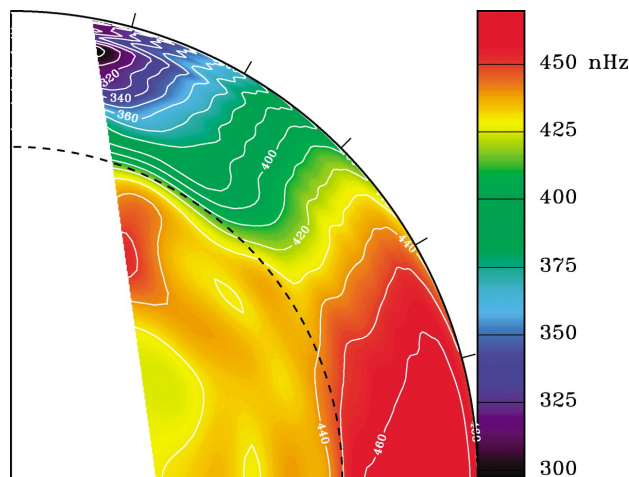


Figure 1.4: Internal rotation profile of the Sun inferred from helioseismology. A rotation rate of 450 nHz corresponds to a rotation period of 26 days and one of 325 nHz corresponds to a period of 36 days. The image extends from the solar equator on the lower right to the pole on the upper left, averaged for both hemispheres. Courtesy of the High Altitude Observatory (HAO) of the National Center for Atmospheric research (NCAR)<sup>2</sup>.

<sup>2</sup><http://www.hao.ucar.edu/research/lsv/lsvConvectionBackground.php>

Este documento incorpora firma electrónica, y es copia auténtica de un documento electrónico archivado por la ULL según la Ley 39/2015.  
Su autenticidad puede ser contrastada en la siguiente dirección <https://sede.ull.es/validacion/>

Identificador del documento: 963882

Código de verificación: QDmfX6JG

Firmado por: MANUEL DIAZ ALFARO  
UNIVERSIDAD DE LA LAGUNA

Fecha: 26/06/2017 15:24:15

FERNANDO JAVIER PEREZ HERNANDEZ  
UNIVERSIDAD DE LA LAGUNA

26/06/2017 15:25:57

ERNESTO PEREDA DE PABLO  
UNIVERSIDAD DE LA LAGUNA

28/06/2017 13:21:41

## 1.2 The Solar Cycle

Sunspots, darker and cooler regions at the photosphere, an example of which is shown in Figure 1.2, have been systematically observed since the beginning of the seventeenth century. The long-term observational record shows a periodicity in the presence and distribution of sunspots with a mean period of 11 years, discovered by Schwabe (1844). This period is referred to as a solar cycle. In 1849 Rudolf Wolf initiated in the Zürich Observatory a systematic programme to record the numbers of sunspots and groups of sunspots visible on the Sun on a daily basis and compute a sunspot index (Wolf, 1861), which is now known as the international sunspot number or the Wolf number. He later extended his work backwards to 1749 using previous observations. Thus, conventionally, the cycle starting in 1755 is known as Solar Cycle 1 and from this the numbering is extended into the future. The international sunspot number is nowadays maintained and produced by the Royal Observatory of Belgium, in Brussels, under the *Sunspot Index and Long-term Solar Observations* programme (SILSO)<sup>3</sup>. The original data series has been replaced since 1 July 2015 with a revised data series, referred to as version 2.0, which has become the official standard (Clette *et al.*, 2014). With this revision, the international sunspot number provides a harmonized value to assess photospheric variability in terms of counting sunspots and groups of sunspots continuously from the mid-eighteenth century. Other similar indices are also available, such as the Boulder Sunspot Number, the American Sunspot Number, or the Group Sunspot Number (Hoyt and Schatten, 1998; Hathaway, Wilson, and Reichmann, 2002). Figure 1.5 shows 13-month smoothed monthly averages of the daily international sunspot number for all the available record since the beginning of Solar Cycle 1 in 1755.

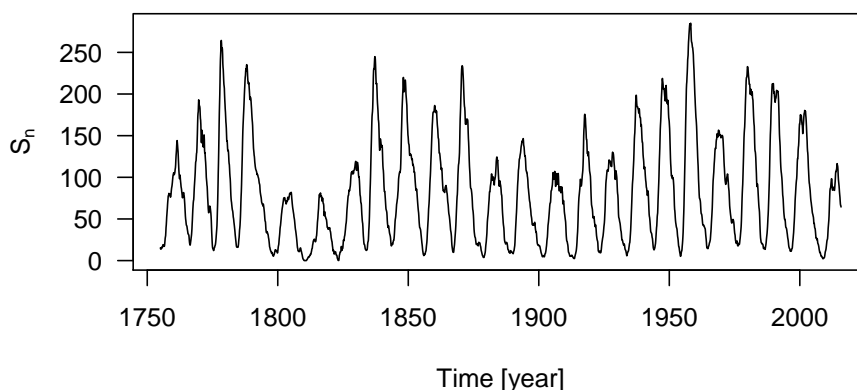


Figure 1.5: International sunspot number  $S_n$  for the existing record of solar cycles starting in 1755 according to its current official standard—version 2.0—. The displayed values have been monthly-averaged and smoothed in overlapping intervals of 13 months.

<sup>3</sup><http://sidc.be/silso/>

Este documento incorpora firma electrónica, y es copia auténtica de un documento electrónico archivado por la ULL según la Ley 39/2015.  
Su autenticidad puede ser contrastada en la siguiente dirección <https://sede.ull.es/validacion/>

Identificador del documento: 963882

Código de verificación: QDmfX6JG

Firmado por: MANUEL DIAZ ALFARO  
UNIVERSIDAD DE LA LAGUNA

Fecha: 26/06/2017 15:24:15

FERNANDO JAVIER PEREZ HERNANDEZ  
UNIVERSIDAD DE LA LAGUNA

26/06/2017 15:25:57

ERNESTO PEREDA DE PABLO  
UNIVERSIDAD DE LA LAGUNA

28/06/2017 13:21:41

Despite the long-term utility of integral indices such as the international sunspot number, the hemispheric area occupied by sunspots represents a more physical magnitude recording solar activity (Fligge and Solanki, 1997; Baranyi *et al.*, 2001; Balmaceda *et al.*, 2009). Among different indices recording sunspot area we find the RGO<sup>4</sup> Sunspot Area and the USAF/NOAA<sup>5</sup> Sunspot Area, which show a correlation of about 99% with the international sunspot number. The lower panel of Figure 1.6 shows the average daily values of the area occupied by sunspots in terms of percentages of the visible hemisphere. The correspondence with the international sunspot number (Figure 1.5) is easily seen. The record of the position—longitude and latitude—of sunspots provides more detailed information. Sunspots appear in two bands on either side of the solar equator, keeping overall symmetry with respect to the equator. At the beginning of a solar cycle sunspots appear at latitudes of about 20°–25°. With the progression of the cycle, sunspots appear at a broader range of latitudes, but their mean central latitude approaches the equator, but avoiding a narrow band near it. This behaviour, referred to as the Spörer Law of Zones, is illustrated by the so-called butterfly diagram (Maunder, 1903, 1904). The upper panel of Figure 1.6 shows an example of the butterfly diagram with the areal distributions of sunspots with respect to latitude and time.

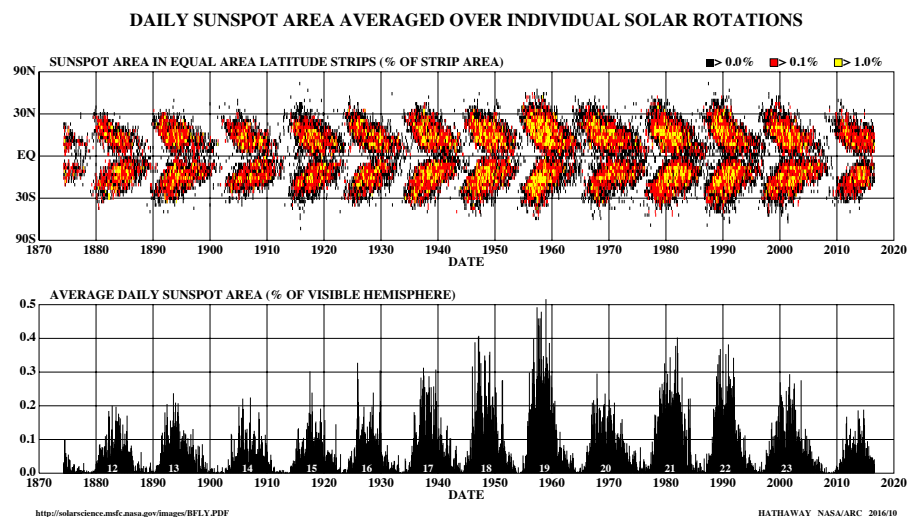


Figure 1.6: Upper panel: Butterfly diagram, *i.e.* areal distribution of sunspots with respect to latitude and time. Lower panel: Average daily sunspot coverage. Courtesy of David H. Hathaway (NASA/MSFC)<sup>6</sup>.

It was not until the early twentieth century that Hale discovered the magnetic origin of sunspots (Hale, 1908). This allowed more complex studies of photospheric

<sup>4</sup>Royal Greenwich Observatory

<sup>5</sup>United States Air Force/National Oceanic and Atmospheric Administration

<sup>6</sup><http://solarscience.msfc.nasa.gov/images/bfly.pdf>

Este documento incorpora firma electrónica, y es copia auténtica de un documento electrónico archivado por la ULL según la Ley 39/2015.  
Su autenticidad puede ser contrastada en la siguiente dirección <https://sede.ull.es/validacion/>

Identificador del documento: 963882

Código de verificación: QDmfX6JG

Firmado por: MANUEL DIAZ ALFARO  
UNIVERSIDAD DE LA LAGUNA

Fecha: 26/06/2017 15:24:15

FERNANDO JAVIER PEREZ HERNANDEZ  
UNIVERSIDAD DE LA LAGUNA

26/06/2017 15:25:57

ERNESTO PEREDA DE PABLO  
UNIVERSIDAD DE LA LAGUNA

28/06/2017 13:21:41

activity in terms of magnetic polarity. A large number of sunspots appear in pairs, with one leading and one trailing sunspot—according to rotation—. Whenever this occurs, they are generally of opposite polarity. Besides, the corresponding group in the other hemisphere shows reverse polarities. For each hemisphere, the polarity of any leading sunspot, and consequently that of the trailing sunspot, is kept throughout each solar cycle, reversing polarities at the beginning of the next solar cycle. This is known as Hale's Polarity Laws (Hale *et al.*, 1919). Furthermore, in binary groups the trailing sunspot is generally at a higher latitude than the leading one, this tilt increasing with latitude, what is known as Joy's Law (Hale *et al.*, 1919).

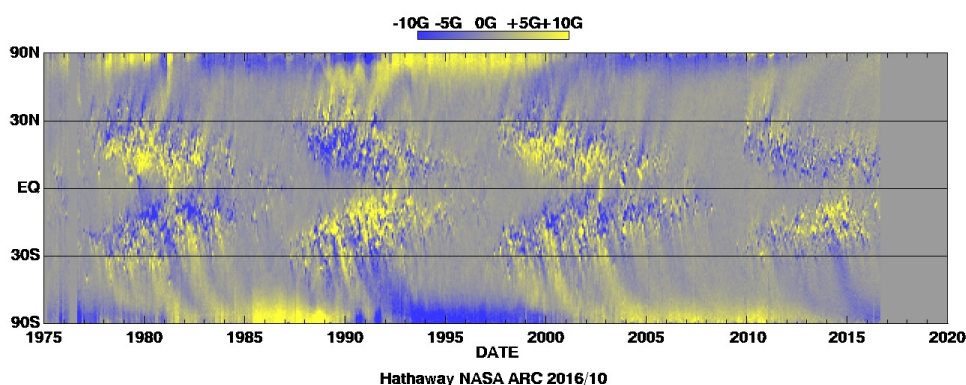


Figure 1.7: Evolution of the longitudinally averaged radial magnetic field with respect to latitude. The data have been obtained from instruments on Kitt Peak and onboard SOHO. Courtesy of David H. Hathaway (NASA/MSFC)<sup>7</sup>.

Sunspots are in fact the photospheric visual manifestation of active regions, perturbed areas of the Sun where magnetic fields are concentrated. They also inhibit convection locally. The sunspots last much longer than if they would be only a photospheric phenomenon. Thus, they must extend into deeper layers of the Sun, but their underlying structure remains still subject to discussion (Parker, 1979). Moradi *et al.* (2010) present a comprehensive review of the current state-of-the-art different models of sunspot subphotospheric structure. Apart from sunspots on the photosphere, active regions may produce disturbance features throughout the whole solar atmosphere such as flares, coronal loops, prominences, or even coronal mass ejections (CMEs). But active regions are not the only elements to show reversals in polarity over time. In fact, the magnetic field at the poles also experiences a change in polarity at the solar maximum (Babcock, 1959). Thus, magnetic fields at the poles and at latitudes with active regions are out of phase about half a cycle. Figure 1.7 shows the evolution of the longitudinally averaged radial magnetic field and its dependence with latitude for the last few solar cycles. The butterfly-diagram pattern is shown at lower latitudes illustrating Hale's polarity and Joy's laws. We

<sup>7</sup><http://solarscience.msfc.nasa.gov/images/magbfly.jpg>

Este documento incorpora firma electrónica, y es copia auténtica de un documento electrónico archivado por la ULL según la Ley 39/2015.  
Su autenticidad puede ser contrastada en la siguiente dirección <https://sede.ull.es/validacion/>

Identificador del documento: 963882

Código de verificación: QDmfX6JG

Firmado por: MANUEL DIAZ ALFARO  
UNIVERSIDAD DE LA LAGUNA

Fecha: 26/06/2017 15:24:15

FERNANDO JAVIER PEREZ HERNANDEZ  
UNIVERSIDAD DE LA LAGUNA

26/06/2017 15:25:57

ERNESTO PEREDA DE PABLO  
UNIVERSIDAD DE LA LAGUNA

28/06/2017 13:21:41

can also observe the reversal of polarity of polar magnetic fields with an offset of half a cycle with respect to the polarity change in the active regions at lower latitudes. A poleward drift migration of photospheric magnetic fields is also clearly present, what is believed to be caused by the transport of magnetic energy released by the decay of active regions at low latitudes.

The sunspot indices presented above can be useful to study the long-term evolution of solar activity. We can also use other indices as well, *e.g.* indices derived from magnetic measurements in the Sun such as the *Mount Wilson Plage Strength Index* (MPSI) or the *Mount Wilson Sunspot Index* (MWSI) (Parker, Ulrich, and Pap, 1998), from helioseismic measurements (González Hernández *et al.*, 2014), or from radio signals from the Sun, such as the 10.7 cm radio flux ( $F_{10.7}$ ) (Covington, 1969). All of the latter show different degrees of correlation with the former. Other magnitudes, non-directly dependent on solar observations, such as the measurement of the  $^{14}\text{C}$  and  $^{10}\text{Be}$  isotopes on Earth, correlate with solar cycle variations to an acceptable extent (Stuiver and Quay, 1980; Beer *et al.*, 1990; Masarik and Beer, 1999). This can be used to extend studies of the solar cycle into the past using geological data before records of solar activity were available, albeit with higher uncertainty. Ermolli *et al.* (2014) presents a general overview of different indices able to measure solar-cycle variations. Some of them constitute a valuable input in numerical models used to study solar cycles and make predictions for the near future. A detailed comprehensive review of the observational phenomena related to the solar cycle is provided by Hathaway (2010).

The processes involved in the cyclic regeneration and evolution of the magnetic field of the Sun have been englobed under the term solar dynamo. There is a significant agreement that the magnetic cycle is produced by the inductive action of plasma motions in the solar interior. Any model for the solar dynamo should reproduce the observable evidence, basically the cyclic evolution from a mainly poloidal configuration of the magnetic field at the beginning of a solar cycle to a mainly toroidal configuration at the solar maximum, and then to a poloidal configuration again, but of opposite polarity. It should also reproduce other evidence, such as the offset in the reversal of the magnetic fields at the poles, and Joy's and Hale's polarity laws.

It is generally accepted that differential rotation acts on the poloidal magnetic field of the Sun, which is dragged by the solar plasma, and modifies its configuration to produce strong toroidal magnetic fields that emerge through the photosphere to form active regions. This is called the  $\omega$ -effect. However, the process to explain the generation of a poloidal field of reversed polarity from a mainly toroidal configuration is more problematic.

The first considered models are based on magnetic flux transport and are known today as Babcock-Leighton models (Babcock, 1961; Leighton, 1969; Wang and Sheeley, 1991; Dikpati and Charbonneau, 1999). Their proposed mechanism for the conversion from a toroidal to a poloidal magnetic field is based on the tilt described by Joy's law of bipolar magnetic regions, *i.e.* active regions with two components

Este documento incorpora firma electrónica, y es copia auténtica de un documento electrónico archivado por la ULL según la Ley 39/2015.  
Su autenticidad puede ser contrastada en la siguiente dirección <https://sede.ull.es/validacion/>

Identificador del documento: 963882

Código de verificación: QDmfX6JG

Firmado por: MANUEL DIAZ ALFARO  
UNIVERSIDAD DE LA LAGUNA

Fecha: 26/06/2017 15:24:15

FERNANDO JAVIER PEREZ HERNANDEZ  
UNIVERSIDAD DE LA LAGUNA

26/06/2017 15:25:57

ERNESTO PEREDA DE PABLO  
UNIVERSIDAD DE LA LAGUNA

28/06/2017 13:21:41

of opposite polarity. On the one hand, the leading component would migrate to the equator where it would be neutralized with the leading component of opposite polarity from the other hemisphere. On the other hand, the trailing component would migrate to the pole where it would contribute to the reversal of the polar magnetic field. This poleward migration may pose a problem as the poloidal fields this model creates at the surface are weak and could be distorted when passing through the turbulent convection zone. Besides, whereas the poleward migration is considered a key component in the generation of the poloidal field here, other kind of models explain it as an external manifestation of an underlying phenomenon. These models also tend to operate independently in each hemisphere, which could lead to a loss of synchrony between the northern and southern hemispheres.

The tachocline, the narrow shear layer located at the base of the convection zone where solid rotation of the radiative interior changes to differential rotation in the convective envelope (Spiegel and Zahn, 1992), is generally believed today to play an important role in the solar dynamo. It should be noted that the tachocline is in general located partly in the convection zone and partly in the radiative zone, whose upper part hosts a convective overshoot region, where material from the convective layers above can penetrate by inertia. Further details about the location of the tachocline are reviewed in Section 1.3.3. The high radial gradient in angular velocity, maximal here, produces a strong shear that makes this layer ideal for storing magnetic fields. There is a consensus that toroidal magnetic fields are pumped downwards into the convective overshoot layer following the gradient of turbulence intensity, what is called the  $\gamma$ -effect (Dorch and Nordlund, 2001; Tobias *et al.*, 2001). The toroidal magnetic fields are then stored into the stably stratified lower layers of the tachocline. With time, the stored toroidal magnetic field gets stronger and eventually could be released due to an instability and ascend to the surface by magnetic buoyancy (Moreno-Insertis, Schüssler, and Ferriz-Mas, 1992; Schüssler *et al.*, 1994). Whereas the typical rise times of a flux tube in the convection zone is short, flux tubes can be stored in the tachocline during time scales comparable with the duration of the solar cycle (Moreno-Insertis, 1983). The oscillatory nature of this field could also produce an oscillation in the penetration extent of the overshoot layer (Spiegel and Weiss, 1980).

For interface-dynamo models the  $\omega$ -effect takes place in the tachocline itself. The strong rotational gradient is believed to turn poloidal into toroidal magnetic fields in the upper convective part of the tachocline before being transported down. However, for mean-field or distributed dynamos, this layer is too narrow (Durney, De Young, and Passot, 1990) to generate the magnetic flux observed at the surface, and they consider that the toroidal magnetic field is generated by means of the magnetic dragging by the differentially rotating material throughout the convection zone (Nordlund *et al.*, 1992). In these latter models the regeneration of the poloidal field is explained with the aid of the so-called  $\alpha$ -effect (Rüdiger and Brandenburg, 1995). Here helicity is produced by the Coriolis force acting on turbulent convection, *i.e.* turbulence produces an electric current that flows along the magnetic lines and,

Este documento incorpora firma electrónica, y es copia auténtica de un documento electrónico archivado por la ULL según la Ley 39/2015.  
Su autenticidad puede ser contrastada en la siguiente dirección <https://sede.ull.es/validacion/>

Identificador del documento: 963882

Código de verificación: QDmfX6JG

Firmado por: MANUEL DIAZ ALFARO  
UNIVERSIDAD DE LA LAGUNA

Fecha: 26/06/2017 15:24:15

FERNANDO JAVIER PEREZ HERNANDEZ  
UNIVERSIDAD DE LA LAGUNA

26/06/2017 15:25:57

ERNESTO PEREDA DE PABLO  
UNIVERSIDAD DE LA LAGUNA

28/06/2017 13:21:41

if the magnetic lines follow a toroidal configuration, the current will in turn generate a poloidal magnetic field by induction. The quick buoyancy of any concentration of magnetic flux in the convection zone prior to being sufficiently amplified is a major problem associated with distributed dynamos or mean-field models. Another one lies in the fact that the generation of the poloidal field can eventually retrofeed the  $\alpha$ -effect and halt the generation of the poloidal field. Brandenburg (2005) discussed the possibility that the solar-dynamo effects could be concentrated below the photosphere and driven by a radial shear in the outer 35 Mm of the Sun. However, it encounters similar difficulties as distributed dynamos.

Models with interface dynamos also locate the production of the poloidal field at the tachocline itself. Using a two-layer model, Parker (1993); MacGregor and Charbonneau (1997); Charbonneau and MacGregor (1997) solved the problem of the halt of the  $\alpha$ -effect by retrofeeding. In this model, poloidal fields are generated in the upper layers of the tachocline, above the layer where toroidal fields are generated. Turbulent diffusion facilitates the transfer of poloidal and toroidal magnetic fields between layers. The presence of a strong concentration of magnetic field in the thin overshoot layer inhibits convection in this layer and stabilises the model. The main drawback of interface dynamos is that the values of the parameters of the models are usually critical and very slight variations of them can stop reproducing the observable behaviour of the Sun.

We have presented briefly the characteristics of the most common solar-dynamo models. Weiss and Thompson (2009); Charbonneau (2010); Hughes, Rosner, and Weiss (2012) discuss with greater detail these and other models for the solar dynamo. Besides the generation of poloidal and toroidal magnetic flux, a successful model should also explain the Joy's and Hale's polarity laws, and another observed evidence such as the shorter duration of the rising part of a solar cycle, the Waldmeier effect, in which the amplitude and length of a solar cycle are inversely proportional (Waldmeier, 1935, 1939; Richards, Rogers, and Richards, 2009), the presence of double-peak maxima with a separation of 1.3 years during some solar cycles, the existence of long-term cycles, such as the Gleißberg cycle of 88 years (Gleißberg, 1939), or the eventual presence of grand minima, such as the Maunder minimum (Ribes and Nesme-Ribes, 1993), among others.

Despite lack of full consensus, it is clear that the tachocline itself plays a key role in the solar dynamo. It is the generally-believed location for the  $\omega$ -effect. Although several possible locations have been proposed for the location of the  $\alpha$ -effect, when this effect is distributed throughout the convection zone, it would eventually halt due to retrofeeding. Thus, the tachocline is also the most likely location for the  $\alpha$ -effect as well. In this scenario, toroidal fields are created locally by the drag of differentially-rotating material exerted on poloidal fields. They are then transported downwards by turbulent pumping—the  $\gamma$ -effect—and convection overshooting, and they are stored in the stably stratified region in the lower part of the tachocline for times comparable to the duration of the solar cycle. Instabilities can produce the release of some of these stored fields that ascend to the photosphere thanks to magnetic buoyancy

Este documento incorpora firma electrónica, y es copia auténtica de un documento electrónico archivado por la ULL según la Ley 39/2015.  
Su autenticidad puede ser contrastada en la siguiente dirección <https://sede.ull.es/validacion/>

Identificador del documento: 963882

Código de verificación: QDmfX6JG

Firmado por: MANUEL DIAZ ALFARO  
UNIVERSIDAD DE LA LAGUNA

Fecha: 26/06/2017 15:24:15

FERNANDO JAVIER PEREZ HERNANDEZ  
UNIVERSIDAD DE LA LAGUNA

26/06/2017 15:25:57

ERNESTO PEREDA DE PABLO  
UNIVERSIDAD DE LA LAGUNA

28/06/2017 13:21:41

and create surface magnetic phenomena there. The confinement of strong magnetic fields in a thin stratified layer within the tachocline inhibits convection locally, which in turn intensifies this confinement and separates the layers where magnetic fields are generated above and where they are stored below. The  $\alpha$ -effect operates in the upper layers of the tachocline, above the  $\omega$ -effect, producing poloidal fields that are pumped down and stored. The absence of strong magnetic fields in the generation layer avoids the retrofeeding issues that eventually halt the  $\alpha$ -effect in distributed dynamos. Figure 1.8 illustrates the structure of the tachocline following the model by Parker (1993); MacGregor and Charbonneau (1997); Charbonneau and MacGregor (1997). A comprehensive review of the tachocline can be found in Hughes, Rosner, and Weiss (2012).



Figure 1.8: Diagram illustrating the location and structure of the tachocline. The red-coloured region represents the convection zone and the blue-coloured region, the radiation zone. The separation between both is marked as BCZ, for the base of the convection zone. Convective overshooting produces a region in the upper part of the radiative envelope that is still accessible for material being carried by inertia from the convection zone above. This is represented with the aid of blue circles. The stably stratified layers below are represented with parallel blue horizontal lines. The tachocline in general comprises part of the convection zone and part of the radiative zone and its extension is signalled in the diagram with the aid of a black rectangle. The limits of the different structures can move with the solar cycle and also with latitude.

Este documento incorpora firma electrónica, y es copia auténtica de un documento electrónico archivado por la ULL según la Ley 39/2015.  
Su autenticidad puede ser contrastada en la siguiente dirección <https://sede.ull.es/validacion/>

Identificador del documento: 963882

Código de verificación: QDmfX6JG

Firmado por: MANUEL DIAZ ALFARO  
UNIVERSIDAD DE LA LAGUNA

Fecha: 26/06/2017 15:24:15

FERNANDO JAVIER PEREZ HERNANDEZ  
UNIVERSIDAD DE LA LAGUNA

26/06/2017 15:25:57

ERNESTO PEREDA DE PABLO  
UNIVERSIDAD DE LA LAGUNA

28/06/2017 13:21:41

### 1.3 Helioseismology

The measurement of physical magnitudes in the solar interior can be of valuable aid to improve models explaining the solar dynamo and the 22-year cycle of solar magnetic activity. Although direct observation of the solar interior is not possible due to the opacity of the convection zone to electromagnetic radiation, the discovery of solar oscillations in the year 1960 and the resulting study of acoustic waves in the Sun opened an indirect way to infer properties of the solar interior. In that year, Leighton, Noyes, and Simon (1962), using spectroheliograms taken simultaneously in the redder and bluer zones of the solar spectrum, observed a pattern of variable intensity, discovering oscillations with a period of 5 minutes. They had observed radial movements in the solar surface through Doppler shifts and proved the existence of oscillatory movements in the photosphere.

Later, solar oscillations were proved to be the visible manifestation of acoustic standing waves trapped in the solar interior (Ulrich, 1970; Leibacher and Stein, 1971) and it was observed that they were concentrated in a discrete frequency spectrum (Deubner, 1975; Rhodes, Ulrich, and Simon, 1977; Claverie *et al.*, 1979), proving that their origin laid in processes in the solar interior. In this way, a new field of solar physics was born and developed, which allowed the study of the current conditions of the solar interior through helioseismic methods, similar to those used in geophysics to study the interior of the Earth. Helioseismology has demonstrated since then to be a strong set of tools to study the solar interior through the observation and characterization of acoustic and gravity waves on its surface. Chaplin (2006) provides a narrative historical review of this process of development of helioseismology.

Local helioseismology techniques developed at a later stage. They allow to resolve and study the whole structure of the wavefield observed at the surface, and not only their oscillation eigenmodes. These techniques allow to study locally perturbations in the solar interior or at its surface, providing a three-dimensional vision of the Sun. The presence of magnetic fields that modify the physical properties of the solar interior can be studied through different local helioseismology methods.

#### 1.3.1 Acoustic modes

The Sun, as other stars, is formed by plasma in hydrostatic equilibrium, where any transient perturbation can give origin to the formation of waves due to the apparition of a restoring force opposing the perturbation. The strong stratification of temperature and density in the solar interior results in the formation of resonant cavities in which acoustic waves are confined. Besides, the temperature stratification originates changes with depth in the sound speed and thus the raypaths of waves propagating downwards are progressively curved due to refraction as they penetrate into deeper layers of the solar interior and eventually start propagating back upwards. Near the surface those waves are reflected back into the solar interior due to a sharp increase in the acoustic cut-off frequency caused by a sharp reduction of density. The origin of oscillations in the Sun is believed to be located in the shallow

Este documento incorpora firma electrónica, y es copia auténtica de un documento electrónico archivado por la ULL según la Ley 39/2015.  
Su autenticidad puede ser contrastada en la siguiente dirección <https://sede.ull.es/validacion/>

Identificador del documento: 963882

Código de verificación: QDmfX6JG

Firmado por: MANUEL DIAZ ALFARO  
UNIVERSIDAD DE LA LAGUNA

Fecha: 26/06/2017 15:24:15

FERNANDO JAVIER PEREZ HERNANDEZ  
UNIVERSIDAD DE LA LAGUNA

26/06/2017 15:25:57

ERNESTO PEREDA DE PABLO  
UNIVERSIDAD DE LA LAGUNA

28/06/2017 13:21:41

subphotosphere, where waves are driven by turbulent convection (Goldreich and Keeley, 1977).

Small oscillations in a spherical domain can be represented by a linear superposition of individual oscillation modes characterised by a set of three indices: the radial order  $n$ , the angular order  $\ell$ , and the azimuthal order  $m$ . They represent respectively the number of nodes along the radial direction, the number of nodal circles in the spherical surface, and the number of nodal circles that pass through the poles. To a good approximation, the non-radial dependency can be expressed as spherical harmonics  $Y_\ell^m(\theta, \varphi)$ . For each particular mode, characterized by the temporal frequency and the three indices  $n$ ,  $\ell$ , and  $m$ , the position and size of the resonant cavity varies. Thus, different modes will penetrate up to a different layer in the solar interior.

Acoustic modes are often referred to as p-modes or pressure modes. Their restoring force is pressure and in the Sun they have typical frequencies above 1 mHz, being specially intense in the range 2.5–4.5 mHz, corresponding to a period of approximately 5 minutes. These are the ones considered in this work. The modes that lack radial nodes ( $n = 0$ ) are specifically called fundamental modes, f-modes, or even surface gravity modes. Also present in the Sun are gravitational modes or g-modes, which are completely different in origin. Their restoring force is gravity, or negative buoyancy, they have typical frequencies of  $\approx 0.4$  mHz, and are confined below the convection zone. Therefore they are impractical for helioseismic probing of the solar interior.

Although resonant cavities present a reflecting boundary beneath the photosphere, part of the confined standing waves is not reflected but passes through the interface as an evanescent wave, which allows us to observe the acoustic behaviour at the surface as a velocity or Doppler-shift field. Besides, we can select specific modes and tune the specific depth from which we want to receive information. Any perturbation located at that specific layer will modify the corresponding acoustic mode and leave an imprint on it that we can interpret upon observation at the photosphere.

In the Sun the mean acoustic travel time from the centre to the photosphere is approximately one hour, which is very low compared to typical time scales or decay times of solar phenomena. Therefore, the inferences obtained from acoustic oscillations represent real-time results of what is happening in the Sun.

### 1.3.2 Local helioseismology

Global helioseismology tools study the eigenmodes of the Sun and variations of frequency values to infer changes in the solar structure with the aid of inversion techniques. However, though they are capable of resolving absolute latitude, they fail to resolve longitude or distinguish between northern and southern hemisphere. As a consequence, detecting phenomena such as meridional flows or longitudinal variations in any physical magnitude of the Sun is impossible therewith. A new set of tools, englobed under the term local helioseismology, has been developed more recently in order to interpret the whole structure of the wavefield observed at the solar surface, allowing for full spatial resolution. These techniques of local helioseismology allow the

Este documento incorpora firma electrónica, y es copia auténtica de un documento electrónico archivado por la ULL según la Ley 39/2015.  
Su autenticidad puede ser contrastada en la siguiente dirección <https://sede.ull.es/validacion/>

Identificador del documento: 963882

Código de verificación: QDmfX6JG

Firmado por: MANUEL DIAZ ALFARO  
UNIVERSIDAD DE LA LAGUNA

Fecha: 26/06/2017 15:24:15

FERNANDO JAVIER PEREZ HERNANDEZ  
UNIVERSIDAD DE LA LAGUNA

26/06/2017 15:25:57

ERNESTO PEREDA DE PABLO  
UNIVERSIDAD DE LA LAGUNA

28/06/2017 13:21:41

study of local variations in the solar interior or at its surface, being able to provide a three-dimensional view of the Sun, as can be seen in Duvall *et al.* (1996). The presence of magnetic fields in the solar interior modifies the physical properties thereof, and therefore, they may be studied making use of methods of local helioseismology. Using different approaches, several techniques have been developed in the field of local helioseismology (Gizon and Birch, 2005; Schunker, 2010).

The Fourier-Hankel spectral method is one of the them. It was introduced by Braun, Duvall, and Labonte (1987) in order to study the wave absorption by sunspots. Here, the observed p-mode amplitudes are decomposed into ingoing and outgoing waves—Hankel functions and their Fourier-transformed counterparts—in an annular region around a sunspot using a cylindrical coordinate system centred on the sunspot. This method allows the comparison of ingoing and outgoing waves, having proved that sunspots are strong absorbers of energy and shifters of the phase of incoming p- and f-modes (Braun, Duvall, and Labonte, 1988; Braun *et al.*, 1992; Braun, 1995).

Ring-diagram analysis, introduced by Hill (1988), constitutes a generalization of global helioseismology tools applied to local areas of the Sun. This method studies three-dimensional  $\mathbf{k} - \omega$  datacubes<sup>8</sup> of the local power spectra of solar oscillations computed over a small patch at the solar surface, which is tracked as it moves across the disk. The datacubes show a characteristic ring pattern, which gives the name to the method. The power spectra are fitted using different methods (*e.g.* Patrón *et al.*, 1997; Schou and Bogart, 1998; Basu, Antia, and Tripathy, 1999) and the fit parameters can eventually be inverted in order to determine the physical magnitudes underneath the patch over which the local spectrum has been computed and fitted using mainly the RLS (Hansen, 1998; Larsen, 1998) and the OLA (Backus and Gilbert, 1968) methods. Ring-diagram analysis has proved a powerful tool to study horizontal flows below the solar surface (*e.g.* Patrón *et al.*, 1998; González Hernández *et al.*, 1998, 1999; Baldner *et al.*, 2013; Komm *et al.*, 2015).

Time-distance helioseismology, introduced by Duvall *et al.* (1993), measures the travel time of waves between two points on the solar surface, using the cross-covariance function of the Doppler magnitudes at the two locations. The cross-covariance functions can also be computed between a central point and the average Doppler magnitude of the surrounding annulus to study the divergence of flows. The division of the annular region into quadrants further allows to determine the direction of the flow. However, cross-covariance functions can have a large amount of realisation noise and therefore, some averaging is usually required to compute travel times from them, *e.g.* via Gabor wavelets fitting (Duvall *et al.*, 1997), or one-parameter fitting (Gizon and Birch, 2002, 2004). Inversion methods are required to extract the information about the local structure and dynamics of the solar interior from the measured travel times. Meridional circulation, which is a principal component in some solar-dynamo models, has been one of the major discoveries achieved with time-distance helioseismology (Giles *et al.*, 1997).

Helioseismic holography, a technique in which this work is based, was proposed

<sup>8</sup> $\mathbf{k}$  is the horizontal wavevector, which can be decomposed into  $k_x$  and  $k_y$

Este documento incorpora firma electrónica, y es copia auténtica de un documento electrónico archivado por la ULL según la Ley 39/2015.  
Su autenticidad puede ser contrastada en la siguiente dirección <https://sede.ull.es/validacion/>

Identificador del documento: 963882

Código de verificación: QDmfX6JG

Firmado por: MANUEL DIAZ ALFARO  
UNIVERSIDAD DE LA LAGUNA

Fecha: 26/06/2017 15:24:15

FERNANDO JAVIER PEREZ HERNANDEZ  
UNIVERSIDAD DE LA LAGUNA

26/06/2017 15:25:57

ERNESTO PEREDA DE PABLO  
UNIVERSIDAD DE LA LAGUNA

28/06/2017 13:21:41

initially at a theoretical level by Roddier (1975) and developed at a practical level by Lindsey and Braun (1990, 1997, 2000a). This technique utilizes the observed acoustic wavefield at the surface of the Sun to make estimates of the wavefield on any other location at the solar surface or interior at any instant of time. Its development, based on holography in optics, abundantly uses optical terminology. An analogue application is seismic migration, used in geophysics to study the interior of the geosphere by means of the determination of the seismic wavefield in the interior of the Earth (*e.g.* Hagedoorn, 1954; Claerbout, 1985). Acoustic imaging, developed in parallel, follows a similar technique to helioseismic holography, making also reconstructions of the wavefield in the solar interior (*e.g.* Chang *et al.*, 1997; Chou *et al.*, 2003). Helioseismic holography has been used to study subphotospheric flows (Braun, Birch, and Lindsey, 2004) and seismic sources from flares (Donea *et al.*, 2006), but its major application has been to map areas of strong magnetic field (Braun *et al.*, 1998). Specially, the mapping of active regions in the non-visible far-side hemisphere of the Sun (Lindsey and Braun, 2000b; Braun and Lindsey, 2001) has proved a reliable tool to infer magnetic fields at the far-side photosphere (González Hernández, Hill, and Lindsey, 2007; Liewer *et al.*, 2014), which is a powerful input for space weather forecasting (Fontenla *et al.*, 2009; González Hernández, 2013; González Hernández *et al.*, 2014).

Direct modelling is a more recent local helioseismology technique introduced by Woodard (2002). It estimates flows in the interior of the Sun from direct inversions of the correlations in the Fourier domain. Its aim has remained with the detection of subsurface flows (Woodard, 2007, 2009).

The main input for local helioseismology techniques is formed by high-resolution dopplergrams, *i.e.* maps of the radial velocity at the solar surface. The deployment of different networks of telescopes distributed throughout the Earth has provided in the last decades a continuous flux of data for helioseismology. Among them we can find the *Taiwan Oscillations Network* (TON; Chou *et al.*, 1995) and the *Global Oscillation Network Group* (GONG; Harvey *et al.*, 1996; Leibacher, 1999), the latter providing the observational data used in this thesis. Spatial instruments have also provided helioseismic data with high continuity, such as the *Michelson Doppler Imager* (MDI; Scherrer *et al.*, 1995) onboard the *Solar and Heliospheric Observatory* (SOHO), or, more recently, the *Helioseismic and Magnetic Imager* (HMI; Scherrer *et al.*, 2012) onboard the *Solar Dynamics Orbiter* (SDO).

### 1.3.3 Helioseismic inferences about the base of the convection zone and tachocline

Helioseismology has already provided interesting results concerning the base of the convection zone and the tachocline. The base of the convection zone has been found to be a spherical surface located at  $0.712 R_{\odot}$  with the aid of global helioseismology (Baldner and Basu, 2008; Antia and Basu, 2011). Global helioseismology techniques have also been used to estimate the location and thickness of the tachocline. Its thickness is estimated to range between  $0.006R_{\odot}$  and  $0.09R_{\odot}$  (*e.g.* Kosovichev, 1996; Basu, 1997; Corbard *et al.*, 1999; Elliott and Gough, 1999). Some studies

Este documento incorpora firma electrónica, y es copia auténtica de un documento electrónico archivado por la ULL según la Ley 39/2015.  
Su autenticidad puede ser contrastada en la siguiente dirección <https://sede.ull.es/validacion/>

Identificador del documento: 963882

Código de verificación: QDmfX6JG

Firmado por: MANUEL DIAZ ALFARO  
UNIVERSIDAD DE LA LAGUNA

Fecha: 26/06/2017 15:24:15

FERNANDO JAVIER PEREZ HERNANDEZ  
UNIVERSIDAD DE LA LAGUNA

26/06/2017 15:25:57

ERNESTO PEREDA DE PABLO  
UNIVERSIDAD DE LA LAGUNA

28/06/2017 13:21:41

have also demonstrated that the tachocline is prolate, its position being estimated at  $\approx 0.69R_{\odot}$  at the equator, and  $\approx 0.71R_{\odot}$  at a latitude of  $60^{\circ}$ . Therefore, in the equatorial region, the tachocline would lie fully inside the radiative envelope, below the base of the convection zone, but it would enter the convection zone at higher latitudes (*e.g.* Charbonneau *et al.*, 1999; Basu and Antia, 2003; Antia and Basu, 2011).

The sound-speed profile in the interior of the Sun and its differences with standard solar models have also been studied with both global and local helioseismology techniques. Gough *et al.* (1996); Kosovichev *et al.* (1997) inferred profiles of the variation of the sound speed with respect to a standard solar model, which showed a peak value of  $\delta c^2/c^2 \approx 4 \cdot 10^{-3}$  at about  $\approx 0.67R_{\odot}$  using global helioseismology. Consistent results were obtained by Zhao *et al.* (2009) using a time-distance technique.

The variability of the acoustic behaviour in the vicinity of the base of the convection zone with the solar cycle has also been studied. Chou and Serebryanskiy (2002, 2005); Eff-Darwich *et al.* (2002); Serebryanskiy and Chou (2005); Baldner and Basu (2008), using different techniques of global and local helioseismology, have presented upper limits or evidences for that temporal variation, studying changes in the properties of modes with lower turning points near the base of the convection zone. Their obtained values for the relative sound-speed variation between solar minimum and solar maximum lie in the range  $\delta c/c = (1-9) \cdot 10^{-5}$ .

#### 1.4 Numerical simulations of the Sun

Numerical simulations have been used extensively in solar physics to model and characterise the phenomena and physical properties of the Sun at very different scales. Simulations are abundant for characterizing sunspots (*e.g.* Rempel, Schüssler, and Knölker, 2009; Rempel *et al.*, 2009; Cheung *et al.*, 2010; Felipe, Khomenko, and Collados, 2011; Rempel, 2015) or the granulation and other aspects of convection (*e.g.* Stein and Nordlund, 2000; Beeck *et al.*, 2013a,b, 2015a,b). Other layers and phenomena of the Sun have also been studied with the aid of numerical simulations, such as the chromosphere, the corona, the solar wind, or the relation between the Sun and the heliosphere, among others (*e.g.* Hayashi *et al.*, 2006; Khomenko and Collados Vera, 2012; Khomenko *et al.*, 2014; Yalim and Poedts, 2014).

Numerical simulations can also prove useful to validate local helioseismic techniques and analyse their response and accuracy when applied to regions of the Sun of which direct observation is not possible (*e.g.* Braun *et al.*, 2012; DeGrave, Jackiewicz, and Rempel, 2014a,b). More particularly, a collection of numerical simulations based on the work by Hartlep and Mansour (2004, 2005) have proved successful to validate and characterize different applications of local helioseismology, some of which have been used in this work. They have been used to validate time-distance far-side imaging (Hartlep *et al.*, 2008), to validate the detection of typical perturbations in sound speed at the tachocline with the aid of a time-distance

Este documento incorpora firma electrónica, y es copia auténtica de un documento electrónico archivado por la ULL según la Ley 39/2015.  
Su autenticidad puede ser contrastada en la siguiente dirección <https://sede.ull.es/validacion/>

Identificador del documento: 963882

Código de verificación: QDmfX6JG

Firmado por: MANUEL DIAZ ALFARO  
UNIVERSIDAD DE LA LAGUNA

Fecha: 26/06/2017 15:24:15

FERNANDO JAVIER PEREZ HERNANDEZ  
UNIVERSIDAD DE LA LAGUNA

26/06/2017 15:25:57

ERNESTO PEREDA DE PABLO  
UNIVERSIDAD DE LA LAGUNA

28/06/2017 13:21:41

procedure (Zhao *et al.*, 2009), to test the detection of emerging active regions through time-distance imaging (Hartlep *et al.*, 2011), and seismic holography (Braun, 2014), to study the response of seismic holography of active regions with respect to their longitudinal position (Díaz Alfaro *et al.*, 2013), and to test the detection of deep meridional flows through time-distance seismology (Hartlep *et al.*, 2013).

## 1.5 Objectives

The adaptation and test of the validity of phase-sensitive helioseismic holography for imaging seismic perturbations in the solar interior at layers in the vicinity of the base of the convection zone and tachocline constitute the major aim of this thesis. Detecting seismic signals in these layers and characterising their evolution may help to better understand and characterise the solar dynamo and the phenomena involved in the cycle of solar activity and the evolution of solar magnetism.

To this end, the technique is applied first of all to numerically simulated data with perturbations in the sound speed at the depths of interest to measure the response of the technique to sound-speed variations. The effects of shallower seismic features on the deeper layers of interest are then assessed with the aid of simulations with sound-speed perturbations located at the solar surface and in the shallow subphotosphere mimicking photospheric and emerging active regions respectively. These results are presented in Chapter 3.

The technique is finally applied to actual solar observations in order to infer sound-speed variations with respect to a standard solar model at the depths of interest using the response function determined with the numerically simulated data of Chapter 3. Chapter 4 presents the inferred sound speed at two solar minima and the evolution of sound speed between periods of low and high activity. The inferred sound-speed values are compared with previous results to assess the validity of the technique. The limitations of the technique are explored and possible improvements are suggested.

Este documento incorpora firma electrónica, y es copia auténtica de un documento electrónico archivado por la ULL según la Ley 39/2015.  
Su autenticidad puede ser contrastada en la siguiente dirección <https://sede.ull.es/validacion/>

Identificador del documento: 963882

Código de verificación: QDmfX6JG

Firmado por: MANUEL DIAZ ALFARO  
UNIVERSIDAD DE LA LAGUNA

Fecha: 26/06/2017 15:24:15

FERNANDO JAVIER PEREZ HERNANDEZ  
UNIVERSIDAD DE LA LAGUNA

26/06/2017 15:25:57

ERNESTO PEREDA DE PABLO  
UNIVERSIDAD DE LA LAGUNA

28/06/2017 13:21:41

# 2

## Methodology

Helioseismic holography, introduced in Section 1.3.2, estimates the acoustic wavefield at any location in the solar interior or at the solar surface at any instant of time making use of the observed wavefield, *i.e.* the line-of-sight Doppler velocity at the solar surface. As such, it is an ideal technique to infer properties of areas of the Sun not accessible to direct observation.

In this chapter we present the phase-sensitive helioseismic holography technique used in this work. It is based on the currently-used technique applied on a regular basis to GONG data to produce maps of the inferred magnetic activity in the non-visible far-side hemisphere of the Sun, which has been adapted here for use at deeper layers near the base of the convection zone.

### 2.1 Acoustic egression and ingression

The acoustic egression and ingression are the two main computations in helioseismic holography. The acoustic egression  $H_+$  at a focus at or below the solar surface is calculated as the regression of the acoustic field observed over a limited region of the surface (the pupil) backwards in time through a solar model. The acoustic ingression  $H_-$ , calculated as the progression of the acoustic field forwards in time, constitutes its time-reversed counterpart. Therefore, the egression and ingression represent an estimate of the acoustic wavefield at a certain point (the focus) assuming that it results only from waves respectively converging to, or diverging from, that focus.

Helioseismic holography can be approached in the spectral Fourier domain, which facilitates filtering of modes and improves computational performance. In the Fourier domain, the egression and the ingression are given by:

$$\hat{H}_{\pm}(\mathbf{r}, \nu) = \int_{\mathcal{P}_{\pm}} \hat{G}_{\pm}(\mathbf{r}, \theta', \varphi', \nu) \hat{\Psi}_{\text{obs}}(\theta', \varphi', \nu) d\Omega', \quad (2.1)$$

where  $\hat{\Psi}_{\text{obs}}$  is the Fourier-transformed wavefield, *i.e.* the Fourier-transformed line-of-sight Doppler velocity observed at the surface of the Sun,  $\hat{G}_{\pm}$  are Green's functions

Este documento incorpora firma electrónica, y es copia auténtica de un documento electrónico archivado por la ULL según la Ley 39/2015.  
Su autenticidad puede ser contrastada en la siguiente dirección <https://sede.ull.es/validacion/>

Identificador del documento: 963882

Código de verificación: QDmfX6JG

Firmado por: MANUEL DIAZ ALFARO  
UNIVERSIDAD DE LA LAGUNA

Fecha: 26/06/2017 15:24:15

FERNANDO JAVIER PEREZ HERNANDEZ  
UNIVERSIDAD DE LA LAGUNA

26/06/2017 15:25:57

ERNESTO PEREDA DE PABLO  
UNIVERSIDAD DE LA LAGUNA

28/06/2017 13:21:41

corresponding to gravito-acoustic waves emanating from ( $\hat{G}_-$ ) or arriving to ( $\hat{G}_+$ ) the focus and propagating through the solar interior,  $\mathbf{r}$  represents the position of the focal point,  $\theta'$  and  $\varphi'$  represent the position of a given point at the solar surface within the pupil ( $\mathcal{P}_\pm$ ), and  $\nu$  is the frequency.

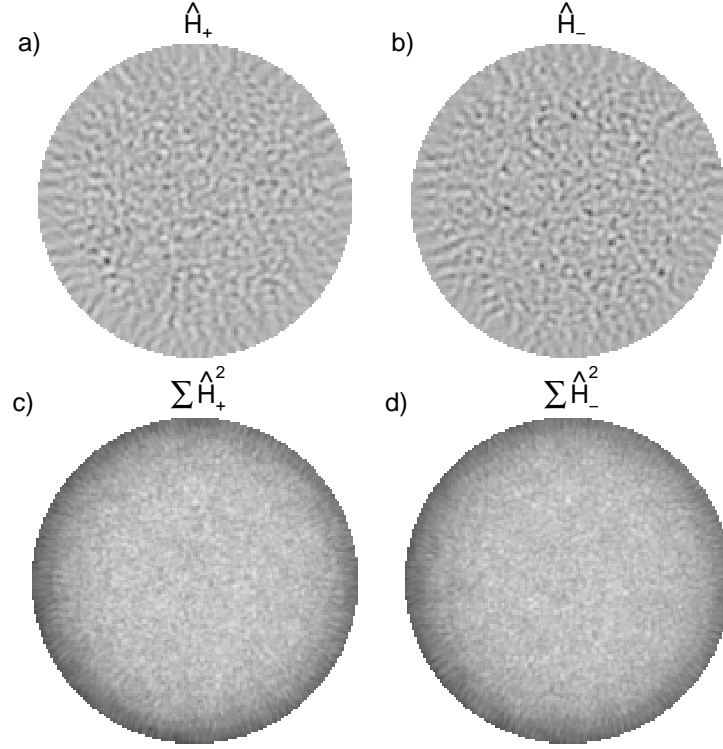


Figure 2.1: Above: map of the real part of the egression  $\hat{H}_+$  (a) and of the ingression  $\hat{H}_-$  (b) functions for a frequency  $\nu = 3.312$  mHz for GONG observations from 1 January 2015 computed using  $1 \times 1$  skip helioseismic holography with Green's functions in the polar-expansion approach of Pérez Hernández and González Hernández (2010). Below: power maps of the above egression (c) and ingression (d) functions for a frequency span between 2.5 and 4.5 mHz.

Figure 2.1 shows the real part of the egression  $\hat{H}_+$  (a) and of the ingression  $\hat{H}_-$  (b) computed for a frequency  $\nu = 3.312$  mHz, created using 24 h of GONG observations, corresponding to 1 January 2015. The seismic maps have been created with Green's functions in the polar-expansion approach of Pérez Hernández and González Hernández (2010) in a  $1 \times 1$  skip subjacent-vantage configuration, as discussed in Sections 2.3 and 2.4. Equation (2.1) is used to compute the values of the egression and of the ingression for each particular pixel of the map for all the considered values in the frequency interval between  $\nu \approx 2.5$  mHz and  $\nu \approx 4.5$  mHz with a step of  $\delta\nu \approx 8$   $\mu$ Hz. In addition, panels (c) and (d) show the power of the egression and

Este documento incorpora firma electrónica, y es copia auténtica de un documento electrónico archivado por la ULL según la Ley 39/2015.  
Su autenticidad puede ser contrastada en la siguiente dirección <https://sede.ull.es/validacion/>

Identificador del documento: 963882

Código de verificación: QDmfX6JG

Firmado por: MANUEL DIAZ ALFARO  
UNIVERSIDAD DE LA LAGUNA

Fecha: 26/06/2017 15:24:15

FERNANDO JAVIER PEREZ HERNANDEZ  
UNIVERSIDAD DE LA LAGUNA

26/06/2017 15:25:57

ERNESTO PEREDA DE PABLO  
UNIVERSIDAD DE LA LAGUNA

28/06/2017 13:21:41

of the ingression respectively. They correspond to the integration over a frequency span of the square of the egression and of the ingression amplitudes respectively and follow the equation:

$$P_{\pm}(\mathbf{r}) = \int_{\nu} \hat{H}_{\pm}(\mathbf{r}, \nu) d\nu. \quad (2.2)$$

Egression power maps (c) are used in acoustic power holography and have been successful confirming previous discoveries of p-mode absorption in sunspots made with Fourier-Hankel analysis applying this technique to observations taken with TON (Braun, Duvall, and Labonte, 1987, 1988). They have been used later to map areas of solar activity (*e.g.* Braun *et al.*, 1998; Lindsey and Braun, 1998; Braun and Lindsey, 1999; Lindsey and Braun, 2000a).

## 2.2 Phase-sensitive seismic holography

More sensitive than acoustic power holography is phase-sensitive seismic holography, which as well as being sensitive to absorptions and sources of seismic power is also sensitive to its refraction and scattering. This technique, developed by Lindsey and Braun (2000a) and Braun and Lindsey (2000), makes a phase-coherent wave-mechanical reconstruction of the acoustic field of the solar interior comparing the acoustic egression  $\hat{H}_+$  with the acoustic ingression  $\hat{H}_-$ .

Waves travelling through an active region experience a travel delay or phase shift (Braun *et al.*, 1992; Duvall *et al.*, 1996), which can be used to map areas of strong magnetic field. The reconstruction of the acoustic field at some point beneath the solar surface, expressed as  $\hat{H}_{\pm}$ , by phase-coherent acoustic progression or regression of the observed wavefield at the surface  $\hat{\Psi}_{\text{obs}}$ , is done assuming a nominal acoustic model devoid of submerged acoustic anomalies. Therefore, when the focal point is located in a perturbed area, there appears a phase shift—or time delay—between the ingression and the egression functions, whereas in the quiet Sun, where actual acoustic anomalies are not present, the egression and the ingression functions are statistically correlated.

In the Fourier domain, the egression-ingression correlation can be expressed as the integral of the product between  $\hat{H}_+$  and  $\hat{H}_-$ ,

$$C(\mathbf{r}) = Ae^{-i\phi(\mathbf{r})} = \int_{\nu_1}^{\nu_2} \hat{H}_+(\mathbf{r}, \nu) \hat{H}_-^*(\mathbf{r}, \nu) d\nu, \quad (2.3)$$

where  $\hat{H}_-^*$  represents the complex conjugate of the ingression function  $\hat{H}_-$ . The phase of the correlation,  $\phi(\mathbf{r})$ , is related to the perturbed mean travel time  $\Delta\tau$  and the mean frequency  $\langle\nu\rangle$  by:

$$\phi(\mathbf{r}) = 2\pi\langle\nu\rangle\Delta\tau. \quad (2.4)$$

Este documento incorpora firma electrónica, y es copia auténtica de un documento electrónico archivado por la ULL según la Ley 39/2015.  
Su autenticidad puede ser contrastada en la siguiente dirección <https://sede.ull.es/validacion/>

Identificador del documento: 963882

Código de verificación: QDmfX6JG

Firmado por: MANUEL DIAZ ALFARO  
UNIVERSIDAD DE LA LAGUNA

Fecha: 26/06/2017 15:24:15

FERNANDO JAVIER PEREZ HERNANDEZ  
UNIVERSIDAD DE LA LAGUNA

26/06/2017 15:25:57

ERNESTO PEREDA DE PABLO  
UNIVERSIDAD DE LA LAGUNA

28/06/2017 13:21:41

### 2.3 Green's functions

The outgoing Green's function  $\hat{G}_+(\mathbf{r}, \theta, \varphi, \nu)$  represents the theoretical subsurface disturbance at the focus ( $\mathbf{r}$ ) producing a unit transient at the surface at a certain point  $(\theta, \varphi)$  within the pupil for a Sun devoid of anomalies. The ingoing Green's function  $\hat{G}_-$  is its time-reversed counterpart, representing the theoretical disturbance at the surface producing a unit transient originating at the focus ( $\mathbf{r}$ ).  $\hat{G}_\pm$  represent the nominal acoustic model of the Sun as complex propagators, which evolve the acoustic field backwards ( $\hat{G}_+$ ) and forwards ( $\hat{G}_-$ ) in time.

Green's functions can be calculated using the eikonal approximation or a full set of wave-mechanical equations (Lindsey and Braun, 2004; Schunker *et al.*, 2005). Green's functions computed with the eikonal approximation, also referred to as ray theory, have been used extensively in far-side seismic holography to map active regions in the non-visible hemisphere of the Sun (Lindsey and Braun, 2000b; Braun and Lindsey, 2001; González Hernández, Hill, and Lindsey, 2007). This approximation is formally only valid for high frequencies and high angular degrees  $\ell$ . Therefore, it is appropriate for creating seismic maps of the solar surface. However, when attempting to probe deeper layers in the Sun lower angular degrees  $\ell$  are necessary. In this work, we make use of Green's functions calculated through their polar expansion, as developed by Pérez Hernández and González Hernández (2010).

We consider the scalar field ( $\tilde{\Psi}$ ) given by:

$$\tilde{\Psi} = -\rho^{-\frac{1}{2}}\delta p, \quad (2.5)$$

where  $\rho$  is the density of the base unperturbed state and  $\delta p$  is a Lagrangian pressure fluctuation. We assume its base state to be non-dependent on time, and therefore can be decomposed, using Fourier analysis, as a superposition of monochromatic waves:

$$\tilde{\Psi}(r, t) = \Psi(r, \omega)e^{-i\omega t}. \quad (2.6)$$

The corresponding wave equation for each monochromatic component of the scalar field ( $\Psi$ ) under the adiabatic, plane-parallel and Cowling approximations can be expressed as:

$$\nabla^2\Psi - \frac{\omega_{\text{BV}}^2}{\omega^2}\nabla_{\text{h}}^2\Psi + \frac{1}{c^2}(\omega^2 - \omega_{\text{c}}^2)\Psi = 0, \quad (2.7)$$

where  $\nabla_{\text{h}}^2$  represents the terms including horizontal derivatives in the  $\nabla^2$  operator;  $\omega_{\text{BV}}$  is the Brunt-Väisälä buoyancy frequency;  $c$  is the sound speed; and  $\omega_{\text{c}}$  is the acoustic cut-off frequency.

We apply Equation (2.7) to Green's functions, taking into account that they represent the resulting disturbance created by a unit transient impulse in a medium devoid of acoustic anomalies. After some mathematical manipulation we can split the solution into angular and radial terms for each individual angular order  $\ell$ , and operate them separately. For the angular dependencies two different solutions are obtained: a prograde solution ( $G_\ell^{\theta+}$ ) and a retrograde solution ( $G_\ell^{\theta-}$ ). Unlike in other formalisms, no asymptotic approximation has been considered when solving

Este documento incorpora firma electrónica, y es copia auténtica de un documento electrónico archivado por la ULL según la Ley 39/2015.  
Su autenticidad puede ser contrastada en la siguiente dirección <https://sede.ull.es/validacion/>

Identificador del documento: 963882

Código de verificación: QDmfX6JG

Firmado por: MANUEL DIAZ ALFARO  
UNIVERSIDAD DE LA LAGUNA

Fecha: 26/06/2017 15:24:15

FERNANDO JAVIER PEREZ HERNANDEZ  
UNIVERSIDAD DE LA LAGUNA

26/06/2017 15:25:57

ERNESTO PEREDA DE PABLO  
UNIVERSIDAD DE LA LAGUNA

28/06/2017 13:21:41

the angular part of the wave equation. Therefore, higher precision can be expected when using these Green's functions with low or intermediate angular degrees  $\ell$ . With respect to the radial part two solutions are also obtained: an outgoing solution ( $G_\ell^{r+}$ ) and an ingoing solution ( $G_\ell^{r-}$ ). However, the asymptotic approximation has been used in this case. Combining, on the one hand, the outgoing solution for the radial dependencies together with the prograde solution for the angular dependencies, and, on the other hand, the ingoing and retrograde solutions, we get a full expression for Green's functions. For each angular order  $\ell$  the expression for the outgoing prograde solution ( $G_\ell^+$ ) is given by:

$$G_\ell^+ = \frac{i(2\ell+1)}{8\pi r_0 \sqrt{k_r(r_0)}} r^{-1} k_r^{-\frac{1}{2}} \csc^{\frac{1}{2}} \theta \cdot B_{\ell+} \left[ \frac{i}{2} \left( Q_\ell \frac{dB_{\ell-}}{d\theta} - \frac{dQ_\ell}{d\theta} B_{\ell-} \right) \right] \exp \left( i \int_{r_0}^r k_r^2 dr \right), \quad (2.8)$$

where  $r_0$  represents the focus,  $r$  and  $\theta$  are the radial and angular position of evaluation of the Green's function at the pupil, considering that the angular variable  $\theta$  is measured using a coordinate system where the polar axis goes in the direction from the origin of coordinates to the focus,

$$Q_\ell = \sqrt{\sin \theta} P_\ell(\cos \theta), \quad (2.9)$$

with  $P_\ell(\cos \theta)$  a Legendre polynomial, and

$$B_{\ell\pm} = k_\ell^{-\frac{1}{2}} \exp \left( \pm i \int_{\theta_0}^\theta k_\ell d\theta \right), \quad (2.10)$$

being  $k_r$  and  $k_\ell$  the corresponding radial and angular components of the wave vector. A full expansion of the mathematical procedure with detailed steps can be found in the Appendix.

Equation (2.8) is used to calculate Green's functions for each value of angular order  $\ell$  and each frequency within the resonant cavity, between the reflection points given by  $k_r^2 = 0$ . Nevertheless, as for simplicity we are considering only a cosinusoidal function instead of using it together with the Airy function, which is the solution of Equation (A.7) (Appendix) near the turning points, this proposed solution diverges from the real solution in the vicinities of the turning points. This issue is solved by making Green's functions equal to zero at the points between the inner turning point and the first zero above it.

Green's functions for each frequency are obtained by adding the  $\ell$ -dependent solutions ( $G_\ell^+$ ):

$$G^+(\mathbf{r}|\mathbf{r}_0, \omega) = \sum_{\ell=\ell_1}^{\ell_2} G_\ell^+. \quad (2.11)$$

Then they are normalized, so that the same weight is given to any of the considered frequencies:

$$G_{\text{norm}}^+(\mathbf{r}|\mathbf{r}_0, \omega) = \frac{G^+(\mathbf{r}|\mathbf{r}_0, \omega)}{\langle |G^+(\mathbf{r}|\mathbf{r}_0, \omega)| \rangle}. \quad (2.12)$$

Este documento incorpora firma electrónica, y es copia auténtica de un documento electrónico archivado por la ULL según la Ley 39/2015.  
Su autenticidad puede ser contrastada en la siguiente dirección <https://sede.ull.es/validacion/>

Identificador del documento: 963882

Código de verificación: QDmfX6JG

Firmado por: MANUEL DIAZ ALFARO  
UNIVERSIDAD DE LA LAGUNA

Fecha: 26/06/2017 15:24:15

FERNANDO JAVIER PEREZ HERNANDEZ  
UNIVERSIDAD DE LA LAGUNA

26/06/2017 15:25:57

ERNESTO PEREDA DE PABLO  
UNIVERSIDAD DE LA LAGUNA

28/06/2017 13:21:41

Finally, in this work, ingoing Green's functions are computed as the complex conjugate of outgoing ones:  $G_- = G_+^*$ . They can alternatively be computed individually for each  $\ell$  and added as done with the outgoing Green's functions.

### 2.3.1 Phase-shift correction

Surface effects such as non-adiabaticity and the dynamics of convection, present in the uppermost layers of the Sun, where the asymptotic approximation is not valid, are large enough to be neglected. These effects were studied by Lindsey and Braun (2004) using empirical local control correlations, drawing the focus to the solar surface and comparing the acoustic egression and the acoustic ingression at the solar surface with the acoustic wavefield.

Alternatively, these effects can be taken into account by means of the introduction of a phase shift at the upper turning point,  $\delta\alpha$ , which allows to correct from asymptotic, non-adiabatic and non-spheric effects. Following Pérez Hernández and González Hernández (2010), we add the phase shift directly to Green's functions as:

$$\mathcal{G}_{\pm}(\mathbf{r}, \theta, \varphi, \nu) = G_{\pm}(\mathbf{r}, \theta, \varphi, \nu) \exp(2i\tilde{s}\pi\delta\alpha), \quad (2.13)$$

where  $\mathcal{G}_{\pm}$  are phase-shift-corrected Green's functions, and  $\tilde{s}$  is the number of surface reflections.

To a good approximation,  $\delta\alpha$  does not depend on the angular order  $\ell$  and is a function of frequency alone. Following Gough (1984); Deubner and Gough (1984),  $\delta\alpha(\nu)$  can be estimated with the following equation:

$$\int_{r_1}^{r_2} \left[ \frac{1}{c^2} (\omega^2 - \omega_c^2) - \left( 1 - \frac{\omega_{\text{BV}}^2}{\omega^2} \right) \frac{\ell(\ell+1)}{r^2} \right]^{\frac{1}{2}} dr = \pi \left( n - \frac{1}{2} - \delta\alpha \right), \quad (2.14)$$

where  $n$  is the radial order of the mode and the other variables have been previously defined. This equation represents the dispersion relation corresponding to Equation (2.7) in the asymptotic approximation.

In a case where only the formal reflection bounces at the surface introduce a phase shift, we would consider  $\tilde{s} = s - 1$ , where  $s$  is the number of inner reflections or skips. Yet, the pupil is so close to the upper turning point that it can account for an additional phase shift of about half a bounce. Therefore, in practice, we should take  $\tilde{s} = s - 1/2$  when the focus is below the uppermost layers of the Sun. Analogously, when we draw the focus to the surface, we should take into account an additional half bounce, and we should consider  $\tilde{s} = s$ . Therefore, throughout this work, we will use  $\tilde{s} = s - 1/2$  for phase-shift correction of seismic maps with submerged foci, and we will use  $\tilde{s} = s$  in order to create seismic maps at the solar surface.

In this work, following Pérez Hernández and González Hernández (2010), we have used observed eigenfrequencies from  $\nu = 2.5$  mHz to  $\nu = 4.5$  mHz and degrees between  $\ell = 20$  and  $\ell = 80$  taken from MDI data to compute a phase-shift correction independent of  $r$ . This phase shift includes all the aspects that were neglected in the wave equations, but we must assume the focus above or below the uppermost superadiabatic layers, which is the case here.

Este documento incorpora firma electrónica, y es copia auténtica de un documento electrónico archivado por la ULL según la Ley 39/2015.  
Su autenticidad puede ser contrastada en la siguiente dirección <https://sede.ull.es/validacion/>

Identificador del documento: 963882

Código de verificación: QDmfX6JG

Firmado por: MANUEL DIAZ ALFARO  
UNIVERSIDAD DE LA LAGUNA

Fecha: 26/06/2017 15:24:15

FERNANDO JAVIER PEREZ HERNANDEZ  
UNIVERSIDAD DE LA LAGUNA

26/06/2017 15:25:57

ERNESTO PEREDA DE PABLO  
UNIVERSIDAD DE LA LAGUNA

28/06/2017 13:21:41

With observed eigenvalues, we can obtain  $\delta\alpha(\nu)$ . We only consider modes of intermediate and high degree, as the Cowling approximation is not satisfied so well by modes of lower degrees. The empirical phase shift relation is fitted to a polynomial of degree 10, which is used to introduce the empirical phase-shift correction in the computation of the used Green's functions. Figure 2.2 shows the empirical phase-shift correction obtained from MDI data and the fitted polynomial to that curve.

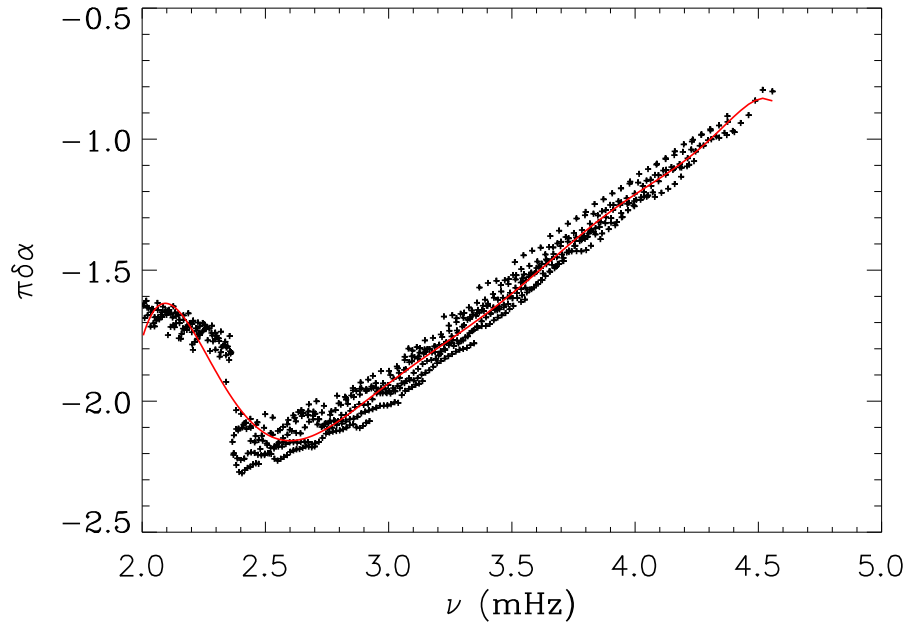


Figure 2.2: Phase-shift correction computed from MDI data with frequencies from  $\nu = 2.5$  mHz to  $\nu = 4.5$  mHz and considering angular degrees from  $\ell = 20$  to  $\ell = 80$  using Equation (2.14). The solid red line represents a fitted polynomial of degree 10. Courtesy of Pérez Hernández and González Hernández (2010).

## 2.4 Pupils

In the ideal case, our computations would use input data from the whole solar surface. However, in practice, this is not the case, and only a restricted area of the solar surface, called the pupil, is used to compute both egression and ingression functions. Pupils used in helioseismic holography are usually annular or have a shape that is a fraction of an annulus. In this work, we consider pupils of annular shape (spherical zones) with the focus at its centre, which are autoconjugate, *i.e.* the pupil for the egression function is the same as the pupil for the corresponding ingression function.

The ratio between the horizontal extent of the pupils and the depth of the focus determines the vantage of the helioseismic reconstruction (Lindsey and Braun,

Este documento incorpora firma electrónica, y es copia auténtica de un documento electrónico archivado por la ULL según la Ley 39/2015.  
Su autenticidad puede ser contrastada en la siguiente dirección <https://sede.ull.es/validacion/>

Identificador del documento: 963882

Código de verificación: QDmfX6JG

Firmado por: MANUEL DIAZ ALFARO  
UNIVERSIDAD DE LA LAGUNA

Fecha: 26/06/2017 15:24:15

FERNANDO JAVIER PEREZ HERNANDEZ  
UNIVERSIDAD DE LA LAGUNA

26/06/2017 15:25:57

ERNESTO PEREDA DE PABLO  
UNIVERSIDAD DE LA LAGUNA

28/06/2017 13:21:41

2000a, 2004, 2005). The superjacent vantage sets the focus below the solar surface, considering waves that travel directly upward from a submerged source to the overlying solar surface or *vice versa*. In the subjacent vantage (see (a) in Figure 2.3), the inner radius of the pupil is much larger than the depth of the focus. This way, waves travel originally downward from the surface and are refracted back upward to converge in the focal point or *vice versa*. In the lateral vantage (see (b)–(f) in Figure 2.3) the inner radius of the pupil is much smaller than the depth of the focus. Here, waves travel originally downward, at some point before or after reaching the focus are refracted back upward, and continue its travel and reach the surface on the opposite side of the pupil. As expected, here waves converge when approaching the focus and diverge when leaving it. In the lateral vantage, the inner radius of the pupil follows the outer radius of the pupil on the opposite side, *i.e.* a wave emanating from a point in the pupil located on its inner radius would follow a raypath that after passing through the focus and being refracted back upwards would emerge at a point in the pupil located on its outer radius on the opposite side. Figure 2.3 illustrates the configuration of the pupils for the subjacent vantage for a focus at the solar surface (a), and for the lateral vantage at several focal depths (b–f). It also shows the most extreme ray paths for each configuration. The extension of the pupils follows the specific configurations used in this work, as described below in Table 2.1 and Figure 2.3.

Vantage	Focus depth from solar surface [Mm]	Focus distance from solar centre [ $R_{\odot}$ ]	Inner pupil radius along solar surface [Mm]	Pupil width along solar surface [Mm]
Subjacent	0.348	0.9995	208.8	728.9
Lateral	50	0.9282	27.0	179.4
Lateral	69.6	0.9	37.9	233.2
Lateral	139.2	0.8	76.6	375.8
Lateral	208.8	0.7	115.7	601.4
Lateral	300	0.5690	176.6	681.0

Table 2.1: Extensions of pupils shown in Figure 2.3 measured along the solar surface considering a spherical Sun with a solar radius of 696 Mm.

In this work we use the subjacent vantage to create seismic maps of the solar surface. For the computations under the subjacent vantage, the pupil extends from  $\approx 17^\circ$  to  $60^\circ$ , and angular degrees,  $\ell$ , between 27 and 146 are considered. The lateral vantage is also used in this work in order to create seismic maps of submerged focal planes. The considered external raypaths open  $\pm 45^\circ$  from the horizontal direction (Lindsey and Braun, 2005; Braun, 2014). Under this vantage the pupil extends horizontally as the focus submerges, resulting in lower signal-to-noise ratio in the shallowest focal depths. In both vantages, as stated before, the pupil for both the ingressions ( $\mathcal{P}_+$ ) and egressions ( $\mathcal{P}_-$ ) are the same for each considered focus.

The number of reflection bounces at the surface before arriving at the focus or after departing from it also affects the extension of the pupil. In this work we use  $1 \times 1$  skip seismic holography, with one skip, or zero reflection bounces at the surface

Este documento incorpora firma electrónica, y es copia auténtica de un documento electrónico archivado por la ULL según la Ley 39/2015.  
Su autenticidad puede ser contrastada en la siguiente dirección <https://sede.ull.es/validacion/>

Identificador del documento: 963882

Código de verificación: QDmfX6JG

Firmado por: MANUEL DIAZ ALFARO  
UNIVERSIDAD DE LA LAGUNA

Fecha: 26/06/2017 15:24:15

FERNANDO JAVIER PEREZ HERNANDEZ  
UNIVERSIDAD DE LA LAGUNA

26/06/2017 15:25:57

ERNESTO PEREDA DE PABLO  
UNIVERSIDAD DE LA LAGUNA

28/06/2017 13:21:41

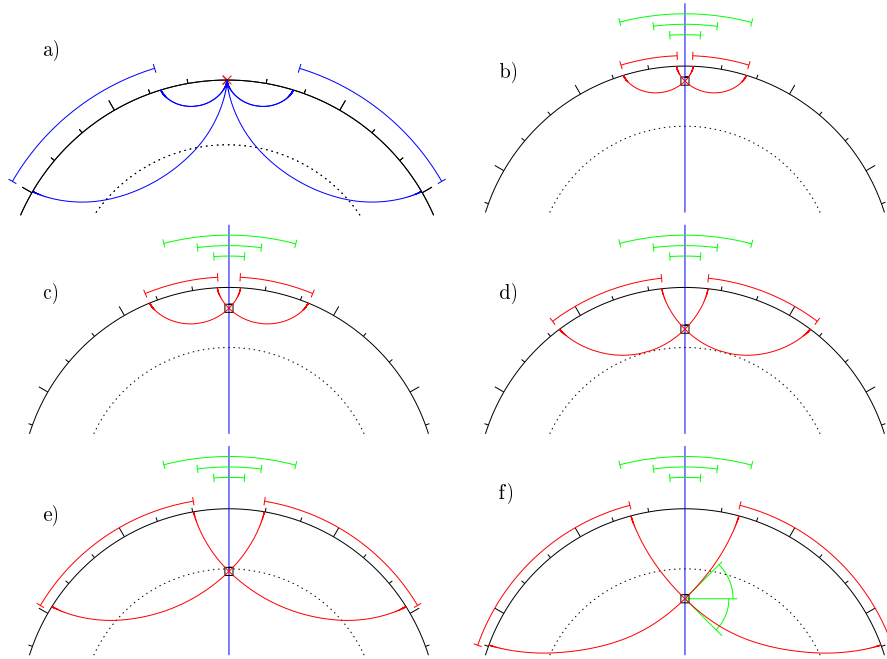


Figure 2.3: a) Scheme of the subjacent-vantage configuration, showing the extension of the utilized annular pupil and the most extreme ray paths for a focal point (red cross) at the solar surface for one-skip holography. The pupil extends between  $\approx 17^\circ$  and  $60^\circ$ . b-f) Scheme of the lateral-vantage configuration, showing in red the extensions of the annular pupils for focal points at positions of 50 Mm below the photosphere (b),  $0.9 R_\odot$  (c),  $0.8 R_\odot$  (d),  $0.7 R_\odot$  (e), and 300 Mm below the photosphere (f) for one-skip holography. The most extreme ray paths are also represented in red. The foci, marked with a square, are located at the crossings of the corresponding raypaths. The green angles located on f) illustrate the span of  $\pm 45^\circ$  from the horizontal direction used for the determination of the pupils. In all panels, the dashed line represents the position of the base of the convection zone. Each interval in the angular scale corresponds to  $10^\circ$ . The blue lines represent the vertical lines passing through the foci. For comparison, the extensions of the P1, P2, and P3 simulated active regions (Section 3.1.2) with radii of 45, 90 and 180 Mm are shown in green.

both for the ingression and egression functions, *i.e.* we consider waves that propagate from the focus to the solar surface and *vice versa*.  $1 \times 1$  skip holography has proved useful to create seismic maps of the central area of the front side of the Sun (Díaz Alfaro *et al.*, 2013; González Hernández *et al.*, 2014; MacDonald *et al.*, 2015). Other configurations are used to map seismically other regions of the Sun.  $2 \times 2$  skip holography, correlating the egression and ingression functions from waves that have experienced one reflection at the surface, is used to map the central area of the far side of the Sun (Lindsey and Braun, 2000b), whereas  $1 \times 3$  skip holography, correlating the egression function computed from waves that have not bounced at the surface with the ingression function computed from waves that have bounced twice at the surface, or *vice versa*, is used to map the peripheral areas of the Sun, both in the front and in the far side (Braun and Lindsey, 2001; González Hernández *et al.*, 2014).

Este documento incorpora firma electrónica, y es copia auténtica de un documento electrónico archivado por la ULL según la Ley 39/2015.  
Su autenticidad puede ser contrastada en la siguiente dirección <https://sede.ull.es/validacion/>

Identificador del documento: 963882

Código de verificación: QDmfX6JG

Firmado por: MANUEL DIAZ ALFARO  
UNIVERSIDAD DE LA LAGUNA

Fecha: 26/06/2017 15:24:15

FERNANDO JAVIER PEREZ HERNANDEZ  
UNIVERSIDAD DE LA LAGUNA

26/06/2017 15:25:57

ERNESTO PEREDA DE PABLO  
UNIVERSIDAD DE LA LAGUNA

28/06/2017 13:21:41

## 2.5 Procedure

In this work helioseismic holography is applied to different datasets, both numerically simulated and observational. The input data in all the considered cases are formed by line-of-sight dopplergrams, with a cadence of 60 s. Actual observational data are processed in spans of 24 h, whereas simulated data are processed in shorter spans due to limited availability. The procedure can be summarised as a number of consecutive steps detailed as follows:

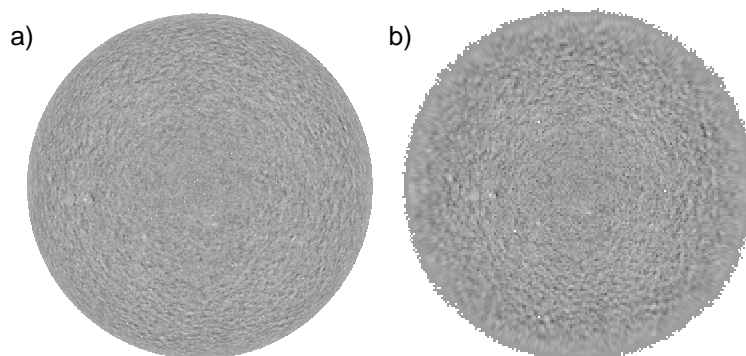


Figure 2.4: a) Example of input dopplergram, corresponding to a  $839 \times 839$  pixel GONG network merged dopplergram for 1 January 2015 at 13:21 UT. b) Example of the corresponding  $200 \times 200$  Postel-projected dopplergram.

1. Each individual dopplergram is Postel-projected onto a  $200 \times 200$  pixel map. Examples of an input dopplergram and of its corresponding Postel projection are shown in Figure 2.4 (a) and (b) respectively. The Postel-projected dopplergrams are then stacked into a datacube for each dataspan interval. For observational data, the datacubes have lengths of 1440 frames, corresponding to 24 h of data. For the considered simulations, they have lengths of 1024 or 824 frames, corresponding to shorter timespans. The temporal profile of each pixel is analysed to remove its average, linear temporal trend and bad-quality pixels. A three-dimensional Fourier transform is applied to the Postel-projected datacube in both spatial directions and time and the data within a bandpass between 2.5 and 4.5 mHz are extracted.
2. Green's functions are computed as described in Section 2.3 to create seismic maps at the solar surface and at depths up to 300 Mm using  $1 \times 1$  skip seismic holography with frequencies between 2.5 mHz and 4.5 mHz. For producing the surface maps, Green's functions are created for a focal plane at a nominal position of  $0.9995R_{\odot}$ , very close to the solar surface, to be able to consider an outgoing wave in the equations described in Section 2.3. The pupil extends from  $\approx 17^{\circ}$  to  $60^{\circ}$  under a subjacent vantage. Angular degrees,  $\ell$ , between 27 and 146 are considered in the computations. For the case with submerged foci, Green's

Este documento incorpora firma electrónica, y es copia auténtica de un documento electrónico archivado por la ULL según la Ley 39/2015.  
Su autenticidad puede ser contrastada en la siguiente dirección <https://sede.ull.es/validacion/>

Identificador del documento: 963882

Código de verificación: QDmfX6JG

Firmado por: MANUEL DIAZ ALFARO  
UNIVERSIDAD DE LA LAGUNA

Fecha: 26/06/2017 15:24:15

FERNANDO JAVIER PEREZ HERNANDEZ  
UNIVERSIDAD DE LA LAGUNA

26/06/2017 15:25:57

ERNESTO PEREDA DE PABLO  
UNIVERSIDAD DE LA LAGUNA

28/06/2017 13:21:41

functions are created for different focal planes with depths ranging generally from 50 Mm to 300 Mm with a span of 1 Mm. In this case, Green's functions are computed under a lateral vantage, with an opening angle of  $\pm 45^\circ$  from the horizontal plane, with pupils of varying extensions depending on the depth of the focal plane. Angular degrees,  $\ell$ , spanning from 0 to 170 are considered. In general, we have not considered depths above 50 Mm to avoid the lower signal-to-noise ratio in the shallower layers using a  $1 \times 1$  skip lateral-vantage configuration. However, for one type of the studied simulations, with numerical sound-speed perturbations in the shallow subphotosphere, we have extended the depth range up to depths as low as 25 Mm. The empirical phase-shift correction (Section 2.3.1) is applied to Green's functions only for the observational data, but not for the numerical simulations, as they do not include the dynamics of

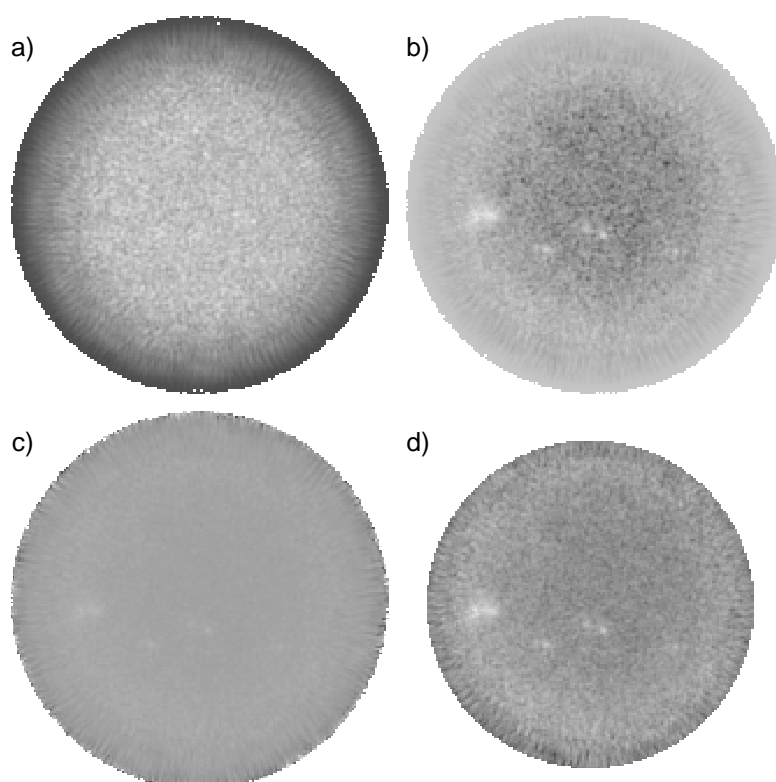


Figure 2.5: Example maps of the real part (a) and of the imaginary part (b) of a complex correlation map, of their corresponding phase shift (c), and of the same phase shift after application of a mask to select only the pixels within a radius of  $65'$  from the disk centre. All the maps correspond to the processing of a 24 h GONG dataset from 1 January 2015 with the focal plane located at the solar surface under the subjacent-vantage configuration described in Section 2.4.

Este documento incorpora firma electrónica, y es copia auténtica de un documento electrónico archivado por la ULL según la Ley 39/2015.  
Su autenticidad puede ser contrastada en la siguiente dirección <https://sede.ull.es/validacion/>

Identificador del documento: 963882

Código de verificación: QDmfX6JG

Firmado por: MANUEL DIAZ ALFARO  
UNIVERSIDAD DE LA LAGUNA

Fecha: 26/06/2017 15:24:15

FERNANDO JAVIER PEREZ HERNANDEZ  
UNIVERSIDAD DE LA LAGUNA

26/06/2017 15:25:57

ERNESTO PEREDA DE PABLO  
UNIVERSIDAD DE LA LAGUNA

28/06/2017 13:21:41

convection and non-adiabaticity in the oscillation equations.

3. The acoustic egression and ingression functions are calculated using Equation (2.1) for each pixel at the different focal depths, considering the corresponding pupils in the lateral vantage for the submerged focal planes and in the subjacent vantage for the focal plane at the surface. Focal planes should be understood as manifolds of constant depth. An example for a particular frequency has previously been shown in Figure 2.1.
4. Complex correlation maps between the egression and ingression functions are computed using Equation (2.3), and phase-shift maps are calculated. An

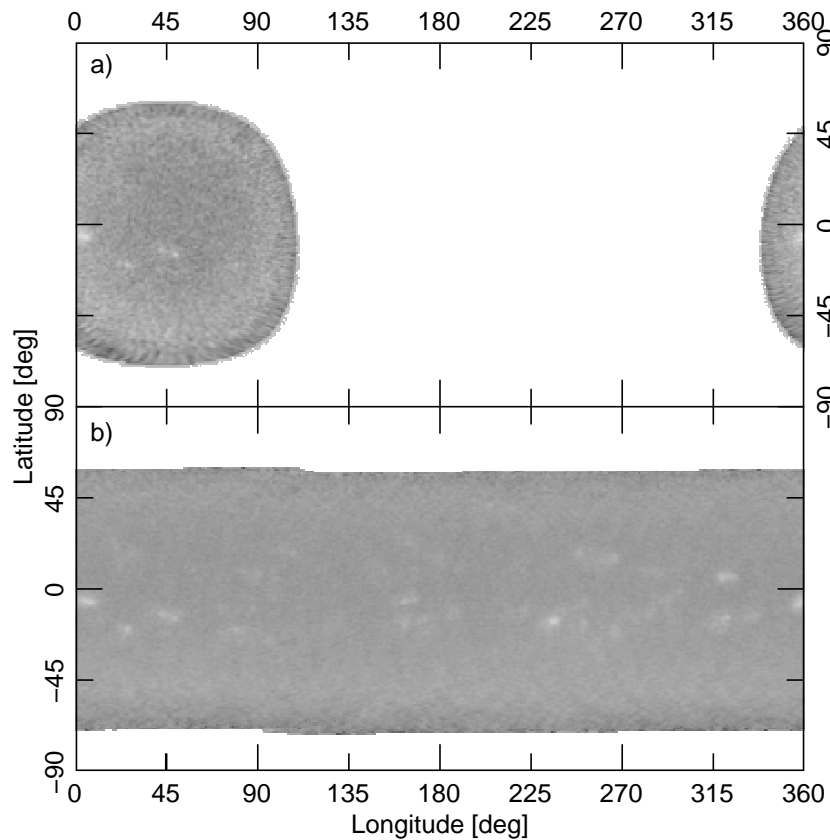


Figure 2.6: a) Phase-shift map projected onto a longitude-latitude map for a focal plane located at the solar surface under the subjacent-vantage configuration of a 24 h GONG dataset from 1 January 2015. b) Combination of consecutive phase-shift maps at the surface for the interval 28 December 2014–23 January 2015, corresponding to Bartels's rotation BR2475. Each tick shows a step of  $45^\circ$

Este documento incorpora firma electrónica, y es copia auténtica de un documento electrónico archivado por la ULL según la Ley 39/2015.  
Su autenticidad puede ser contrastada en la siguiente dirección <https://sede.ull.es/validacion/>

Identificador del documento: 963882

Código de verificación: QDmfX6JG

Firmado por: MANUEL DIAZ ALFARO  
UNIVERSIDAD DE LA LAGUNA

Fecha: 26/06/2017 15:24:15

FERNANDO JAVIER PEREZ HERNANDEZ  
UNIVERSIDAD DE LA LAGUNA

26/06/2017 15:25:57

ERNESTO PEREDA DE PABLO  
UNIVERSIDAD DE LA LAGUNA

28/06/2017 13:21:41

example for the real and imaginary parts of a complex correlation map is shown in Figure 2.5 (a) and (b) respectively, with its corresponding phase shift in (c).

5. As the noise is quite higher near the borders of the image in the  $1 \times 1$  skip scheme due to geometrical limitations for foci closer to the limb, part of whose pupil lies in the non-visible hemisphere, a mask is applied to the data to select only the pixels within a radius of  $65^\circ$  from the disk centre. Figure 2.5 (d) shows an example of a phase-shift map after application of that mask.
6. We convert each Postel phase-shift map to a longitude-latitude map. Then we average as many maps centred at different longitudes as necessary to produce a reconstructed longitude-latitude map covering the whole solar perimeter for every depth. The averages are weighted accordingly to account for the number of maps used to create the average for each particular pixel. An example is shown in Figure 2.6.

Este documento incorpora firma electrónica, y es copia auténtica de un documento electrónico archivado por la ULL según la Ley 39/2015.  
Su autenticidad puede ser contrastada en la siguiente dirección <https://sede.ull.es/validacion/>

Identificador del documento: 963882

Código de verificación: QDmfX6JG

Firmado por: MANUEL DIAZ ALFARO  
UNIVERSIDAD DE LA LAGUNA

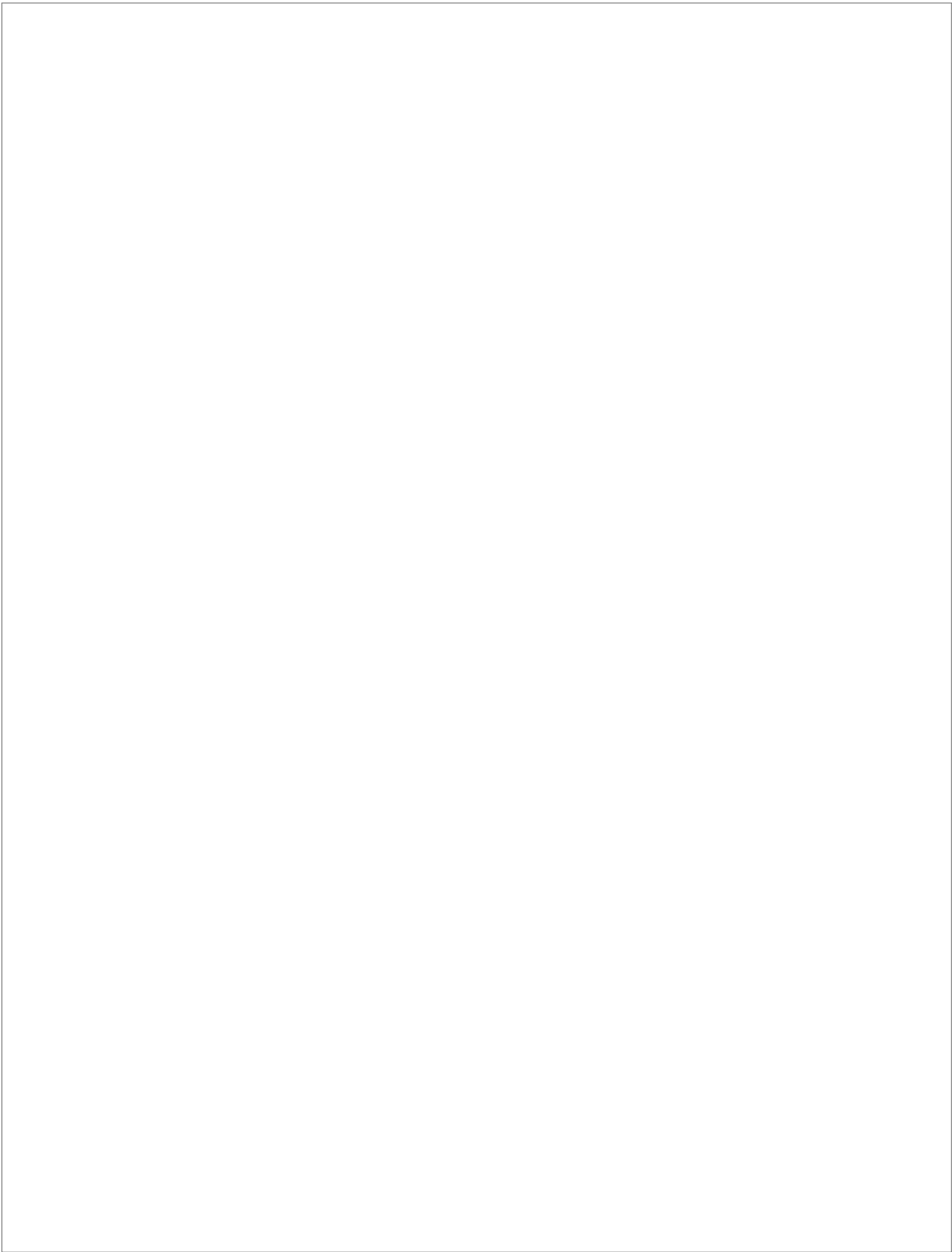
Fecha: 26/06/2017 15:24:15

FERNANDO JAVIER PEREZ HERNANDEZ  
UNIVERSIDAD DE LA LAGUNA

26/06/2017 15:25:57

ERNESTO PEREDA DE PABLO  
UNIVERSIDAD DE LA LAGUNA

28/06/2017 13:21:41



Este documento incorpora firma electrónica, y es copia auténtica de un documento electrónico archivado por la ULL según la Ley 39/2015.  
Su autenticidad puede ser contrastada en la siguiente dirección <https://sede.ull.es/validacion/>

Identificador del documento: 963882

Código de verificación: QDmfX6JG

Firmado por: MANUEL DIAZ ALFARO  
UNIVERSIDAD DE LA LAGUNA

Fecha: 26/06/2017 15:24:15

FERNANDO JAVIER PEREZ HERNANDEZ  
UNIVERSIDAD DE LA LAGUNA

26/06/2017 15:25:57

ERNESTO PEREDA DE PABLO  
UNIVERSIDAD DE LA LAGUNA

28/06/2017 13:21:41

# 3

## Numerical simulations with sound-speed perturbations

In this chapter we test the phase-sensitive helioseismic-holographic technique described in Chapter 2 with the aid of publicly available numerical simulations based on the work by Hartlep and Mansour (2004, 2005) containing sound-speed perturbations. We make use of three different collections of simulations, with sound-speed perturbations of different nature.

First, we consider simulations with sound-speed perturbations longitudinally distributed and centred at a depth of  $0.7R_{\odot}$ , in the vicinity of the base of the convection zone and the tachocline (Zhao *et al.*, 2009). Then, we consider simulations with localized sound-speed perturbations at the solar surface, representing active regions and concentrations of photospheric magnetic fields (Hartlep *et al.*, 2008). Finally, in the last collection the sound-speed perturbations are located in the subphotosphere at depths between 20 Mm and 50 Mm, mimicking emerging active regions (Hartlep *et al.*, 2011).

The first collection of simulations has been previously used to successfully recover the sound-speed perturbed profile using time-distance helioseismology (Zhao *et al.*, 2009). The second one has been used to validate time-distance far-side imaging (Hartlep *et al.*, 2008; Ilonidis, Zhao, and Hartlep, 2009) and to test the dependence of seismic holography of active regions on their longitudinal position (Díaz Alfaro *et al.*, 2013). The third collection of simulations has been used to test the detection of emerging active regions using time-distance helioseismology (Hartlep *et al.*, 2011) and seismic holography (Braun, 2014). Other simulations following the same mathematical scheme have also proved successful, *e.g.* to test the detection of deep meridional flows using time-distance imaging (Hartlep *et al.*, 2013).

We first present the main characteristics of the numerical simulations, then we outline the specifics of the technique as applied to the simulations, and finally we present and discuss the results of the tests applied to simulations with sound-speed perturbations at a depth of  $0.7R_{\odot}$ , at the photosphere, and in the subphotosphere.

Este documento incorpora firma electrónica, y es copia auténtica de un documento electrónico archivado por la ULL según la Ley 39/2015.  
Su autenticidad puede ser contrastada en la siguiente dirección <https://sede.ull.es/validacion/>

Identificador del documento: 963882

Código de verificación: QDmfX6JG

Firmado por: MANUEL DIAZ ALFARO  
UNIVERSIDAD DE LA LAGUNA

Fecha: 26/06/2017 15:24:15

FERNANDO JAVIER PEREZ HERNANDEZ  
UNIVERSIDAD DE LA LAGUNA

26/06/2017 15:25:57

ERNESTO PEREDA DE PABLO  
UNIVERSIDAD DE LA LAGUNA

28/06/2017 13:21:41

### 3.1 Numerical simulations

The simulated data contain acoustic waves numerically propagated through a spherical domain representing the Sun. The solar oscillations are modelled using linearised Euler equations in an unperturbed static background, taken from model S (Christensen-Dalsgaard *et al.*, 1996) matched to a model of the chromosphere (Vernazza, Avrett, and Loeser, 1981), where certain localised variations of the sound speed have been introduced. The localisation and shape of these variations in the sound speed constitute the main difference among the considered datasets. Besides, the simulations do not consider magnetic fields or flows and non-reflecting boundary conditions at the upper boundary are met by means of an absorbing buffer layer, set to zero in the interior and increasing smoothly into the buffer layer.

Certain simplifications have been taken in the wave equations, such as the neglect of perturbations of the gravitational potential (Cowling approximation), the use of the adiabatic approximation, and the neglect of the entropy gradient of the background model to make the equations convectively stable. Although this lowers the acoustic cut-off frequency, the use of acoustic modes quite below the cut-off frequency keeps its influence to a minimum.

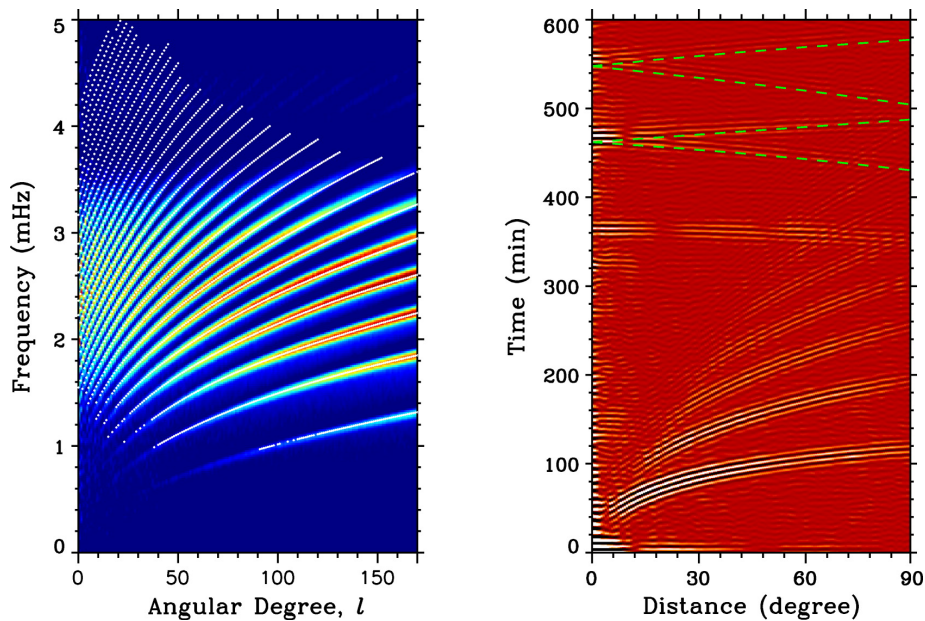


Figure 3.1: Oscillation power spectrum (left) and time-distance diagram (right) of a simulated dataset with the prescribed characteristics. For comparison with solar observations, white dots in the left panel show the observed frequencies from 144 days of MDI medium- $l$  data using the averaged-spectrum method (Rhodes *et al.*, 1997). Courtesy of Hartlep *et al.* (2008).

Este documento incorpora firma electrónica, y es copia auténtica de un documento electrónico archivado por la ULL según la Ley 39/2015.  
Su autenticidad puede ser contrastada en la siguiente dirección <https://sede.ull.es/validacion/>

Identificador del documento: 963882

Código de verificación: QDmfX6JG

Firmado por: MANUEL DIAZ ALFARO  
UNIVERSIDAD DE LA LAGUNA

Fecha: 26/06/2017 15:24:15

FERNANDO JAVIER PEREZ HERNANDEZ  
UNIVERSIDAD DE LA LAGUNA

26/06/2017 15:25:57

ERNESTO PEREDA DE PABLO  
UNIVERSIDAD DE LA LAGUNA

28/06/2017 13:21:41

The oscillations are driven stochastically by including density perturbations near the solar surface and they are numerically discretised under a Galerkin schema, using fourth-order B-splines for the radial dependencies, where the separation between numerical points is inversely proportional to the sound speed, and spherical harmonics with angular degrees  $\ell$  ranging from 0 to 170 for the angular dependencies. Two-thirds dealiasing is used and time integration is done using a staggered Yee scheme (Yee, 1966). The range of considered degrees reproduces the solar oscillation power spectrum well, as can be seen in Figure 3.1, taken from Hartlep *et al.* (2008), which compares in the left panel the eigenspectrum of the Sun from observational medium- $\ell$  data taken from MDI and that of the simulations. The right panel shows the time-distance diagram of the same simulated dataset, being comparable to time-distance diagrams computed from actual solar observations—*e.g.* Figure 1.35(a) of Rozelot and Neiner, 2011.

Further details of the simulations and the full expansion of the equations used can be found in Hartlep and Mansour (2004, 2005); Hartlep *et al.* (2008).

All but one of the simulations used in these tests span about 17 h, comprising 1024 maps of wave velocity (artificial dopplergrams) with a cadence of one minute stored in FITS files in heliographic coordinates and arbitrary velocity units. The other simulation, namely S6, differs from the rest in the fact that it spans about 14 h, containing only 824 maps. The individual maps in all the simulations contain  $512 \times 256$  pixels covering the whole solar surface.

### 3.1.1 Sound-speed perturbations at $0.7 R_{\odot}$

The simulations with sound-speed perturbations at  $0.7 R_{\odot}$  (Zhao *et al.*, 2009) are publicly available on the Internet.<sup>1</sup> Besides a reference unperturbed simulation, we use two different simulated datasets with introduced perturbations in the sound speed with respect to the background model. The introduced perturbation in each of the perturbed simulations has a two-dimensional Gaussian shape in each hemisphere, with axial symmetry; therefore, being non-dependent on longitude. The position and width of the Gaussian perturbations are the same for both hemispheres in both perturbed datasets, but they have different amplitudes. They satisfy the following equation:

$$\frac{\delta c}{c_0} = A_N \cdot e^{-\left(\frac{(r-r_0)^2}{2\sigma_r^2} + \frac{(\varphi-\varphi_{N,0})^2}{2\sigma_{\varphi}^2}\right)} + A_S \cdot e^{-\left(\frac{(r-r_0)^2}{2\sigma_r^2} + \frac{(\varphi-\varphi_{S,0})^2}{2\sigma_{\varphi}^2}\right)}, \quad (3.1)$$

where  $r$  and  $\varphi$  are the radial and latitudinal coordinates, the perturbations are centred radially at  $r_0 = 0.7R_{\odot}$  with a FWHM of  $0.082R_{\odot}$  and a width  $\sigma_r = 0.035R_{\odot}$ , and latitudinally at  $30^\circ$  ( $\varphi_{N,0} = 30^\circ$ ,  $\varphi_{S,0} = -30^\circ$ ) with a FWHM of  $35^\circ$  and a width  $\sigma_{lat} = 15^\circ$ , as shown in Table 3.1. The perturbations have maximum amplitudes of  $A_N = 0.7\%$  and  $A_N = 0.65\%$  in the northern hemisphere, and of  $A_S = 0.5\%$  and  $A_S = 0.55\%$  in the southern hemisphere for the two simulations respectively, as shown

<sup>1</sup>[http://sun.stanford.edu/~thartlep/Site/Artificial\\_Data/Entries/2011/3/17\\_Sound\\_speed\\_perturbations\\_in\\_the\\_tachocline\\_region.html](http://sun.stanford.edu/~thartlep/Site/Artificial_Data/Entries/2011/3/17_Sound_speed_perturbations_in_the_tachocline_region.html)

Este documento incorpora firma electrónica, y es copia auténtica de un documento electrónico archivado por la ULL según la Ley 39/2015.  
Su autenticidad puede ser contrastada en la siguiente dirección <https://sede.ull.es/validacion/>

Identificador del documento: 963882

Código de verificación: QDmfX6JG

Firmado por: MANUEL DIAZ ALFARO  
UNIVERSIDAD DE LA LAGUNA

Fecha: 26/06/2017 15:24:15

FERNANDO JAVIER PEREZ HERNANDEZ  
UNIVERSIDAD DE LA LAGUNA

26/06/2017 15:25:57

ERNESTO PEREDA DE PABLO  
UNIVERSIDAD DE LA LAGUNA

28/06/2017 13:21:41

in Table 3.2. Figure 3.2 shows a map of the perturbation in the sound speed with respect to depth and latitude for the first simulation (T1).

	Radial	Latitudinal
Centre	$0.7R_{\odot}$	$30^{\circ}$
FWHM	$0.082R_{\odot}$	$35^{\circ}$
Width	$0.035R_{\odot}$	$15^{\circ}$

Table 3.1: Spatial parameters of the sound-speed perturbations in the T1-T2 simulations.

Dataset No.	Northern amplitude	Southern amplitude
T1	0.70%	0.50%
T2	0.65%	0.55%

Table 3.2: Amplitudes of the sound-speed perturbations centred at the northern and southern hemispheres for both perturbed simulations T1 and T2.

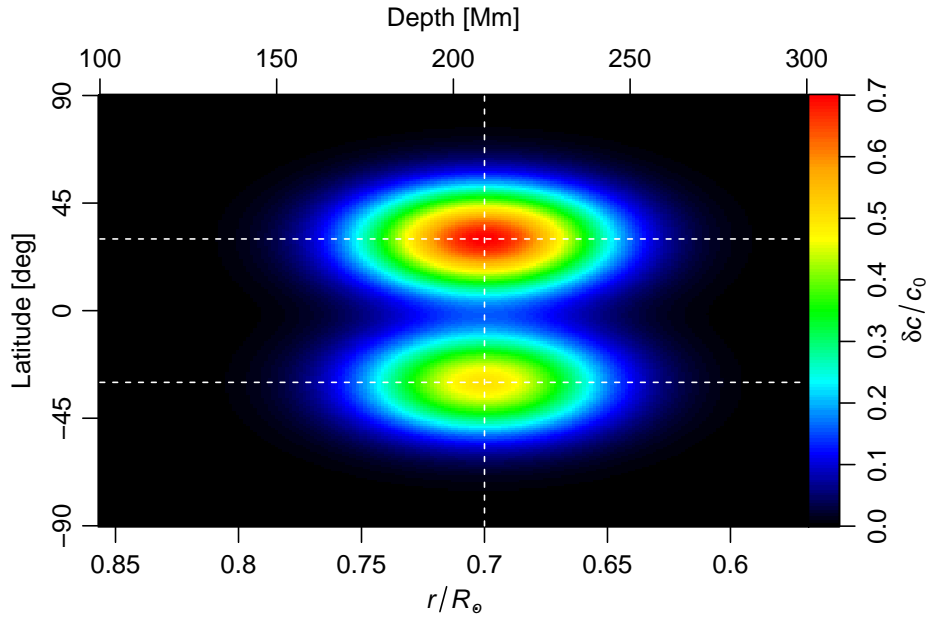


Figure 3.2: Sound-speed perturbation model with a 0.7% variation in the North hemisphere and a 0.5% variation in the South hemisphere with respect to the sound speed of the background unperturbed model, which corresponds to the simulated dataset T1. The dashed white lines serve to mark the centres of the two Gaussian perturbations.

### 3.1.2 Localized sound-speed perturbations in the photosphere

The simulated datasets with perturbations in the sound speed located at the solar surface are also publicly available.<sup>2</sup> We make use of three of the datasets available, containing one perturbed region of three different horizontal extensions.

The solar active regions are modelled here by a circular region in which the sound speed ( $c$ ) differs from the unperturbed value in the background standard model ( $c_0$ )

<sup>2</sup>[http://sun.stanford.edu/~junwei/farside\\_simu\\_data.html](http://sun.stanford.edu/~junwei/farside_simu_data.html)

Este documento incorpora firma electrónica, y es copia auténtica de un documento electrónico archivado por la ULL según la Ley 39/2015.  
Su autenticidad puede ser contrastada en la siguiente dirección <https://sede.ull.es/validacion/>

Identificador del documento: 963882

Código de verificación: QDmfX6JG

Firmado por: MANUEL DIAZ ALFARO  
UNIVERSIDAD DE LA LAGUNA

Fecha: 26/06/2017 15:24:15

FERNANDO JAVIER PEREZ HERNANDEZ  
UNIVERSIDAD DE LA LAGUNA

26/06/2017 15:25:57

ERNESTO PEREDA DE PABLO  
UNIVERSIDAD DE LA LAGUNA

28/06/2017 13:21:41

as:

$$\left(\frac{c}{c_0}\right)^2 = 1 + \begin{cases} \left(1 + \cos \pi \frac{\alpha}{\alpha_d}\right) g(h) & : \left|\frac{\alpha}{\alpha_d}\right| \leq 1; \\ 0 & : \frac{\alpha}{\alpha_d} > 1; \end{cases} \quad (3.2)$$

where  $\alpha$  is the angular distance from the centre of the perturbed region,  $\alpha_d$  is the corresponding maximum angular extension and  $h$  is the distance from the solar surface. The radial vertical profile  $g(h)$ , shown in Figure 3.3, taken from Hartlep *et al.* (2008), is based on an empirically-inverted profile derived from an actual sunspot (NOAA active region 8243 on 18 June 1998) using time-distance helioseismology (Kosovichev, Duvall, and Scherrer, 2000). Although a number of other inversions confirmed the profile (*e.g.* Jensen *et al.*, 2001; Sun, Chou, and TON Team, 2002; Basu, Antia, and Bogart, 2004; Couvidat, Birch, and Kosovichev, 2006; Kosovichev and Duvall, 2006; Zharkov, Nicholas, and Thompson, 2007), some of them suggested that the sound-speed profile could probably extend deeper than originally inferred, especially for larger active regions. Therefore, the radial profile used in the simulations has been extended into deeper layers, up to a depth of 30 Mm. Three numerical datasets are considered, with different horizontal sizes  $\alpha_d = 3.7^\circ$ ,  $7.4^\circ$ , and  $14.8^\circ$ , corresponding to radii at the solar surface of 45 Mm (P1), 90 Mm (P2), and 180 Mm (P3).

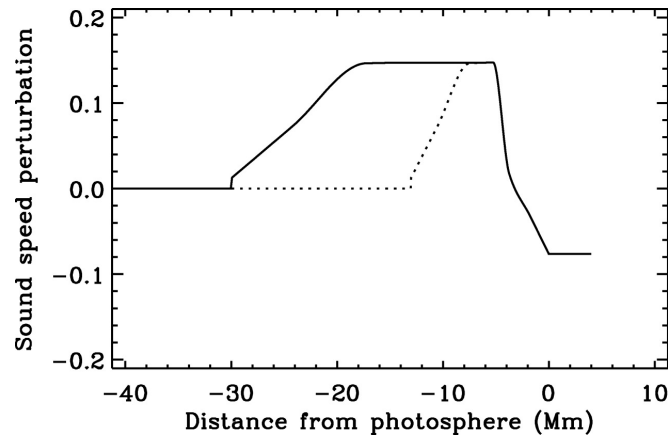


Figure 3.3: Radial vertical profile of the sound-speed perturbation (solid). In dots, the original non-extended profile derived from inversions of a sunspot in NOAA active region 8243 on 18 June 1998 using time-distance helioseismology (Kosovichev, Duvall, and Scherrer, 2000). Positive values of distance are above the photosphere whereas negative values of distance are below it. - Taken from Hartlep *et al.* (2008).

Este documento incorpora firma electrónica, y es copia auténtica de un documento electrónico archivado por la ULL según la Ley 39/2015.  
Su autenticidad puede ser contrastada en la siguiente dirección <https://sede.ull.es/validacion/>

Identificador del documento: 963882

Código de verificación: QDmfX6JG

Firmado por: MANUEL DIAZ ALFARO  
UNIVERSIDAD DE LA LAGUNA

Fecha: 26/06/2017 15:24:15

FERNANDO JAVIER PEREZ HERNANDEZ  
UNIVERSIDAD DE LA LAGUNA

26/06/2017 15:25:57

ERNESTO PEREDA DE PABLO  
UNIVERSIDAD DE LA LAGUNA

28/06/2017 13:21:41

### 3.1.3 Localized sound-speed perturbations in the shallow subphotosphere

The datasets with localised sound-speed perturbations in the shallow subphotosphere (Hartlep *et al.*, 2011) are also publicly available on the Internet.<sup>3</sup> Each of the localised sound-speed perturbations in these datasets follow the same shape in the horizontal direction as in the perturbations described in Section 3.1.2, which were located at the solar surface. However, their vertical expression is different. In this case, instead of following a vertical expression derived from solar observations as in Section 3.1.2, an *ad hoc* expression is used for the vertical dependence as well. The full expression is given by the following equation—see Hartlep *et al.* (2011)—where the sound speed ( $c$ ) differs from the sound speed of the standard model ( $c_0$ ) as:

$$\left(\frac{c}{c_0}\right)^2 = 1 + A \begin{cases} \frac{1}{4} \left(1 + \cos \pi \frac{\alpha}{\alpha_d}\right) \left(1 + \cos \pi \frac{z-z_s}{d_s}\right) & : \left|\frac{\alpha}{\alpha_d}\right| \leq 1, \left|\frac{z-z_s}{d_s}\right| \leq 1; \\ 0 & : \left|\frac{\alpha}{\alpha_d}\right| > 1, \left|\frac{z-z_s}{d_s}\right| > 1; \end{cases} \quad (3.3)$$

where  $z$  is the depth from the photosphere and  $\alpha$  is the angular distance from the centre of the considered perturbation.  $z_s$ ,  $d_s$ ,  $\alpha_d$ , and  $A$  are parameters corresponding to the central depth of the perturbation, its vertical extent, its angular horizontal extent, and its amplitude.

Dataset No.	Central sound-speed perturbation	Amplitude A	Central depth $z_s$ [Mm]
S1	-5%	-0.0975	50
S2	-5%	-0.0975	40
S3	-5%	-0.0975	30
S4	-5%	-0.0975	20
S5	-10%	-0.19	30
S6	-10%	-0.19	20

Table 3.3: Central sound-speed reduction, amplitude, and central depth for the perturbations introduced in the simulations with subsurface sound-speed perturbations (S1–S6).

We use six datasets (S1 to S6) with different combinations of central depths ( $z_s$ ) between 20 Mm and 50 Mm and reductions in the sound speed of 5% and 10%, corresponding to values of the amplitude  $A = -0.0975$  and  $A = -0.19$  respectively, as shown in Table 3.3. In all the cases the amplitude ( $A$ ) is negative, denoting a reduction in the value of the sound speed. All six datasets contain three perturbations, centred, in each of them, at the same central depth, and with the same amplitude. The vertical extent ( $d_s$ ) is 20 Mm in all the cases. Three different angular horizontal extents were considered for the three perturbations, with values of  $\alpha_d = 3.7^\circ$ ,  $7.4^\circ$ , and  $14.8^\circ$ , which correspond to horizontal radii at the surface of 45 Mm, 90 Mm, and 180 Mm. They are centred horizontally at the longitudes and latitudes shown in Table 3.4. An example acoustic power map— $\sum v_D^2$ —of the S6 dataset is shown in Figure 3.4 to illustrate the location of the three perturbations.

<sup>3</sup>[http://sun.stanford.edu/~thartlep/Site/Artificial\\_Data/Entries/2012/3/21\\_Subsurface\\_sound\\_speed\\_perturbations.html](http://sun.stanford.edu/~thartlep/Site/Artificial_Data/Entries/2012/3/21_Subsurface_sound_speed_perturbations.html)

Este documento incorpora firma electrónica, y es copia auténtica de un documento electrónico archivado por la ULL según la Ley 39/2015.  
Su autenticidad puede ser contrastada en la siguiente dirección <https://sede.ull.es/validacion/>

Identificador del documento: 963882

Código de verificación: QDmfX6JG

Firmado por: MANUEL DIAZ ALFARO  
UNIVERSIDAD DE LA LAGUNA

Fecha: 26/06/2017 15:24:15

FERNANDO JAVIER PEREZ HERNANDEZ  
UNIVERSIDAD DE LA LAGUNA

26/06/2017 15:25:57

ERNESTO PEREDA DE PABLO  
UNIVERSIDAD DE LA LAGUNA

28/06/2017 13:21:41

Alias	Angular horizontal extent $\alpha_d$	Horizontal radius at the surface [Mm]	Central latitude	Central longitude
small	3.7°	45	20° S	180°
medium	7.4°	90	20° N	90°
big	14.8°	180	20° N	270°

Table 3.4: Horizontal extents at the surface and central latitudes and longitudes of the three perturbations of different sizes considered in each of the perturbed datasets with subsurface sound-speed perturbations (S1–S6).

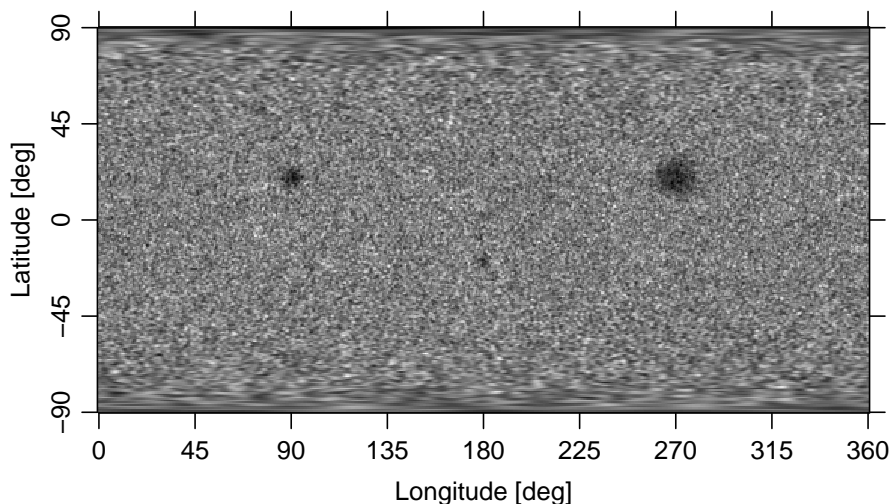


Figure 3.4: Acoustic power map for the S6 simulation, with three perturbations of different sizes at different latitudinal and longitudinal positions centred at a depth of 20 Mm and with a reduction of 10% in the sound speed with respect to the background model. The nominal positions of the three structures can be seen in Table 3.4.

Figure 3.5 shows the structure of the perturbation in the sound speed for the medium perturbation of the S1 dataset. Vertical and horizontal cuts are shown at different distances from the centre of the perturbation.

### 3.2 Technique

Except for the S6 simulation, all the simulations comprise 1024 full-Sun artificial dopplergrams of  $512 \times 256$  pixels in heliographic coordinates. The S6 simulation spans only 824 artificial dopplergrams. All of them are in arbitrary velocity units, and hence, they have been rescaled to values consistent with the mean distribution velocity values of GONG dopplergrams. The rescaled simulations have then been transformed into line-of-sight dopplergrams spanning only one hemisphere— $180^\circ$  in longitude. For each of the simulations, this process has been repeated 24 times, offsetting the longitude interval by  $15^\circ$ , in order to map the full solar surface, and producing 24 different sets of line-of-sight dopplergrams per simulation.

Este documento incorpora firma electrónica, y es copia auténtica de un documento electrónico archivado por la ULL según la Ley 39/2015.  
Su autenticidad puede ser contrastada en la siguiente dirección <https://sede.ull.es/validacion/>

Identificador del documento: 963882

Código de verificación: QDmfX6JG

Firmado por: MANUEL DIAZ ALFARO  
UNIVERSIDAD DE LA LAGUNA

Fecha: 26/06/2017 15:24:15

FERNANDO JAVIER PEREZ HERNANDEZ  
UNIVERSIDAD DE LA LAGUNA

26/06/2017 15:25:57

ERNESTO PEREDA DE PABLO  
UNIVERSIDAD DE LA LAGUNA

28/06/2017 13:21:41

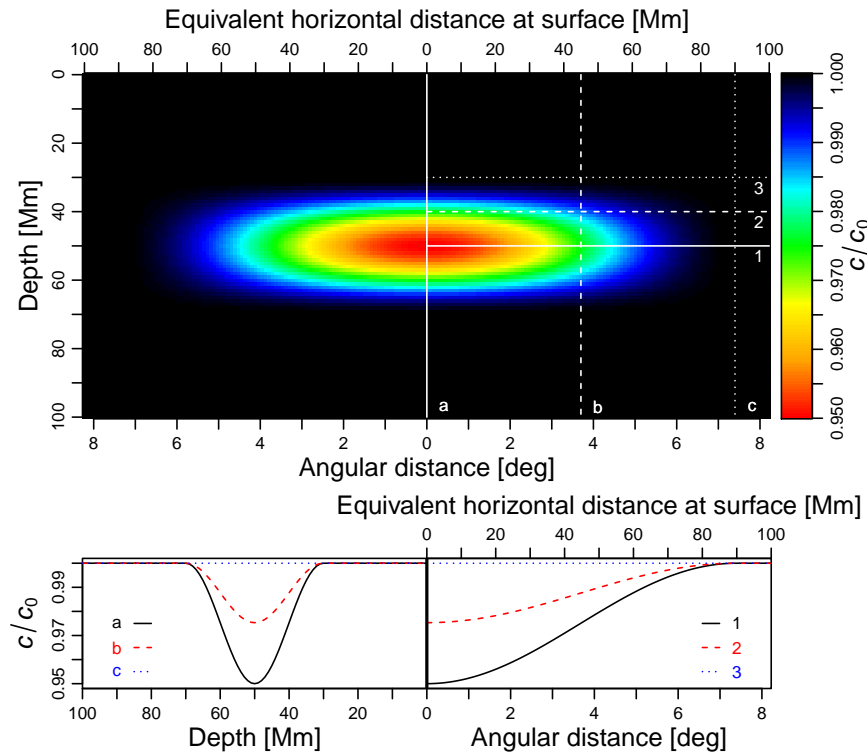


Figure 3.5: Sound-speed ratio with respect to the background sound speed  $c/c_0$  in the simulation for the medium perturbation of the S1 dataset. The perturbation is centred at 50 Mm below the solar surface and has an angular horizontal extent of  $\alpha_d = 7.4^\circ$ , corresponding to an equivalent radius of 90 Mm at the solar surface. The vertical extent is  $d_s = 20$  Mm. Above: variation of the sound-speed ratio with depth and horizontal distance. Below left: vertical profile at the centre of the perturbation (solid black), at half its total horizontal extent:  $7.4/2^\circ$  (dashed red), and at the border of its horizontal extent:  $7.4^\circ$  (dotted blue), corresponding to the vertical solid, dashed and dotted white lines in the above image respectively. Below right: horizontal profile at the centre of the perturbation (solid black), at half its total radial extent: 10 Mm (dashed red) and at the border of its radial extent: 20 Mm (dotted blue), corresponding to the horizontal solid, dashed and dotted white lines in the above image respectively.

A general estimate of the instrument error for the GONG 1-min velocity images used in this work is  $3 \text{ m s}^{-1}$  (J. W. Harvey, private communication). A similar level of precision for the simulations is accomplished by adding a noise layer to each of the dopplergrams from the simulations. This noise layer is created with the aid of a random number generator following a Gaussian distribution with a variance equal to the mean GONG instrument error— $\sigma = 3 \text{ ms}^{-1}$ .

We apply the general procedure described in Section 2.5 to each of the series formed by line-of-sight dopplergrams for each of the simulated sets and for each of the 24

Este documento incorpora firma electrónica, y es copia auténtica de un documento electrónico archivado por la ULL según la Ley 39/2015.  
Su autenticidad puede ser contrastada en la siguiente dirección <https://sede.ull.es/validacion/>

Identificador del documento: 963882

Código de verificación: QDmfX6JG

Firmado por: MANUEL DIAZ ALFARO  
UNIVERSIDAD DE LA LAGUNA

Fecha: 26/06/2017 15:24:15

FERNANDO JAVIER PEREZ HERNANDEZ  
UNIVERSIDAD DE LA LAGUNA

26/06/2017 15:25:57

ERNESTO PEREDA DE PABLO  
UNIVERSIDAD DE LA LAGUNA

28/06/2017 13:21:41

considered longitude intervals. Phase-shift maps are created at the surface and at depths between 50 Mm and 300 Mm in the general case, which are further extended to also include the interval 25 Mm–50 Mm in the case of the S1–S6 simulations and the R simulation used therewith. For each depth of each of the simulations, the longitude-latitude phase-shift maps from the 24 considered longitude intervals are conveniently averaged as detailed in point 6. of Section 2.5, in order to create phase shift maps covering the whole solar perimeter.

The constructed longitude-latitude-depth full-Sun phase-shift maps for the simulations are combined into a three-dimensional datacube, which is used directly for later analysis in the simulations with perturbations at the photosphere (P1–P3), and in the shallow subphotosphere (S1–S6), as well as in the reference simulation (R). However, in the simulations with perturbations at the tachocline (T1, T2), there is no longitudinal-dependence of the sound-speed perturbations. Hence, to increase the signal-to-noise ratio, the longitude-latitude phase-shift maps are contracted by means of an average in the longitudinal direction and the results are joined for the different focal depths to create a phase-shift seismic map depending only on latitude and depth for each of the two simulations. The reference simulation data (R) are also contracted to be used together with the T1-T2 simulations. The same contraction scheme is later applied for GONG data in Chapter 4.

### 3.3 Results

#### 3.3.1 Sound-speed perturbations at $0.7 R_{\odot}$

We apply the technique detailed in Chapter 2 and Section 3.2 to create phase-shift maps depending on latitude and depth for the two datasets with perturbations centred at  $0.7 R_{\odot}$  (T1 and T2) and for the reference unperturbed dataset (R). As noted before, in these simulations the perturbations are not restrained to localized values of longitude; therefore, unlike in upcoming Sections 3.3.2 and 3.3.3, we have averaged the phase-shift maps along the longitudinal axis in order to increase the signal-to-noise ratio, as we do in Section 4 for the observational data.

Figure 3.6 shows two examples of the reconstructed seismic maps: for the perturbed dataset T1 (a) and for the reference unperturbed dataset R (b), with the aid of the same colour scale. The corresponding means between  $-45^{\circ}$  and  $+45^{\circ}$  are shown in Figure 3.7 for T1 in black and for R in blue. In both figures, we can observe an overall increase in phase shift with submerging focal plane up to  $\approx 0.75R_{\odot}$ . This overall increase is modulated in the uppermost layers of the maps by an oscillation pattern formed by bands of phase shift with little variation with latitude. These bands show minima and maxima at similar positions for the T1 and R simulations, but have stronger values for the perturbed dataset. However, at layers below  $\approx 0.75R_{\odot}$  they attenuate considerably. The possible origin of the bands will be discussed thoroughly at a later section. The previous two effects obscure the Gaussian-shaped perturbation in the raw seismic map [Figure 3.6(a)]. With respect to the other perturbed dataset T2, the behaviour of its reconstructed phase shift is

Este documento incorpora firma electrónica, y es copia auténtica de un documento electrónico archivado por la ULL según la Ley 39/2015.  
Su autenticidad puede ser contrastada en la siguiente dirección <https://sede.ull.es/validacion/>

Identificador del documento: 963882

Código de verificación: QDmfX6JG

Firmado por: MANUEL DIAZ ALFARO  
UNIVERSIDAD DE LA LAGUNA

Fecha: 26/06/2017 15:24:15

FERNANDO JAVIER PEREZ HERNANDEZ  
UNIVERSIDAD DE LA LAGUNA

26/06/2017 15:25:57

ERNESTO PEREDA DE PABLO  
UNIVERSIDAD DE LA LAGUNA

28/06/2017 13:21:41

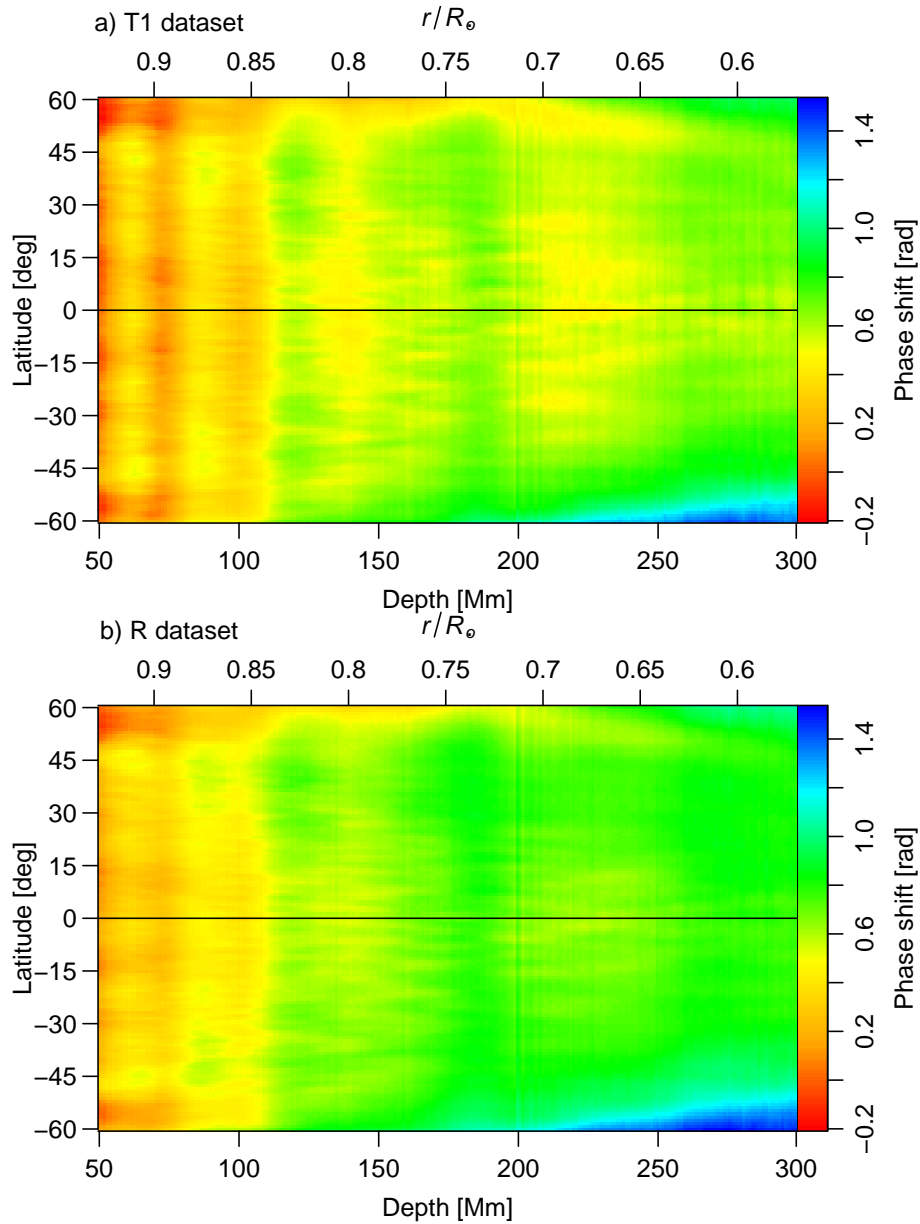


Figure 3.6: Latitude-depth map of the longitudinally-averaged reconstructed phase shift of the perturbed numerical simulation T1 (a) and of the reference simulation R (b). The T1 simulation has nominal Gaussian-shaped perturbations in the sound speed with respect to the background model centred at  $0.7 R_{\odot}$  and at  $\pm 30^{\circ}$  of latitude with central amplitudes in the sound-speed variation with respect to model S values of 0.7% in the northern hemisphere and 0.5% in the southern hemisphere. The black horizontal line represents the equator. The same colour scale, which indicates the phase shift in radians, is used in both plots.

Este documento incorpora firma electrónica, y es copia auténtica de un documento electrónico archivado por la ULL según la Ley 39/2015.  
Su autenticidad puede ser contrastada en la siguiente dirección <https://sede.ull.es/validacion/>

Identificador del documento: 963882

Código de verificación: QDmfX6JG

Firmado por: MANUEL DIAZ ALFARO  
UNIVERSIDAD DE LA LAGUNA

Fecha: 26/06/2017 15:24:15

FERNANDO JAVIER PEREZ HERNANDEZ  
UNIVERSIDAD DE LA LAGUNA

26/06/2017 15:25:57

ERNESTO PEREDA DE PABLO  
UNIVERSIDAD DE LA LAGUNA

28/06/2017 13:21:41

very similar to the one shown for T1, being their mutual differences negligible with the scales used in these figures. Figure 3.7 shows also a peak-like feature at  $\approx 200$  Mm, appearing in all the considered simulations, and being an artefact produced by the change in the model used to reconstruct the solar interior at this layer where its acoustic behaviour couples the radiative interior with the convective envelope. This transition layer, located at  $\approx 200$  Mm  $\approx 0.71R_{\odot}$  in the model, is shown as a dashed vertical line in Figure 3.7.

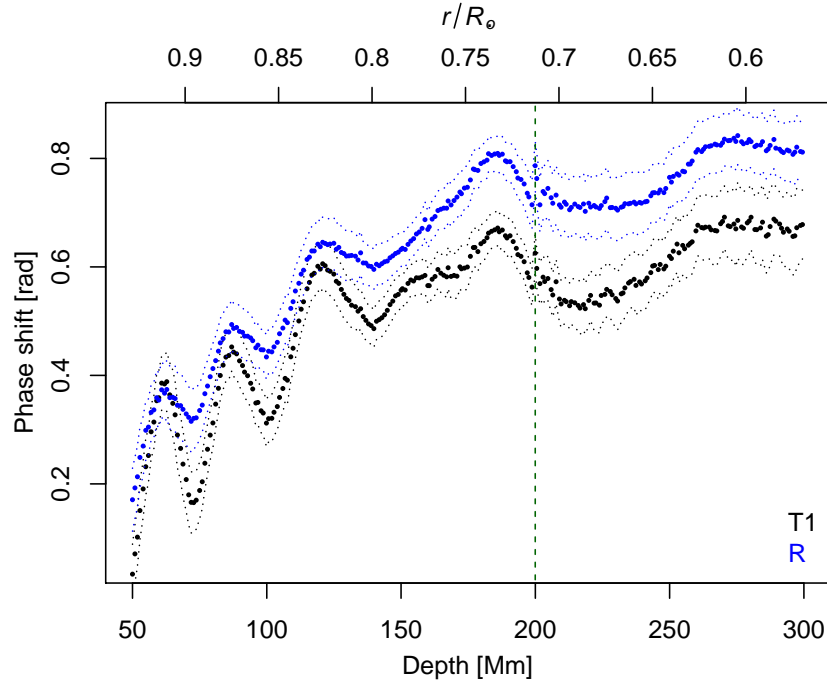


Figure 3.7: Variation with depth of the longitudinally-and-latitudinally-averaged reconstructed phase shift for the perturbed numerical simulation T1 (black) and for the reference simulation R (blue). The average in latitude is restricted to the interval between  $-45^\circ$  and  $+45^\circ$ . The standard deviation from the mean value for each simulation is shown with a thinner dotted line in the same colour. The T1 simulation has nominal Gaussian-shaped perturbations centred at  $0.7 R_{\odot}$  and at  $\pm 30^\circ$  of latitude with central amplitudes in the sound-speed variation with respect to model S values of 0.7% in the northern hemisphere and of 0.5% in the southern hemisphere. The vertical green dashed line marks the location in which model S transitions from the radiative interior to the convective envelope.

As seen in Section 2.4, the use of the lateral vantage in the deep-focus reconstruction of the seismic field of the simulations determines the size of the considered pupils, which increase when the focal plane submerges. This fact causes that the response of the reconstructing technique has a dependence on depth and that is the reason for the observed overall reduction in phase shift up to  $\approx 0.75R_{\odot}$ . At

Este documento incorpora firma electrónica, y es copia auténtica de un documento electrónico archivado por la ULL según la Ley 39/2015.  
Su autenticidad puede ser contrastada en la siguiente dirección <https://sede.ull.es/validacion/>

Identificador del documento: 963882

Código de verificación: QDmfX6JG

Firmado por: MANUEL DIAZ ALFARO  
UNIVERSIDAD DE LA LAGUNA

Fecha: 26/06/2017 15:24:15

FERNANDO JAVIER PEREZ HERNANDEZ  
UNIVERSIDAD DE LA LAGUNA

26/06/2017 15:25:57

ERNESTO PEREDA DE PABLO  
UNIVERSIDAD DE LA LAGUNA

28/06/2017 13:21:41

about this depth the increasing pupil of the submerging focus reaches the limit radius of the observed Sun and this phenomenon stops. The use of an unperturbed reference simulation R is intended to correct for this and other unwanted effects originating within the framework of the applied seismic technique.

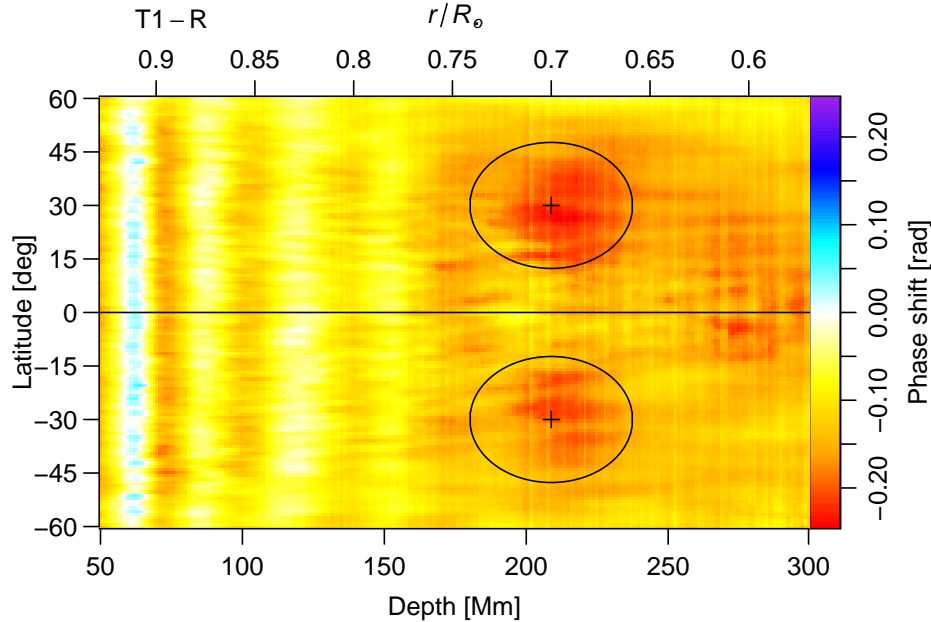


Figure 3.8: Latitude-depth map of the longitudinally-averaged reconstructed phase shift of the perturbed numerical simulations T1 with respect to the reference simulation R. The T1 simulation has nominal Gaussian-shaped perturbations centred at  $0.7 R_{\odot}$  and at  $\pm 30^{\circ}$  of latitude with central amplitudes in the sound-speed variation with respect to model S values of 0.7% in the northern hemisphere and of 0.5% in the southern hemisphere. The black horizontal line represents the equator. The crosses mark the nominal centres of the perturbations. Ellipses corresponding to the nominal FWHM of the simulated perturbations are shown in black for comparison. The colour scale indicates the phase shift in radians.

Figure 3.8 shows a preliminary attempt of the application of this correction to one of the perturbed datasets. It shows the relative phase-shift difference between the T1 and R phase-shift maps shown in Figure 3.7 (a) and (b) respectively. Two areas of relative lower phase shift appear at the positions of the nominal perturbations, whose nominal centre and FWHM have been represented with the aid of black crosses and ellipses. Although the overall slope-like reduction in phase shift is corrected, the phase-shift bands remain. Besides, the overall value of the background of this reference-corrected T1 seismic map in areas far away from the perturbations is still different from zero, as a constant phase-shift displacement between the reference and perturbed simulations is systematically present at all latitudes, also visible in Figure 3.7. We discuss the origin of this offset later, but for the time being we just try to remove it. In order to obtain a value for this offset, we consider the relative

Este documento incorpora firma electrónica, y es copia auténtica de un documento electrónico archivado por la ULL según la Ley 39/2015.  
Su autenticidad puede ser contrastada en la siguiente dirección <https://sede.ull.es/validacion/>

Identificador del documento: 963882

Código de verificación: QDmfX6JG

Firmado por: MANUEL DIAZ ALFARO  
UNIVERSIDAD DE LA LAGUNA

Fecha: 26/06/2017 15:24:15

FERNANDO JAVIER PEREZ HERNANDEZ  
UNIVERSIDAD DE LA LAGUNA

26/06/2017 15:25:57

ERNESTO PEREDA DE PABLO  
UNIVERSIDAD DE LA LAGUNA

28/06/2017 13:21:41

phase-shift maps between the perturbed datasets (T1, T2) and the reference one (R)—*e.g.* T1–R shown in Figure 3.8—, and for each of the four perturbations present in T1 and T2 we apply a least squares fit to a Gaussian distribution with the same centre and FWHM as the nominal perturbations in the simulations, considering only the points within the corresponding area of nominal FWHM. The fitted phase-shift amplitudes are plotted against the nominal sound-speed perturbation in Figure 3.9. The corresponding error bars are calculated as the root mean squares of the fit residuals within the corresponding area of nominal FWHM. The points are fitted to a line, also shown in the plot, with the following expression:

$$\phi = 0.14 - 12.90 \cdot \frac{\delta c}{c}, \quad (3.4)$$

whose intercept term of  $\approx 0.14$  rad provides the value of the systematic displacement between the perturbed datasets and the reference one. On the other hand, the slope term, with a value of  $-12.90$  for  $\delta c/c$  expressed as per-unit values, gives a preliminary linear relation between phase shift and sound-speed variation.

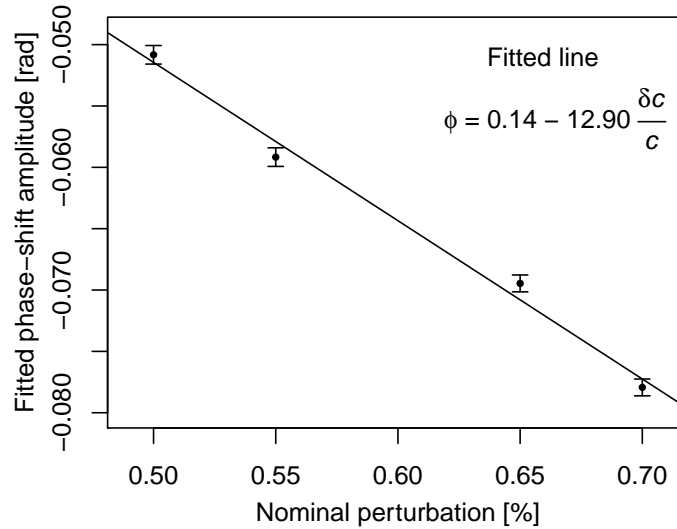


Figure 3.9: Variation of the phase-shift fitted amplitudes for each of the considered Gaussian-shaped sound-speed perturbations present in the two reconstructed perturbed phase-shift maps (T1, T2) relative to the reference one (R) with respect to the nominal sound-speed perturbation. A linear fit to the data, also shown, estimates the systematic offset between the perturbed simulations and the reference one.

We subtract the intercept term of Equation (3.4) from the reconstructed phase shift of the reference simulation (R). Figure 3.10 shows the phase-shift means between  $-45^\circ$

Este documento incorpora firma electrónica, y es copia auténtica de un documento electrónico archivado por la ULL según la Ley 39/2015.  
Su autenticidad puede ser contrastada en la siguiente dirección <https://sede.ull.es/validacion/>

Identificador del documento: 963882

Código de verificación: QDmfX6JG

Firmado por: MANUEL DIAZ ALFARO  
UNIVERSIDAD DE LA LAGUNA

Fecha: 26/06/2017 15:24:15

FERNANDO JAVIER PEREZ HERNANDEZ  
UNIVERSIDAD DE LA LAGUNA

26/06/2017 15:25:57

ERNESTO PEREDA DE PABLO  
UNIVERSIDAD DE LA LAGUNA

28/06/2017 13:21:41

and  $+45^\circ$  for the R simulation after offset correction in red. The T1 means previously shown in Figure 3.8 is also shown here in black. Here, at about  $0.75 R_\odot$  there is a recession of the perturbed T1 phase shift from the corrected reference, which is an indicator of the recovery of the sound-speed perturbation.

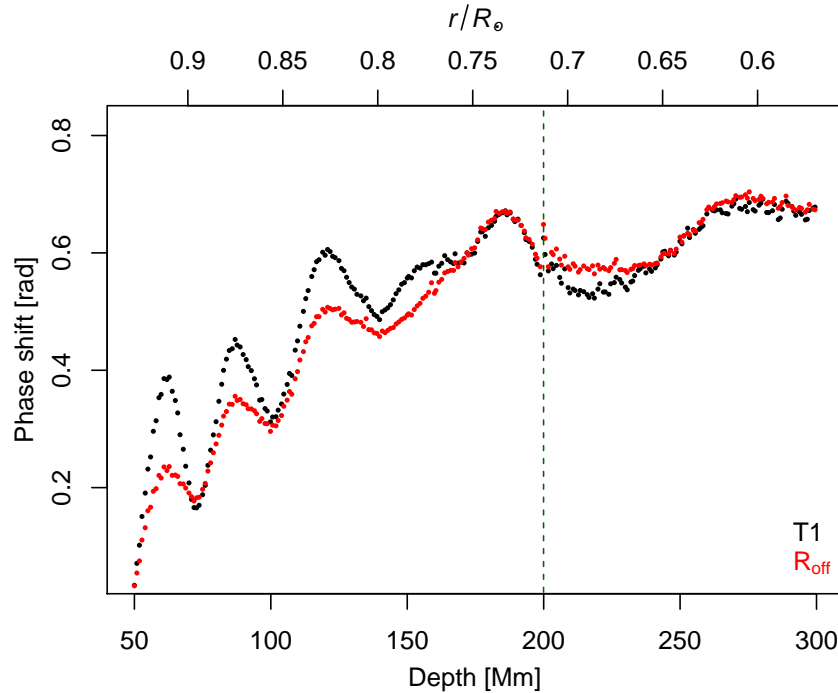


Figure 3.10: Variation with depth of the longitudinally-and-latitude-averaged reconstructed phase shift for the perturbed numerical simulation T1 (black) and for the reference simulation R (blue), where the reference simulation has been offset  $\approx -0.14$  rad to correct the systematic offset between the perturbed simulations and the reference one ( $R_{\text{off}} = R - 0.14$ ). The average in latitude is restricted to the interval between  $-45^\circ$  and  $+45^\circ$ . The standard deviation from the mean value for each simulation remains the same as in Figure 3.7 and has been left un-plotted for greater plot clarity. The T1 simulation has nominal Gaussian-shaped perturbations centred at  $0.7 R_\odot$  and at  $\pm 30^\circ$  of latitude with central amplitudes in the sound-speed variation with respect to model S values of 0.7% in the northern hemisphere and of 0.5% in the southern hemisphere.

The map of the relative phase shift between the T1 perturbed simulation and the reference one after offset correction is shown in Figure 3.11. The perturbations are recovered in both hemispheres around their nominal positions:  $\pm 30^\circ$  and  $0.7 R_\odot$ . As expected from the nominal amplitudes of the simulated perturbations, the recovered phase-shift intensity is higher in the northern hemisphere. We apply least squares fits to Gaussian distributions for each of the perturbations in the T1 and T2 phase-shift maps relative to the offset-corrected reference R dataset. As done before, we consider fixed centre and FWHM for the fits, with the same values as the

Este documento incorpora firma electrónica, y es copia auténtica de un documento electrónico archivado por la ULL según la Ley 39/2015.  
Su autenticidad puede ser contrastada en la siguiente dirección <https://sede.ull.es/validacion/>

Identificador del documento: 963882

Código de verificación: QDmfX6JG

Firmado por: MANUEL DIAZ ALFARO  
UNIVERSIDAD DE LA LAGUNA

Fecha: 26/06/2017 15:24:15

FERNANDO JAVIER PEREZ HERNANDEZ  
UNIVERSIDAD DE LA LAGUNA

26/06/2017 15:25:57

ERNESTO PEREDA DE PABLO  
UNIVERSIDAD DE LA LAGUNA

28/06/2017 13:21:41

nominal perturbations, considering only the points of the maps in the area within the nominal FWHM. We get amplitude values ranging between  $-0.051$  rad for the 0.5%-sound-speed perturbation and  $-0.078$  rad for the 0.7%-sound-speed perturbation. Shall we consider Equation (2.4) and a mean frequency of  $\langle \nu \rangle = 3.5$  mHz, these values correspond to mean time delays of  $\Delta\tau = -2.21$  s for the 0.5%-sound-speed perturbation and  $\Delta\tau = -3.54$  s for the 0.7% sound-speed perturbation. In comparison with Figure 3.8, the amplitudes of the bands are reduced in Figure 3.11. However, they are not completely removed. We discuss later the implications and possible origin of this phenomenon.

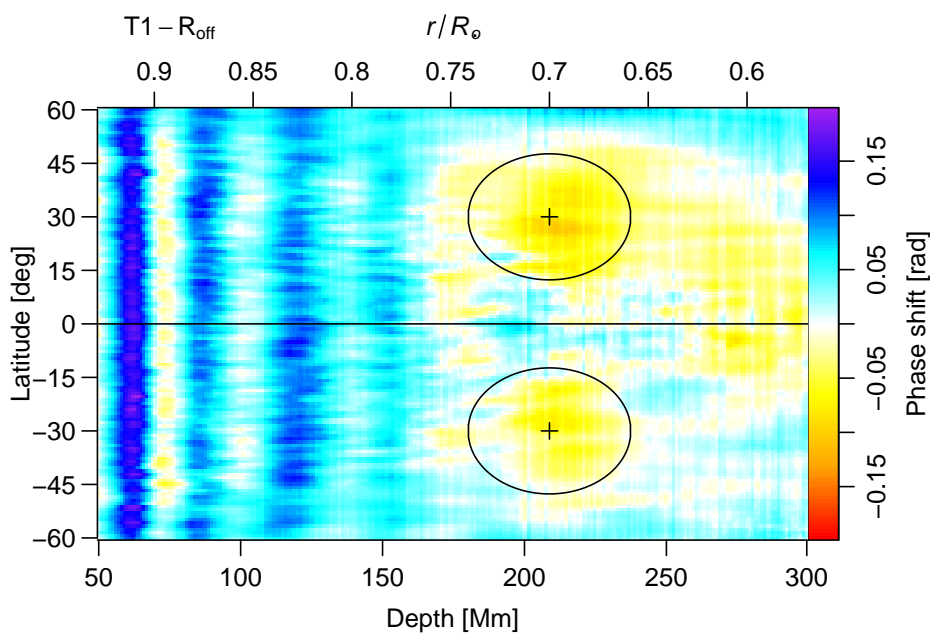


Figure 3.11: Latitude-depth map of the longitudinally-averaged reconstructed phase shift of the perturbed numerical simulations T1 with respect to the reference simulation R, where the reference simulation has been previously offset  $\approx -0.14$  rad to correct the systematic offset between the perturbed simulations and the reference one. The T1 simulation has nominal Gaussian-shaped perturbations centred at  $0.7 R_{\odot}$  and at  $\pm 30^{\circ}$  of latitude with central amplitudes in the sound-speed variation with respect to model S values of 0.7% in the northern hemisphere and of 0.5% in the southern hemisphere. The black horizontal line represents the equator. The crosses mark the nominal centres of the perturbations. Ellipses corresponding to the nominal FWHM of the simulated perturbations are shown in black for comparison. The colour scale indicates the phase shift in radians.

Figure 3.12 shows the relative phase-shift map between both perturbed simulations T1 and T2, namely the T1 phase-shift minus the T2 phase-shift. A negative perturbation in phase shift is neatly visible in the northern hemisphere and a positive perturbation in the southern hemisphere. Greater sound speeds produce shorter time delays, and therefore, are expected to originate lower phase shifts in the reconstructed maps, which is the observed behaviour here, as the relative sound-speed difference is

Este documento incorpora firma electrónica, y es copia auténtica de un documento electrónico archivado por la ULL según la Ley 39/2015.  
Su autenticidad puede ser contrastada en la siguiente dirección <https://sede.ull.es/validacion/>

Identificador del documento: 963882

Código de verificación: QDmfX6JG

Firmado por: MANUEL DIAZ ALFARO  
UNIVERSIDAD DE LA LAGUNA

Fecha: 26/06/2017 15:24:15

FERNANDO JAVIER PEREZ HERNANDEZ  
UNIVERSIDAD DE LA LAGUNA

26/06/2017 15:25:57

ERNESTO PEREDA DE PABLO  
UNIVERSIDAD DE LA LAGUNA

28/06/2017 13:21:41

+0.05% in the northern and  $-0.05\%$  in the southern hemispheres. The black crosses and ellipses show the centre and FWHM of the nominal perturbations for reference. We will discuss later the complete disappearance of the band structure, present in previous phase-shift reconstructions, and completely removed here.

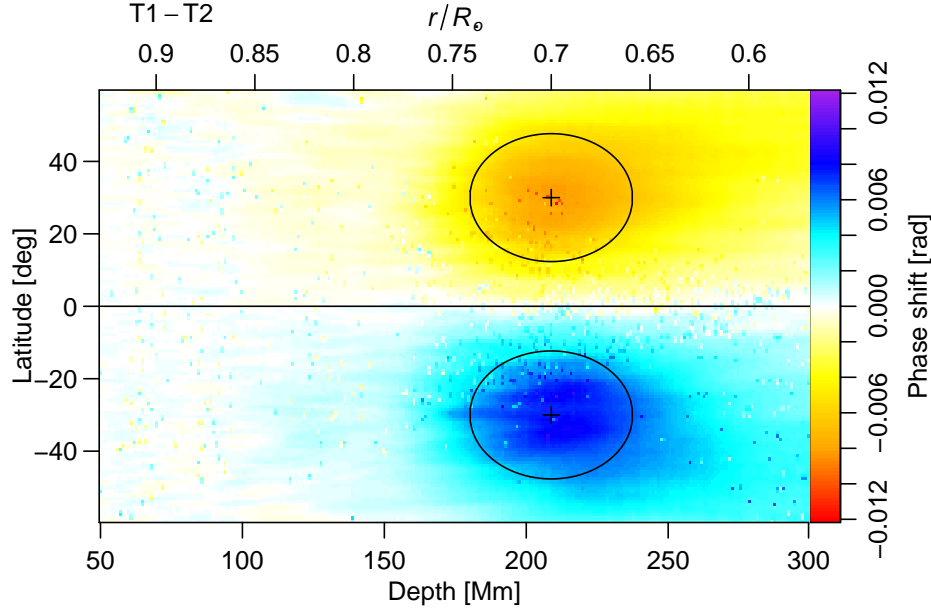


Figure 3.12: Latitude-depth map of the longitudinally-averaged relative phase shift between the perturbed numerical simulations T1 and T2, i.e the phase-shift map for the T1 simulation minus the corresponding phase-shift map for the T2 simulation. Both simulations have Gaussian-shaped perturbations in the sound speed with respect to the background model centred at  $0.7 R_{\odot}$  and at  $\pm 30^{\circ}$  of latitude with central amplitudes of 0.7% in the northern hemisphere and 0.5% in the southern hemisphere in T1, and of 0.65% in the northern hemisphere and 0.55% in the southern hemisphere in T2. The black horizontal line represents the equator. The crosses mark the nominal centres of the perturbations. Ellipses corresponding to the nominal FWHM of the simulated perturbations are shown in black for comparison. The colour scale indicates the phase shift in radians.

Figure 3.13 shows cuts of Figure 3.12 at fixed latitudes of  $\pm 30^{\circ}$  (a) and at a fixed depth of 208 Mm ( $\approx 0.7 R_{\odot}$ ) (b), which correspond to the nominal central positions of the perturbations. The profile of the northern perturbations difference is shown in blue, whereas that of the southern perturbations difference is shown in red. For easier comparison, the northern phase-shift difference has been reversed in the plot. We apply a least squares fit to a double Gaussian distribution with the same centre and FWHM as the nominal values for the perturbations introduced in the simulations, considering for the fit only the points of the map within the areas of the nominal FWHM. The fitted phase-shift amplitude is 0.0084 rad. Considering Equation (2.4) and a mean frequency of  $\langle \nu \rangle = 3.5$  mHz, this value correspond to a mean travel time delay of  $\Delta\tau = 0.38$  s for an original sound-speed decrease of 0.05%.

Este documento incorpora firma electrónica, y es copia auténtica de un documento electrónico archivado por la ULL según la Ley 39/2015.  
Su autenticidad puede ser contrastada en la siguiente dirección <https://sede.ull.es/validacion/>

Identificador del documento: 963882

Código de verificación: QDmfX6JG

Firmado por: MANUEL DIAZ ALFARO  
UNIVERSIDAD DE LA LAGUNA

Fecha: 26/06/2017 15:24:15

FERNANDO JAVIER PEREZ HERNANDEZ  
UNIVERSIDAD DE LA LAGUNA

26/06/2017 15:25:57

ERNESTO PEREDA DE PABLO  
UNIVERSIDAD DE LA LAGUNA

28/06/2017 13:21:41

The relation between phase shift and the sound-speed difference producing it would be:

$$\phi = -16.80 \cdot \frac{\delta c}{c}, \quad (3.5)$$

which gives the relationship between sound-speed variation and equivalent reconstructed phase-shift, for variations in the sound speed  $\delta c/c$  expressed as per-unit values.

The corresponding cuts of the fitted Gaussian distribution are also plotted in Figure 3.13 in black dashed lines for comparison. Although for the sake of clearer visual comparison both the reconstructed profile and that of the fitted nominal perturbation are shown as positive values, it should be remarked that a decrease in the sound speed creates a relative positive phase shift and *vice versa*.

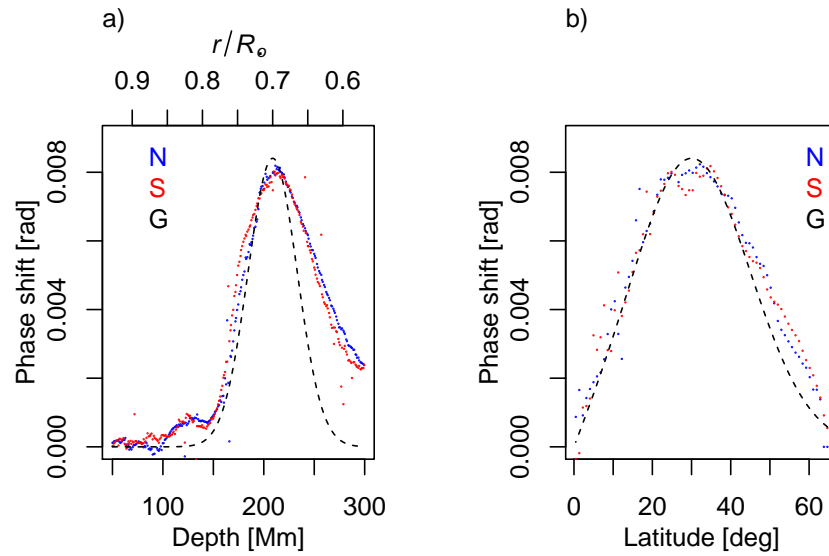


Figure 3.13: Relative longitudinally-averaged phase shift between the perturbed numerical simulations T1 and T2 with respect to depth at latitudes of  $\pm 30^\circ$  (a) and with respect to latitude at a depth of 208 Mm ( $\approx 0.7R_\odot$ ) (b). The phase shift profiles corresponding to the northern hemisphere are shown in blue and the profiles corresponding to the southern hemisphere are shown in red. The northern hemisphere difference has been reversed to be expressed as positive values. The corresponding cuts of a fitted bi-dimensional Gaussian with an amplitude of 0.0084 rad, centred at the same position, and with the same FWHM, as the nominal perturbations introduced in simulations T1 and T2, are shown in black dashes for reference. This figure represents horizontal cuts (a) and a vertical cut (b) of Figure 3.12.

Regarding to depth [Figure 3.13(a)], a clear broadening appears at higher depths, behaviour that was also observed by Zhao *et al.* (2009) using time-distance helioseismology. Besides, a slight deepening in the central position of the reconstructed perturbation is also present, being  $\approx 0.015 R_\odot$  below the nominal position. As confirmed in Sections 3.3.2 and 3.3.3, the larger size of pupils for deeper focal planes under a lateral-vantage scheme tends to deepen the reconstructed

Este documento incorpora firma electrónica, y es copia auténtica de un documento electrónico archivado por la ULL según la Ley 39/2015.  
Su autenticidad puede ser contrastada en la siguiente dirección <https://sede.ull.es/validacion/>

Identificador del documento: 963882

Código de verificación: QDmfX6JG

Firmado por: MANUEL DIAZ ALFARO  
UNIVERSIDAD DE LA LAGUNA

Fecha: 26/06/2017 15:24:15

FERNANDO JAVIER PEREZ HERNANDEZ  
UNIVERSIDAD DE LA LAGUNA

26/06/2017 15:25:57

ERNESTO PEREDA DE PABLO  
UNIVERSIDAD DE LA LAGUNA

28/06/2017 13:21:41

seismic signal and widen it in the direction of depth. With respect to the latitudinal dependence [Figure 3.13(b)], the recovered profiles follow clearly a Gaussian-like distribution, with a slight broadening at higher latitudes. This may be caused by the lower sensitivity of seismic holography for pixels located near the limb for the visible near side of the Sun using a  $1 \times 1$  skip schema, as part of the ideal pupil lies in the non-visible far side of the Sun. This broadening at high latitudes may be improved by considering input dopplergrams of higher resolution, *i.e.* of  $800 \times 800$  pixels. Besides, the peak-like artefact at  $\approx 200$  Mm has been completely removed here.

The origin of the banding is not very clear. As seen later in Chapter 4, strong bands, as they appear in the reconstructed seismic maps of the simulations, are not present in the helioseismic reconstruction of the solar interior for GONG solar observations even in the raw data; where the oscillations are much weaker. There we see that the regular procedure is to apply the technique to the observations in intervals of 24 h of data. We have applied the same technique to two shorter sets of GONG observations, spanning  $1024 \text{ min} \approx 17 \text{ h}$ , the same timespan as the simulations. However, the strong banding does not appear there either. Therefore, we must conclude that the banding is not produced by the shorter timespan of the simulations and its origin must be looked for elsewhere.

Although the background state of the simulations is based on model S, it was slightly modified with the inclusion of a model for the chromosphere, the neglect of the entropy gradient and different upper boundary conditions so as to make the simulations more realistic. Green's functions applied in the reconstructing scheme have been computed using an unmodified model S. These differences between the model used to populate the simulations and the one used to reconstruct the solar interior thereof may have had an influence in the observed banding in the upper layers of the reconstructed phase shift. Besides, at certain layers the modes reach the limit of their resonant cavity and stop to be included in the calculation of Green's functions used to reconstruct the acoustic field of the solar interior, which may also contribute to the formation of bands.

The purpose of applying the same technique to an unperturbed reference simulation is to remove the effects originating from the technique itself, such as the banding. Although part of the unwanted effects are removed after subtracting, part of the banding remains and there is a systematic overall offset between the reconstructed phase shift of the reference and perturbed simulations. However, as seen in Figures 3.12 and 3.13 the bands disappear completely when considering the relative reconstructed phase shift between the two perturbed simulations. Although the simulations were generated using the same scheme, it is possible that some minor improvement in the code between the computations of the different sets may have played a role here. Whereas the perturbed simulations T1 and T2 were computed together in the same time frame, the reference simulation R had been generated the previous year. Some minor changes in the code may explain why the relative phase shift between T1 and T2 remove all the unwanted effects, whereas the relative phase

Este documento incorpora firma electrónica, y es copia auténtica de un documento electrónico archivado por la ULL según la Ley 39/2015.  
Su autenticidad puede ser contrastada en la siguiente dirección <https://sede.ull.es/validacion/>

Identificador del documento: 963882

Código de verificación: QDmfX6JG

Firmado por: MANUEL DIAZ ALFARO  
UNIVERSIDAD DE LA LAGUNA

Fecha: 26/06/2017 15:24:15

FERNANDO JAVIER PEREZ HERNANDEZ  
UNIVERSIDAD DE LA LAGUNA

26/06/2017 15:25:57

ERNESTO PEREDA DE PABLO  
UNIVERSIDAD DE LA LAGUNA

28/06/2017 13:21:41

shift between T1 and R does not. Besides, the introduced differences in the code may have resulted in a slightly different acoustic behaviour of the resonant cavity of the simulations. This could be interpreted as a change in the seismic radius of the simulated Sun. The seismic radius, a concept introduced by Schou *et al.* (1997), indicates a measurement of the solar radius achieved through helioseismology. It should be interpreted as a measurement of changes in the resonant cavity in which waves propagates rather than changes in the physical radius of the Sun, with which does not necessarily agree. In the real Sun an anticorrelation between seismic radius and solar activity has been observed (Dziembowski, Goode, and Schou, 2001; Lefebvre and Kosovichev, 2005; Kholikov and Hill, 2008; González Hernández, Scherrer, and Hill, 2009). Analogously, a change in the overall acoustic properties of the simulated Sun could be the reason for the offset between the R and T1-T2 simulations. The specific dates of production of the other simulations, whose results are shown in Sections 3.3.2 and 3.3.3, and their mean overall phase-shift values further supports this explanation.

### 3.3.2 Localized sound-speed perturbations in the photosphere

In Section 3.3.1 we have shown the capability of the current technique of detecting perturbations in the sound speed at the base of the convection zone at least for variations as low as  $\delta c/c = 5 \cdot 10^{-4}$  in an ideal case with no perturbations at the upper layers, including the solar surface. Nevertheless, magnetic activity is actually present at the solar surface with stronger values than near the base of the convection zone. Although helioseismic holography aims at reconstructing the acoustic field of the Sun at a specific focal depth, the technique also includes out-of-focus contributions from other depths the waves have travelled through. In the particular case of having typical magnetic fields at the base of the convection zone together with typical magnetic activity at the surface, out-of-focus contributions from the surface stronger magnetic fields may add considerable noise to or even obscure completely the detection of the former. We asses here the influence of surface activity at the helioseismic reconstruction of the acoustic field at deep layers of the Sun with the aid of the numerical simulations with sound-speed perturbations at the surface (P1, P2, P3) described in Section 3.1.2 (Hartlep *et al.*, 2008).

Therefore, we apply the technique detailed in Chapter 2 and Section 3.2 to the P1–P3 simulations to produce three-dimensional maps of phase shift depending on latitude, longitude and depth. Figure 3.14 shows in black the reconstructed mean phase-shift profile for the simulation P1 between  $-45^\circ$  and  $+45^\circ$  of latitude, and between  $315^\circ$  and  $45^\circ$  of longitude, corresponding to an unperturbed region, diametrically opposite to the area where the perturbations are located. It should be noted that unlike in previous Section 3.3.1 where the perturbations were longitudinally homogeneous, here the perturbations are limited to a certain extent in longitude and this causes a slight increase in the standard deviation of the mean value when averaging over the longitudinal axis. The mean phase shift of the unperturbed simulation R after offset correction is shown in red for comparison.

Este documento incorpora firma electrónica, y es copia auténtica de un documento electrónico archivado por la ULL según la Ley 39/2015.  
Su autenticidad puede ser contrastada en la siguiente dirección <https://sede.ull.es/validacion/>

Identificador del documento: 963882

Código de verificación: QDmfX6JG

Firmado por: MANUEL DIAZ ALFARO  
UNIVERSIDAD DE LA LAGUNA

Fecha: 26/06/2017 15:24:15

FERNANDO JAVIER PEREZ HERNANDEZ  
UNIVERSIDAD DE LA LAGUNA

26/06/2017 15:25:57

ERNESTO PEREDA DE PABLO  
UNIVERSIDAD DE LA LAGUNA

28/06/2017 13:21:41

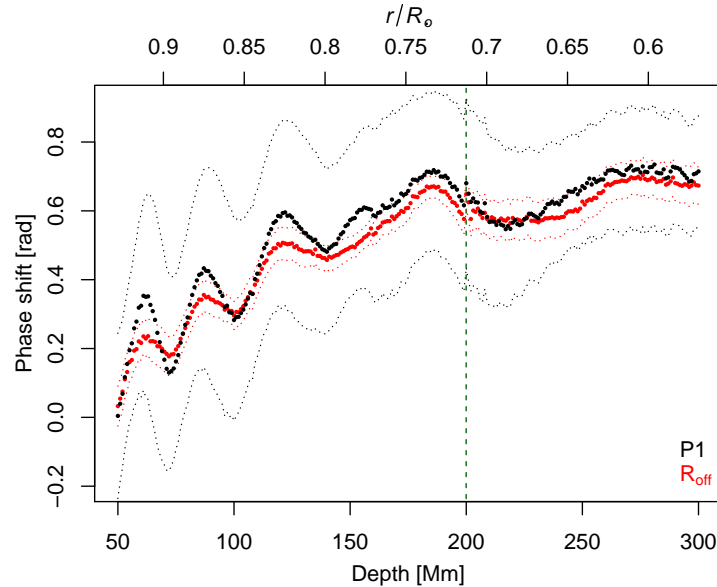


Figure 3.14: Variation with depth of the longitudinally-and-latitude-averaged reconstructed phase shift for the perturbed numerical simulation P1 (black) in an area devoid of sound-speed perturbations between  $-45^\circ$  and  $+45^\circ$  of latitude and between  $315^\circ$  and  $45^\circ$  of longitude and for the reference simulation R (red), with the offset inferred in Section 3.3.1 ( $R_{\text{off}} = R - 0.14$ ), for all longitude values. The standard deviation from the mean value for each simulation is shown with a thinner dotted line in the same colour. The vertical green dashed line marks the location in which model S transitions from the radiative interior to the convective envelope.

We can observe the presence of bands in the upper layers of the P1 simulation, but of different values as those from the R simulation, as happened between the T1 and T2 simulations on the one hand, and the R simulation on the other hand. As discussed before in Section 3.3.1, ongoing improvements to the simulating code between the generating moment of the P1–P3 and that of the R simulations make the R simulation an imperfect tool for banding correction. In this case, we have considered each simulation separately and have computed the depth-dependent means in the unperturbed area defined before—latitude between  $-45^\circ$  and  $+45^\circ$  and longitude between  $315^\circ$  and  $45^\circ$ —; which have been subtracted from each simulation to remove the depth-dependent banding structure.

Figure 3.15 shows maps of the phase-shift reconstruction at the surface for the three considered simulations (P1, P2, P3), with increasing perturbation sizes. Due to its geometry, in the lateral vantage the pupil is extremely narrow for phase-shift computations at the surface and uppermost layers of the Sun. Therefore, the subjacent vantage, as detailed in Section 2.4, used commonly for imaging the solar surface, was also used here to produce these maps of the photosphere. However, phase shift computations at focal planes below the solar surface were created using the lateral vantage, as done in Section 3.3.1.

Este documento incorpora firma electrónica, y es copia auténtica de un documento electrónico archivado por la ULL según la Ley 39/2015.  
Su autenticidad puede ser contrastada en la siguiente dirección <https://sede.ull.es/validacion/>

Identificador del documento: 963882

Código de verificación: QDmfX6JG

Firmado por: MANUEL DIAZ ALFARO  
UNIVERSIDAD DE LA LAGUNA

Fecha: 26/06/2017 15:24:15

FERNANDO JAVIER PEREZ HERNANDEZ  
UNIVERSIDAD DE LA LAGUNA

26/06/2017 15:25:57

ERNESTO PEREDA DE PABLO  
UNIVERSIDAD DE LA LAGUNA

28/06/2017 13:21:41

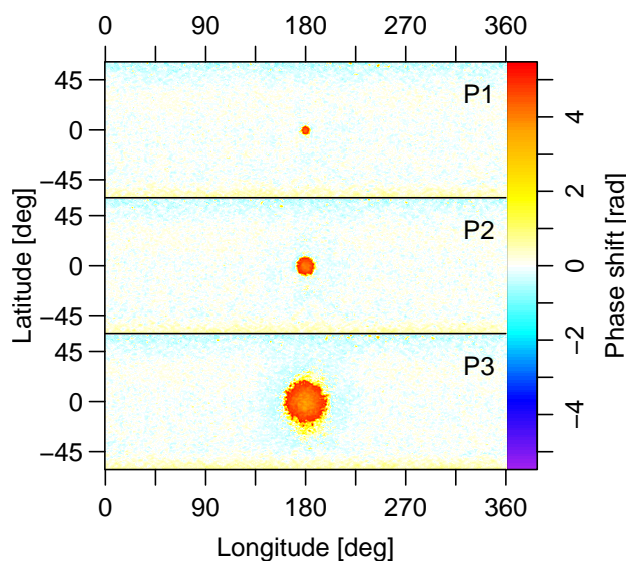


Figure 3.15: Phase shift map at the surface for the P1, P2, and P3 simulations, with sound-speed perturbations located at the photosphere, with equivalent radii at the solar surface of 45 Mm, 90 Mm, and 180 Mm respectively. The seismic holography technique was applied here under the subjacent vantage. The colour scale, common for the three maps, shows the phase shift in radians.

Figures 3.16 and 3.17 allow the study of the penetration of the considered perturbations and the depth reached by each of them. Figure 3.16 show longitude-latitude phase-shift maps at different depths, 50 Mm (a), 100 Mm (b), 150 Mm (c), and 200 Mm (d), for the P1 (top), P2 (middle), and P3 (bottom) simulations. Figure 3.17(a) show depth-longitude phase-shift maps at a fixed latitude of  $0^\circ$ , at which the perturbations are centred, for the P1 (top), P2 (middle) and P3 (bottom) simulations. Figure 3.17(b) show depth-latitude phase-shift maps at a fixed longitude of  $180^\circ$ , at which the perturbations are centred, for the P1 (top), P2 (middle) and P3 (bottom) simulations. As the phase-shift maps show, the recovered seismic signals of the surface perturbations extend deeper than their nominal location covering the upper 30 Mm from the photosphere. We observe that deeper penetrations of the perturbed seismic phase shift occur for horizontally more extensive areas of surface sound-speed perturbations. This is a consequence of the lateral-vantage geometry of the considered pupils: helioseismic computations for deeper focal planes are created with pupils comprising larger areas at the surface.

From Figures 3.16 and 3.17, we observe that the P1 perturbation penetrates up to  $\approx 70$  Mm, the P2 perturbation reaches  $\approx 150$  Mm and the P3 perturbation reaches the layers of the base of the convection zone and tachocline. These results must be considered together with the typical sizes of actual solar active regions. In fact, the

Este documento incorpora firma electrónica, y es copia auténtica de un documento electrónico archivado por la ULL según la Ley 39/2015.  
Su autenticidad puede ser contrastada en la siguiente dirección <https://sede.ull.es/validacion/>

Identificador del documento: 963882

Código de verificación: QDmfX6JG

Firmado por: MANUEL DIAZ ALFARO  
UNIVERSIDAD DE LA LAGUNA

Fecha: 26/06/2017 15:24:15

FERNANDO JAVIER PEREZ HERNANDEZ  
UNIVERSIDAD DE LA LAGUNA

26/06/2017 15:25:57

ERNESTO PEREDA DE PABLO  
UNIVERSIDAD DE LA LAGUNA

28/06/2017 13:21:41

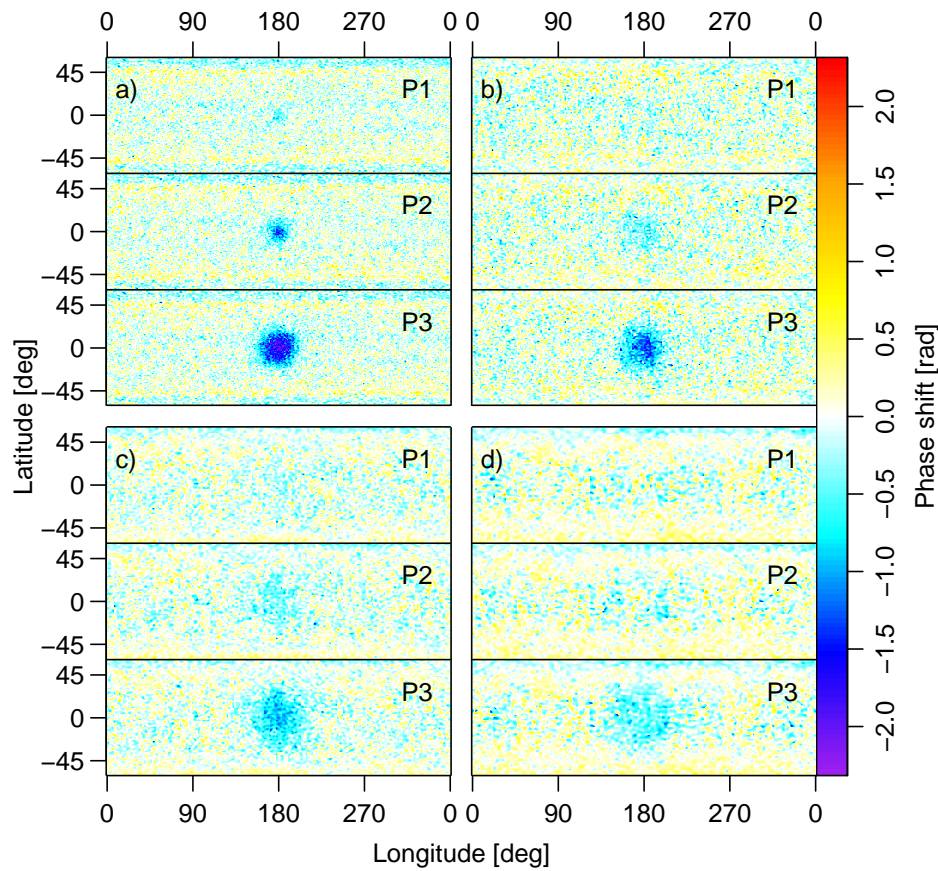


Figure 3.16: Longitude-latitude maps of the reconstructed phase shift for the P1, P2 and P3 simulations at depths of 50 Mm (a), 100 Mm (b), 150 Mm (c), and 200 Mm (d). For each depth the top, middle and bottom panels correspond respectively to the P1, P2 and P3 simulations. The colour scale indicates the phase shift in radians.

size of the largest active region in the last quarter of a century (NOAA2192) surpasses only slightly the size of the smallest perturbation (P1). Therefore, although we have seen that phase-shift contributions of larger perturbations reach layers in the vicinity of the base of the convection zone and tachocline, isolated active regions of typical sizes do not seem to produce significant contribution to the reconstructed acoustic field at these layers.

Este documento incorpora firma electrónica, y es copia auténtica de un documento electrónico archivado por la ULL según la Ley 39/2015.  
Su autenticidad puede ser contrastada en la siguiente dirección <https://sede.ull.es/validacion/>

Identificador del documento: 963882

Código de verificación: QDmfX6JG

Firmado por: MANUEL DIAZ ALFARO  
UNIVERSIDAD DE LA LAGUNA

Fecha: 26/06/2017 15:24:15

FERNANDO JAVIER PEREZ HERNANDEZ  
UNIVERSIDAD DE LA LAGUNA

26/06/2017 15:25:57

ERNESTO PEREDA DE PABLO  
UNIVERSIDAD DE LA LAGUNA

28/06/2017 13:21:41

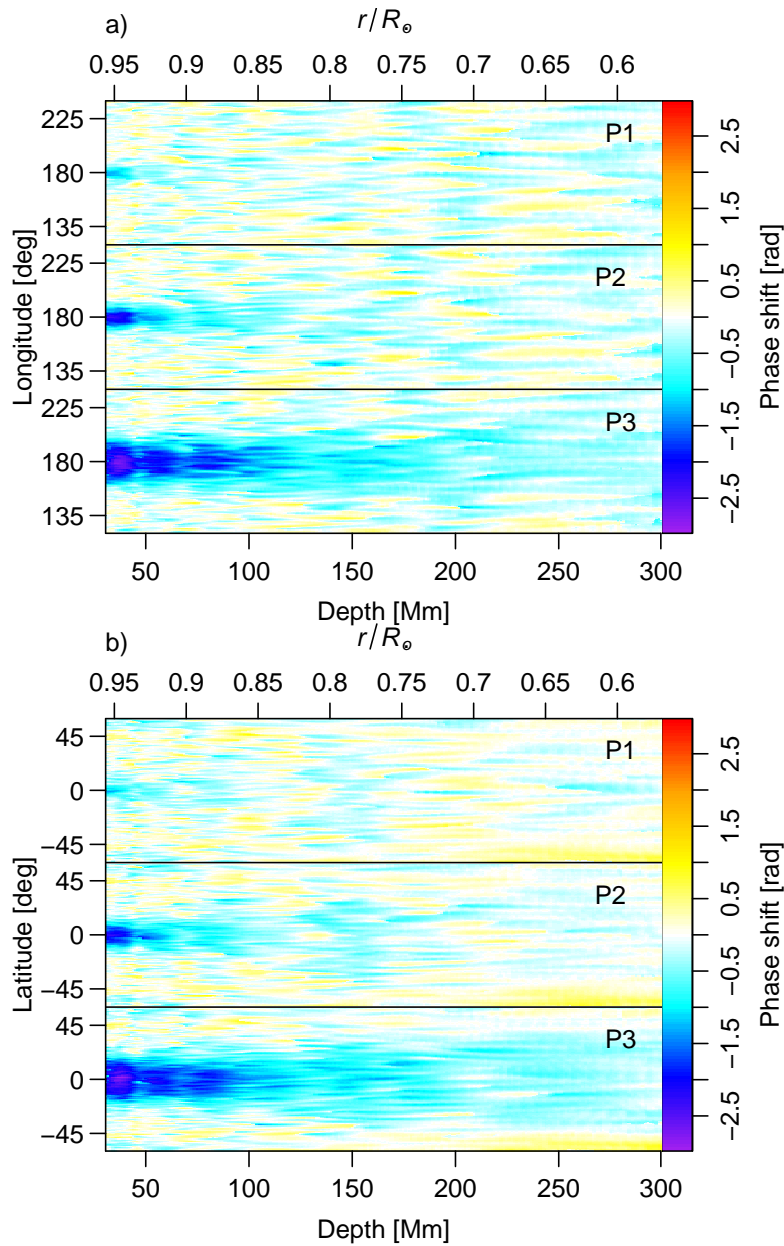


Figure 3.17: a) Longitude-depth maps of the reconstructed phase shift at a fixed latitude of  $0^{\circ}$  for the P1 (top), P2 (middle), and P3 (bottom) simulations. b) Latitude-depth maps of the reconstructed phase shift at a fixed longitude of  $180^{\circ}$  for the P1 (top), P2 (middle), and P3 (bottom) simulations. The fixed values of latitude (a) and longitude (b) correspond to the centre of the nominal perturbations. The colour scale indicates the phase shift in radians.

Este documento incorpora firma electrónica, y es copia auténtica de un documento electrónico archivado por la ULL según la Ley 39/2015.  
Su autenticidad puede ser contrastada en la siguiente dirección <https://sede.ull.es/validacion/>

Identificador del documento: 963882

Código de verificación: QDmfX6JG

Firmado por: MANUEL DIAZ ALFARO  
UNIVERSIDAD DE LA LAGUNA

Fecha: 26/06/2017 15:24:15

FERNANDO JAVIER PEREZ HERNANDEZ  
UNIVERSIDAD DE LA LAGUNA

26/06/2017 15:25:57

ERNESTO PEREDA DE PABLO  
UNIVERSIDAD DE LA LAGUNA

28/06/2017 13:21:41

### 3.3.3 Localized sound-speed perturbations in the shallow subphotosphere

We also apply the technique detailed in Chapter 2 and Section 3.2 to the six numerical datasets with sound-speed perturbations located in the upper layers below the photosphere (20–50 Mm) described in Section 3.1.3 (Hartlep *et al.*, 2011). As done before, in Section 3.3.2, we have created 3-dimensional phase-shift maps depending on latitude, longitude and depth for each of the numerical datasets.

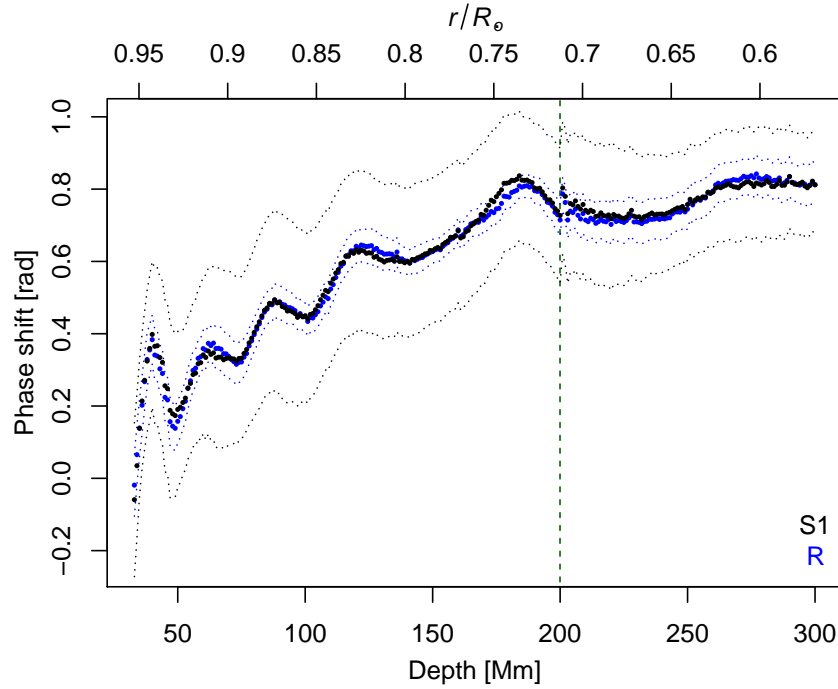


Figure 3.18: Variation with depth of the longitudinally-and-latitude-averaged reconstructed phase shift for the perturbed numerical simulation S1 (black) in an area devoid of sound-speed perturbations between  $-45^\circ$  and  $+45^\circ$  of latitude and between  $315^\circ$  and  $45^\circ$  of longitude and for the reference simulation R (blue) for all longitude values. The standard deviation from the mean value for each simulation is shown with a thinner dotted line in the same colour. The vertical green dashed line marks the location in which model S transitions from the radiative interior to the convective envelope.

Figure 3.18 shows in black the reconstructed mean phase-shift profile for the simulation S1 between  $-45^\circ$  and  $+45^\circ$  of latitude and between  $315^\circ$  and  $45^\circ$  of longitude, which corresponds to an unperturbed region. The unoffset mean phase shift of the unperturbed simulation R is shown in blue for comparison. As in the simulation presented in Section 3.3.2, here the perturbations are also limited to a certain extent in longitude, which produces a slight increase in the standard deviation

Este documento incorpora firma electrónica, y es copia auténtica de un documento electrónico archivado por la ULL según la Ley 39/2015.  
Su autenticidad puede ser contrastada en la siguiente dirección <https://sede.ull.es/validacion/>

Identificador del documento: 963882

Código de verificación: QDmfX6JG

Firmado por: MANUEL DIAZ ALFARO  
UNIVERSIDAD DE LA LAGUNA

Fecha: 26/06/2017 15:24:15

FERNANDO JAVIER PEREZ HERNANDEZ  
UNIVERSIDAD DE LA LAGUNA

26/06/2017 15:25:57

ERNESTO PEREDA DE PABLO  
UNIVERSIDAD DE LA LAGUNA

28/06/2017 13:21:41

of the mean value when averaging over the longitudinal axis. We can observe the presence of bands in the upper layers of the S1 simulation, with a very similar pattern to those from the R simulation, with respect to both position and intensity. This similarity is maintained along all the simulations with subphotospheric sound-speed perturbations (S1–S6). This seems to indicate that between the computation of the R simulation and that of the S1–S6 simulations the changes made to the computation code were, if any, insignificant. Therefore, we can use here the R simulation to remove from the S1–S6 simulations the banding structure, as well as other unwanted artefacts originating from the technique, by simple subtraction without further complications.

Figure 3.19 shows maps of the reconstructed phase shift with respect to longitude and depth at a fixed latitude of  $+20^\circ$  for the S1 (a), S2 (b), S3 (c), S4 (d), and S5 (e) simulations, and at a fixed latitude of  $-20^\circ$  for the S5 simulation (f). As seen in Table 3.4 (Section 3.1.3), the nominal big and medium perturbations are centred at  $+20^\circ$  whereas the nominal small perturbation is centred at  $-20^\circ$ . The perturbations are recovered at their expected positions: the recovered perturbation at a longitude of  $270^\circ$  in panels (a–e) corresponds to the big perturbation, the medium perturbation is recovered in panels (a–e) at a longitude of  $90^\circ$  and the small perturbation is recovered in panel (f) at a longitude of  $180^\circ$ .

The effect of the depth of the perturbation on the reconstructed phase shift is studied through panels (a) to (d). The nominal perturbations are centred at varying depths of 50 Mm (a), 40 Mm (b), 30 Mm (c), and 20 Mm (d), but share all the other parameters. Although we observe that the most intense part of the recovered perturbation moves to shallower layers from (a) to (d), as the nominal perturbation emerge, we can also notice that the deeper extent of the recovered perturbed area is very similar throughout panels (a) to (d) for both the big and medium perturbations. This behaviour is due to the geometrical configuration of the pupils: the shallower a perturbed region is located, the wider in the vertical direction a coherent phase-shift perturbation it can produce.

The comparison of panels (c) and (e), corresponding both to perturbations of the same size and location, centred at 30 Mm, but with a different value for the sound-speed decrease, being 5% (c) and 10% (d) respectively, allows a way to assess the effect of the intensity of the sound-speed perturbation on the seismic maps. The recovered perturbations in (e) show higher values of phase shift, but the physical extension and penetration of the perturbation is significantly the same for both cases.

Panels (e) and (f) show the recovered phase shift for the three different-sized perturbations in simulation S5, where the nominal horizontal extent of the perturbation is the only variate. The recovered phase shift of sound-speed perturbations that extend horizontally more extends not only into horizontally wider areas (longitudinally), but also into deeper layers.

Although we observe that shallower and horizontally more extensive sound-speed perturbations produce significant coherent seismic signal to deeper layers using helioseismic holography, all of the studied cases here kept their seismic effects well above the base of the convection zone.

Este documento incorpora firma electrónica, y es copia auténtica de un documento electrónico archivado por la ULL según la Ley 39/2015.  
Su autenticidad puede ser contrastada en la siguiente dirección <https://sede.ull.es/validacion/>

Identificador del documento: 963882

Código de verificación: QDmfX6JG

Firmado por: MANUEL DIAZ ALFARO  
UNIVERSIDAD DE LA LAGUNA

Fecha: 26/06/2017 15:24:15

FERNANDO JAVIER PEREZ HERNANDEZ  
UNIVERSIDAD DE LA LAGUNA

26/06/2017 15:25:57

ERNESTO PEREDA DE PABLO  
UNIVERSIDAD DE LA LAGUNA

28/06/2017 13:21:41

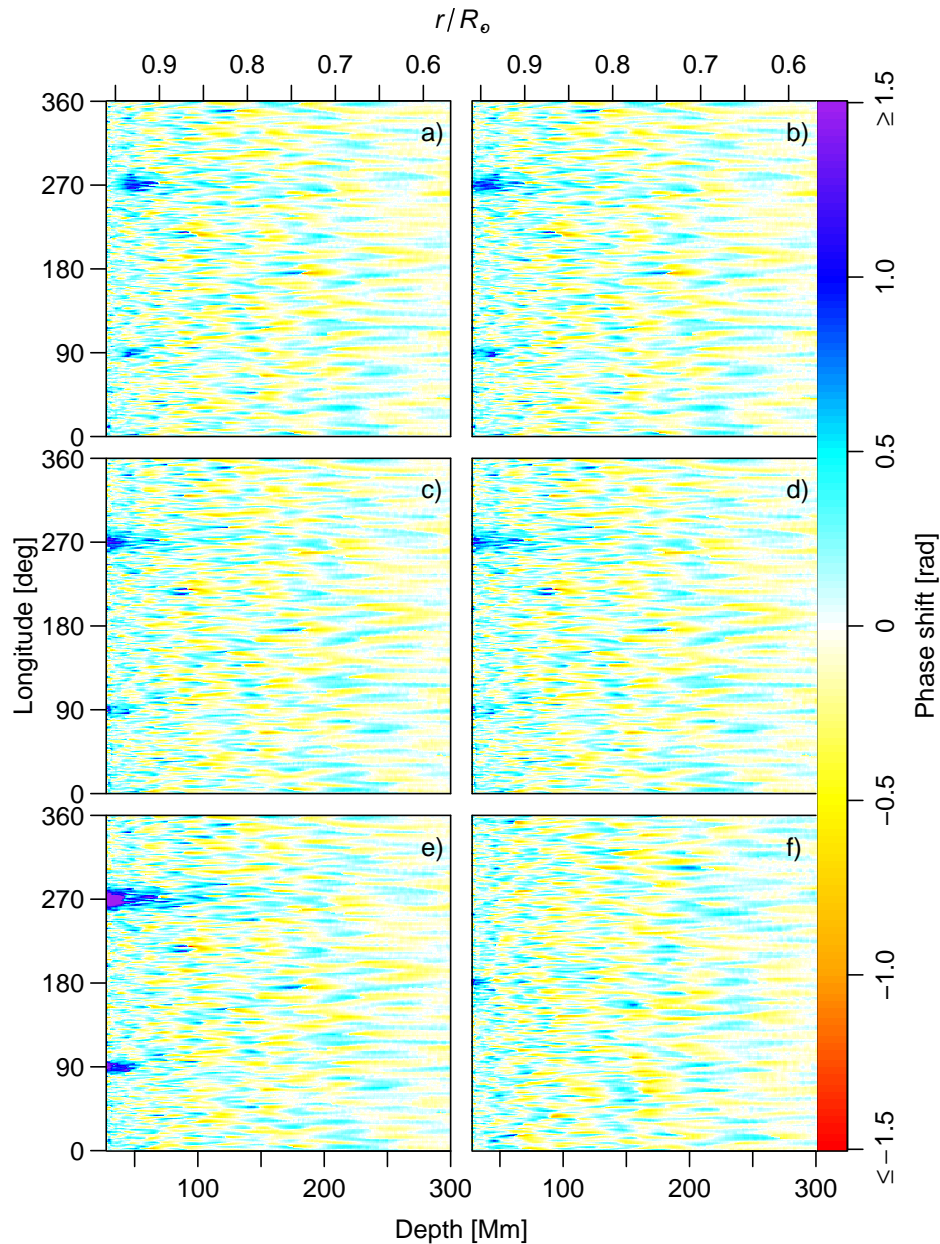


Figure 3.19: Longitude-depth maps of the reconstructed phase-shift at a fixed latitude of  $+20^\circ$ , at which the nominal big and medium perturbations are centred, for the S1 (a), S2 (b), S3 (c), S4 (d), and S5 (e) simulations, and at a fixed latitude of  $-20^\circ$ , at which the nominal small perturbations are centred, for the S5 (f) simulation. The colour scale indicates the phase shift in radians and it has been saturated for values  $\leq -1.5$  rad and  $\geq 1.5$  rad to enhance contrast.

Este documento incorpora firma electrónica, y es copia auténtica de un documento electrónico archivado por la ULL según la Ley 39/2015.  
Su autenticidad puede ser contrastada en la siguiente dirección <https://sede.ull.es/validacion/>

Identificador del documento: 963882

Código de verificación: QDmfX6JG

Firmado por: MANUEL DIAZ ALFARO  
UNIVERSIDAD DE LA LAGUNA

Fecha: 26/06/2017 15:24:15

FERNANDO JAVIER PEREZ HERNANDEZ  
UNIVERSIDAD DE LA LAGUNA

26/06/2017 15:25:57

ERNESTO PEREDA DE PABLO  
UNIVERSIDAD DE LA LAGUNA

28/06/2017 13:21:41

### 3.4 Discussion

We have proved the validity of phase-sensitive helioseismic holography to probe the base of the convection zone and tachocline and successfully recover perturbations in the sound-speed as low as 0.05% in an ideal case devoid of other activity at the solar surface or in the subphotosphere. Besides, the general profile of the perturbations is recovered accurately, with only a slight deepening and a small broadening at higher latitudes and deeper layers. This broadening may be caused by the relatively high realization noise in the simulations and the lower sensitivity of high-latitude pixels. The recovered seismic signals correlate linearly with the introduced perturbations in the sound speed. This result provides a tool for calibrating helioseismic signals from actual solar observation in terms of sound-speed variations.

Although the purpose of helioseismic holography is to provide a reconstruction of the acoustic field of the solar interior at a particular focus, non-coherent defocused contributions of waves travelling through the area where the considered focus lies add an out-of-focus term to the inferred seismic signal that may increase the signal-to-noise or even obscure the detection completely. Surface solar activity may be of great importance in the real Sun and have an effect here, specially near the maximum of solar activity. We have assessed this effect with the aid of simulations with isolated sound-speed perturbations at the photosphere. We have observed that the reconstructed signal of sound-speed perturbations restrained to a thin layer at the solar surface extends deeper than their perturbed precursors. Actually, the reconstructed signal extends deeper for perturbations with greater horizontal area. This is a direct consequence of the lateral-vantage geometry of the pupils. Although for the largest-considered perturbation the recovered perturbed signal reaches the vicinity of the base of the convection zone, for the smaller ones, it stay well above it. Typical sizes of active regions in the real Sun are within the range of the smallest-considered perturbation and should produce no significant seismic signal at the base of the convection zone.

Another source from out-of-focus contributions could consist of submerged emerging active regions, what has been assessed with different simulations with sound-speed perturbations between 20 Mm and 50 Mm of depth. As in the previous case, the reconstructed signal of sound-speed perturbations extends into deeper layers than those in which the nominal perturbation is present. However, for all the cases here, the deepest extension of the recovered perturbations stays well above the base of the convection zone and tachocline. Considering simulations with varying physical properties, we have studied the effect of these on the penetration of the recovered signal. First, the increase or decrease in the intensity of the perturbation as long as the shape and physical extension of the perturbed area remains the same produce no significant change in the extension in depth of the recovered signal. Second, for perturbations with the same intensity and size centred at varying depths, the shallower they are located, the deeper they extend with respect to their central position. And finally, perturbations of the same intensity and located at the same depth penetrate into deeper layers when they occupy larger areas horizontally.

Este documento incorpora firma electrónica, y es copia auténtica de un documento electrónico archivado por la ULL según la Ley 39/2015.  
Su autenticidad puede ser contrastada en la siguiente dirección <https://sede.ull.es/validacion/>

Identificador del documento: 963882

Código de verificación: QDmfX6JG

Firmado por: MANUEL DIAZ ALFARO  
UNIVERSIDAD DE LA LAGUNA

Fecha: 26/06/2017 15:24:15

FERNANDO JAVIER PEREZ HERNANDEZ  
UNIVERSIDAD DE LA LAGUNA

26/06/2017 15:25:57

ERNESTO PEREDA DE PABLO  
UNIVERSIDAD DE LA LAGUNA

28/06/2017 13:21:41

Although the contribution of subsurface activity has proved non significant, the detailed study thereof helps to confirm the result obtained from simulations with perturbations at the solar surface: that the unwanted penetration of parasite seismic signal is due to a geometrical limitation of the technique itself, because of the way the pupils are determined.

We have seen that individual active regions of typical sizes have no significant influence on seismic signal at deep layers. However, in the real Sun magnetic activity is present everywhere at the surface, especially at the solar maximum. Surface magnetic activity do not conform a large enough simply connected space to produce a significant reconstructed seismic signal visible as a simply connected perturbation, because quiescent regions between active regions would break the spatial coherence. However, it could be possible that, with abundant surface activity, the individual contributions of multiple separated active regions could coalesce to produce a significant overall contribution in the seismic signal at the base of the convection zone that could decrease the signal-to-noise ratio and blur the detection of actual perturbations present at the deep layers. This should be taken into consideration to proceed with the utmost care when interpreting the seismic results from actual solar observations.

We have used a reference unperturbed simulation for correcting the unwanted artefacts originating in the technique itself in the studied simulations. However, although we get a clean direct correction for the S1–S6 simulations in Section 3.3.3, differences introduced in the simulating code between the computation of the reference simulation, and the T1–T2 and P1–P3 simulations do not produce completely corrected results. A reference unperturbed simulation can be used to correct from technique artefacts, but we must proceed carefully because analogue discrepancies can be present there between the model used to compute the reference simulation and the acoustic medium of the Sun.

Este documento incorpora firma electrónica, y es copia auténtica de un documento electrónico archivado por la ULL según la Ley 39/2015.  
Su autenticidad puede ser contrastada en la siguiente dirección <https://sede.ull.es/validacion/>

Identificador del documento: 963882

Código de verificación: QDmfX6JG

Firmado por: MANUEL DIAZ ALFARO  
UNIVERSIDAD DE LA LAGUNA

Fecha: 26/06/2017 15:24:15

FERNANDO JAVIER PEREZ HERNANDEZ  
UNIVERSIDAD DE LA LAGUNA

26/06/2017 15:25:57

ERNESTO PEREDA DE PABLO  
UNIVERSIDAD DE LA LAGUNA

28/06/2017 13:21:41

# 4

## The Solar Interior through the solar cycle

In the previous chapter we have proved the feasibility of the application of helioseismic holography to recover sound-speed perturbations at the base of the convection zone with the aid of numerical simulations. In this chapter we apply the technique to regular observations taken by the *Global Oscillation Network Group* (GONG; Harvey *et al.*, 1996; Leibacher, 1999) between the years 1995 and 2015, covering more than one and a half cycles of solar activity, using the results from the simulated data in Chapter 3 as a calibration.

First, we analyse the variations in the inferred sound-speed profile at the base of the convection zone with respect to a solar model at the two solar minima present in the GONG dataspan, recovering sound-speed values consistent with previous results. Then, we study the relative variation of the reconstructed sound speed at the base of the convection zone along the solar cycle. A preliminary study of part of the observational data analysed in this thesis has already been published (Díaz Alfaro *et al.*, 2016).

### 4.1 Observational Data

The observational data used in this thesis are formed by velocity images or dopplergrams taken by GONG. GONG is an international network of six instruments located around the Earth at the Big Bear Solar Observatory in California, the High Altitude Observatory at Mauna Loa in Hawaii, the Learmonth Solar Observatory in Western Australia, the Udaipur Solar Observatory in India, the *Observatorio del Teide* in Tenerife, and the Cerro Tolo Inter-American Observatory in Chile. The network is managed by the US National Solar Observatory, which is operated by the Association of Universities for Research in Astronomy, under a cooperative agreement with the US National Science Foundation. The instruments are Fourier tachometers based on Michelson interferometry observing at the photospheric line Ni  $\lambda 6768 \text{ \AA}$ . They provide nearly continuous line-of-sight dopplergrams with a nominal cadence of 60 s.

Este documento incorpora firma electrónica, y es copia auténtica de un documento electrónico archivado por la ULL según la Ley 39/2015.  
Su autenticidad puede ser contrastada en la siguiente dirección <https://sede.ull.es/validacion/>

Identificador del documento: 963882

Código de verificación: QDmfX6JG

Firmado por: MANUEL DIAZ ALFARO  
UNIVERSIDAD DE LA LAGUNA

Fecha: 26/06/2017 15:24:15

FERNANDO JAVIER PEREZ HERNANDEZ  
UNIVERSIDAD DE LA LAGUNA

26/06/2017 15:25:57

ERNESTO PEREDA DE PABLO  
UNIVERSIDAD DE LA LAGUNA

28/06/2017 13:21:41

The system became operational in 1995 with  $256 \times 256$  pixel detectors, with a spatial resolution of  $8 \times 10$  arcsec per rectangular pixel. In 2001 the detectors were replaced by others with  $1024 \times 1024$  square pixels, each with a spatial resolution of  $2 \times 2$  arcsec. The two epochs corresponding to the original and upgraded configurations are referred to as GONG Classic and GONG+, respectively. Beyond the increased spatial resolution, the GONG+ update came with an optimised observing strategy to produce additional data products such as merged dopplergrams, formed by the combination of observed velocity maps acquired concurrently at multiple sites into a single network velocity map. In order to do so, single-site images are preprocessed to remove the rotational velocity of the Sun and the motion of the Earth, and to correct for the ellipticity of the solar disk and the residual misalignment of the solar North. This strategy was ported in 2015 to GONG-Classic data. Then, GONG-Classic single-site dopplergrams were combined to produce merged network dopplergrams in the 1995–2001 period (Hughes *et al.*, 2016). The main differences between GONG-Classic and GONG+ data regard spatial resolution and precision in the angular alignment, which is higher for GONG+ merged dopplergrams. The detailed reducing process to produce merged network dopplergrams from the observed data at single sites is thoroughly described as part of the global and local helioseismology pipelines, available at the GONG website on the Internet.<sup>1</sup> The resulting merged dopplergrams are stored in  $251 \times 251$  pixel (GONG Classic) and  $839 \times 839$  pixel (GONG+) FITS files with a cadence of 1 min. An example of a merged dopplergram from each GONG epoch is shown in Figure 4.1: a merged dopplergram from GONG Classic (a), corresponding to 1 May 2000 at 12:00 UT, and a merged dopplergram from GONG+ (b), corresponding to 1 January 2010 at 12:00 UT. The higher resolution of GONG+ dopplergrams is clearly noticeable there.

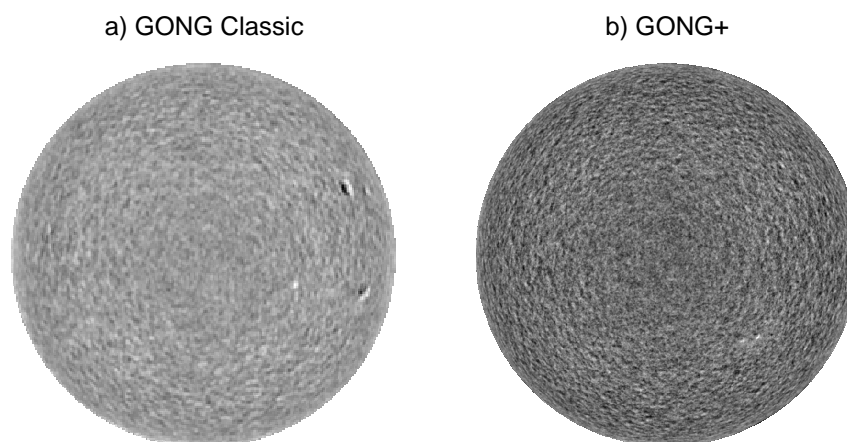


Figure 4.1: Examples of GONG merged dopplergrams from GONG Classic (a), corresponding to 1 May 2000 at 12:00 UT, and from GONG+ (b), corresponding to 1 January 2010 at 12:00 UT.

<sup>1</sup>[http://gong.nso.edu/data/DMAC\\_documentation/](http://gong.nso.edu/data/DMAC_documentation/)

Este documento incorpora firma electrónica, y es copia auténtica de un documento electrónico archivado por la ULL según la Ley 39/2015.  
Su autenticidad puede ser contrastada en la siguiente dirección <https://sede.ull.es/validacion/>

Identificador del documento: 963882

Código de verificación: QDmfX6JG

Firmado por: MANUEL DIAZ ALFARO  
UNIVERSIDAD DE LA LAGUNA

Fecha: 26/06/2017 15:24:15

FERNANDO JAVIER PEREZ HERNANDEZ  
UNIVERSIDAD DE LA LAGUNA

26/06/2017 15:25:57

ERNESTO PEREDA DE PABLO  
UNIVERSIDAD DE LA LAGUNA

28/06/2017 13:21:41

In this work we utilise available merged dopplergrams from GONG Classic and GONG+. The used GONG-Classic merged dopplergrams extend between 27 May 1995 and 21 May 2001. During this period there are some gaps in the available data: *e.g.* the data of 17 December 1996 is unavailable due to technical reasons, the data between 30 May 1999 and 1 August 1999 is missing crucial calibration information necessary for the merging process, and on 21 April 2001 there were no GONG observations. We also use GONG+ merged dopplergrams between 11 August 2001 and 31 July 2015, with no interruptions or gaps.

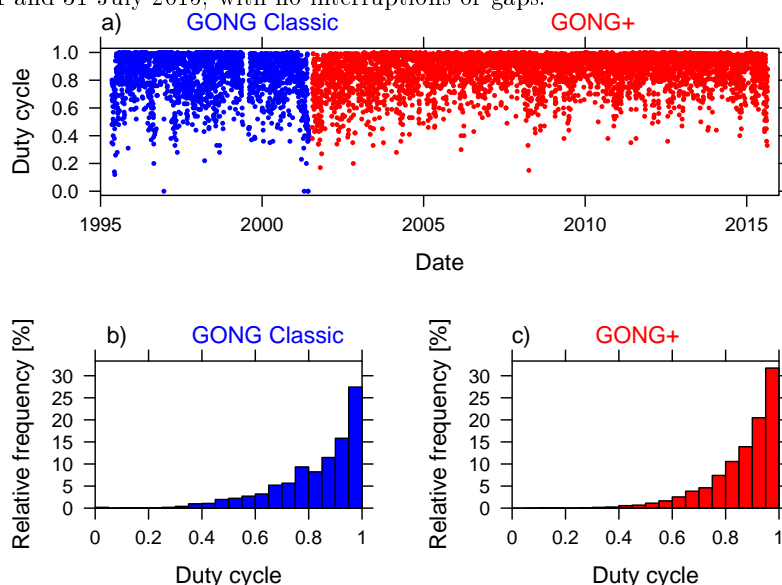


Figure 4.2: a) Daily duty cycle values for GONG Classic (blue) and for GONG+ (red) merged dopplergrams. b), c) Corresponding relative frequency of duty cycle values in intervals of 0.05 for GONG Classic (b) and GONG+ (c). Duty cycle values represent the fraction of each UT day for which one-minute cadence network velocity maps are available.

The fraction of time during which quality GONG data are available varies due to weather and other kind of operational disruptions. Daily duty cycle for the merged dopplergrams represents the fraction of each UT day for which one-minute cadence network velocity maps are available. Figure 4.2(a) shows GONG daily duty cycle values for available GONG data. Histograms of the relative frequency of daily duty cycle values in intervals of 0.05 are also shown separately for GONG Classic (b) and GONG+ (c). It can be seen that network stations provide data with high continuity. Besides higher resolution in GONG+ data, there has also been an improvement regarding data coverage from GONG Classic, where the mean duty cycle was 0.83, to GONG+<sup>2</sup>, where the mean duty cycle has reached 0.87. The fraction of days with duty cycle values of at least 0.8 has also increased from GONG Classic ( $\approx 65\%$ ) to GONG+<sup>2</sup> ( $\approx 79\%$ ).

<sup>2</sup>GONG+ duty cycle measured up to 25 August 2015.

Este documento incorpora firma electrónica, y es copia auténtica de un documento electrónico archivado por la ULL según la Ley 39/2015.  
Su autenticidad puede ser contrastada en la siguiente dirección <https://sede.ull.es/validacion/>

Identificador del documento: 963882

Código de verificación: QDmfX6JG

Firmado por: MANUEL DIAZ ALFARO  
UNIVERSIDAD DE LA LAGUNA

Fecha: 26/06/2017 15:24:15

FERNANDO JAVIER PEREZ HERNANDEZ  
UNIVERSIDAD DE LA LAGUNA

26/06/2017 15:25:57

ERNESTO PEREDA DE PABLO  
UNIVERSIDAD DE LA LAGUNA

28/06/2017 13:21:41

BR	Begin	End									
2210	1995-05-27	1995-06-22	2244	1997-11-30	1997-12-26	2278	2000-06-05	2000-07-01	2313	2003-01-06	2003-02-01
2211	1995-06-23	1995-07-19	2245	1997-12-27	1998-01-22	2279	2000-07-02	2000-07-28	2314	2003-02-02	2003-02-28
2212	1995-07-20	1995-08-15	2246	1998-01-23	1998-02-18	2280	2000-07-29	2000-08-24	2315	2003-03-01	2003-03-27
2213	1995-08-16	1995-09-11	2247	1998-02-19	1998-03-17	2281	2000-08-25	2000-09-20	2316	2003-03-28	2003-04-23
2214	1995-09-12	1995-10-08	2248	1998-03-18	1998-04-13	2282	2000-09-21	2000-10-17	2317	2003-04-24	2003-05-20
2215	1995-10-09	1995-11-04	2249	1998-04-14	1998-05-10	2283	2000-10-18	2000-11-13	2318	2003-05-21	2003-06-16
2216	1995-11-05	1995-12-01	2250	1998-05-11	1998-06-06	2284	2000-11-14	2000-12-10	2319	2003-06-17	2003-07-13
2217	1995-12-02	1995-12-28	2251	1998-06-07	1998-07-03	2285	2000-12-11	2001-01-06	2320	2003-07-14	2003-08-09
2218	1995-12-29	1996-01-24	2252	1998-07-04	1998-07-30	2286	2001-01-07	2001-02-02	2321	2003-08-10	2003-09-05
2219	1996-01-25	1996-02-20	2253	1998-07-31	1998-08-26	2287	2001-02-03	2001-03-01	2322	2003-09-06	2003-10-02
2220	1996-02-21	1996-03-18	2254	1998-08-27	1998-09-22	2288	2001-03-02	2001-03-28	2323	2003-10-03	2003-10-29
2221	1996-03-19	1996-04-14	2255	1998-09-23	1998-10-19	2289	2001-03-29	2001-04-24	2324	2003-10-30	2003-11-25
2222	1996-04-15	1996-05-11	2256	1998-10-20	1998-11-15	2290	2001-04-25	2001-05-21	2325	2003-11-26	2003-12-22
2223	1996-05-12	1996-06-07	2257	1998-11-16	1998-12-12				2326	2003-12-23	2004-01-18
2224	1996-06-08	1996-07-04	2258	1998-12-13	1999-01-08				2327	2004-01-19	2004-02-14
2225	1996-07-05	1996-07-31	2259	1999-01-09	1999-02-04	2294	2001-08-11	2001-09-06	2328	2004-02-15	2004-03-12
2226	1996-08-01	1996-08-27	2260	1999-02-05	1999-03-03	2295	2001-09-07	2001-10-03	2329	2004-03-13	2004-04-08
2227	1996-08-28	1996-09-23	2261	1999-03-04	1999-03-30	2296	2001-10-04	2001-10-30	2330	2004-04-09	2004-05-05
2228	1996-09-24	1996-10-20	2262	1999-03-31	1999-04-26	2297	2001-10-31	2001-11-26	2331	2004-05-06	2004-06-01
2229	1996-10-21	1996-11-16	2263	1999-04-27	1999-05-23	2298	2001-11-27	2001-12-23	2332	2004-06-02	2004-06-28
2230	1996-11-17	1996-12-13				2299	2001-12-24	2002-01-19	2333	2004-06-29	2004-07-25
2231	1996-12-14	1997-01-09				2300	2002-01-20	2002-02-15	2334	2004-07-26	2004-08-21
2232	1997-01-10	1997-02-05				2301	2002-02-16	2002-03-14	2335	2004-08-22	2004-09-17
2233	1997-02-06	1997-03-04	2267	1999-08-13	1999-09-08	2302	2002-03-15	2002-04-10	2336	2004-09-18	2004-10-14
2234	1997-03-05	1997-03-31	2268	1999-09-09	1999-10-05	2303	2002-04-11	2002-05-07	2313	2003-01-06	2003-02-01
2235	1997-04-01	1997-04-27	2269	1999-10-06	1999-11-01	2304	2002-05-08	2002-06-03	2314	2003-02-02	2003-02-28
2236	1997-04-28	1997-05-24	2270	1999-11-02	1999-11-28	2305	2002-06-04	2002-06-30	2315	2003-03-01	2003-03-27
2237	1997-05-25	1997-06-20	2271	1999-11-29	1999-12-25	2306	2002-07-01	2002-07-27	2316	2003-03-28	2003-04-23
2238	1997-06-21	1997-07-17	2272	1999-12-26	2000-01-21	2307	2002-07-28	2002-08-23	2317	2003-04-24	2003-05-20
2239	1997-07-18	1997-08-13	2273	2000-01-22	2000-02-17	2308	2002-08-24	2002-09-19	2318	2003-05-21	2003-06-16
2240	1997-08-14	1997-09-09	2274	2000-02-18	2000-03-15	2309	2002-09-20	2002-10-16	2319	2003-06-17	2003-07-13
2241	1997-09-10	1997-10-06	2275	2000-03-16	2000-04-11	2310	2002-10-17	2002-11-12	2320	2003-07-14	2003-08-09
2242	1997-10-07	1997-11-02	2276	2000-04-12	2000-05-08	2311	2002-11-13	2002-12-09	2321	2003-08-10	2003-09-05
2243	1997-11-03	1997-11-29	2277	2000-05-09	2000-06-04	2312	2002-12-10	2003-01-05	2322	2003-09-06	2003-10-02

Este documento incorpora firma electrónica, y es copia auténtica de un documento electrónico archivado por la ULL según la Ley 39/2015.  
Su autenticidad puede ser contrastada en la siguiente dirección <https://sede.ull.es/validacion/>

Identificador del documento: 963882

Código de verificación: QDMfX6JG

Firmado por: MANUEL DIAZ ALFARO  
UNIVERSIDAD DE LA LAGUNA

Fecha: 26/06/2017 15:24:15

FERNANDO JAVIER PEREZ HERNANDEZ  
UNIVERSIDAD DE LA LAGUNA

26/06/2017 15:25:57

ERNESTO PEREDA DE PABLO  
UNIVERSIDAD DE LA LAGUNA

28/06/2017 13:21:41

BR	Begin	End									
2347	2003-07-12	2005-08-07	2381	2008-01-16	2008-02-11	2415	2010-07-22	2010-08-17	2449	2013-01-25	2013-02-20
2348	2003-08-08	2005-09-03	2382	2008-02-12	2008-03-09	2416	2010-08-18	2010-09-13	2450	2013-02-21	2013-03-19
2349	2003-09-04	2005-09-30	2383	2008-03-10	2008-04-05	2417	2010-09-14	2010-10-10	2451	2013-03-20	2013-04-15
2350	2003-10-01	2005-10-27	2384	2008-04-06	2008-05-02	2418	2010-10-11	2010-11-06	2452	2013-04-16	2013-05-12
2351	2003-10-28	2005-11-23	2385	2008-05-03	2008-05-29	2419	2010-11-07	2010-12-03	2453	2013-05-13	2013-06-08
2352	2003-11-24	2005-12-20	2386	2008-05-30	2008-06-25	2420	2010-12-04	2010-12-30	2454	2013-06-09	2013-07-05
2353	2003-12-21	2006-01-16	2387	2008-06-26	2008-07-22	2421	2010-12-31	2011-01-26	2455	2013-07-06	2013-08-01
2354	2006-01-17	2006-02-12	2388	2008-07-23	2008-08-18	2422	2011-01-27	2011-02-22	2456	2013-08-02	2013-08-28
2355	2006-02-13	2006-03-11	2389	2008-08-19	2008-09-14	2423	2011-02-23	2011-03-21	2457	2013-08-29	2013-09-24
2356	2006-03-12	2006-04-07	2390	2008-09-15	2008-10-11	2424	2011-03-22	2011-04-17	2458	2013-09-25	2013-10-21
2357	2006-04-08	2006-05-04	2391	2008-10-12	2008-11-07	2425	2011-04-18	2011-05-14	2459	2013-10-22	2013-11-17
2358	2006-05-05	2006-05-31	2392	2008-11-08	2008-12-04	2426	2011-05-15	2011-06-10	2460	2013-11-18	2013-12-14
2359	2006-06-01	2006-06-27	2393	2008-12-05	2008-12-31	2427	2011-06-11	2011-07-07	2461	2013-12-15	2014-01-10
2360	2006-06-28	2006-07-24	2394	2009-01-01	2009-01-27	2428	2011-07-08	2011-08-03	2462	2014-01-11	2014-02-06
2361	2006-07-25	2006-08-20	2395	2009-01-28	2009-02-23	2429	2011-08-04	2011-08-30	2463	2014-02-07	2014-03-05
2362	2006-08-21	2006-09-16	2396	2009-02-24	2009-03-22	2430	2011-08-31	2011-09-26	2464	2014-03-06	2014-04-01
2363	2006-09-17	2006-10-13	2397	2009-03-23	2009-04-18	2431	2011-09-27	2011-10-23	2465	2014-04-02	2014-04-28
2364	2006-10-14	2006-11-09	2398	2009-04-19	2009-05-15	2432	2011-10-24	2011-11-19	2466	2014-04-29	2014-05-25
2365	2006-11-10	2006-12-06	2399	2009-05-16	2009-06-11	2433	2011-11-20	2011-12-16	2467	2014-05-26	2014-06-21
2366	2006-12-07	2007-01-02	2400	2009-06-12	2009-07-08	2434	2011-12-17	2012-01-12	2468	2014-06-22	2014-07-18
2367	2007-01-03	2007-01-29	2401	2009-07-09	2009-08-04	2435	2012-01-13	2012-02-08	2469	2014-07-19	2014-08-14
2368	2007-01-30	2007-02-25	2402	2009-08-05	2009-08-31	2436	2012-02-09	2012-03-06	2470	2014-08-15	2014-09-10
2369	2007-02-26	2007-03-24	2403	2009-09-01	2009-09-27	2437	2012-03-07	2012-04-02	2471	2014-09-11	2014-10-07
2370	2007-03-25	2007-04-20	2404	2009-09-28	2009-10-24	2438	2012-04-03	2012-04-29	2472	2014-10-08	2014-11-03
2371	2007-04-21	2007-05-17	2405	2009-10-25	2009-11-20	2439	2012-04-30	2012-05-26	2473	2014-11-04	2014-11-30
2372	2007-05-18	2007-06-13	2406	2009-11-21	2009-12-17	2440	2012-05-27	2012-06-22	2474	2014-12-01	2014-12-27
2373	2007-06-14	2007-07-10	2407	2009-12-18	2010-01-13	2441	2012-06-23	2012-07-19	2475	2014-12-28	2015-01-23
2374	2007-07-11	2007-08-06	2408	2010-01-14	2010-02-09	2442	2012-07-20	2012-08-15	2476	2015-01-24	2015-02-19
2375	2007-08-07	2007-09-02	2409	2010-02-10	2010-03-08	2443	2012-08-16	2012-09-11	2477	2015-02-20	2015-03-18
2376	2007-09-03	2007-09-29	2410	2010-03-09	2010-04-04	2444	2012-09-12	2012-10-08	2478	2015-03-19	2015-04-14
2377	2007-09-30	2007-10-26	2411	2010-04-05	2010-05-01	2445	2012-10-09	2012-11-04	2479	2015-04-15	2015-05-11
2378	2007-10-27	2007-11-22	2412	2010-05-02	2010-05-28	2446	2012-11-05	2012-12-01	2480	2015-05-12	2015-06-07
2379	2007-11-23	2007-12-19	2413	2010-05-29	2010-06-24	2447	2012-12-02	2012-12-28	2481	2015-06-08	2015-07-04
2380	2007-12-20	2008-01-15	2414	2010-06-25	2010-07-21	2448	2012-12-29	2013-01-24	2482	2015-07-05	2015-07-31

Table 4.1: Table showing the beginning and ending dates for each of the Bartels's rotations, accounting for the GONG data used in this work. For the two Bartels's rotations outmarked in blue, i.e. BR2231 and BR2289, two dates do not have available merged data, 17 December 1996 and 21 April 2001, respectively. The two gaps in the table, BR2264–BR2266 and BR2291–BR2293, account for a gap in the merged data (30 May 1999–1 August 1999) and for the transition period from GONG Classic to GONG+, respectively. The shading separates alternating years.

Este documento incorpora firma electrónica, y es copia auténtica de un documento electrónico archivado por la ULL según la Ley 39/2015.  
Su autenticidad puede ser contrastada en la siguiente dirección <https://sede.ull.es/validacion/>

Identificador del documento: 963882

Código de verificación: QDmfX6JG

Firmado por: MANUEL DIAZ ALFARO  
UNIVERSIDAD DE LA LAGUNA

Fecha: 26/06/2017 15:24:15

FERNANDO JAVIER PEREZ HERNANDEZ  
UNIVERSIDAD DE LA LAGUNA

26/06/2017 15:25:57

ERNESTO PEREDA DE PABLO  
UNIVERSIDAD DE LA LAGUNA

28/06/2017 13:21:41

## 4.2 Technique

The input for the general procedure described in Section 2.5 is formed by  $251 \times 251$  pixel GONG-Classic and  $839 \times 839$  pixel GONG+ merged network dopplergrams. Each UT day, formed by 1440 dopplergrams, is processed separately to produce  $200 \times 200$  pixel seismic phase-shift maps at the surface and at depths in the range of 50–300 Mm with a step of 1 Mm. As done in previous cases in Chapter 3, the subjacent vantage is used to determine the pupils for the reconstruction of the seismic field at the surface, while the lateral vantage with external raypaths opening  $\pm 45^\circ$  from the horizontal plane is used to determine the pupils for the seismic maps below the solar surface. The empirical phase-shift correction (Section 2.3.1) is applied to Green's functions in order to correct from the effects present in the uppermost layers of the Sun, and not considered in the mathematical formalism of Green's functions, such as asymptotic, non-adiabatic and non-spheric effects. Due to the high volume of computations required to produce the seismic phase-shift maps at his stage, we have made use of the HTCondor distributed computing software together with the LaPalma<sup>3</sup> and Teide-HPC<sup>4</sup> supercomputers.

Seismic phase-shift maps are projected onto a longitude-latitude grid, and then combined and averaged in 267 groups of 27 consecutive days, each covering the whole solar perimeter and accounting for approximately one solar rotation. These groups of 27 days of data are processed so that they correspond to Bartels's rotations numbers. The Bartels's rotation number, introduced by Julius Bartels, with day one of Bartels's rotation 1 (BR1) assigned arbitrarily to 8 February 1832, constitutes a serial number for counting the rotations of the Sun. Table 4.1 contains the full list of Bartels's rotations used in this work with their corresponding starting and ending dates. The 267 considered Bartels's rotations start at 27 May 1995 for BR2210 and end at 31 July 2015 for BR2482. During this time interval Bartels's rotations BR2264–BR2266 and BR2291–BR2293 are missing due to the unavailability of merged velocity data for the corresponding time interval. Besides, for each of Bartels's rotations BR2231 and BR2289 a day of merged velocity data was unavailable. As the longitude-latitude seismic maps for the other 26 days cover reasonably well the whole perimeter of the Sun, the combined maps for those two Bartels's rotations have been computed with only 26 days of data.

Finally, the combined phase-shift maps have been collapsed along the longitudinal axis to produce seismic maps depending on latitude and depth for each of the considered Bartels's rotations, which are analysed in upcoming Section 4.3.

<sup>3</sup>The LaPalma supercomputer, located at the *Centro de Astrofísica en La Palma* of the *Instituto de Astrofísica de Canarias*, in San Antonio de Breña Baja (La Palma), is one of the eight nodes of the Spanish Supercomputing Network (*Red Española de Supercomputación*). It has a peak capacity of 9.4 TFLOPS, with 256 CPUs totalling 1024 cores with 2GB of RAM per core.

<sup>4</sup>Teide High Performance Computing is a supercomputer located at the *Instituto Tecnológico y de Energías Renovables* (ITER, SA) in Granadilla de Abona (Tenerife). It has a theoretical peak performance of 340.8 TFLOPS, being composed of a total of 17,800 computing cores and 36 TB of memory. It is currently the second most powerful supercomputer in Spain. URL: <http://teidehpc.iter.es>

Este documento incorpora firma electrónica, y es copia auténtica de un documento electrónico archivado por la ULL según la Ley 39/2015.  
Su autenticidad puede ser contrastada en la siguiente dirección <https://sede.ull.es/validacion/>

Identificador del documento: 963882

Código de verificación: QDmfX6JG

Firmado por: MANUEL DIAZ ALFARO  
UNIVERSIDAD DE LA LAGUNA

Fecha: 26/06/2017 15:24:15

FERNANDO JAVIER PEREZ HERNANDEZ  
UNIVERSIDAD DE LA LAGUNA

26/06/2017 15:25:57

ERNESTO PEREDA DE PABLO  
UNIVERSIDAD DE LA LAGUNA

28/06/2017 13:21:41

### 4.3 Results

#### 4.3.1 Inferred sound-speed at the base of the convection zone at solar minima

The international sunspot number, introduced in Section 1.2, provides a harmonized value accounting for long-term solar activity in terms of counting sunspots and groups of sunspots. Figure 4.3 shows in blue the monthly mean international sunspot number for the timespan of GONG observations. The current standard for the determination of the international sunspot number adopted on 1 July 2015—version 2.0—is used here and throughout this thesis. A 13-month smoothed monthly sunspot number is superimposed in red. We have used it to select two time intervals corresponding to 13 continuous Bartels's rotations, each accounting for approximately one year, at the two solar minima of solar activity having occurred during the lifespan of GONG. Here and in Section 4.3.2 we have made selections spanning approximately one year to minimize a one-year-period effect present in the data and likely linked to the orbital movement of the Earth around the Sun. During the minimum between Solar Cycle 22 and Solar Cycle 23, we select Bartels's rotations BR2219–BR2231, extending from 25

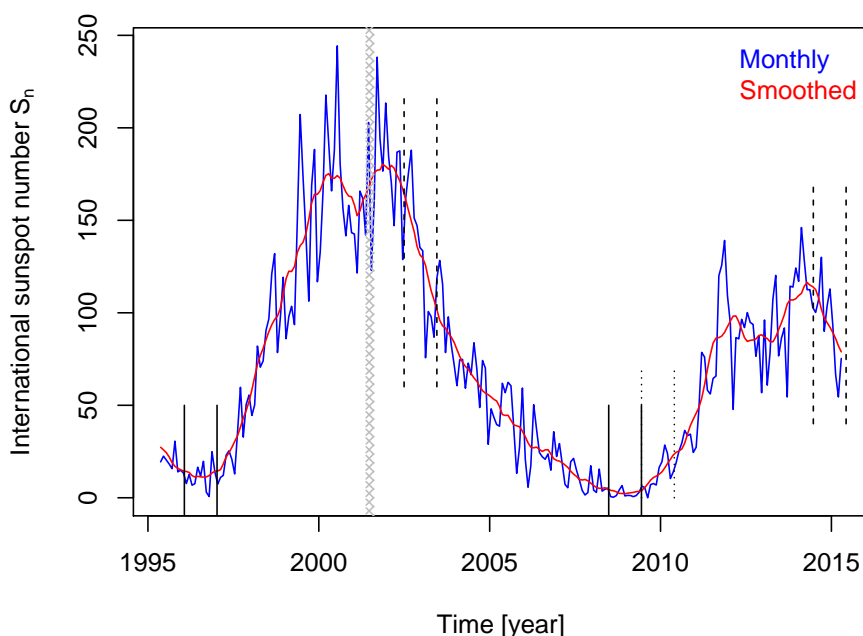


Figure 4.3: Monthly mean international sunspot number (blue) and 13-month smoothed monthly sunspot number (red) for the timespan of GONG observations from SILSO data, Royal Observatory of Belgium, Brussels. The vertical solid bars signal the starting and ending dates of the intervals at the solar minima analysed in Section 4.3.1, *i.e.* BR2219–BR2231 and BR2387–BR2399. The dashed and dotted bars signalled the starting and ending dates of the periods introduced in Section 4.3.2 at high activity and the alternate one at low activity respectively. The crossed area marks the gap between the GONG-Classic and GONG+ configurations.

Este documento incorpora firma electrónica, y es copia auténtica de un documento electrónico archivado por la ULL según la Ley 39/2015.  
Su autenticidad puede ser contrastada en la siguiente dirección <https://sede.ull.es/validacion/>

Identificador del documento: 963882

Código de verificación: QDmfX6JG

Firmado por: MANUEL DIAZ ALFARO  
UNIVERSIDAD DE LA LAGUNA

Fecha: 26/06/2017 15:24:15

FERNANDO JAVIER PEREZ HERNANDEZ  
UNIVERSIDAD DE LA LAGUNA

26/06/2017 15:25:57

ERNESTO PEREDA DE PABLO  
UNIVERSIDAD DE LA LAGUNA

28/06/2017 13:21:41

January 1996 to 9 January 1997, using GONG-Classic data processed following the strategy summarised in Section 4.1 (Hughes *et al.*, 2016). The other interval extends from 26 June 2008 to 11 June 2009, during the minimum between Solar Cycle 23 and Solar Cycle 24, comprising Bartels's rotations BR2387–BR2399, and using GONG+ data. Results for the latter interval have already been published in Díaz Alfaro *et al.* (2016). The starting and ending dates for the two periods are signalled with vertical solid bars in Figure 4.3.

For each of the  $2 \times 13$  Bartels's rotations at the solar minima, we have averaged the seismic phase shift between  $45^\circ$  N and  $45^\circ$  S. Then, for each of the two 13-Bartels-rotation intervals the phase-shift averages were combined separately by further averaging in order to increase the signal-to-noise ratio. Standard deviations of these latter means have been computed as a measure of the uncertainty. It should be noted though that this is an overestimation of the error measurement. The resulting variation with depth of the combined phase shift averaged between  $45^\circ$  N and  $45^\circ$  S is shown in Figure 4.4 for the BR2219–BR2231 minimum in a solid red curve and for the BR2387–BR2399 minimum in a solid blue curve. The uncertainty estimations are shown superimposed as dots in the same colour of the corresponding minimum.

We have described in Chapter 3 the presence of a systematic offset between some of the perturbed data and the reference one, which we have interpreted as due to changes in the simulating code affecting the overall internal properties of the numerically simulated Sun. We can observe here a similar offset between the different phase-shift profiles derived from solar observations. As in the numerically simulated cases before, the origin of this overall offset seems to be found at global changes in the acoustic properties of the real Sun. However, in this particular case it could be due to the different sensitivity of GONG+ and GONG Classic. We discuss further this behaviour in the upcoming sections.

The peak-like artefact described in Chapter 3 and present in the phase-shift results at  $\approx 200$  Mm is produced by changes in the model used for the computation of Green's functions at layers where its acoustic behaviour transitions from the radiative interior into the convective envelope. As expected, this artefact is also present in the phase-shift latitudinal averages for the observational data. We make use of it in order to measure the offset between the averaged numerically-simulated reference phase shift presented in Section 3 and each of the averaged phase shifts at solar minima, and we offset the reference calibration for each minimum accordingly in order to remove not only the unwanted technique-produced effects from the seismic signal of the observational data but also the overall effects related to the overall variation. The offset reference phase shift calibrated for the BR2219–BR2231 minimum is also plotted in Figure 4.4 in black dashes.

On the one hand, the presence of bands is much more reduced in the actual solar seismic maps as it was in the phase-shift maps of the simulations. On the other hand, some small features, such as small peaks, are still present at certain depths at the observational maps as they were in the simulated data. These unwanted artefacts may originate at layers where modes start or stop to be included in the computation

Este documento incorpora firma electrónica, y es copia auténtica de un documento electrónico archivado por la ULL según la Ley 39/2015.  
Su autenticidad puede ser contrastada en la siguiente dirección <https://sede.ull.es/validacion/>

Identificador del documento: 963882

Código de verificación: QDmfX6JG

Firmado por: MANUEL DIAZ ALFARO  
UNIVERSIDAD DE LA LAGUNA

Fecha: 26/06/2017 15:24:15

FERNANDO JAVIER PEREZ HERNANDEZ  
UNIVERSIDAD DE LA LAGUNA

26/06/2017 15:25:57

ERNESTO PEREDA DE PABLO  
UNIVERSIDAD DE LA LAGUNA

28/06/2017 13:21:41

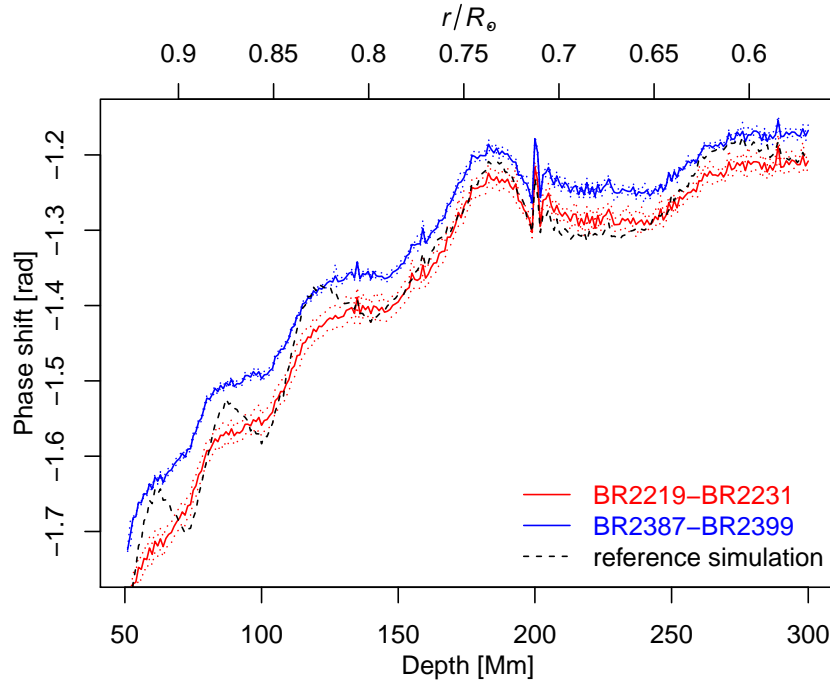


Figure 4.4: Variation with respect to depth of the mean phase shift for the GONG's 27-day Bartels rotations from BR2219 to BR2231 (solid red), and from BR2387 to BR2399 (solid blue), latitudinally-averaged between  $45^\circ$  N and  $45^\circ$  S. BR2219–BR2231 extend from 25 January 1996 to 9 January 1997, at the minimum between Solar Cycle 22 and Solar Cycle 23, and BR2387–BR2399 extend from 26 June 2008 to 11 June 2009, at the minimum between Solar Cycle 23 and Solar Cycle 24. Standard deviations are shown in a dotted curve in the same colour as the corresponding mean value. The mean phase shift within the same latitude interval of the offset simulated reference dataset, calibrated for use with BR2219–BR2231, is shown in a black dashed curve.

of Green's functions due to the different reflection boundaries of different individual modes. Besides, they disappear in the maps of the relative phase shift between the observational and the reference data, which further supports the premise that they are technique-related artefacts, correctable with *i.e.* a reference simulation.

With the aid of the offset reference phase-shift maps calibrated specifically for each of the two datasets at solar minima considered in the observational data, we calibrate the phase-shift maps of them with respect to a standard solar model, namely model S (Christensen-Dalsgaard *et al.*, 1996). The inferred relation between phase shift and sound-speed variation, obtained from simulated data in Section 3.3.1 and expressed as Equation (3.5) is applied to the two sets of data after the previous calibration to express these seismic maps in terms of variations of the sound speed. Figure 4.5 shows the inferred sound-speed variation latitudinally averaged between  $45^\circ$  N and  $45^\circ$  S for BR2219–BR2231 (red) and for BR2397–BR2399 (blue). Both profiles are very similar and show a peak at about  $0.68 R_\odot$ , which would indicate an underestimation of the sound speed at this position in model S in the range of  $\delta c^2/c^2 \approx (3-4) \cdot 10^{-3}$ .

Este documento incorpora firma electrónica, y es copia auténtica de un documento electrónico archivado por la ULL según la Ley 39/2015.  
Su autenticidad puede ser contrastada en la siguiente dirección <https://sede.ull.es/validacion/>

Identificador del documento: 963882

Código de verificación: QDmfX6JG

Firmado por: MANUEL DIAZ ALFARO  
UNIVERSIDAD DE LA LAGUNA

Fecha: 26/06/2017 15:24:15

FERNANDO JAVIER PEREZ HERNANDEZ  
UNIVERSIDAD DE LA LAGUNA

26/06/2017 15:25:57

ERNESTO PEREDA DE PABLO  
UNIVERSIDAD DE LA LAGUNA

28/06/2017 13:21:41

The inferred sound-speed profile also shows a valley located at  $\approx 0.61R_{\odot}$  and some residuals of the banding oscillation seem to be still present at the upper layers. The shape of the profile of the sound speed recovered with seismic holography is generally consistent with previous results obtained using different techniques (Gough *et al.*, 1996; Kosovichev *et al.*, 1997; Zhao *et al.*, 2009). However, the magnitudes of the distinctive features, even though of the same order, do not match previous results so accurately. This behaviour seems to indicate that the technique used in this thesis would require finer calibration.

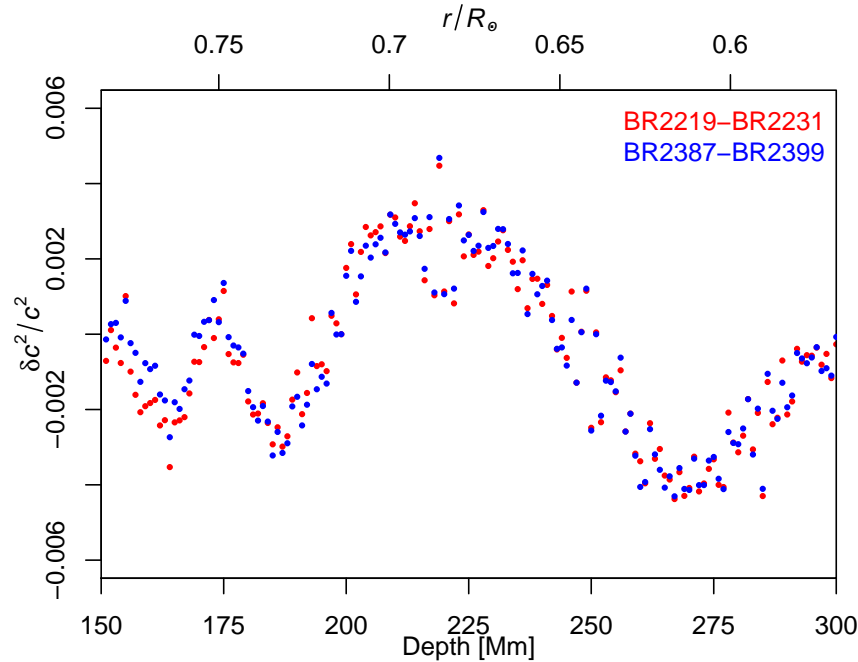


Figure 4.5: Latitudinally-averaged inferred sound-speed perturbation between  $45^{\circ}$  N and  $45^{\circ}$  S with respect to standard solar model S corresponding to the sound-speed maps in Figure 4.6. The inferred profile of Bartels's rotations BR2219–BR2231 at the solar minimum between Solar Cycle 22 and Solar Cycle 23, between 25 January 1996 and 9 January 1997, is shown in red, and that of BR2387–BR2399, spanning between 26 June 2008 and 11 June 2009, at the following solar minimum, is shown in blue.

Figure 4.6 shows maps of the inferred sound-speed for BR2219–BR2231 (a) and BR2387–BR299 (b) with no latitudinal average. In both cases there is an increase in the sound speed of the real Sun with respect to that of model S in the near-equatorial region between  $\approx 200$ – $250$  Mm, which is the main contributor to the peak in the averaged profile shown in Figure 4.5. However, the enhancement of sound speed with respect to the solar model does not extend to higher latitudes. In fact, in the southern hemisphere at latitudes higher than  $\approx 30^{\circ}$  S for BR2219–BR2231, and higher than  $\approx 20^{\circ}$  S for BR2387–BR2399 there is a reduction in the sound speed with respect to

Este documento incorpora firma electrónica, y es copia auténtica de un documento electrónico archivado por la ULL según la Ley 39/2015.  
Su autenticidad puede ser contrastada en la siguiente dirección <https://sede.ull.es/validacion/>

Identificador del documento: 963882

Código de verificación: QDmfX6JG

Firmado por: MANUEL DIAZ ALFARO  
UNIVERSIDAD DE LA LAGUNA

Fecha: 26/06/2017 15:24:15

FERNANDO JAVIER PEREZ HERNANDEZ  
UNIVERSIDAD DE LA LAGUNA

26/06/2017 15:25:57

ERNESTO PEREDA DE PABLO  
UNIVERSIDAD DE LA LAGUNA

28/06/2017 13:21:41

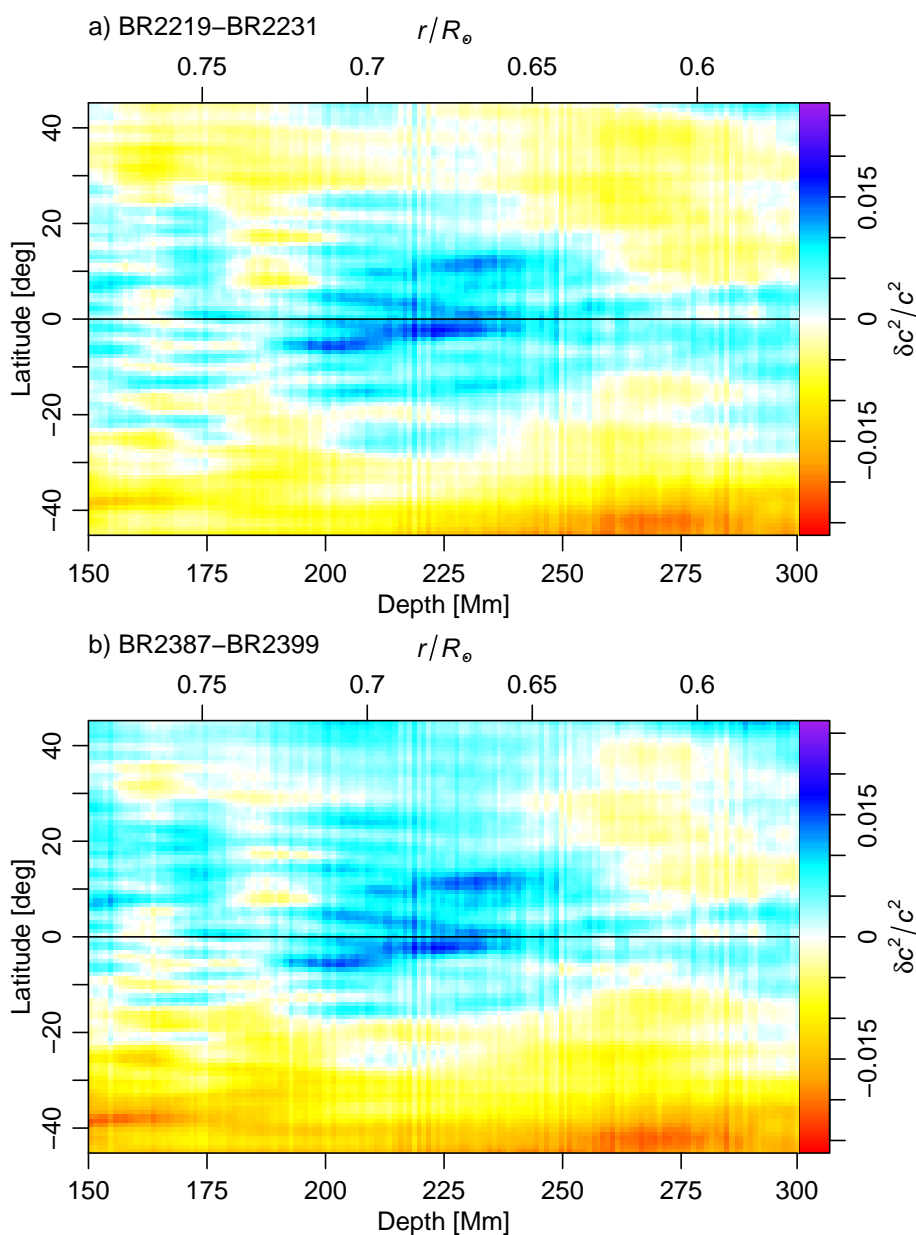


Figure 4.6: Sound-speed perturbation maps with respect to standard solar model S for time intervals corresponding to Bartels's rotations BR2219–BR2231 (a) and BR2387–BR2399 (b) inferred from the phase-shift map of GONG data averaged per Bartels's rotation with respect to a calibrated offset simulated unperturbed phase-shift map. BR2219–BR2231 extend from 25 January 1996 to 9 January 1997, at the solar minimum between Solar Cycle 22 and Solar Cycle 23, and BR2387–BR2399 span between 26 June 2008 and 11 June 2009, at the following solar minimum. The black horizontal lines in both panels represent the equator.

Este documento incorpora firma electrónica, y es copia auténtica de un documento electrónico archivado por la ULL según la Ley 39/2015.  
Su autenticidad puede ser contrastada en la siguiente dirección <https://sede.ull.es/validacion/>

Identificador del documento: 963882

Código de verificación: QDmfX6JG

Firmado por: MANUEL DIAZ ALFARO  
UNIVERSIDAD DE LA LAGUNA

Fecha: 26/06/2017 15:24:15

FERNANDO JAVIER PEREZ HERNANDEZ  
UNIVERSIDAD DE LA LAGUNA

26/06/2017 15:25:57

ERNESTO PEREDA DE PABLO  
UNIVERSIDAD DE LA LAGUNA

28/06/2017 13:21:41

the solar model. This reduction begins  $\approx 5^\circ\text{--}10^\circ$  closer to the equator in the depth ranges of 150–200 Mm and 250–300 Mm. A similar case presents in the northern hemisphere, though with less intense reductions of the sound speed, being weaker for BR2387–BR2399. Zhao *et al.* (2009) also observed a latitudinal variation at the base of the convection zone, but in their case the perturbation was found to be weaker near the equator. They were surprised that a latitudinal variation appeared and indicated that it would require further investigation and modelling of instrumental effects. In our case, the geometrical limitations of pupils for foci at higher latitudes could play some role in the origin of the observed latitudinal variation.

We can see in Figure 4.6 that the maps for the two selected minima are very similar to each other even though they are separated  $\approx 12$  years. Some of the asymmetries shown between the northern and the southern hemispheres are kept between the oldest (a) and the most recent dataset (b). Moreover, in upcoming Section 4.3.2 Figure 4.8 shows the phase-shift variation between two intervals of Bartels's rotations, where the reference simulation has not been used, and no hemispheric asymmetry is apparent there. We have seen in Figure 4.4 that the reference simulation allows the recovery of a latitudinally-averaged profile of sound speed, which is generally consistent in shape with previous results. However, the close likeness of Figure 4.6 (a) and (b) indicates that the reference simulation could contain some internal structure shown as a hemispheric variation, which could be introducing some contaminating artefacts into the seismic maps at the moment of applying the reference correction.

#### 4.3.2 Variations of the inferred sound speed along the solar cycle

Figure 4.4 showed a systematic overall phase shift at all depths between the reconstructed seismic signal of the two time intervals at solar minima considered in Section 4.3.1—BR2219–BR2231 and BR2387–BR2399—. This phenomenon is generally present throughout the span of the GONG data used in this work and different overall phase-shift offsets appear between different Bartels's rotations or groups of them. It is similar to the observed offset between the reconstructed seismic signal of the different numerically simulated datasets in Chapter 3. We discussed there that the overall offset could be explained by changes introduced in the simulating code, which led to slightly different acoustic behaviours of the resonant cavity of the simulated Sun. Analogously, here the origin could be at global changes in the acoustic properties of the Sun. A possible cause could lie at the observed variation of the solar seismic radius along the solar cycle (Lefebvre and Kosovichev, 2005; Kholikov and Hill, 2008; González Hernández, Scherrer, and Hill, 2009). It could also originate in the variation of the overall distribution of surface activity.

As discussed in Chapter 3, the aim of helioseismic holography is to reconstruct the acoustic field of the Sun at a particular location. However, seismic features present at layers the waves have travelled through on their way to the focus can add out-of-focus contributions to the seismic computations. For the helioseismically inferred seismic signal at deeper layers, together with the focused contributions from seismic

Este documento incorpora firma electrónica, y es copia auténtica de un documento electrónico archivado por la ULL según la Ley 39/2015.  
Su autenticidad puede ser contrastada en la siguiente dirección <https://sede.ull.es/validacion/>

Identificador del documento: 963882

Código de verificación: QDmfX6JG

Firmado por: MANUEL DIAZ ALFARO  
UNIVERSIDAD DE LA LAGUNA

Fecha: 26/06/2017 15:24:15

FERNANDO JAVIER PEREZ HERNANDEZ  
UNIVERSIDAD DE LA LAGUNA

26/06/2017 15:25:57

ERNESTO PEREDA DE PABLO  
UNIVERSIDAD DE LA LAGUNA

28/06/2017 13:21:41

perturbations located there, we can expect contributions from other two main sources: out-of-focus contributions from photospheric activity and also from global changes in the acoustic properties of the Sun along the solar cycle. Whereas photospheric activity could affect differently the reconstruction at different locations, according to the specific distribution of active regions at any particular moment, we could expect global variations to affect the reconstructed seismic signal more homogeneously at any depth or latitude. Therefore, we could expect any global variation in the acoustic properties to appear as an overall phase shift between periods of time, as shown in Figure 4.4.

With the previous in mind, we now assess the global effect of solar activity in the recovered phase shift at the photosphere and at the base of the convection zone. For each individual Bartels's rotation we have calculated the mean phase shift between  $45^\circ$  N and  $45^\circ$  S at the photosphere—using the subjacent vantage seismic computations—and at the inferred location of the base of the convection zone, specifically in a 5-Mm-wide interval centred at  $0.685 R_\odot$ , depth at which we have detected the enhancement of sound speed with respect to standard model S at low activity. We have also calculated averages of the daily international sunspot number in intervals of 27 days corresponding to the Bartels's rotations shown in Table 4.1 so that equal parsing facilitates comparison with the evolution of the mean phase shift at the photosphere and at the base of the convection zone and reduces side effects of numerical discretisation. Figure 4.7 (a) shows the evolution with time of the photospheric mean phase shift (a) and of the mean phase shift at the inferred location of the base of the convection zone (c). GONG-Classic data are shown in blue, whereas GONG+ data are shown in red. In both cases we have applied an overall specific offset calculated so that the means of each plot is zero. We have plotted the *ad hoc* Bartels's rotation sunspot number with respect to the mean offset phase shift of the GONG+ data at the photosphere (b) and at the detected base of the convection zone (d) together with a linear fit in both cases. The correlation is 0.91 for the photosphere and 0.80 for the base of the convection zone. The linear fits have been used to rescale the Bartels's rotation sunspot number for both cases and its rescaled variation is shown in (a) and (c) in black dots accordingly. It should be noted that this rescaled sunspot number shown in (a) and (c) is inverted with respect to the international sunspot number  $S_n$ , as the phase shift and the sunspot number are anticorrelated.

We have seen in both cases that the inverted Bartels's rotation sunspot number follows approximately the profile for GONG+ data, but fails for GONG-Classic data, probably because of the limitations of the creation of merged dopplergrams from single-site dopplergrams without all the additional calibration data introduced in the observing procedure after the update to GONG+ (Hughes *et al.*, 2016). Although the correlation between photospheric activity—measured by the sunspot number—and the seismic phase shift at the photosphere (a,b) is higher than for the phase shift at the recovered position of the base of the convection zone (c,d), the latter is still high enough (0.80). The international sunspot number proxies photospheric activity; thus,

Este documento incorpora firma electrónica, y es copia auténtica de un documento electrónico archivado por la ULL según la Ley 39/2015.  
Su autenticidad puede ser contrastada en la siguiente dirección <https://sede.ull.es/validacion/>

Identificador del documento: 963882

Código de verificación: QDmfX6JG

Firmado por: MANUEL DIAZ ALFARO  
UNIVERSIDAD DE LA LAGUNA

Fecha: 26/06/2017 15:24:15

FERNANDO JAVIER PEREZ HERNANDEZ  
UNIVERSIDAD DE LA LAGUNA

26/06/2017 15:25:57

ERNESTO PEREDA DE PABLO  
UNIVERSIDAD DE LA LAGUNA

28/06/2017 13:21:41

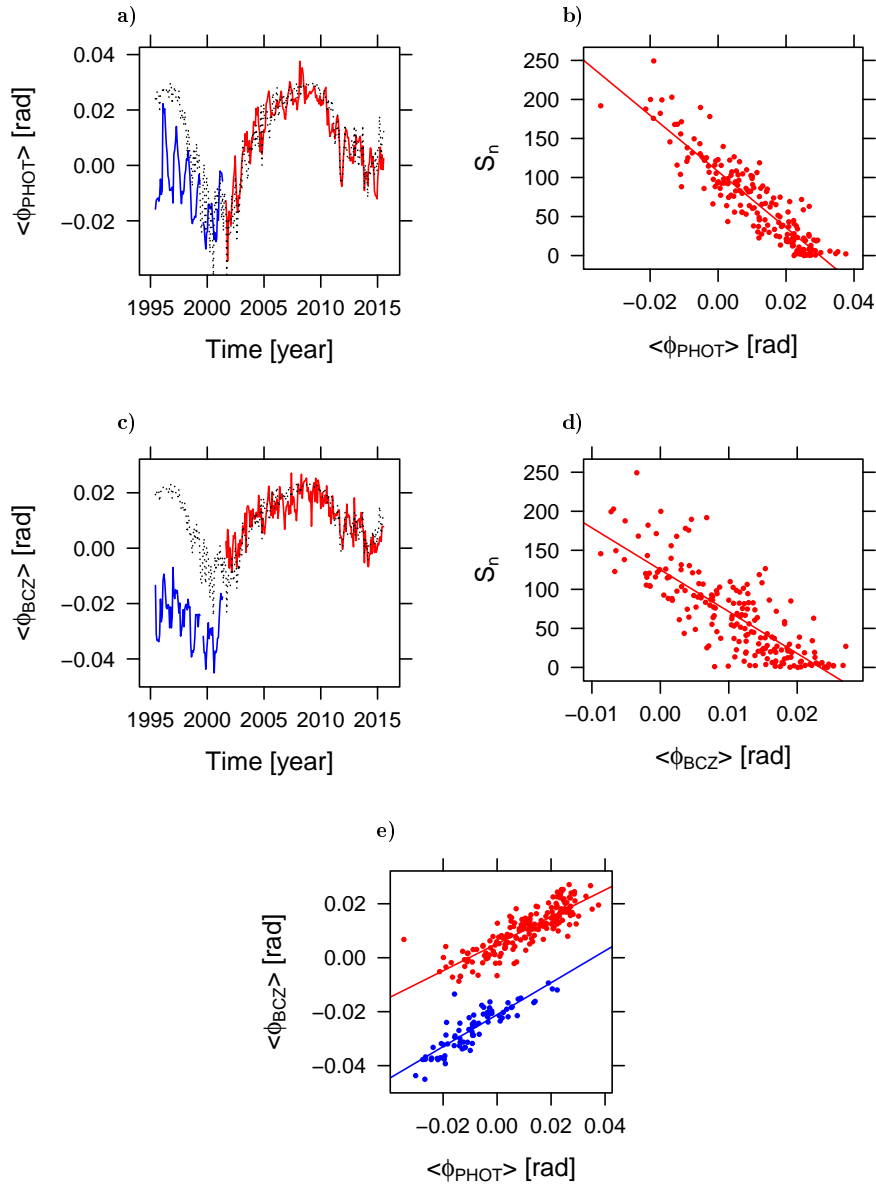


Figure 4.7: Evolution of the mean value of the relative phase shift between 45° S and 45° N at the solar surface (a) and at the base of the convection zone (c). In both cases the phase shift is shown relative to its mean value. GONG-Classic data is shown in blue and GONG+ data is shown in red. The daily international sunspot number averaged in intervals of Bartel's rotation is shown against the relative phase shift for the GONG+ epoch at the solar surface (b) and at the base of the convection zone (d), with fitted lines. The daily international sunspot number averaged in intervals of Bartel's rotations is transformed into phase-shift values with the aid of the correlation relation shown in (b) and (d), and shown in black dots in (a) and (c). e) Correlation between the mean relative phase shift at the base of the convection zone and that at the solar surface for GONG Classic (blue) and GONG+ (red). The phase shift has been averaged between 45° S and 45° N and for the base of the convection zone at a 5-Mm wide interval centred at  $0.68 R_{\odot}$  has been used. Fitted lines are shown in the corresponding colours for the two GONG epochs separately.

Este documento incorpora firma electrónica, y es copia auténtica de un documento electrónico archivado por la ULL según la Ley 39/2015.  
Su autenticidad puede ser contrastada en la siguiente dirección <https://sede.ull.es/validacion/>

Identificador del documento: 963882

Código de verificación: QDmfX6JG

Firmado por: MANUEL DIAZ ALFARO  
UNIVERSIDAD DE LA LAGUNA

Fecha: 26/06/2017 15:24:15

FERNANDO JAVIER PEREZ HERNANDEZ  
UNIVERSIDAD DE LA LAGUNA

26/06/2017 15:25:57

ERNESTO PEREDA DE PABLO  
UNIVERSIDAD DE LA LAGUNA

28/06/2017 13:21:41

we are observing an important overall correspondence between global photospheric activity and the inferred seismic signal at the layers of interest. Furthermore, Figure 4.7 (e), showing the phase shift at the location of the inferred base of the convection zone with respect to the phase shift at the photosphere for GONG-Classic (blue) and GONG+ (red), supports this premise. Both cases adjust linearly with correlation values of 0.83 for GONG-Classic and 0.84 for GONG+. The origin of these correlations may rest in the direct evolution with the solar cycle of helioseismic magnitudes both at the photosphere and at the base of the convection zone, but it may also indicate that the influence of global photospheric activity in the reconstruction of the seismic magnitudes at the deep layers of the base of the convection zone and tachocline, at least globally, could be important, or likely a combination of both. In Section 4.4 we will assess with greater detail the influence of the photospheric layers in the helioseismic reconstruction of deeper layers.

Using GONG+ data, we study now the variation of the reconstructed sound speed between periods of high and low solar activity. As done previously in Section 4.3.1, the international sunspot number, shown in Figure 4.3, has been used to select an interval shortly after the maximum of Solar Cycle 23, covering 13 Bartels's rotations, BR2306–BR2318, extending from 1 July 2002 to 16 June 2003, and another time interval at the maximum of Solar Cycle 24, BR2468–BR2480, extending from 22 June 2014 to 7 June 2015, and covering also 13 consecutive Bartels's rotations. The starting and ending dates of the two periods are signalled with dashed bars in Figure 4.3. Although we have used GONG-Classic data for one of the intervals presented in Section 4.3.1, the reader should note that the two datasets selected here only include GONG+ data, due to the lower quality of GONG-Classic discussed previously and shown in Figure 4.7.

We have calculated the phase-shift differences between BR2387–BR2399—solar minimum—and each of the high-activity periods separately—BR2306–BR2318 and BR2468–BR2480—and have corrected the offset from them by subtracting the mean value of the corresponding difference. The purpose of this subtraction is to remove the global phase-shift variability, which includes phase-shift changes that may have arisen from variations in the solar seismic radius, *i.e.* in the global acoustic properties of the Sun, and from the global influence of photospheric activity described above. We have limited the mean to the range 150–300 Mm to optimise this correction for the deeper layers where the base of the convection zone and tachocline are located. Equation (3.5) has been applied to the offset-corrected phase-shift differences to infer the associated variations in sound speed. To avoid higher noise values, we have also excluded latitudes higher than  $45^\circ$  in both hemispheres. Figure 4.8 shows a map of the inferred sound-speed difference between BR2387–BR2399, at the solar minimum between Solar Cycle 23 and Solar Cycle 24, and BR2468–BR2480, at the solar maximum of Solar Cycle 24. Here and in the following cases, the sense of the difference is high activity minus low activity. We observe a suppression of sound speed in the vicinity of the equator, up to  $\approx 20^\circ$ – $30^\circ$ , and an enhancement of sound speed at higher latitudes at high activity. At latitudes between  $\approx 15^\circ$  and  $\approx 30^\circ$  we

Este documento incorpora firma electrónica, y es copia auténtica de un documento electrónico archivado por la ULL según la Ley 39/2015.  
Su autenticidad puede ser contrastada en la siguiente dirección <https://sede.ull.es/validacion/>

Identificador del documento: 963882

Código de verificación: QDmfX6JG

Firmado por: MANUEL DIAZ ALFARO  
UNIVERSIDAD DE LA LAGUNA

Fecha: 26/06/2017 15:24:15

FERNANDO JAVIER PEREZ HERNANDEZ  
UNIVERSIDAD DE LA LAGUNA

26/06/2017 15:25:57

ERNESTO PEREDA DE PABLO  
UNIVERSIDAD DE LA LAGUNA

28/06/2017 13:21:41

can observe at certain depths the presence of regions of higher sound speed in the shape of tongues that penetrate toward lower latitudes. Similar features appear in maps of sound-speed differences for other time intervals. In the particular case shown in Figure 4.8 this effect is more intense in the northern hemisphere.

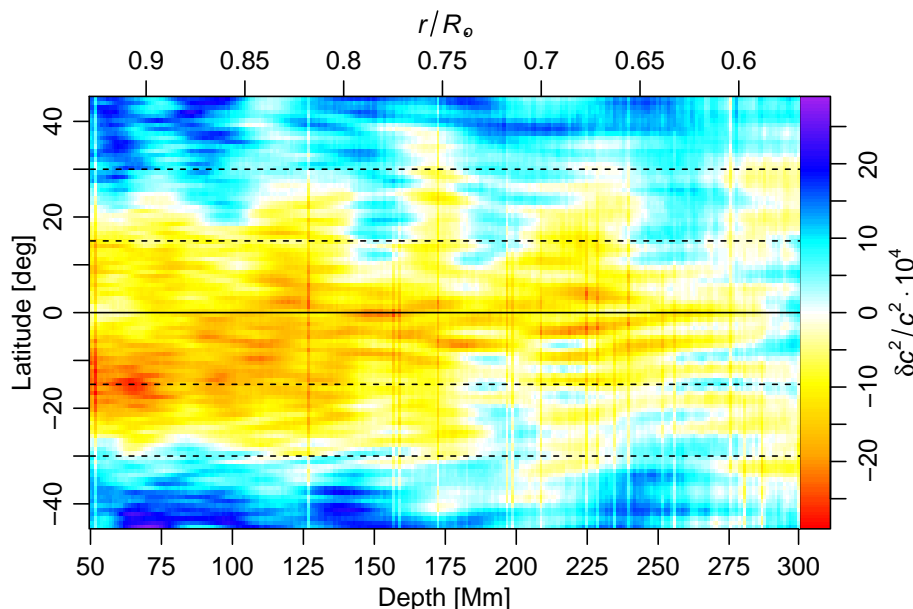


Figure 4.8: Latitude-depth map of the inferred sound-speed variation between BR2387–BR2399, at the solar minimum between Solar Cycle 23 and Solar Cycle 24, and BR2468–BR2480, at the solar maximum of Solar Cycle 24, after correcting for global offset. The colour scale indicates the sound-speed variation in units of  $10^{-4}$ . The solid horizontal line represents the equator and the dashed horizontal lines represent locations at  $15^\circ$  and  $30^\circ$  of latitude in both hemispheres.

In the shallower layers, we can observe a higher decrease in the inferred sound-speed variation around  $\approx 15^\circ$  in the Southern hemisphere with respect to the Northern hemisphere. Hemispheric sunspot numbers allow to assess the hemispheric variability of solar activity. For both the minimum and the maximum intervals considered in Figure 4.8 the hemispheric sunspot numbers show higher solar activity in the Southern hemisphere. However, this excess of activity in the Southern hemisphere is higher for the considered maximum interval, what is consistent with the observed behaviour here.

In order to compare the data with previous results that lack latitudinal resolution, we show in Figure 4.9 the latitudinally averaged inferred sound-speed variation between BR2387–BR2399—low activity—and BR2306–BR2318—high activity—in red, and between BR2387–BR2399—low activity—and BR2468–BR2480—high activity—in black. While the latter case represents the chronological evolution of

Este documento incorpora firma electrónica, y es copia auténtica de un documento electrónico archivado por la ULL según la Ley 39/2015.  
Su autenticidad puede ser contrastada en la siguiente dirección <https://sede.ull.es/validacion/>

Identificador del documento: 963882

Código de verificación: QDmfX6JG

Firmado por: MANUEL DIAZ ALFARO  
UNIVERSIDAD DE LA LAGUNA

Fecha: 26/06/2017 15:24:15

FERNANDO JAVIER PEREZ HERNANDEZ  
UNIVERSIDAD DE LA LAGUNA

26/06/2017 15:25:57

ERNESTO PEREDA DE PABLO  
UNIVERSIDAD DE LA LAGUNA

28/06/2017 13:21:41

the sound speed, the former is anti chronological. We observe for both cases that at  $\approx 0.68 R_{\odot}$  there is a decrease in sound speed at high activity and an enhancement below it.

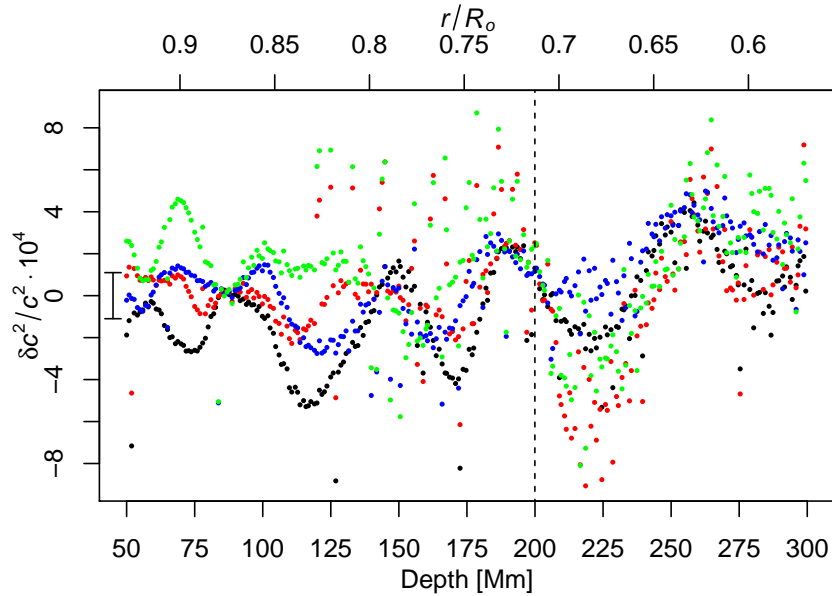


Figure 4.9: Inferred sound-speed variation latitudinally averaged between  $45^{\circ}$  N and  $45^{\circ}$  S of periods of high solar activity with respect to periods of low solar activity. All the considered intervals span 13 Bartels's rotations of GONG+ data. BR2306–BR2318 with respect to BR2387–BR2399 is shown in red, BR2468–BR2480 with respect to BR2387–BR2399 in black, BR2306–BR2318 with respect to BR2400–BR2412 in green, and BR2468–BR2480 with respect to BR2400–BR2412 in blue. An estimation of the uncertainty is shown on the left side of the plot. The vertical dashed line represents the location of the base of the convection zone. The sound-speed variation is shown in units of  $10^{-4}$ .

Baldner and Basu (2008) applied a principal component analysis to the evolution of eigenfrequencies of the Sun measured from MDI and GONG observations along Solar Cycle 23 and with the aid of an inversion they reconstructed the sound speed variation between high and low activity (view Figure 5 of their article). It should be noted that although Baldner and Basu (2008) described their results in terms of high activity with respect to low activity as we are doing, they plotted low activity minus high activity instead; and therefore, their plots show inverted results. They also obtained a depression in sound speed at the base of the convection zone for high activity and an enhancement below it for the MDI and GONG data. Their results for the GONG data showed the peaks in sound speed slightly displaced toward deeper

Este documento incorpora firma electrónica, y es copia auténtica de un documento electrónico archivado por la ULL según la Ley 39/2015.  
Su autenticidad puede ser contrastada en la siguiente dirección <https://sede.ull.es/validacion/>

Identificador del documento: 963882

Código de verificación: QDmfX6JG

Firmado por: MANUEL DIAZ ALFARO  
UNIVERSIDAD DE LA LAGUNA

Fecha: 26/06/2017 15:24:15

FERNANDO JAVIER PEREZ HERNANDEZ  
UNIVERSIDAD DE LA LAGUNA

26/06/2017 15:25:57

ERNESTO PEREDA DE PABLO  
UNIVERSIDAD DE LA LAGUNA

28/06/2017 13:21:41

layers with respect to their MDI counterparts, with the depression at  $\approx 0.7R_{\odot}$ . In Chapter 3 (Figure 3.13) we observed that the technique used in this thesis recovered the central layer of a numerically simulated perturbation nominally located at a depth of  $0.70 R_{\odot}$  at a slightly deeper layer of  $\approx 0.685 R_{\odot}$ . Taking into account this deepening, the positions of the inferred depression and enhancement in sound speed at high activity seem consistent with the results for GONG from Baldner and Basu (2008).

Regarding the intensity of the sound-speed peaks, Baldner and Basu (2008) got a decrease of sound speed at the base of the convection zone at high activity of  $\delta c^2/c^2 \simeq 7 \cdot 10^{-5}$ , consistent with previous results, whereas our inferred values for the two presented cases (red and black dots) are generally between 3 and 8 times higher. We have also obtained higher values for the enhancement in sound speed below the convection zone at high activity, approximately 4 times their values. Both the depression and the enhancement in sound speed at high activity are larger for the case including the high activity period at Solar Cycle 23 (red) than for the case with it at Solar Cycle 24 (black). This result is consistent with the fact that the maximum of Solar Cycle 23 was much stronger than that of Solar Cycle 24, as can be seen in Figure 4.3 with the aid of the international sunspot number.

In the previous cases we have considered the same time interval at low activity. To ensure that the results are not conditioned by the choice of a particular low-activity dataset, we have chosen another set of Bartels's rotations around the same solar minimum and have inferred sound-speed differences of the high-activity datasets with respect to the alternative low-activity one. We have selected BR2400–BR2412, spanning from 12 June 2009 to 28 May 2010, and have also represented the sound-speed variation with respect to it of BR2306–BR2318 in blue and of BR2468–BR280 in green in Figure 4.9. The starting and ending dates thereof are also signalled in Figure 4.3 with dotted bars. The results at the deep layers of interest show relative depressions or enhancements at the same positions as in the previous cases, being consistent with the description and analysis above.

We have calculated standard deviations of the studied means, and using standard error propagation, we have calculated estimations of the uncertainty of the plotted differences. The values for these uncertainties are quite homogeneous throughout the considered depth interval and for the four plotted differences. For the sake of clarity, we have combined them in an averaged uncertainty value ( $\pm 1.09 \cdot 10^{-4}$ ), which is shown on the left side of Figure 4.9.

We have observed that at the deepest-considered layers the variation of the inferred sound-speed difference is consistent throughout the four considered cases. However, at shallower layers, above  $\approx 0.8 R_{\odot}$ , the inferred sound-speed differences for the four different cases show important variability, a strong oscillatory behaviour and do not have depressions and peaks at the same positions. Error correlation can produce oscillatory behaviours in heliosismic inversions (Howe and Thompson, 1996). A similar behaviour could be expected in helioseismic holography. This effect seems also to be present in Figure 5 of Baldner and Basu (2008), mostly noticeable in the

Este documento incorpora firma electrónica, y es copia auténtica de un documento electrónico archivado por la ULL según la Ley 39/2015.  
Su autenticidad puede ser contrastada en la siguiente dirección <https://sede.ull.es/validacion/>

Identificador del documento: 963882

Código de verificación: QDmfX6JG

Firmado por: MANUEL DIAZ ALFARO  
UNIVERSIDAD DE LA LAGUNA

Fecha: 26/06/2017 15:24:15

FERNANDO JAVIER PEREZ HERNANDEZ  
UNIVERSIDAD DE LA LAGUNA

26/06/2017 15:25:57

ERNESTO PEREDA DE PABLO  
UNIVERSIDAD DE LA LAGUNA

28/06/2017 13:21:41

shallower layers where the signal of interest is lower. In this work, the oscillatory behaviour in the upper layers of Figure 4.9 can also originate in error correlation, which could be amplified due to the influence of photospheric activity, stronger at shallower layers, as the evolution of photospheric activity experiences higher degrees of variability, whereas at the base of the convection zone and tachocline the evolution is expected to be smoother and more homogeneous from one solar cycle to the next. Here, we have subtracted two GONG datasets for each case, which would have removed any artefacts intrinsically associated to the technique, such as the variation of phase shift from the shallower layers to  $\approx 0.75 R_{\odot}$ , shown in *i.e.* Figure 4.4, and originating in the fact that the size of the pupils also varies with depth, or the band-like oscillation shown in previous plots, or any artefact introduced by the reference simulation discussed in Section 4.3.1. However, in order to assess what part of the seismically-inferred sound-speed variation at the shallower layers comes from actual perturbations at those layers and what part constitutes an optical parasite propagation of a perturbation above, a larger set of simulations with different combinations of photospheric and subphotospheric activity should be used.

The evolution from low to high activity for individual latitudes can be studied with the aid of Figure 4.10. Here we have considered  $5^{\circ}$ -wide latitudinal means centred at the equator,  $15^{\circ}$ , and  $30^{\circ}$ , where the two hemispheres have been averaged, at the bottom, middle and top panels respectively. Alike in the mean latitudinal values shown in Figure 4.9, we also observe in Figure 4.10 that for the separate latitudes the four considered sound-speed differences follow consistent profiles at deeper layers, while at the shallower layers they do not. The recession of sound speed found at  $\approx 0.68 R_{\odot}$  in Figure 4.9 is found at the three considered latitudes, but the enhancement located below that layer does not seem to appear at the equator.

On the one hand, at the shallow layers at  $0^{\circ}$  and  $15^{\circ}$  the sound-speed differences seem to follow two separate groups—the profiles corresponding to the high activity period of Solar Cycle 23 (red and green) and those corresponding to that of Solar Cycle 24 (black and blue)—, appearing between the groups a larger difference than between the individual differences in each group. Within each of the observed separate groups, the two components differ only in a one-year offset at the solar minimum. Thus, the observed disagreement between the two groups of differences at the shallow layers at  $0^{\circ}$  and  $15^{\circ}$  could originate in the different behaviour at the two solar maxima. On the other hand, at  $30^{\circ}$  we do not observe such a clear correlation between the components of the two previous groups at the shallow layers. At  $30^{\circ}$  the occurrence of active regions on the rising phase of a solar cycle is higher and, even with an offset of one year within a solar minimum, the changes at the distribution of photospheric magnetic field may be important. Therefore, the observed variability at the shallow layers at  $30^{\circ}$  could originate in the variable distribution of emerging active regions or submerged parasite seismic images of photospheric active regions, concentrating at  $\approx 30^{\circ}$  at the beginning of a solar cycle according to the Spörer Law.

Baldner and Basu (2008) also presented profiles of inferred sound-speed variations at certain latitudes applying inversion techniques to frequency splittings (Figure 9

Este documento incorpora firma electrónica, y es copia auténtica de un documento electrónico archivado por la ULL según la Ley 39/2015.  
Su autenticidad puede ser contrastada en la siguiente dirección <https://sede.ull.es/validacion/>

Identificador del documento: 963882

Código de verificación: QDmfX6JG

Firmado por: MANUEL DIAZ ALFARO  
UNIVERSIDAD DE LA LAGUNA

Fecha: 26/06/2017 15:24:15

FERNANDO JAVIER PEREZ HERNANDEZ  
UNIVERSIDAD DE LA LAGUNA

26/06/2017 15:25:57

ERNESTO PEREDA DE PABLO  
UNIVERSIDAD DE LA LAGUNA

28/06/2017 13:21:41

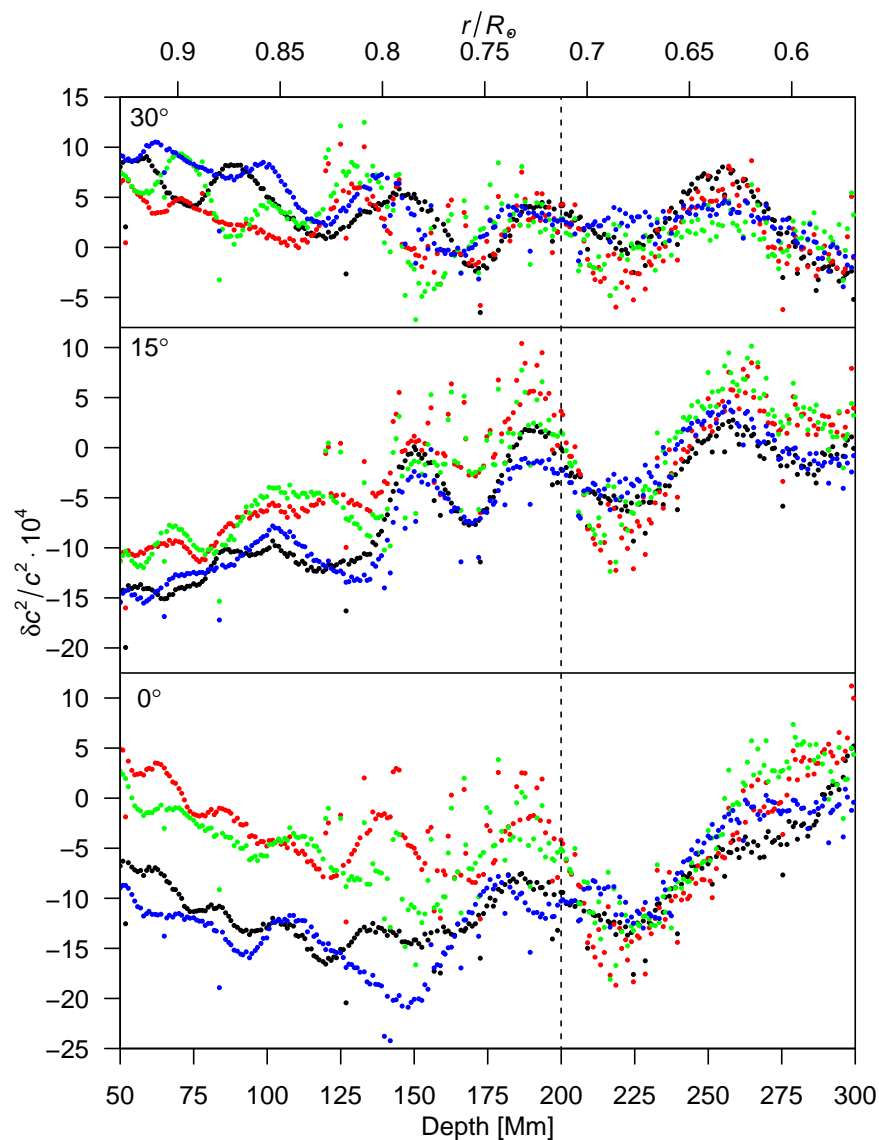


Figure 4.10: Inferred sound-speed variation of periods of high solar activity with respect to periods of low solar activity at three different latitude intervals centred at  $0^\circ$  (bottom panel),  $15^\circ$  (middle panel), and  $30^\circ$  (top panel). The latitude intervals are  $5^\circ$  wide and both hemispheres have been averaged. All the considered time intervals span 13 Bartels's rotations of GONG+ data. BR2306–BR2318 with respect to BR2387–BR2399 is shown in red, BR2468–BR2480 with respect to BR2387–BR2399 in black, BR2306–BR2318 with respect to BR2400–BR2412 in green, and BR2468–BR2480 with respect to BR2400–BR2412 in blue. The vertical dashed line represents the location of the base of the convection zone. The sound-speed variation is shown in units of  $10^{-4}$ . The scale of the sound-speed variation is kept throughout the three panels.

Este documento incorpora firma electrónica, y es copia auténtica de un documento electrónico archivado por la ULL según la Ley 39/2015.  
Su autenticidad puede ser contrastada en la siguiente dirección <https://sede.ull.es/validacion/>

Identificador del documento: 963882

Código de verificación: QDmfX6JG

Firmado por: MANUEL DIAZ ALFARO  
UNIVERSIDAD DE LA LAGUNA

Fecha: 26/06/2017 15:24:15

FERNANDO JAVIER PEREZ HERNANDEZ  
UNIVERSIDAD DE LA LAGUNA

26/06/2017 15:25:57

ERNESTO PEREDA DE PABLO  
UNIVERSIDAD DE LA LAGUNA

28/06/2017 13:21:41

thereof). No clear match is found between our results and theirs. However, it should be noted that their technique to calculate the sound-speed variation at individual latitudes includes inversions independent to the ones they used to calculate the global sound-speed variation and the former is expected to be less accurate than the latter. In our case, the sound-speed variations presented in Figure 4.9 are the means between  $45^\circ$  N and  $45^\circ$  S of the corresponding variations at individual latitudes.

#### 4.4 Discussion

We have applied a seismic holography technique to a series of GONG data to reconstruct the seismic field in the solar interior. The size of the pupils, which is determined by the used lateral-vantage scheme, increases when the focus is set at a deeper layer. Thus, the response function of the technique varies with depth. This fact causes the overall reduction in phase-shift shown in the uncalibrated phase-shift profiles. This effect lasts up to a depth of approximately  $0.75 R_\odot$ . Below this layer the size of the pupil reaches the limiting radius of the observed hemisphere of the Sun and the effect stabilises. Besides, different modes resonate in cavities of different extensions and at certain layers, where modes reach the limit of their resonating cavities, they stopped to be include in the code generating Green's functions. These two facts may have produced the bands which are found in the upper layers of the seismic reconstruction of the simulations and of the actual solar interior.

We have determined the variation in the sound-speed profile with respect to standard solar model S at two solar minima and have calibrated it with the aid of the results from the numerical simulations presented in Chapter 3. We have detected an enhancement in the sound speed in the real Sun with respect to the model of approximately  $\delta c^2/c^2 \approx 3 \cdot 10^{-3}$  at a radius of  $\approx 0.68 R_\odot$ , consistent with previous results obtained using other techniques of global and local helioseismology.

We have used an unperturbed numerical dataset as a reference to calibrate the inferred seismic phase shift with respect to model S. However, we have encountered several complications when applying this reference dataset. Although the reference simulation is based on model S as its background state, it was slightly modified for higher realism with the inclusion of a model for the chromosphere, the neglect of the entropy gradient, and different upper boundary conditions. Green's functions were computed using an unmodified model S instead. This disagreement may have been the cause for the lack of full correction of the banding artefacts in the shallower layers of the seismic phase shift. In order to completely remove the banding Green's functions could be computed using the background model of the simulations. A phase-shift correction assessing the differences between the two models would have a similar effect.

Applying the technique to different time series, each of them spanning 13 Bartels rotations, we have obtained the sound-speed variation between periods of high and low activity in the Sun. We have detected a mean decrease at  $\approx 0.68 R_\odot$  at high activity of approximately  $\delta c^2/c^2 \approx -4 \cdot 10^{-4}$  and an enhancement of approximately

Este documento incorpora firma electrónica, y es copia auténtica de un documento electrónico archivado por la ULL según la Ley 39/2015.  
Su autenticidad puede ser contrastada en la siguiente dirección <https://sede.ull.es/validacion/>

Identificador del documento: 963882

Código de verificación: QDmfX6JG

Firmado por: MANUEL DIAZ ALFARO  
UNIVERSIDAD DE LA LAGUNA

Fecha: 26/06/2017 15:24:15

FERNANDO JAVIER PEREZ HERNANDEZ  
UNIVERSIDAD DE LA LAGUNA

26/06/2017 15:25:57

ERNESTO PEREDA DE PABLO  
UNIVERSIDAD DE LA LAGUNA

28/06/2017 13:21:41

$\delta c^2/c^2 \approx 4 \cdot 10^{-4}$  below it. As expected, we have also observed that these peaks are stronger for the time differences including data from the solar maximum with higher activity levels.

Previous results show these features at slightly shallower locations, with the decrease at  $\approx 0.70 R_{\odot}$ . We showed in Chapter 3 that the considered technique tends to extend the inferred seismic signal toward deeper layers and recover perturbations slightly deeper than expected. As a matter of fact, the centre of the perturbations from Section 3.3.1, nominally located at  $0.70 R_{\odot}$ , was helioseismically inferred at  $\approx 0.685 R_{\odot}$ , which is consistent with the location difference here.

The inferred sound-speed variation at shallower layers shows different peaks that are of the same order of magnitude as the two peaks described above, while in previous results they are considerably smaller. This oscillatory behaviour may originate partly in error correlations that appear when applying the same technique to the same datasets as is done here or in helioseismic inversions. Another influence may come, as seen in Sections 3.3.2 and 3.3.3, from the parasite out-of-focus contributions of surface activity on the inferred seismic signal at these layers. It is also possible that the reconstructed sound-speed values at the shallowest layers may be overestimated. We have also shown that the response function has a dependence on depth due to the different size of the pupils for focal planes at different depths. However, we have considered a relation between phase shift and sound-speed variation, which is non-dependent on depth, based only on their values at  $0.70 R_{\odot}$ . A series of simulations with sound-speed perturbations at varying depths could help to determine the variation of the response function with depth. It could also help to establish the relation between the inferred location of a detected feature and the actual location, slightly above it as seen before.

Although the profile of the recovered variations at the base of the convection zone and below it are consistent with previous results and the location of the inferred peaks is also consistent with previous results, the values are not. Previous results show values that are between 3 and 8 times lower than ours. However, the consistency of these results throughout different time series at both high and low solar activity seems to indicate that the obtained results are real variations occurring at the deep layers of interest and not out-of-focus contaminations from shallower phenomena. Probably the series of simulations suggested above could also help to fine-tune the relation between phase shift and sound-speed variation and reduce this discrepancy.

We have interpreted variations in phase shift as originating from changes in the ambient sound speed alone. However, magnetic activity or material motions can also produce variations in phase shift. Inversion techniques could help to reconstruct the different physical magnitudes from the seismic maps or improve the calibration of the technique (see Sun, Chou, and TON Team, 2002).

We have also shown that the technique is capable of producing maps of sound-speed variation with respect to model S with spatial resolution. While at lower latitudes, the inferred sound-speed variation in the shallowest layers are very similar when only the low-activity dataset differs, at  $30^\circ$ , they show also high degrees of variability in that

Este documento incorpora firma electrónica, y es copia auténtica de un documento electrónico archivado por la ULL según la Ley 39/2015.  
Su autenticidad puede ser contrastada en la siguiente dirección <https://sede.ull.es/validacion/>

Identificador del documento: 963882

Código de verificación: QDmfX6JG

Firmado por: MANUEL DIAZ ALFARO  
UNIVERSIDAD DE LA LAGUNA

Fecha: 26/06/2017 15:24:15

FERNANDO JAVIER PEREZ HERNANDEZ  
UNIVERSIDAD DE LA LAGUNA

26/06/2017 15:25:57

ERNESTO PEREDA DE PABLO  
UNIVERSIDAD DE LA LAGUNA

28/06/2017 13:21:41

case too. This is explained by the fact that at low activity, during the beginning of the rise part of a solar cycle, most solar activity occurs around  $30^\circ$ . Therefore, more variability between these time series could be expected at  $30^\circ$ .

We have demonstrated in Chapter 3 that individual active regions of typical sizes do not modify the results of seismic magnitudes at the deep layers of interest. However, in periods of high activity an important fraction of the solar surface is covered by active regions. The quiescent regions between active regions could be expected to break the necessary spatial coherence for their seismic influence to coalesce into significant values. We have obtained correlation values of 0.80 between the mean seismic signal at the base of the convection zone and the international sunspot number and of 0.84 between the mean seismic signals at the base of the convection zone and at the photosphere. However, we have empirically seen that the recovered sound-speed profile seems to indicate that out-of-focus effects from shallower layers, including photospheric activity, are not important enough in the real Sun as to obscure the detection of the small variations near the base of the convection zone between periods of high and low activity. Still, it could be interesting to assess the effects of multiple active regions in the technique with the aid of more realistic numerical simulations including at the same time perturbations at the tachocline level and a variable number of perturbations at the solar surface.

GONG data could be used at a higher spatial resolution (González Hernández *et al.*, 2013), as well as HMI dopplergrams, which could provide results with higher resolution and reduce the out-of-focus contributions of photospheric activity. MDI dopplergrams could also be used to extend this study into the past and together with GONG and HMI data to compare results from different instruments. Following the experience of far-side seismic holography, the technique could also be extended to include  $1 \times 3$  skip computations to measure the sound-speed variations at higher latitudes.

Este documento incorpora firma electrónica, y es copia auténtica de un documento electrónico archivado por la ULL según la Ley 39/2015.  
Su autenticidad puede ser contrastada en la siguiente dirección <https://sede.ull.es/validacion/>

Identificador del documento: 963882

Código de verificación: QDmfX6JG

Firmado por: MANUEL DIAZ ALFARO  
UNIVERSIDAD DE LA LAGUNA

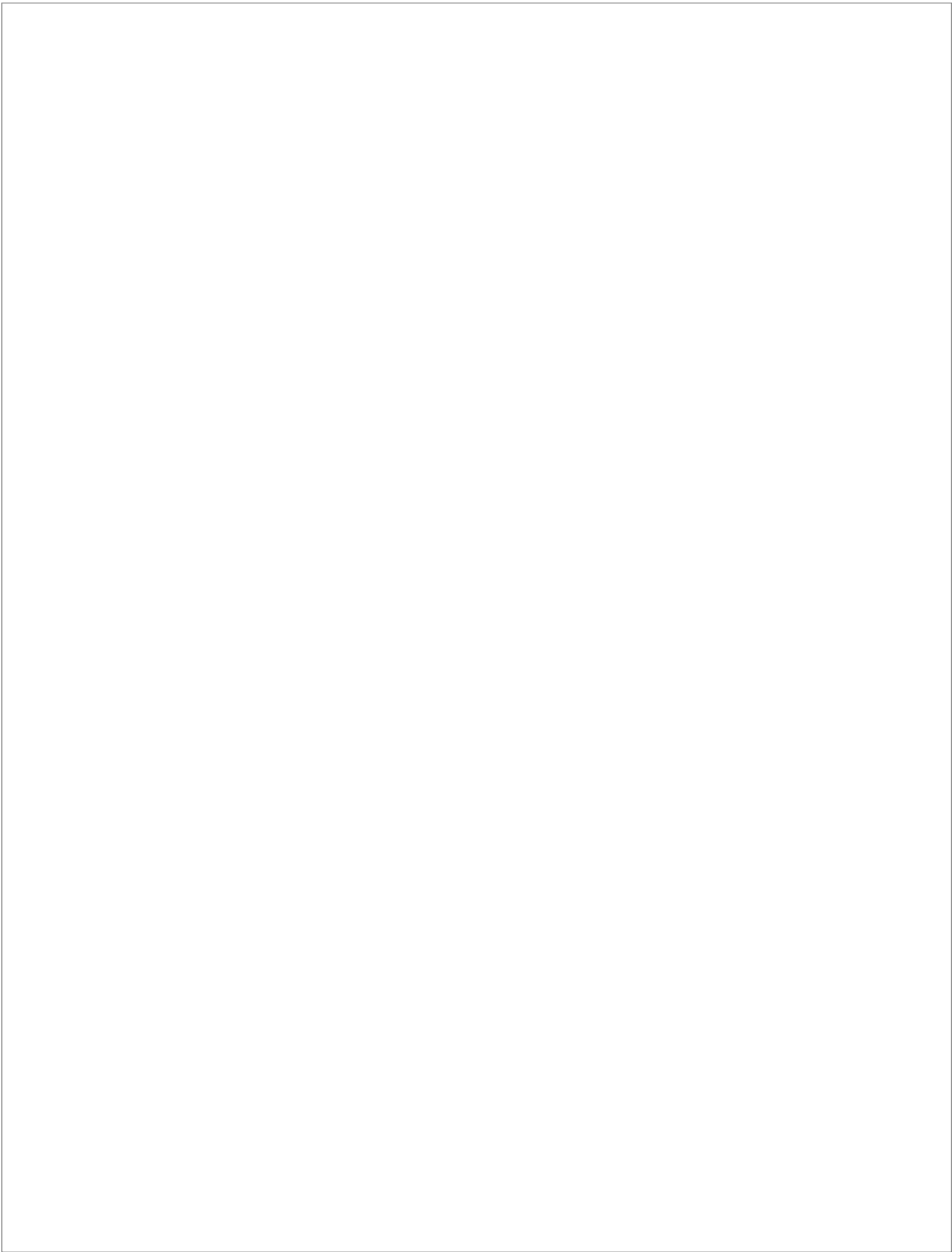
Fecha: 26/06/2017 15:24:15

FERNANDO JAVIER PEREZ HERNANDEZ  
UNIVERSIDAD DE LA LAGUNA

26/06/2017 15:25:57

ERNESTO PEREDA DE PABLO  
UNIVERSIDAD DE LA LAGUNA

28/06/2017 13:21:41



Este documento incorpora firma electrónica, y es copia auténtica de un documento electrónico archivado por la ULL según la Ley 39/2015.  
Su autenticidad puede ser contrastada en la siguiente dirección <https://sede.ull.es/validacion/>

Identificador del documento: 963882

Código de verificación: QDmfX6JG

Firmado por: MANUEL DIAZ ALFARO  
UNIVERSIDAD DE LA LAGUNA

Fecha: 26/06/2017 15:24:15

FERNANDO JAVIER PEREZ HERNANDEZ  
UNIVERSIDAD DE LA LAGUNA

26/06/2017 15:25:57

ERNESTO PEREDA DE PABLO  
UNIVERSIDAD DE LA LAGUNA

28/06/2017 13:21:41

# 5

## Conclusions

In this thesis we have presented a comprehensive study of the application of helioseismic holography, a local helioseismology utility, in order to infer the sound speed profile at the base of the convection zone and its variability along the solar cycle. First, we have explored the applicability of the procedure with the aid of different numerical simulations. Then, we have applied the helioseismic holography technique to GONG solar observations covering over one and a half solar cycles. In this chapter we briefly summarize the main results and conclusions resulting from this work.

- We have detailedly presented a local helioseismology technique capable of reconstructing the seismic wavefield of the solar interior, porting the procedure in use for imaging the far-side non-visible hemisphere of the Sun, and adapting it for use in the solar interior, including the base of the convection zone and the tachocline.
- We have recovered the profile of numerically simulated sound-speed perturbations located at the tachocline with respect to a standard solar model, of the same order of magnitudes as actual variations in the sound speed in the real Sun. We have observed a slight deepening in the detection, recovering the perturbation about  $0.015 R_{\odot}$  below its nominal position, and a slight broadening, mainly at deeper layers and higher latitudes. However, the general overall shape of the perturbation is kept. We have detected variations as low as  $\delta c/c = 5 \cdot 10^{-4}$  in the sound speed.
- In order to study the effect of shallower sound-speed perturbations on the recovery of sound-speed perturbations at the layers of interest, we have applied the same procedure to numerical simulations with sound-speed perturbations in the photosphere and in the upper 20–50 Mm of the subphotosphere. Due to geometrical restrains, all the perturbations extend deeper than their nominal position. We observed that the recovered seismic response extends deeper for broader perturbations and for shallower perturbations, detecting the largest

Este documento incorpora firma electrónica, y es copia auténtica de un documento electrónico archivado por la ULL según la Ley 39/2015.  
Su autenticidad puede ser contrastada en la siguiente dirección <https://sede.ull.es/validacion/>

Identificador del documento: 963882

Código de verificación: QDmfX6JG

Firmado por: MANUEL DIAZ ALFARO  
UNIVERSIDAD DE LA LAGUNA

Fecha: 26/06/2017 15:24:15

FERNANDO JAVIER PEREZ HERNANDEZ  
UNIVERSIDAD DE LA LAGUNA

26/06/2017 15:25:57

ERNESTO PEREDA DE PABLO  
UNIVERSIDAD DE LA LAGUNA

28/06/2017 13:21:41

penetration for photospheric perturbations. The intensity of the perturbation does not seem to have an influence on the extension of the inferred seismic signal. Besides all this, for the typical sizes of active regions in the real Sun the submerged seismic influence of an isolated active region at the surface remains well above the base of the convection zone.

- We have applied the technique to observational data at two solar minima and have inferred the sound-speed profile with respect to standard model S. It shows an enhancement at  $\approx 0.68 R_{\odot}$  of approximately  $\delta c^2/c^2 \approx 3 \cdot 10^{-3}$ , generally consistent with previous results from global and local helioseismology.
- Using observational data at different time intervals through the solar cycle, we have determined the sound-speed variation between periods of high and low activity. The two main features of the variation profiles are a decrease in sound speed at  $\approx 0.68 R_{\odot}$  of approximately  $\delta c^2/c^2 \approx -4 \cdot 10^{-4}$  and an enhancement below it of approximately  $\delta c^2/c^2 \approx 4 \cdot 10^{-4}$  at high activity with respect to low activity periods. These features are stronger for differences including a maximum with higher activity levels. Although previous results show the decrease and enhancement in sound speed at slightly shallower layers and with lower values, we have explained this discrepancy in terms of the limitations of the current technique and have proposed how to solve it. We have also shown that the method is capable of detecting latitudinal variations and infer sound-speed variations with spatial resolution.
- We have demonstrated that helioseismic holography is capable of detecting solar-cycle variations in sound speed. It is a technique fit to study the evolution of the physical magnitudes at the base of the convection zone and at the tachocline and could prove valuable for improving our knowledge of the solar dynamo. Although the current technique shows certain limitations, we have suggested some experiments that could contribute to a better calibration of it and to assess its response function with respect to depth.

Este documento incorpora firma electrónica, y es copia auténtica de un documento electrónico archivado por la ULL según la Ley 39/2015.  
Su autenticidad puede ser contrastada en la siguiente dirección <https://sede.ull.es/validacion/>

Identificador del documento: 963882

Código de verificación: QDmfX6JG

Firmado por: MANUEL DIAZ ALFARO  
UNIVERSIDAD DE LA LAGUNA

Fecha: 26/06/2017 15:24:15

FERNANDO JAVIER PEREZ HERNANDEZ  
UNIVERSIDAD DE LA LAGUNA

26/06/2017 15:25:57

ERNESTO PEREDA DE PABLO  
UNIVERSIDAD DE LA LAGUNA

28/06/2017 13:21:41

# A

## Appendix: Green's functions

Green's functions constitute one of the main ingredients of helioseismic holography. They convey the acoustic behaviour of a model of the Sun into the process of reconstruction of the seismic field in the solar interior or at the solar surface. In this appendix, we present the full mathematical development to obtain the expression of Green's functions [Equation (2.8)], following Pérez Hernández and González Hernández (2010).

A scalar field  $\Psi$ , defined as:

$$\tilde{\Psi} = -\rho^{-\frac{1}{2}}\delta p, \quad (\text{A.1})$$

where  $\rho$  is the density of the base unperturbed state and  $\delta p$  is a Lagrangian pressure fluctuation, which we assume to have a base state non dependent on time, can be expressed, using Fourier analysis, as a superposition of monochromatic waves:

$$\tilde{\Psi}(r, t) = \Psi(r, \omega)e^{-i\omega t}. \quad (\text{A.2})$$

The wave equation in the adiabatic, Cowling, and plane-parallel approximation for the monochromatic  $\Psi$  is given by—see Gough, 1993; Pérez Hernández and González Hernández, 2010—:

$$\nabla^2\Psi - \frac{\omega_{\text{BV}}^2}{\omega^2}\nabla_{\text{h}}^2\Psi + \frac{1}{c^2}(\omega^2 - \omega_{\text{c}}^2)\Psi = 0, \quad (\text{A.3})$$

where  $\nabla_{\text{h}}^2$  represents the terms including horizontal derivatives in the  $\nabla^2$  operator,  $\omega_{\text{BV}}$  is the Brunt-Väisälä buoyancy frequency,  $c$  is the sound speed, and  $\omega_{\text{c}}$  is the acoustic cut-off frequency.

Shall we introduce the wave operator  $\mathcal{L}$ , which we split into two:

$$\mathcal{L} = \mathcal{L}_0 + \mathcal{L}', \quad (\text{A.4})$$

and which we assume to account for the behaviour of the actual oscillations in the Sun in accordance to:

$$\mathcal{L}\Psi = \mathcal{L}_0\Psi + \mathcal{L}'\Psi = 0, \quad (\text{A.5})$$

Este documento incorpora firma electrónica, y es copia auténtica de un documento electrónico archivado por la ULL según la Ley 39/2015.  
Su autenticidad puede ser contrastada en la siguiente dirección <https://sede.ull.es/validacion/>

Identificador del documento: 963882

Código de verificación: QDmfX6JG

Firmado por: MANUEL DIAZ ALFARO  
UNIVERSIDAD DE LA LAGUNA

Fecha: 26/06/2017 15:24:15

FERNANDO JAVIER PEREZ HERNANDEZ  
UNIVERSIDAD DE LA LAGUNA

26/06/2017 15:25:57

ERNESTO PEREDA DE PABLO  
UNIVERSIDAD DE LA LAGUNA

28/06/2017 13:21:41

where  $\mathcal{L}_0$  includes the terms in equilibrium for a reference model with spherical symmetry and  $\mathcal{L}'$  includes all departures from the reference model, such as due to velocity or magnetic fields, or non-spherical phenomena. Under these considerations, the equilibrium operator  $\mathcal{L}_0$  is given by:

$$\mathcal{L}_0 = \nabla^2 - \frac{\omega_{\text{BV},0}^2}{\omega^2} \nabla_{\text{h}}^2 + \frac{1}{c_0^2} (\omega^2 - \omega_{\text{c},0}^2), \quad (\text{A.6})$$

where  $\omega_{\text{BV},0}$ ,  $c_0$ , and  $\omega_{\text{c},0}$  are the Brunt-Väisälä buoyancy frequency, the sound speed, and the acoustic cut-off frequency of a spherically symmetric reference model.

Green's functions are the solutions of the wave equation for a point source:

$$\mathcal{L}_0 G(\mathbf{r}|\mathbf{r}_0; \omega) = -\delta(\mathbf{r} - \mathbf{r}_0), \quad (\text{A.7})$$

where  $\mathbf{r}$  is the position where the Green's function is evaluated, and  $\mathbf{r}_0$  is the position of the focus.

For a spherically symmetric reference model, we can express the solution to Equation (A.7) in terms of spherical harmonics for each frequency as:

$$G(\mathbf{r}|\mathbf{r}_0) = \sum_{\ell=0}^{\infty} g_{\ell}(r|r_0) \sum_{m=-\ell}^{\ell} Y_{\ell m}^*(\theta_0, \varphi_0) Y_{\ell m}(\theta, \varphi) = \frac{1}{4\pi} \sum_{\ell=0}^{\infty} g_{\ell}(r|r_0) (2\ell+1) P_{\ell}(\mu), \quad (\text{A.8})$$

where  $P_{\ell}(\mu)$  is a Legendre polynomial and

$$\mu = \cos \theta \cos \theta_0 + \sin \theta \sin \theta_0 \cos(\varphi - \varphi_0). \quad (\text{A.9})$$

As the reference model has spherical symmetry, we can direct the polar axis in the direction of the focus. Thus,  $\theta_0 = 0$  and  $\varphi_0 = 0$ , and the argument of the Legendre polynomial in Equation (A.8) reduces to

$$\mu = \cos \theta. \quad (\text{A.10})$$

Equation (A.8) can be expressed as the product of a term including all the radial dependencies by another containing all the angular dependencies:

$$G(\mathbf{r}|\mathbf{r}_0) = \frac{1}{4\pi} \sum_{\ell=0}^{\infty} G_{\ell}^r G_{\ell}^{\theta}, \quad (\text{A.11})$$

where the radial components are given by:

$$G_{\ell}^r = g_{\ell}(r|r_0), \quad (\text{A.12})$$

and the angular ones by:

$$G_{\ell}^{\theta} = (2\ell+1) P_{\ell}(\cos \theta). \quad (\text{A.13})$$

We can use this premise to split Equation (A.7) into two separate equations for the radial and angular dependencies.

Este documento incorpora firma electrónica, y es copia auténtica de un documento electrónico archivado por la ULL según la Ley 39/2015.  
Su autenticidad puede ser contrastada en la siguiente dirección <https://sede.ull.es/validacion/>

Identificador del documento: 963882

Código de verificación: QDmfX6JG

Firmado por: MANUEL DIAZ ALFARO  
UNIVERSIDAD DE LA LAGUNA

Fecha: 26/06/2017 15:24:15

FERNANDO JAVIER PEREZ HERNANDEZ  
UNIVERSIDAD DE LA LAGUNA

26/06/2017 15:25:57

ERNESTO PEREDA DE PABLO  
UNIVERSIDAD DE LA LAGUNA

28/06/2017 13:21:41

### A.1 Angular part

Equation (A.13) can be decomposed into prograde and retrograde solutions by solving the following equation for the Legendre polynomials:

$$\frac{d^2 Q_\ell(\theta)}{d\theta^2} + k_\ell^2 Q_\ell(\theta) = 0, \quad (\text{A.14})$$

where

$$Q_\ell(\theta) = \sqrt{\sin \theta} P_\ell(\cos \theta), \quad (\text{A.15})$$

and  $k_\ell$  is the angular component of the wave vector, given by

$$k_\ell = \left( \ell + \frac{1}{2} \right)^2 + \frac{1}{4 \sin^2 \theta}. \quad (\text{A.16})$$

We split the angular solution  $Q_\ell(\theta)$  into a prograde and retrograde terms, which in a first-order Liouville-Green expansion can be written as:

$$Q_\ell(\theta) = \beta_{\ell+}(\theta) B_{\ell+}(\theta) + \beta_{\ell-}(\theta) B_{\ell-}(\theta), \quad (\text{A.17})$$

with

$$B_{\ell\pm} = k_\ell^{-\frac{1}{2}} \exp \left( \pm i \int_{\theta_0}^{\theta} k_\ell d\theta \right), \quad (\text{A.18})$$

where  $\theta_0$  refers to the focal angular position. In the asymptotic approximation, not used for the angular dependency, the  $\beta_{\ell\pm}$ -parameters would be assumed to be constant. However, here we consider them as osculating parameters that have a smooth variation, and, hence, we can impose the following additional condition on the derivatives of Equation (A.17):

$$\frac{dQ_\ell(\theta)}{d\theta} = \beta_{\ell+}(\theta) \frac{dB_{\ell+}(\theta)}{d\theta} + \beta_{\ell-}(\theta) \frac{dB_{\ell-}(\theta)}{d\theta}. \quad (\text{A.19})$$

From the system of equations formed by Equations (A.17) and (A.19) we can express  $\beta_{\ell\pm}$  in terms of  $Q_\ell$ ,  $B_\ell$  and their derivatives:

$$\beta_{\ell\pm} = \pm \frac{i}{2} \left( Q_\ell \frac{dB_{\ell\mp}}{d\theta} - \frac{dQ_\ell}{d\theta} B_{\ell\mp} \right). \quad (\text{A.20})$$

Taking Equation (A.13) and combining it with Equation (A.15):

$$G_\ell^\theta = (2\ell + 1) P_\ell(\cos \theta) = (2\ell + 1) \csc^{\frac{1}{2}} \theta \cdot Q_\ell, \quad (\text{A.21})$$

we can express the angular prograde ( $G_\ell^{\theta+}$ ) and retrograde ( $G_\ell^{\theta-}$ ) dependencies of Green's equation as:

$$G_\ell^{\theta\pm} = (2\ell + 1) P_\ell(\cos \theta) = (2\ell + 1) \csc^{\frac{1}{2}} \theta \cdot B_{\ell\pm} \left[ \pm \frac{i}{2} \left( Q_\ell \frac{dB_{\ell\mp}}{d\theta} - \frac{dQ_\ell}{d\theta} B_{\ell\mp} \right) \right], \quad (\text{A.22})$$

where,  $B_{\ell\pm}$  and  $Q_\ell$  are given by Equations (A.18) and (A.15) respectively. We have not considered the asymptotic approximation here; therefore, we can expect higher precision in the application of these Green's functions for low or intermediate angular degrees  $\ell$ .

Este documento incorpora firma electrónica, y es copia auténtica de un documento electrónico archivado por la ULL según la Ley 39/2015.  
Su autenticidad puede ser contrastada en la siguiente dirección <https://sede.ull.es/validacion/>

Identificador del documento: 963882

Código de verificación: QDmfX6JG

Firmado por: MANUEL DIAZ ALFARO  
UNIVERSIDAD DE LA LAGUNA

Fecha: 26/06/2017 15:24:15

FERNANDO JAVIER PEREZ HERNANDEZ  
UNIVERSIDAD DE LA LAGUNA

26/06/2017 15:25:57

ERNESTO PEREDA DE PABLO  
UNIVERSIDAD DE LA LAGUNA

28/06/2017 13:21:41

## A.2 Radial part

Inserting Equation (A.11) into Equation (A.7), after some mathematical manipulation, we reach:

$$\frac{d^2 \tilde{g}_\ell}{dr^2} + k_r^2 \tilde{g}_\ell = 0 : r \neq r_0, \quad (\text{A.23})$$

where the radial variable  $\tilde{g}_\ell(r)$  is defined as:

$$\tilde{g}_\ell(r) = r g_\ell \quad (\text{A.24})$$

and where the radial component  $k_r$  of the local wave vector verifies the equation:

$$k_r^2 = \frac{\omega^2 - \omega_c^2}{c^2} - k_h^2 \left( 1 - \frac{\omega_{\text{BV}}^2}{\omega^2} \right), \quad (\text{A.25})$$

with the horizontal component  $k_h$  expressed as:

$$k_h^2 = \frac{\ell(\ell+1)}{r^2}. \quad (\text{A.26})$$

Using a Liouville-Green expansion of first order, as in the angular case (Section A.1), the solution for the radial dependencies can be expressed in terms of the superposition of an ingoing and an outgoing contribution as:

$$\tilde{g}_\ell(r) = \alpha_{\ell+} C_{\ell+} + \alpha_{\ell-} C_{\ell-}, \quad (\text{A.27})$$

where we apply the asymptotic approximation, *i.e.* we consider that the parameters  $\alpha_{\ell+}$  and  $\alpha_{\ell-}$  are constant, and  $C_{\ell\pm}$  are expressed as:

$$C_{\ell\pm}(r) = k_r^{-\frac{1}{2}} \exp\left(\pm i \int_{r_1}^r k_r dr\right), \quad (\text{A.28})$$

where the radial component  $k_r$  of the local wave vector follows the expression shown in Equation (A.25) and  $r_1$  is the inner turning point.

From Equation (A.7) we obtain the following inhomogeneous initial conditions for Equation (A.23):

$$\tilde{g}_\ell(r_0^- | r_0) = \tilde{g}_\ell(r_0^+ | r_0) \quad (\text{A.29})$$

and

$$\frac{d\tilde{g}_\ell}{dr}(r_0^+ | r_0) - \frac{d\tilde{g}_\ell}{dr}(r_0^- | r_0) = -\frac{1}{r_0}. \quad (\text{A.30})$$

Making some mathematical calculations and introducing Equation (A.28) into the initial conditions [Equations (A.29) and (A.30)], we get the following expression for the constants  $\alpha_{\ell\pm}$ :

$$\alpha_{\ell\pm} = \frac{i}{2r_0} \frac{1}{\sqrt{k_r(r_0)}} \exp\left(\mp i \int_{r_1}^{r_0} k_r dr\right). \quad (\text{A.31})$$

Este documento incorpora firma electrónica, y es copia auténtica de un documento electrónico archivado por la ULL según la Ley 39/2015.  
Su autenticidad puede ser contrastada en la siguiente dirección <https://sede.ull.es/validacion/>

Identificador del documento: 963882

Código de verificación: QDmfX6JG

Firmado por: MANUEL DIAZ ALFARO  
UNIVERSIDAD DE LA LAGUNA

Fecha: 26/06/2017 15:24:15

FERNANDO JAVIER PEREZ HERNANDEZ  
UNIVERSIDAD DE LA LAGUNA

26/06/2017 15:25:57

ERNESTO PEREDA DE PABLO  
UNIVERSIDAD DE LA LAGUNA

28/06/2017 13:21:41

For one-skip holography, the expression for the radial dependencies for the outgoing ( $G_\ell^+$ ) and ingoing ( $G_\ell^-$ ) Green's functions reduces to:

$$\begin{aligned} G_\ell^{r\pm} &= \frac{\tilde{g}_\ell^\pm}{r} = \frac{1}{r} \alpha_{\ell\pm} C_{\ell\pm} = \frac{1}{r} \frac{i}{2r_0} \frac{1}{\sqrt{k_r(r_0)}} \exp\left(\mp i \int_{r_1}^{r_0} k_r dr\right) k_r^{-\frac{1}{2}} \exp\left(\pm i \int_{r_1}^r k_r dr\right) \\ &= \frac{i}{2r_0} \frac{1}{\sqrt{k_r(r_0)}} \frac{1}{r} k_r^{-\frac{1}{2}} \exp\left(\pm i \int_{r_0}^r k_r dr\right). \end{aligned} \quad (\text{A.32})$$

If additional bounces are considered, we would have to introduce a phase shift equals to twice the integral of the radial component of the wave vector between the inner and outer turning points for every bounce of the wave at the outer turning points and a phase shift of  $-\pi/2$  introduced by every reflection.

### A.3 Full expression

Combining the outgoing solution to the radial dependencies together with the prograde solution to the angular dependencies, and the ingoing with the retrograde solutions, we get:

$$G_\ell^\pm = \frac{i(2\ell+1)}{8\pi r_0 \sqrt{k_r(r_0)}} r^{-1} k_r^{-\frac{1}{2}} \csc^{\frac{1}{2}} \theta \cdot B_{\ell\pm} \left[ \frac{i}{2} \left( Q_\ell \frac{dB_{\ell\mp}}{d\theta} - \frac{dQ_\ell}{d\theta} B_{\ell\mp} \right) \right] \exp\left(\pm i \int_{r_0}^r k_r^2 dr\right). \quad (\text{A.33})$$

In this thesis we use the previous expression to calculate outgoing Green's functions for each value of angular order  $\ell$  and each frequency within the resonant cavity, between the reflection points given by  $k_r^2 = 0$ . Nevertheless, as for simplicity we are considering only a cosinusoidal function instead of using it together with the Airy function, which is the solution of Equation (A.7) near the turning points, this proposed solution diverges from the real solution in the vicinities of them as shown in Section 2.3. This issue is solved by making Green's function equal to 0 at the points below its first zero above the inner turning point.

In order to get the global Green's function for every frequency, we add first Green's function for each angular order  $\ell$ :

$$G^+(\mathbf{r}|\mathbf{r}_0, \omega) = \sum_{\ell=\ell_1}^{\ell_2} G_\ell^+, \quad (\text{A.34})$$

where  $\ell_1$  and  $\ell_2$  are the lower and higher angular degrees compatible with the geometry of the considered pupils. Green's functions are normalized for each considered frequency, in order to obtain the same weight for each of them:

$$G_{\text{norm}}^+(\mathbf{r}|\mathbf{r}_0, \omega) = \frac{G^+(\mathbf{r}|\mathbf{r}_0, \omega)}{\langle |G^+(\mathbf{r}|\mathbf{r}_0, \omega)| \rangle}. \quad (\text{A.35})$$

Este documento incorpora firma electrónica, y es copia auténtica de un documento electrónico archivado por la ULL según la Ley 39/2015.  
Su autenticidad puede ser contrastada en la siguiente dirección <https://sede.ull.es/validacion/>

Identificador del documento: 963882

Código de verificación: QDmfX6JG

Firmado por: MANUEL DIAZ ALFARO  
UNIVERSIDAD DE LA LAGUNA

Fecha: 26/06/2017 15:24:15

FERNANDO JAVIER PEREZ HERNANDEZ  
UNIVERSIDAD DE LA LAGUNA

26/06/2017 15:25:57

ERNESTO PEREDA DE PABLO  
UNIVERSIDAD DE LA LAGUNA

28/06/2017 13:21:41

As it can be shown that the ingoing Green's function is the complex conjugate of the outgoing one, we make use of this to compute ingoing Green's functions after the computation of outgoing ones:

$$G_- = G_+^*. \quad (\text{A.36})$$

Este documento incorpora firma electrónica, y es copia auténtica de un documento electrónico archivado por la ULL según la Ley 39/2015.  
Su autenticidad puede ser contrastada en la siguiente dirección <https://sede.ull.es/validacion/>

Identificador del documento: 963882

Código de verificación: QDmfX6JG

Firmado por: MANUEL DIAZ ALFARO  
UNIVERSIDAD DE LA LAGUNA

Fecha: 26/06/2017 15:24:15

FERNANDO JAVIER PEREZ HERNANDEZ  
UNIVERSIDAD DE LA LAGUNA

26/06/2017 15:25:57

ERNESTO PEREDA DE PABLO  
UNIVERSIDAD DE LA LAGUNA

28/06/2017 13:21:41

## References

- Antia, H.M., Basu, S.: 2011, Revisiting the solar tachocline: Average properties and temporal variations. *Astrophys. J. Lett.* **735**, L45.
- Babcock, H.D.: 1959, The Sun's polar magnetic field. *Astrophys. J.* **130**, 364.
- Babcock, H.W.: 1961, The topology of the Sun's magnetic field and the 22-year cycle. *Astrophys. J.* **133**, 572.
- Backus, G., Gilbert, F.: 1968, The resolving power of gross Earth data. *Geophys. J.* **16**, 169.
- Baldner, C.S., Basu, S.: 2008, Solar cycle related changes at the base of the convection zone. *Astrophys. J.* **686**, 1349.
- Baldner, C.S., Basu, S., Bogart, R.S., Burtseva, O., González Hernández, I., Haber, D., Hill, F., Howe, R., Jain, K., Komm, R.W., Rabello-Soares, M.C., Tripathy, S.: 2013, Latest results found with ring-diagram analysis. *Sol. Phys.* **287**, 57.
- Balmaceda, L.A., Solanki, S.K., Krivova, N.A., Foster, S.: 2009, A homogeneous database of sunspot areas covering more than 130 years. *Journal of Geophysical Research (Space Physics)* **114**, A07104.
- Baranyi, T., Gyori, L., Ludmány, A., Coffey, H.E.: 2001, Comparison of sunspot area data bases. *Mon. Not. Roy. Astron. Soc.* **323**, 223.
- Barnes, G., Birch, A.C., Leka, K.D., Braun, D.C.: 2014, Helioseismology of pre-emerging active regions. III. Statistical analysis. *Astrophys. J.* **786**, 19.
- Basu, S.: 1997, Seismology of the base of the solar convection zone. *Mon. Not. Roy. Astron. Soc.* **288**, 572.
- Basu, S., Antia, H.M.: 2003, Changes in solar dynamics from 1995 to 2002. *Astrophys. J.* **585**, 553.
- Basu, S., Antia, H.M., Bogart, R.S.: 2004, Ring-diagram analysis of the structure of solar active regions. *Astrophys. J.* **610**, 1157.
- Basu, S., Antia, H.M., Tripathy, S.C.: 1999, Ring diagram analysis of near-surface flows in the Sun. *Astrophys. J.* **512**, 458.

Este documento incorpora firma electrónica, y es copia auténtica de un documento electrónico archivado por la ULL según la Ley 39/2015.  
Su autenticidad puede ser contrastada en la siguiente dirección <https://sede.ull.es/validacion/>

Identificador del documento: 963882

Código de verificación: QDmfX6JG

Firmado por: MANUEL DIAZ ALFARO  
UNIVERSIDAD DE LA LAGUNA

Fecha: 26/06/2017 15:24:15

FERNANDO JAVIER PEREZ HERNANDEZ  
UNIVERSIDAD DE LA LAGUNA

26/06/2017 15:25:57

ERNESTO PEREDA DE PABLO  
UNIVERSIDAD DE LA LAGUNA

28/06/2017 13:21:41

- Beeck, B., Cameron, R.H., Reiners, A., Schüssler, M.: 2013a, Three-dimensional simulations of near-surface convection in main-sequence stars. I. Overall structure. *Astron. Astrophys.* **558**, A48.
- Beeck, B., Cameron, R.H., Reiners, A., Schüssler, M.: 2013b, Three-dimensional simulations of near-surface convection in main-sequence stars. II. Properties of granulation and spectral lines. *Astron. Astrophys.* **558**, A49.
- Beeck, B., Schüssler, M., Cameron, R.H., Reiners, A.: 2015a, Three-dimensional simulations of near-surface convection in main-sequence stars. III. The structure of small-scale magnetic flux concentrations. *Astron. Astrophys.* **581**, A42.
- Beeck, B., Schüssler, M., Cameron, R.H., Reiners, A.: 2015b, Three-dimensional simulations of near-surface convection in main-sequence stars. IV. Effect of small-scale magnetic flux concentrations on centre-to-limb variation and spectral lines. *Astron. Astrophys.* **581**, A43.
- Beer, J., Blinov, A., Bonani, G., Hofmann, H.J., Finkel, R.C.: 1990, Use of  $^{10}\text{Be}$  in polar ice to trace the 11-year cycle of solar activity. *Nature* **347**, 164.
- Biermann, L.: 1946, Zur Deutung der chromosphärischen Turbulenz und des Exzesses der UV-Strahlung der Sonne. *Naturwissenschaften* **33**(4), 118.
- Birch, A.C., Braun, D.C., Leka, K.D., Barnes, G., Javornik, B.: 2013, Helioseismology of pre-emerging active regions. II. Average emergence properties. *Astrophys. J.* **762**, 131.
- Brandenburg, A.: 2005, The case for a distributed solar dynamo shaped by near-surface shear. *Astrophys. J.* **625**, 539.
- Braun, D.C.: 1995, Scattering of p-modes by sunspots. I. Observations. *Astrophys. J.* **451**, 859.
- Braun, D.C.: 2014, Helioseismic holography of an artificial submerged sound speed perturbation and implications for the detection of pre-emergence signatures of active regions. *Sol. Phys.* **289**, 459.
- Braun, D.C., Lindsey, C.: 1999, Helioseismic images of an active region complex. *Astrophys. J. Lett.* **513**, L79.
- Braun, D.C., Lindsey, C.: 2000, Phase-sensitive holography of solar activity. *Sol. Phys.* **192**, 307.
- Braun, D.C., Lindsey, C.: 2001, Seismic imaging of the far hemisphere of the Sun. *Astrophys. J. Lett.* **560**, L189.
- Braun, D.C., Birch, A.C., Lindsey, C.: 2004, Local helioseismology of near-surface flows. In: Danesy, D. (ed.) *SOHO 14. Helio- and asteroseismology: towards a golden future*, *ESA Special Publication* **559**, 337.

Este documento incorpora firma electrónica, y es copia auténtica de un documento electrónico archivado por la ULL según la Ley 39/2015.  
Su autenticidad puede ser contrastada en la siguiente dirección <https://sede.ull.es/validacion/>

Identificador del documento: 963882

Código de verificación: QDmfX6JG

Firmado por: MANUEL DIAZ ALFARO  
UNIVERSIDAD DE LA LAGUNA

Fecha: 26/06/2017 15:24:15

FERNANDO JAVIER PEREZ HERNANDEZ  
UNIVERSIDAD DE LA LAGUNA

26/06/2017 15:25:57

ERNESTO PEREDA DE PABLO  
UNIVERSIDAD DE LA LAGUNA

28/06/2017 13:21:41

- Braun, D.C., Duvall, T.L. Jr., Labonte, B.J.: 1987, Acoustic absorption by sunspots. *Astrophys. J. Lett.* **319**, L27.
- Braun, D.C., Duvall, T.L. Jr., Labonte, B.J.: 1988, The absorption of high-degree p-mode oscillations in and around sunspots. *Astrophys. J.* **335**, 1015.
- Braun, D.C., Duvall, T.L. Jr., Labonte, B.J., Jefferies, S.M., Harvey, J.W., Pomerantz, M.A.: 1992, Scattering of p-modes by a sunspot. *Astrophys. J. Lett.* **391**, L113.
- Braun, D.C., Lindsey, C., Fan, Y., Fagan, M.: 1998, Seismic holography of solar activity. *Astrophys. J.* **502**, 968.
- Braun, D.C., Birch, A.C., Rempel, M., Duvall, T.L.: 2012, Helioseismology of a realistic magnetoconvective sunspot simulation. *Astrophys. J.* **744**, 77.
- Brown, T.M., Christensen-Dalsgaard, J., Dziembowski, W.A., Goode, P., Gough, D.O., Morrow, C.A.: 1989, Inferring the Sun's internal angular velocity from observed p-mode frequency splittings. *Astrophys. J.* **343**, 526.
- Carrington, R.C.: 1858, On the distribution of the solar spots in latitudes since the beginning of the year 1854, with a map. *Mon. Not. Roy. Astron. Soc.* **19**, 1.
- Carrington, R.C.: 1859, On certain phenomena in the motions of solar spots. *Mon. Not. Roy. Astron. Soc.* **19**, 81.
- Chang, H.-K., Chou, D.-Y., Labonte, B., TON Team: 1997, Ambient acoustic imaging in helioseismology. *Nature* **389**, 825.
- Chaplin, W.J.: 2006, *Music of the Sun*. ISBN 9781851684519.
- Charbonneau, P.: 2010, Dynamo models of the solar cycle. *Living Reviews in Solar Physics* **7**.
- Charbonneau, P., MacGregor, K.B.: 1997, Solar interface dynamos. II. Linear, kinematic models in spherical geometry. *Astrophys. J.* **486**, 502.
- Charbonneau, P., Christensen-Dalsgaard, J., Henning, R., Larsen, R.M., Schou, J., Thompson, M.J., Tomczyk, S.: 1999, Helioseismic constraints on the structure of the solar tachocline. *Astrophys. J.* **527**, 445.
- Cheung, M.C.M., Rempel, M., Title, A.M., Schüssler, M.: 2010, Simulation of the formation of a solar active region. *Astrophys. J.* **720**, 233.
- Chou, D.-Y., Serebryanskiy, A.: 2002, Searching for the signature of the magnetic fields at the base of the solar convection zone with solar cycle variations of p-mode travel time. *Astrophys. J. Lett.* **578**, L157.
- Chou, D.-Y., Serebryanskiy, A.: 2005, In search of the solar cycle variations of p-mode frequencies generated by perturbations in the solar interior. *Astrophys. J.* **624**, 420.
- Chou, D.-Y., Sun, M.-T., Huang, T.-Y., Lai, S.-P., Chi, P.-J., Ou, K.-T., Wang, C.-C., Lu, J.-Y., Chu, A.-L., Niu, C.-S., Mu, T.-M., Chen, K.-R., Chou, Y.-P., Jimenez, A., Rabello-Soares, M.C., Chao, H., Ai, G., Wang, G.-P., Zirin,

Este documento incorpora firma electrónica, y es copia auténtica de un documento electrónico archivado por la ULL según la Ley 39/2015.  
Su autenticidad puede ser contrastada en la siguiente dirección <https://sede.ull.es/validacion/>

Identificador del documento: 963882

Código de verificación: QDmfX6JG

Firmado por: MANUEL DIAZ ALFARO  
UNIVERSIDAD DE LA LAGUNA

Fecha: 26/06/2017 15:24:15

FERNANDO JAVIER PEREZ HERNANDEZ  
UNIVERSIDAD DE LA LAGUNA

26/06/2017 15:25:57

ERNESTO PEREDA DE PABLO  
UNIVERSIDAD DE LA LAGUNA

28/06/2017 13:21:41

- H., Marquette, W., Nenow, J.: 1995, Taiwan Oscillation Network. *Sol. Phys.* **160**, 237.
- Chou, D.-Y., Serebryanskiy, A., Sun, M.-T., TON Team: 2003, Acoustic imaging and time-distance analysis of TON. In: Sawaya-Lacoste, H. (ed.) *GONG+ 2002. Local and global helioseismology: the present and future*, ESA Special Publication **517**, 53.
- Christensen-Dalsgaard, J., Dappen, W., Ajukov, S.V., Anderson, E.R., Antia, H.M., Basu, S., Baturin, V.A., Berthomieu, G., Chaboyer, B., Chitre, S.M., Cox, A.N., Demarque, P., Donatowicz, J., Dziembowski, W.A., Gabriel, M., Gough, D.O., Guenther, D.B., Guzik, J.A., Harvey, J.W., Hill, F., Houdek, G., Iglesias, C.A., Kosovichev, A.G., Leibacher, J.W., Morel, P., Proffitt, C.R., Provost, J., Reiter, J., Rhodes, E.J. Jr., Rogers, F.J., Roxburgh, I.W., Thompson, M.J., Ulrich, R.K.: 1996, The current state of solar modeling. *Science* **272**, 1286.
- Claerbout, J.F.: 1985, *Imaging the earth's interior*, Blackwell Scientific Publications, Inc., Cambridge, MA, USA. ISBN 9780865423046.
- Claverie, A., Isaak, G.R., McLeod, C.P., van der Raay, H.B., Roca Cortés, T.: 1979, Solar structure from global studies of the 5-minute oscillation. *Nature* **282**, 591.
- Clette, F., Svalgaard, L., Vaquero, J.M., Cliver, E.W.: 2014, Revisiting the sunspot number. A 400-year perspective on the solar cycle. *Space Sci. Rev.* **186**, 35.
- Cook, J., Nuccitelli, D., Green, S.A., Richardson, R., Winkler, B., Painting, R., Way, R., Jacobs, P., Skuce, A.: 2013, Quantifying the consensus on anthropogenic global warming in the scientific literature. *Environ. Res. Lett.* **8**(2), 024024.
- Cook, J., Oreskes, N., Doran, P.T., Anderegg, W.R.K., Verheggen, B., Maibach, E.W., Carlton, J.S., Lewandowsky, S., Skuce, A.G., Green, S.A., Nuccitelli, D., Jacobs, P., Richardson, M., Winkler, B., Painting, R., Rice, K.: 2016, Consensus on consensus: A synthesis of consensus estimates on human-caused global warming. *Environ. Res. Lett.* **11**(4), 048002.
- Corbard, T., Blanc-Féraud, L., Berthomieu, G., Provost, J.: 1999, Non linear regularization for helioseismic inversions. Application for the study of the solar tachocline. *Astron. Astrophys.* **344**, 696.
- Couvidat, S., Birch, A.C., Kosovichev, A.G.: 2006, Three-dimensional inversion of sound speed below a sunspot in the Born approximation. *Astrophys. J.* **640**, 516.
- Covington, A.E.: 1969, Solar radio emission at 10.7 cm, 1947-1968. *J. Roy. Astron. Soc. Can.* **63**, 125.
- Cuntz, M., Ulmschneider, P., Musielak, Z.E.: 1998, Self-consistent and time-dependent magnetohydrodynamic chromosphere models for magnetically

Este documento incorpora firma electrónica, y es copia auténtica de un documento electrónico archivado por la ULL según la Ley 39/2015.  
Su autenticidad puede ser contrastada en la siguiente dirección <https://sede.ull.es/validacion/>

Identificador del documento: 963882

Código de verificación: QDmfX6JG

Firmado por: MANUEL DIAZ ALFARO  
UNIVERSIDAD DE LA LAGUNA

Fecha: 26/06/2017 15:24:15

FERNANDO JAVIER PEREZ HERNANDEZ  
UNIVERSIDAD DE LA LAGUNA

26/06/2017 15:25:57

ERNESTO PEREDA DE PABLO  
UNIVERSIDAD DE LA LAGUNA

28/06/2017 13:21:41

- active stars. *Astrophys. J. Lett.* **493**, L117.
- DeGrave, K., Jackiewicz, J., Rempel, M.: 2014a, Time-distance helioseismology of two realistic sunspot simulations. *Astrophys. J.* **794**, 18.
- DeGrave, K., Jackiewicz, J., Rempel, M.: 2014b, Validating time-distance helioseismology with realistic quiet-Sun simulations. *Astrophys. J.* **788**, 127.
- Deubner, F.-L.: 1975, Observations of low wavenumber nonradial eigenmodes of the Sun. *Astron. Astrophys.* **44**, 371.
- Deubner, F.-L., Gough, D.: 1984, Helioseismology: oscillations as a diagnostic of the solar interior. *Annu. Rev. Astron. Astrophys.* **22**, 593.
- Díaz Alfaro, M., Pérez Hernández, F., González Hernández, I., Hartlep, T.: 2013, Active region position effects on seismic holography maps. In: Jain, K., Tripathy, S.C., Hill, F., Leibacher, J.W., Pevtsov, A.A. (eds.) *Fifty years of seismology of the Sun and stars*, *ASP Conf. Ser.* **478**, 317.
- Díaz Alfaro, M., Pérez Hernández, F., González Hernández, I., Hartlep, T.: 2016, Seismic holography of the solar interior near the maximum and minimum of solar activity. *Sol. Phys.* **291**, 1323.
- Dikpati, M., Charbonneau, P.: 1999, A Babcock-Leighton flux transport dynamo with solar-like differential rotation. *Astrophys. J.* **518**, 508.
- Donea, A.-C., Besliu-Ionescu, D., Cally, P.S., Lindsey, C., Zharkova, V.V.: 2006, Seismic emission from a M9.5-class solar flare. *Sol. Phys.* **239**, 113.
- Dorch, S.B.F., Nordlund, Å.: 2001, On the transport of magnetic fields by solar-like stratified convection. *Astron. Astrophys.* **365**, 562.
- Durney, B.R., De Young, D.S., Passot, T.P.: 1990, On the generation of the solar magnetic field in a region of weak buoyancy. *Astrophys. J.* **362**, 709.
- Duvall, T.L. Jr., Jefferies, S.M., Harvey, J.W., Pomerantz, M.A.: 1993, Time-distance helioseismology. *Nature* **362**, 430.
- Duvall, T.L. Jr., Kosovichev, A.G., Scherrer, P.H., Bogart, R.S., Bush, R.I., de Forest, C., Hoeksema, J.T., Schou, J., Saba, J.L.R., Tarbell, T.D., Title, A.M., Wolfson, C.J., Milford, P.N.: 1997, Time-distance helioseismology with the MDI instrument: Initial results. *Sol. Phys.* **170**, 63.
- Duvall, T.L., D'Silva, S., Jefferies, S.M., Harvey, J.W., Schou, J.: 1996, Downflows under sunspots detected by helioseismic tomography. *Nature* **379**, 235.
- Dziembowski, W.A., Goode, P.R., Schou, J.: 2001, Does the Sun shrink with increasing magnetic activity? *Astrophys. J.* **553**, 897.
- Eff-Darwich, A., Korzennik, S.G., Jiménez-Reyes, S.J., Pérez Hernández, F.: 2002, An upper limit on the temporal variations of the solar interior stratification. *Astrophys. J.* **580**, 574.
- Elliott, J.R., Gough, D.O.: 1999, Calibration of the thickness of the solar tachocline. *Astrophys. J.* **516**, 475.

Este documento incorpora firma electrónica, y es copia auténtica de un documento electrónico archivado por la ULL según la Ley 39/2015.  
Su autenticidad puede ser contrastada en la siguiente dirección <https://sede.ull.es/validacion/>

Identificador del documento: 963882

Código de verificación: QDmfX6JG

Firmado por: MANUEL DIAZ ALFARO  
UNIVERSIDAD DE LA LAGUNA

Fecha: 26/06/2017 15:24:15

FERNANDO JAVIER PEREZ HERNANDEZ  
UNIVERSIDAD DE LA LAGUNA

26/06/2017 15:25:57

ERNESTO PEREDA DE PABLO  
UNIVERSIDAD DE LA LAGUNA

28/06/2017 13:21:41

- Ermolli, I., Shibasaki, K., Tlatov, A., van Driel-Gesztelyi, L.: 2014, Solar cycle indices from the photosphere to the corona: Measurements and underlying physics. *Space Sci. Rev.* **186**, 105.
- Felipe, T., Khomenko, E., Collados, M.: 2011, Magnetoacoustic wave energy from numerical simulations of an observed sunspot umbra. *Astrophys. J.* **735**, 65.
- Fligge, M., Solanki, S.K.: 1997, Inter-cycle variations of solar irradiance: Sunspot areas as a pointer. *Sol. Phys.* **173**, 427.
- Fontenla, J.M., Quémerais, E., González Hernández, I., Lindsey, C., Haberreiter, M.: 2009, Solar irradiance forecast and far-side imaging. *Adv. Space Res.* **44**, 457.
- Giles, P.M., Duvall, T.L., Scherrer, P.H., Bogart, R.S.: 1997, A subsurface flow of material from the Sun's equator to its poles. *Nature* **390**, 52.
- Gizon, L., Birch, A.C.: 2002, Time-distance helioseismology: the forward problem for random distributed sources. *Astrophys. J.* **571**, 966.
- Gizon, L., Birch, A.C.: 2004, Time-distance helioseismology: noise estimation. *Astrophys. J.* **614**, 472.
- Gizon, L., Birch, A.C.: 2005, Local helioseismology. *Living Rev. Solar Phys.* **2**.
- Gleißberg, W.: 1939, A long-periodic fluctuation of the Sun-spot numbers. *The Observatory* **62**, 158.
- Goldreich, P., Keeley, D.A.: 1977, Solar seismology. II - The stochastic excitation of the solar p-modes by turbulent convection. *Astrophys. J.* **212**, 243.
- González Hernández, I.: 2013, Helioseismology in space weather. In: Jain, K., Tripathy, S.C., Hill, F., Leibacher, J.W., Pevtsov, A.A. (eds.) *Fifty years of seismology of the Sun and stars*, *ASP Conf. Ser.* **478**, 309.
- González Hernández, I., Hill, F., Lindsey, C.: 2007, Calibration of seismic signatures of active regions on the far side of the Sun. *Astrophys. J.* **669**, 1382.
- González Hernández, I., Scherrer, P., Hill, F.: 2009, A new way to infer variations of the seismic solar radius. *Astrophys. J. Lett.* **691**, L87.
- González Hernández, I., Patrón, J., Roca Cortés, T., Pérez Hernández, F., Jiménez, A., Jiménez-Reyes, S.J., Martín, I., Pallé, P.L., Régulo, C.: 1998, Probing the solar subphotospheric layers using ring analysis. *Astrophys. Space Sci.* **263**, 335.
- González Hernández, I., Patrón, J., Bogart, R.S., SOI Ring Diagram Team, T.: 1999, Meridional flows from ring diagram analysis. *Astrophys. J. Lett.* **510**, L153.

Este documento incorpora firma electrónica, y es copia auténtica de un documento electrónico archivado por la ULL según la Ley 39/2015.  
Su autenticidad puede ser contrastada en la siguiente dirección <https://sede.ull.es/validacion/>

Identificador del documento: 963882

Código de verificación: QDmfX6JG

Firmado por: MANUEL DIAZ ALFARO  
UNIVERSIDAD DE LA LAGUNA

Fecha: 26/06/2017 15:24:15

FERNANDO JAVIER PEREZ HERNANDEZ  
UNIVERSIDAD DE LA LAGUNA

26/06/2017 15:25:57

ERNESTO PEREDA DE PABLO  
UNIVERSIDAD DE LA LAGUNA

28/06/2017 13:21:41

- González Hernández, I., Lindsey, C., Braun, D.C., Bogart, R.S., Scherrer, P.H., Hill, F.: 2013, Far-side helioseismic maps: the next generation. *JPCS* **440**(1), 012029.
- González Hernández, I., Díaz Alfaro, M., Jain, K., Tobiska, W.K., Braun, D.C., Hill, F., Pérez Hernández, F.: 2014, A full-Sun magnetic index from helioseismology inferences. *Sol. Phys.* **289**, 503.
- Gough, D.O.: 1984, On the rotation of the Sun. *Phil. Trans. R. Soc. Lon. A* **313**, 27.
- Gough, D.O.: 1993, Linear adiabatic stellar pulsation. In: Zahn, J.-P., Zinn-Justin, J. (eds.) *Astrophysical fluid dynamics, Les Houches session LXVII*, 399.
- Gough, D.O., Kosovichev, A.G., Toomre, J., Anderson, E., Antia, H.M., Basu, S., Chaboyer, B., Chitre, S.M., Christensen-Dalsgaard, J., Dziembowski, W.A., Eff-Darwich, A., Elliott, J.R., Giles, P.M., Goode, P.R., Guzik, J.A., Harvey, J.W., Hill, F., Leibacher, J.W., Monteiro, M.J.P.F.G., Richard, O., Sekii, T., Shibahashi, H., Takata, M., Thompson, M.J., Vauclair, S., Vorontsov, S.V.: 1996, The seismic structure of the Sun. *Science* **272**, 1296.
- Hagedoorn, J.G.: 1954, A process of seismic reflection interpretation. *Geophys. Prospecting* **2**(2), 85.
- Haigh, J.D.: 2007, The Sun and the Earth's climate. *Living Reviews in Solar Physics* **4**.
- Hale, G.E.: 1908, On the probable existence of a magnetic field in Sun-spots. *Astrophys. J.* **28**, 315.
- Hale, G.E., Ellerman, F., Nicholson, S.B., Joy, A.H.: 1919, The magnetic polarity of Sun-spots. *Astrophys. J.* **49**, 153.
- Hansen, P.C.: 1998, *Rank-deficient and discrete ill-posed problems: numerical aspects of linear inversion*, SIAM Monographs on Mathematical Modeling and Computation, SIAM, Philadelphia, U.S.A..
- Hartlep, T., Mansour, N.N.: 2004, Solar convection simulations using a B-spline method. *Annu. Res. Briefs 2004*, Center for Turbulence Research, NASA Ames/Stanford University.
- Hartlep, T., Mansour, N.N.: 2005, Acoustic wave propagation in the Sun. *Annu. Res. Briefs 2005*, Center for Turbulence Research, NASA Ames/Stanford University.
- Hartlep, T., Zhao, J., Mansour, N.N., Kosovichev, A.G.: 2008, Validating time-distance far-side imaging of solar active regions through numerical simulations. *Astrophys. J.* **689**, 1373.
- Hartlep, T., Kosovichev, A.G., Zhao, J., Mansour, N.N.: 2011, Signatures of emerging subsurface structures in acoustic power maps of the Sun. *Sol. Phys.* **268**, 321.

Este documento incorpora firma electrónica, y es copia auténtica de un documento electrónico archivado por la ULL según la Ley 39/2015.  
Su autenticidad puede ser contrastada en la siguiente dirección <https://sede.ull.es/validacion/>

Identificador del documento: 963882

Código de verificación: QDmfX6JG

Firmado por: MANUEL DIAZ ALFARO  
UNIVERSIDAD DE LA LAGUNA

Fecha: 26/06/2017 15:24:15

FERNANDO JAVIER PEREZ HERNANDEZ  
UNIVERSIDAD DE LA LAGUNA

26/06/2017 15:25:57

ERNESTO PEREDA DE PABLO  
UNIVERSIDAD DE LA LAGUNA

28/06/2017 13:21:41

- Hartlep, T., Zhao, J., Kosovichev, A.G., Mansour, N.N.: 2013, Solar wave-field simulation for testing prospects of helioseismic measurements of deep meridional flows. *Astrophys. J.* **762**, 132.
- Harvey, J.W., Hill, F., Hubbard, R.P., Kennedy, J.R., Leibacher, J.W., Pintar, J.A., Gilman, P.A., Noyes, R.W., Title, A.M., Toomre, J., Ulrich, R.K., Bhatnagar, A., Kennewell, J.A., Marquette, W., Patron, J., Saa, O., Yasukawa, E.: 1996, The *Global Oscillation Network Group* (GONG) project. *Science* **272**, 1284.
- Hathaway, D.H.: 2010, The solar cycle. *Living Reviews in Solar Physics* **7**.
- Hathaway, D.H., Wilson, R.M., Reichmann, E.J.: 2002, Group sunspot numbers: Sunspot cycle characteristics. *Sol. Phys.* **211**, 357.
- Hayashi, K., Benevolenskaya, E., Hoeksema, T., Liu, Y., Zhao, X.P.: 2006, Three-dimensional magnetohydrodynamic simulation of a global solar corona using a temperature distribution map obtained from SOHO EIT measurements. *Astrophys. J. Lett.* **636**, L165.
- Hill, F.: 1988, Rings and trumpets—three-dimensional power spectra of solar oscillations. *Astrophys. J.* **333**, 996.
- Howe, R.: 2009, Solar interior rotation and its variation. *Living Reviews in Solar Physics* **6**.
- Howe, R., Thompson, M.J.: 1996, On the use of the error correlation function in helioseismic inversions. *Mon. Not. Roy. Astron. Soc.* **281**, 1385.
- Howe, R., Christensen-Dalsgaard, J., Hill, F., Komm, R.W., Larsen, R.M., Schou, J., Thompson, M.J., Toomre, J.: 2000, Dynamic variations at the base of the solar convection zone. *Science* **287**, 2456.
- Howe, R., Christensen-Dalsgaard, J., Hill, F., Komm, R., Schou, J., Thompson, M.J.: 2005, Solar convection-zone dynamics, 1995-2004. *Astrophys. J.* **634**, 1405.
- Hoyt, D.V., Schatten, K.H.: 1998, Group sunspot numbers: A new solar activity reconstruction. *Sol. Phys.* **181**, 491.
- Hughes, A.L.H., Jain, K., Kholikov, S., the NISP solar interior group: 2016, GONG ClassicMerge: Pipeline and product. *ArXiv e-prints*.
- Hughes, D.W., Rosner, R., Weiss, N.O.: 2012, *The solar tachocline*. ISBN 9780521861014.
- Ilonidis, S., Zhao, J., Hartlep, T.: 2009, Time-distance solar far-side imaging using three-skip acoustic signals. *Sol. Phys.* **258**, 181.
- Ilonidis, S., Zhao, J., Kosovichev, A.: 2011, Detection of emerging sunspot regions in the solar interior. *Science* **333**, 993.
- Jensen, J.M., Duvall, T.L. Jr., Jacobsen, B.H., Christensen-Dalsgaard, J.: 2001, Imaging an emerging active region with helioseismic tomography. *Astrophys. J. Lett.* **553**, L193.

Este documento incorpora firma electrónica, y es copia auténtica de un documento electrónico archivado por la ULL según la Ley 39/2015.  
Su autenticidad puede ser contrastada en la siguiente dirección <https://sede.ull.es/validacion/>

Identificador del documento: 963882

Código de verificación: QDmfX6JG

Firmado por: MANUEL DIAZ ALFARO  
UNIVERSIDAD DE LA LAGUNA

Fecha: 26/06/2017 15:24:15

FERNANDO JAVIER PEREZ HERNANDEZ  
UNIVERSIDAD DE LA LAGUNA

26/06/2017 15:25:57

ERNESTO PEREDA DE PABLO  
UNIVERSIDAD DE LA LAGUNA

28/06/2017 13:21:41

- Kholikov, S.: 2013, A search for helioseismic signature of emerging active regions. *Sol. Phys.* **287**, 229.
- Kholikov, S., Hill, F.: 2008, Acoustic radius measurements from MDI and GONG. *Sol. Phys.* **251**, 157.
- Khomenko, E., Collados Vera, M.: 2012, Simulations of chromospheric heating by ambipolar diffusion. In: Rimmele, T.R., Tritschler, A., Wöger, F., Collados Vera, M., Socas-Navarro, H., Schlichenmaier, R., Carlsson, M., Berger, T., Cadavid, A., Gilbert, P.R., Goode, P.R., Knölker, M. (eds.) *Second ATST-EAST meeting: Magnetic fields from the photosphere to the corona*, *ASP Conf. Ser.* **463**, 281.
- Khomenko, E., Díaz, A., de Vicente, A., Collados, M., Luna, M.: 2014, Rayleigh-Taylor instability in prominences from numerical simulations including partial ionization effects. *Astron. Astrophys.* **565**, A45.
- Komm, R., González Hernández, I., Howe, R., Hill, F.: 2015, Solar-cycle variation of subsurface meridional flow derived with ring-diagram analysis. *Sol. Phys.* **290**, 3113.
- Kosovichev, A.G.: 1996, Helioseismic constraints on the gradient of angular velocity at the base of the solar convection zone. *Astrophys. J. Lett.* **469**, L61.
- Kosovichev, A.G., Duvall, T.L.: 2006, Active region dynamics. *Space Sci. Rev.* **124**, 1.
- Kosovichev, A.G., Duvall, T.L. Jr., Scherrer, P.H.: 2000, Time-distance inversion methods and results (Invited Review). *Sol. Phys.* **192**, 159.
- Kosovichev, A.G., Schou, J., Scherrer, P.H., Bogart, R.S., Bush, R.I., Hoeksema, J.T., Aloise, J., Bacon, L., Burnette, A., de Forest, C., Giles, P.M., Leibbrand, K., Nigam, R., Rubin, M., Scott, K., Williams, S.D., Basu, S., Christensen-Dalsgaard, J., Dappen, W., Rhodes, E.J. Jr., Duvall, T.L. Jr., Howe, R., Thompson, M.J., Gough, D.O., Sekii, T., Toomre, J., Tarbell, T.D., Title, A.M., Mathur, D., Morrison, M., Saba, J.L.R., Wolfson, C.J., Zayer, I., Milford, P.N.: 1997, Structure and rotation of the solar interior: initial results from the MDI medium- $\ell$  program. *Sol. Phys.* **170**, 43.
- Larsen, R.M.: 1998, Efficient algorithms for helioseismic inversion. PhD thesis, University of Aarhus, Aarhus, Denmark.
- Lefebvre, S., Kosovichev, A.G.: 2005, Changes in the subsurface stratification of the Sun with the 11-year activity cycle. *Astrophys. J. Lett.* **633**, L149.
- Leibacher, J.W.: 1999, The *Global Oscillation Network Group* (GONG) project. *Advances in Space Research* **24**, 173.
- Leibacher, J.W., Stein, R.F.: 1971, A new description of the solar five-minute oscillation. *Astrophys. Lett.* **7**, 191.
- Leighton, R.B.: 1969, A magneto-kinematic model of the solar cycle. *Astrophys. J.* **156**, 1.

Este documento incorpora firma electrónica, y es copia auténtica de un documento electrónico archivado por la ULL según la Ley 39/2015.  
Su autenticidad puede ser contrastada en la siguiente dirección <https://sede.ull.es/validacion/>

Identificador del documento: 963882

Código de verificación: QDmfX6JG

Firmado por: MANUEL DIAZ ALFARO  
UNIVERSIDAD DE LA LAGUNA

Fecha: 26/06/2017 15:24:15

FERNANDO JAVIER PEREZ HERNANDEZ  
UNIVERSIDAD DE LA LAGUNA

26/06/2017 15:25:57

ERNESTO PEREDA DE PABLO  
UNIVERSIDAD DE LA LAGUNA

28/06/2017 13:21:41

- Leighton, R.B., Noyes, R.W., Simon, G.W.: 1962, Velocity fields in the solar atmosphere. I. Preliminary report. *Astrophys. J.* **135**, 474.
- Leka, K.D., Barnes, G., Birch, A.C., González Hernández, I., Dunn, T., Javornik, B., Braun, D.C.: 2013, Helioseismology of pre-emerging active regions. I. Overview, data, and target selection criteria. *Astrophys. J.* **762**, 130.
- Liewer, P.C., González Hernández, I., Hall, J.R., Lindsey, C., Lin, X.: 2014, Testing the reliability of predictions of far-side active regions from helioseismology using STEREO far-side observations of solar activity. *Sol. Phys.* **289**, 3617.
- Lindsey, C., Braun, D.C.: 1990, Helioseismic imaging of sunspots at their antipodes. *Sol. Phys.* **126**, 101.
- Lindsey, C., Braun, D.C.: 1997, Helioseismic holography. *Astrophys. J.* **485**, 895.
- Lindsey, C., Braun, D.C.: 1998, Acoustic signatures of subphotospheric structure underlying sunspots. *Astrophys. J. Lett.* **509**, L129.
- Lindsey, C., Braun, D.C.: 2000a, Basic principles of solar acoustic holography (Invited Review). *Sol. Phys.* **192**, 261.
- Lindsey, C., Braun, D.C.: 2000b, Seismic images of the far side of the Sun. *Science* **287**, 1799.
- Lindsey, C., Braun, D.C.: 2004, Principles of seismic holography for diagnostics of the shallow subphotosphere. *Astrophys. J. Suppl.* **155**, 209.
- Lindsey, C., Braun, D.C.: 2005, The acoustic showerglass. I. Seismic diagnostics of photospheric magnetic fields. *Astrophys. J.* **620**, 1107.
- MacDonald, G.A., Henney, C.J., Díaz Alfaro, M., González Hernández, I., Arge, C.N., Lindsey, C., McAteer, R.T.J.: 2015, Active region morphologies selected from near-side helioseismic data. *Astrophys. J.* **807**, 21.
- MacGregor, K.B., Charbonneau, P.: 1997, Solar interface dynamos. I. Linear, kinematic models in Cartesian geometry. *Astrophys. J.* **486**, 484.
- Masarik, J., Beer, J.: 1999, Simulation of particle fluxes and cosmogenic nuclide production in the Earth's atmosphere. *J. Geophys. Res.* **104**, 12099.
- Maunder, E.W.: 1903, Spörer's law of zones. *The Observatory* **26**, 329.
- Maunder, E.W.: 1904, Note on the distribution of sun-spots in heliographic latitude, 1874-1902. *Mon. Not. Roy. Astron. Soc.* **64**, 747.
- Moradi, H., Baldner, C., Birch, A.C., Braun, D.C., Cameron, R.H., Duvall, T.L., Gizon, L., Haber, D., Hanasoge, S.M., Hindman, B.W., Jackiewicz, J., Khomenko, E., Komm, R., Rajaguru, P., Rempel, M., Roth, M., Schlichenmaier, R., Schunker, H., Spruit, H.C., Strassmeier, K.G., Thompson, M.J., Zharkov, S.: 2010, Modeling the subsurface structure of sunspots. *Sol. Phys.* **267**, 1.

Este documento incorpora firma electrónica, y es copia auténtica de un documento electrónico archivado por la ULL según la Ley 39/2015.  
Su autenticidad puede ser contrastada en la siguiente dirección <https://sede.ull.es/validacion/>

Identificador del documento: 963882

Código de verificación: QDmfX6JG

Firmado por: MANUEL DIAZ ALFARO  
UNIVERSIDAD DE LA LAGUNA

Fecha: 26/06/2017 15:24:15

FERNANDO JAVIER PEREZ HERNANDEZ  
UNIVERSIDAD DE LA LAGUNA

26/06/2017 15:25:57

ERNESTO PEREDA DE PABLO  
UNIVERSIDAD DE LA LAGUNA

28/06/2017 13:21:41

- Moreno-Insertis, F.: 1983, Rise times of horizontal magnetic flux tubes in the convection zone of the Sun. *Astron. Astrophys.* **122**, 241.
- Moreno-Insertis, F., Schüssler, M., Ferriz-Mas, A.: 1992, Storage of magnetic flux tubes in a convective overshoot region. *Astron. Astrophys.* **264**, 686.
- Narain, U., Ulmschneider, P.: 1990, Chromospheric and coronal heating mechanisms. *Space Sci. Rev.* **54**, 377.
- Narain, U., Ulmschneider, P.: 1996, Chromospheric and coronal heating mechanisms II. *Space Sci. Rev.* **75**, 453.
- Nordlund, A., Brandenburg, A., Jennings, R.L., Rieutord, M., Ruokolainen, J., Stein, R.F., Tuominen, I.: 1992, Dynamo action in stratified convection with overshoot. *Astrophys. J.* **392**, 647.
- Parker, D.G., Ulrich, R.K., Pap, J.M.: 1998, Modeling solar UV variations using Mount Wilson Observatory indices. *Sol. Phys.* **177**, 229.
- Parker, E.N.: 1979, Sunspots and the physics of magnetic flux tubes. IX - Umbral dots and longitudinal overstability. *Astrophys. J.* **234**, 333.
- Parker, E.N.: 1993, A solar dynamo surface wave at the interface between convection and nonuniform rotation. *Astrophys. J.* **408**, 707.
- Patrón, J., González Hernández, I., Chou, D.-Y., Sun, M.-T., Mu, T.-M., Loudagh, S., Bala, B., Chou, Y.-P., Lin, C.-H., Huang, I.-J., Jiménez, A., Rabello-Soares, M.C., Ai, G., Wang, G.-P., Zirin, H., Marquette, W., Neno, J., Ehgamberdiev, S., Khalikov, S., TON Team: 1997, Comparison of two fitting methods for ring diagram analysis of very high  $\ell$  solar oscillations. *Astrophys. J.* **485**, 869.
- Patrón, J., González Hernández, I., Jiménez, A., Jiménez-Reyes, S.J., Martín, I., Pallé, P.L., Pérez Hernández, F., Régulo, C., Roca Cortés, T.: 1998, 3-D helioseismology: rings and horizontal flows. *Astrophys. Space Sci.* **263**, 327.
- Pérez Hernández, F., González Hernández, I.: 2010, Green's functions for far-side seismic images: A polar-expansion approach. *Astrophys. J.* **711**, 853.
- Pulkkinen, T.: 2007, Space weather: Terrestrial perspective. *Living Reviews in Solar Physics* **4**.
- Rempel, M.: 2015, Numerical simulations of sunspot decay: On the penumbra-Evershed flow-moat flow connection. *Astrophys. J.* **814**, 125.
- Rempel, M., Schüssler, M., Knölker, M.: 2009, Radiative magnetohydrodynamic simulation of sunspot structure. *Astrophys. J.* **691**, 640.
- Rempel, M., Schüssler, M., Cameron, R.H., Knölker, M.: 2009, Penumbra structure and outflows in simulated sunspots. *Science* **325**, 171.
- Rhodes, E.J. Jr., Ulrich, R.K., Simon, G.W.: 1977, Observations of nonradial p-mode oscillations on the Sun. *Astrophys. J.* **218**, 901.

Este documento incorpora firma electrónica, y es copia auténtica de un documento electrónico archivado por la ULL según la Ley 39/2015.  
Su autenticidad puede ser contrastada en la siguiente dirección <https://sede.ull.es/validacion/>

Identificador del documento: 963882

Código de verificación: QDmfX6JG

Firmado por: MANUEL DIAZ ALFARO  
UNIVERSIDAD DE LA LAGUNA

Fecha: 26/06/2017 15:24:15

FERNANDO JAVIER PEREZ HERNANDEZ  
UNIVERSIDAD DE LA LAGUNA

26/06/2017 15:25:57

ERNESTO PEREDA DE PABLO  
UNIVERSIDAD DE LA LAGUNA

28/06/2017 13:21:41

- Rhodes, E.J. Jr., Kosovichev, A.G., Schou, J., Scherrer, P.H., Reiter, J.: 1997, Measurements of frequencies of solar oscillations from the MDI medium- $\ell$  program. *Sol. Phys.* **175**, 287.
- Ribes, J.C., Nesme-Ribes, E.: 1993, The solar sunspot cycle in the Maunder minimum AD1645 to AD1715. *Astron. Astrophys.* **276**, 549.
- Richards, M.T., Rogers, M.L., Richards, D.S.P.: 2009, Long-term variability in the length of the solar cycle. *PASP* **121**, 797.
- Rodder, F.: 1975, Principle of production of an acoustic hologram of the solar surface. *C. R. Acad. Sci. B* **281**, 93.
- Rozelot, J.-P., Neiner, C.: 2011, *The pulsations of the Sun and the stars*. ISBN 9783642199271.
- Rüdiger, G., Brandenburg, A.: 1995, A solar dynamo in the overshoot layer: cycle period and butterfly diagram. *Astron. Astrophys.* **296**, 557.
- Scherrer, P.H., Bogart, R.S., Bush, R.I., Hoeksema, J.T., Kosovichev, A.G., Schou, J., Rosenberg, W., Springer, L., Tarbell, T.D., Title, A., Wolfson, C.J., Zayer, I., MDI Engineering Team: 1995, The Solar Oscillations Investigation - Michelson Doppler Imager. *Sol. Phys.* **162**, 129.
- Scherrer, P.H., Schou, J., Bush, R.I., Kosovichev, A.G., Bogart, R.S., Hoeksema, J.T., Liu, Y., Duvall, T.L., Zhao, J., Title, A.M., Schrijver, C.J., Tarbell, T.D., Tomczyk, S.: 2012, The *Helioseismic and Magnetic Imager* (HMI) investigation for the *Solar Dynamics Observatory* (SDO). *Sol. Phys.* **275**, 207.
- Schou, J., Bogart, R.S.: 1998, Flows and horizontal displacements from ring diagrams. *Astrophys. J. Lett.* **504**, L131.
- Schou, J., Kosovichev, A.G., Goode, P.R., Dziembowski, W.A.: 1997, Determination of the Sun's seismic radius from the SOHO Michelson Doppler Imager. *Astrophys. J. Lett.* **489**, L197.
- Schunker, H.: 2010, Local helioseismology and the active Sun. *Astron. Nachr.* **331**, 901.
- Schunker, H., Braun, D.C., Cally, P.S., Lindsey, C.: 2005, The local helioseismology of inclined magnetic fields and the showerglass effect. *Astrophys. J. Lett.* **621**, L149.
- Schüssler, M., Caligari, P., Ferriz-Mas, A., Moreno-Insertis, F.: 1994, Instability and eruption of magnetic flux tubes in the solar convection zone. *Astron. Astrophys.* **281**, L69.
- Schwabe, M.: 1844, Sonnenbeobachtungen im Jahre 1843. *Astron. Nachr.* **21**, 233.
- Serebryanskiy, A., Chou, D.-Y.: 2005, Comparison of solar cycle variations of solar p-mode frequencies from GONG and MDI. *Astrophys. J.* **633**, 1187.

Este documento incorpora firma electrónica, y es copia auténtica de un documento electrónico archivado por la ULL según la Ley 39/2015.  
Su autenticidad puede ser contrastada en la siguiente dirección <https://sede.ull.es/validacion/>

Identificador del documento: 963882

Código de verificación: QDmfX6JG

Firmado por: MANUEL DIAZ ALFARO  
UNIVERSIDAD DE LA LAGUNA

Fecha: 26/06/2017 15:24:15

FERNANDO JAVIER PEREZ HERNANDEZ  
UNIVERSIDAD DE LA LAGUNA

26/06/2017 15:25:57

ERNESTO PEREDA DE PABLO  
UNIVERSIDAD DE LA LAGUNA

28/06/2017 13:21:41

- Spiegel, E.A., Weiss, N.O.: 1980, Magnetic activity and variations in solar luminosity. *Nature* **287**, 616.
- Spiegel, E.A., Zahn, J.-P.: 1992, The solar tachocline. *Astron. Astrophys.* **265**, 106.
- Stein, R.F., Nordlund, Å.: 2000, Realistic solar convection simulations. *Sol. Phys.* **192**, 91.
- Stuiver, M., Quay, P.D.: 1980, Changes in atmospheric Carbon-14 attributed to a variable Sun. *Science* **207**, 11.
- Sun, M.-T., Chou, D.-Y., TON Team: 2002, The inversion problem of phase travel time perturbations in acoustic imaging. *Sol. Phys.* **209**, 5.
- Tobias, S.M., Brummell, N.H., Clune, T.L., Toomre, J.: 2001, Transport and storage of magnetic field by overshooting turbulent compressible convection. *Astrophys. J.* **549**, 1183.
- Ulrich, R.K.: 1970, The five-minute oscillations on the solar surface. *Astrophys. J.* **162**, 993.
- Vernazza, J.E., Avrett, E.H., Loeser, R.: 1981, Structure of the solar chromosphere. III - Models of the EUV brightness components of the quiet-sun. *Astrophys. J. Suppl.* **45**, 635.
- Waldmeier, M.: 1935, Neue Eigenschaften der Sonnenfleckenkurve. *Astron. Mitt. Zürich* **14**, 105.
- Waldmeier, M.: 1939, Die Zonenwanderung der Sonnenflecken. *Astron. Mitt. Zürich* **14**, 470.
- Wang, Y.-M., Sheeley, N.R. Jr.: 1991, Magnetic flux transport and the Sun's dipole moment - New twists to the Babcock-Leighton model. *Astrophys. J.* **375**, 761.
- Weiss, N.O., Thompson, M.J.: 2009, The solar dynamo. *Space Sci. Rev.* **144**, 53.
- Wolf, R.: 1861, Abstract of his latest results. *Mon. Not. Roy. Astron. Soc.* **21**, 77.
- Woodard, M.F.: 2002, Solar subsurface flow inferred directly from frequency-wavenumber correlations in the seismic velocity field. *Astrophys. J.* **565**, 634.
- Woodard, M.F.: 2007, Probing supergranular flow in the solar interior. *Astrophys. J.* **668**.
- Woodard, M.F.: 2009, Seismic detection of solar mesogranular-scale flow. *Astrophys. J. Lett.* **706**, L62.
- Yalim, M.S., Poedts, S.: 2014, 3D global magnetohydrodynamic simulations of the solar wind/Earth's magnetosphere interaction. In: Pogorelov, N.V., Audit, E., Zank, G.P. (eds.) *8th international conference of numerical*

Este documento incorpora firma electrónica, y es copia auténtica de un documento electrónico archivado por la ULL según la Ley 39/2015.  
Su autenticidad puede ser contrastada en la siguiente dirección <https://sede.ull.es/validacion/>

Identificador del documento: 963882

Código de verificación: QDmfX6JG

Firmado por: MANUEL DIAZ ALFARO  
UNIVERSIDAD DE LA LAGUNA

Fecha: 26/06/2017 15:24:15

FERNANDO JAVIER PEREZ HERNANDEZ  
UNIVERSIDAD DE LA LAGUNA

26/06/2017 15:25:57

ERNESTO PEREDA DE PABLO  
UNIVERSIDAD DE LA LAGUNA

28/06/2017 13:21:41

- modeling of space plasma flows (ASTRONUM 2013)*, *ASP Conf. Ser.* **488**, 192.
- Yee, K.: 1966, Numerical solution of initial boundary value problems involving Maxwell's equations in isotropic media. *IEEE Trans. Antennas. Propag.* **14**, 302.
- Zhao, J., Hartlep, T., Kosovichev, A.G., Mansour, N.N.: 2009, Imaging the solar tachocline by time-distance helioseismology. *Astrophys. J.* **702**, 1150.
- Zharkov, S., Thompson, M.J.: 2008, Time-distance analysis of the emerging active region NOAA 10790. *Sol. Phys.* **251**, 369.
- Zharkov, S., Nicholas, C.J., Thompson, M.J.: 2007, Time distance study of isolated sunspots. *Astron. Nachr.* **328**, 240.

Este documento incorpora firma electrónica, y es copia auténtica de un documento electrónico archivado por la ULL según la Ley 39/2015.  
Su autenticidad puede ser contrastada en la siguiente dirección <https://sede.ull.es/validacion/>

Identificador del documento: 963882

Código de verificación: QDmfX6JG

Firmado por: MANUEL DIAZ ALFARO  
UNIVERSIDAD DE LA LAGUNA

Fecha: 26/06/2017 15:24:15

FERNANDO JAVIER PEREZ HERNANDEZ  
UNIVERSIDAD DE LA LAGUNA

26/06/2017 15:25:57

ERNESTO PEREDA DE PABLO  
UNIVERSIDAD DE LA LAGUNA

28/06/2017 13:21:41